Department of Physics

Spectroscopic studies of biological tribofilms at hip implant taper junctions and transfer material at MoS_2-steel wear couples

Dissertation

submitted in partial fulfillment of
the requirements for the degree of

Dr. rer. nat.

to the Faculty of Physics
TU Dortmund University, Germany

by

Adrian Wittrock
born in Frankenberg (Eder)

Dortmund, December 2024

Accepted dissertation by the Faculty of Physics of the TU Dortmund University, Germany.

Date of the oral examination: February 10, 2025

Examination board:

Dr. Jörg Debus
Prof. Dr. Carsten Westphal
Prof. Dr.-Ing. Alfons Fischer
Apl. Prof. Dr. Doris Reiter
PD Dr. Andrea Helen Knue

Table of Contents

Table of Contents III

List of Figures VI

List of Tables VII

1 Motivation 3

2 Fundamental Theory 7
2.1 Light-Matter Interactions . . . 7
2.1.1 Light Scattering - A Localized Electric Dipol . . . 9
2.1.2 Inelastic Light Scattering - Raman Effect . . . 10
2.2 Fundamentals of Group Theory for Raman Spectroscopy . . . 15
2.2.1 Application of Symmetry in Raman Spectroscopy . . . 22
2.3 Three-Dimensional Structural Organization of Proteins . . . 23
2.4 Protein Adsorption at Solid-Liquid Interfaces . . . 27
2.4.1 Protein Interactions with the Surface . . . 28
2.4.2 Competitive Adsorption . . . 30
2.4.3 Concentration Dependent Adsorption . . . 30
2.4.4 Metal-Protein Complex Formation . . . 31
2.5 Raman Signals of Selected Materials . . . 32
2.5.1 Raman Signals of Molybdenum disulfide (MoS_2) . . . 32
2.5.2 Raman Signals of Organic Materials . . . 35
2.6 Tribology . . . 39
2.6.1 Friction and Wear . . . 39
2.6.2 Contact Problem - Hertzian Contact . . . 42
2.6.3 Tribology Across Scales . . . 44
2.6.4 The Tribomaterial - The Third-Bodies . . . 48
2.6.5 Metal Structure and Grain Boundaries . . . 50
2.6.6 Tribological Properties of Selected Materials . . . 52

3 Experimental Details 57
3.1 Confocal Raman Scattering Setup . . . 57
3.1.1 Material Penetration Depth of 532 nm Laser Light . . . 59
3.2 Sample Preparation - Solid Lubricants . . . 61
3.2.1 Physical Vapour Deposition (PVD) . . . 61
3.2.2 Layer Thickness Measurements . . . 63
3.2.3 Transfer Material Experiments and Tribometer . . . 64
3.3 Fretting Experiments – Artificial Hip Joints . . . 65

4 Protein-Metal Interactions and CoS_x Tribofilm Formation 69
4.1 Topography of Tribologically Loaded Pins and Cylinders Surface 73
4.2 Raman Spectra of the AWP at the Co-Alloy and High-Nitrogen Steel Pin Surfaces 76
4.2.1 Reference Spectrum of Pure BCS and of Unworn Pin Surfaces 76
4.2.2 Identification of Oxidized Transition Metal Compounds 79
4.2.3 Fretting Induced Changes in the Biotribological Material 81
4.3 Raman Spectra of the FT at the High-Nitrogen Steel and Co-Alloy Pin Surfaces 88
4.3.1 Secondary Structure of BCS within the FT at Both Pin Materials . 88
4.3.2 Formation of sp^2 Hybridized Amorphous Carbon Within the FT . . 89
4.4 Formation of a Nanocrystalline CoS_x Tribomaterial at Hip Implant Taper Junctions 90
4.4.1 Elemental Concentrations and Spatial Distribution of Co-alloy Metals within the FT 91
4.4.2 Spectral Appearance and Origin of the Raman Signals 92
4.4.3 Identification of CoS_x by Laser Induced Oxidation and Raman Spectroscopy 94
4.4.4 Identification CoS_x and Spatial Distribution of Different Elements within the Cross-Section of the Worn Co-alloy Surface by STEM . . 96
4.4.5 Spatial Distribution of CoS_x Within the FT 100
4.5 Conclusion 104

5 MoS_2 Tribomaterial Characterization and Coating Thickness Measurement 109
5.1 Tribomaterial in Steel-MoS_2:X Tribosystems 110
5.1.1 Raman Scattering Spectra at Main and Counter Body and Impact of Doping Element on MoS_2 112
5.1.2 Strain Distribution in MoS_2 Transfer Material on Counter Bodies . . 118
5.1.3 Spatial Distribution of Tribochemical Reaction Products 120
5.1.4 Tribological Induction of Few-Layer Graphene: Structural Characterization and Spatial Distribution 124
5.1.5 Conclusion 126
5.2 Coating Thickness Determination Via Ablation-Raman Coating Thickness Analysis 128
5.2.1 Laser Ablation Series of MoS_2 Layers on Si Wafers for Calibration of the ARCTA Method and Verification on Curved Surfaces 130
5.2.2 Other Coating Systems and the ARCTA Method 133
5.2.3 Spatial Investigation of the Irradiated Area on the MoS_2 Coating . . 136
5.2.4 Conclusion 138

6 Outlook 139

Bibliography 143

List of author's publications 185

List of Figures

2.1 Symmetry Operations Applied to the Vibrational Normal Modes of H_2O. . 14
2.2 Symmetry Operations and Elements of the H_2O molecule. 17
2.3 Flow Chart to Assign a Point Group. 19
2.4 α-, β-, and γ-Amino Acids. 23
2.5 Protein Structure: From Primary Polypeptide Chains to Secondary Configurations and the Tertiary Arrangement. 24
2.6 Peptide Bond and Possible Rotation Angle. 25
2.7 Cystine Complex Formation from Two Cysteine Amino Acids. 26
2.8 Vroman effect and Langmuir Adsorption Isotherm Behavior. 29
2.9 Structure of the Tripeptide Glutathione and its Metal Ion Binding Sites. . . 31
2.10 Structure of 2H-MoS_2 and Vibrational Modes of Bulk MoS_2. 32
2.11 Main Four Wear Mechanisms and Sub-mechanisms. 42
2.12 Schematic of a Hertzian Contact. 43
2.13 Multiscale Nature of Tribology - Main Wear Mechanisms. 45
2.14 Schematic Cross-Section of Metal Surfaces Before and After Tribological Load. 46
2.15 Basal and Edge Planes MoS_2. 53

3.1 Confocal Raman Setup and Extension for Laser Ablation. 58
3.2 Magnetron Sputtering Principels and PVD Chamber Cathode Setup. 62
3.3 Scheme of the Tribological Ball-on-Disc Setup. 64
3.4 Schematic of Hip Implant Fretting Simulation Setup. 66

4.1 Causes for failure of implants 69
4.2 Microscope Images of the Pin Surfaces. 74
4.3 Topography of the Pin Surfaces After Fretting Tests. 75
4.4 Raman Spectra Illustrating the Characteristics of the Dried BCS. 77
4.5 Low-Wavenumber Raman Spectra Comparison Dried BCS versus AWP. . . 80
4.6 High-Wavenumber Raman Spectra Comparison Dried BCS versus AWP. . . 82
4.7 Comparison of Hydrocarbon Vibrations on Both Pin Materials Under Different Fretting Cycles. 85
4.8 Identification of sp^2 Hybridized Amorphous Carbon within the FT through Raman Spectroscopy. 90
4.9 SEM Image and EDS Pattern and Spectrum of the Co-alloy FT. 91
4.10 Raman Mappings of the FT of the Co-alloy Before and After Laser-Induced Oxidation. 93
4.11 Characterization of the CoCrMo Base Material and the CoS_x Tribolayer Using BF-STEM. 97
4.12 Distribution of the Chemical Elements within the Cross-Section, Determined by STEM-EDS. 98

4.13 Analysis of Elemental Distribution Across the Surficial Tribolayer. 99
4.14 Distribution of Sulfur within the Surficial Tribolayer via STEM-EELS Measurements. 99
4.15 Locations where CoS_x can be Identified within the FT of the Co-alloy. . . . 101
4.16 Spacial Raman Mappings within the Co-alloy FT and the Fitting Results. . 103
4.17 Schematic Overview: Agglomerated Tribomaterial Detectable on Both Pin Materials in the AWP Region. 104
4.18 Schematic Overview: CoS_x Formation on the Co-alloy Surface in the FT. . 106

5.1 Raman Scattering Spectrum of MoS_2 Acquired on the Transfer Material: Phonon Modes and Fitting Curves. 112
5.2 SEM Images and Raman Mappings of Tribological Tracks on MoS_2:X Surfaces after Ball-on-Disc Testing, with Corresponding Coefficients of Friction and Wear. 114
5.3 Morphological and Topographical Analysis of Element-Modified MoS_2:X Thin Films. 115
5.4 Probability Densities of Raman Shifts of the E_{2g} and A_{1g} Modes and their Intensity Ratio on the Main and Counter Body Following Tribological Testing of MoS_2:X. 117
5.5 Spatial Distributions of Out-of-Plane and In-Plane Strains are Derived from the $A_{1g}(\Gamma)$ and $E^1_{2g}(\Gamma)$ Raman Modes of MoS_2 Within the Tribological Contact Area. 118
5.6 Identification of Tribochemical Oxides within the Tribomaterial on the Counter Body and their Spatial Distribution. 121
5.7 Characterization of Fe Oxide Phases Present in the Wear Track of Counter Bodies Using Raman Spectroscopy. 122
5.8 Raman Spectral Analysis Reveals a Few-Layer Graphene Presence and its Spatial Distribution on the Counter Body after the Tribological Test. 125
5.9 Schematic Representation of the Spatial Distribution of Tribologically Induced Strains, Oxides, and Graphene Formation in the Transfer Material at the Steel Counter Body Surface. 127
5.10 SEM and Light Microscopic Images of the MoS_2 Coatings Used for the Thickness Measurements with ARCTA. 129
5.11 Raman Spectra Detected During a Laser Ablation Series of a MoS_2 Coating and the Relationship between the Number of High-Energy Laser Pulses and the Coating Thickness. 131
5.12 Applicability of the ARCTA Method for Other Substrates or Multilayer Coatings. 134
5.13 Spatial Distribution of Raman Signals in the Area Irradiated by the High-Energy Laser Following the ARCTA Experiment. 136

6.1 Raman Spectrum of a Ti6Al4V Cylinder within the FT. 139

List of Tables

2.1 List of Symmetry Operations. 16
2.2 Group Multiplication Table for the Point Group C_{2v}. 17
2.3 Character Table for C_{2v} Point Group. 21
2.4 Mulliken Symbols for the Irreducible Representations. 22
2.5 Dihedral Angles for Conformations of the Cysteine Complex. 27
2.6 Frequency Shifts for Raman Active Modes for Monolayer, Bilayer, Trilayer, Quadrilayer, and Bulk MoS_2. 33
2.7 Assignment of Raman Bands to Functional Groups of Organic Materials. . 36
2.8 Occurrence of Amino Acids in Bovine and Human Serum Albumin. 37
2.9 Characteristic Raman Lines of Aromatic Amino Acids. 38

3.1 Objectives Specifications Used in this Thesis. 59
3.2 Penetration Depth of 532 nm Laser Light into Various Materials. 60

4.1 Raman Scattering Lines and Assignments (Organic). 78
4.2 Detected Raman Signals within the FT of Co-alloy Before and After Oxidation. 95

5.1 Impact of Novel Friction and Wear Reduction Technologies on Fuel Efficiency and CO_2 Emissions. 109

Abstract

In this thesis, the structural and chemical characteristics of the tribomaterial using spectroscopic techniques are investigated. Specifically, MoS_2-steel wear couples, commonly employed in industrial applications, and biomedical artificial hip joints are analyzed.
Modular hip implants are widely used to treat arthritis, but complications due to friction and wear at the head-taper interface may cause the necessity for revision surgery. The mechanical-chemical reaction products and structural features at the head-taper interface of Ti6Al4V and low-carbon cobalt alloy or high-nitrogen steel surfaces, which were subjected to *in vitro* fretting corrosion tests using bovine calf serum, are investigated using Raman spectroscopy. From these spectra, protein folding/unfolding, the formation of proteinaceous clusters, and the adsorption behavior of short and long aliphatic chains can be deducted. All these structural changes depend on the hydrophilicity of the metallic surfaces and the duration of the fretting process. The analysis also identifies significant differences in the composition of agglomerated wear particles, including chromates, iron oxides, and adsorbed proteins. On both materials, long fretting duration leads to protein cleavage and the formation of sp^2-hybridized amorphous carbon. Additionally, the formation of a thin (15 nm), areal, nanocrystalline-amorphous CoS_x tribofilm is revealed on the Co-alloy surface. This tribofilm forms from sulfur ions released by cysteine decomposition and cobalt ions from tribocorrosion and may act as an extreme-pressure anti-wear layer. Thus, it may improve the taper junction longevity and mitigate corrosive attacks. The CoS_x compound's structure is similar to that of the solid lubricant MoS_2.
The tribological contact between MoS_2 and steel leads to structural-chemical changes, which are another focus of this thesis. Raman spectroscopy shows compressive and tensile strain within the MoS_2 transfer material. In addition, if MoS_2 is no longer present in the contact area, Mo, S, and Fe oxidation is detected, for instance, Mo_4O_{11} in the Magnéli-phase. Thereby, the formation of tribo-chemical oxides depends on the modifying element. The study also reveals the formation of disordered graphene in a few layers on the counter body surface. The results characterize the structural and chemical features of the MoS_2 transfer material and thus enable the prediction of material failure at microscopic level.
In addition to these mechanism-driven investigations, a novel method, ablation-Raman coating thickness analysis (ARCTA), is developed for coating thickness measurement, especially for curved coatings. This method uses a high-energy pulsed laser to ablate a part of the MoS_2 coating in the µm range, followed by Raman spectroscopy to detect the transition from coating to substrate. The method is calibrated on planar surfaces and applied to curved surfaces, demonstrating that the number of laser pulses required for ablation increases approximately linear to the layer thickness. ARCTA shows significant potential for various applications with advantages over other thickness measurement methods.
In total, this thesis reveals structural-chemical characteristics of biological tribofilms at hip implant taper junctions and transfer material at MoS_2-steel wear couples by spectroscopic studies and develops a novel method for thickness measurement.

Chapter 1

Motivation

In our daily lives, many processes depend on the relative motion between two surfaces within a medium [1, 2]. Examples include activities like walking or cycling, manufacturing processes such as grinding, milling, or turning, and even power plants with turbines. The scientific field that examines these phenomena is tribology [3] and a tribological system comprises these active surfaces, an intermediate medium, and the surrounding medium [4, 5]. The tribological contact results in friction and wear due to fundamental physical-chemical interactions [2, 6]. Friction is the force that opposes the relative motion between two surfaces in contact, but it is essential for transmitting mechanical energy [7, 8]. For example, this force is required to break up intermolecular interactions such as van der Waals forces, hydrogen bonds, and other adhesion forces that form at the contact surface and hinge a movement [9]. Thereby, the strength of the frictional force arises from multiple factors, including the involved materials' characteristics and the normal force pressing the surfaces against each other [7, 8]. The requisite level of friction depends on the application [1, 2, 7]. For instance, low friction is essential for activities such as skiing, whereas high friction is necessary for effective braking, as when a cyclist suddenly stops to avoid an accident. In contrast, wear refers to material loss, which should be as low as possible to ensure a long-lasting tribological system [10, 11]. For instance, the interplay between tribological stress and the formation of thermo-mechanically and chemically induced oxides can significantly affect wear rates, as these oxides may delaminate from the surface [12, 13, 14]. Furthermore, the fundamental interactions within tribological systems result in the conversion of a portion of the energy introduced into the system into forms of energy that are not useful for the intended application, such as heat [7, 15]. This energy dissipation occurs due to various mechanisms, including friction between contacting surfaces, deformation of materials, and energy transformation associated with wear [16, 17]. The higher the proportion of energy utilized for the intended function of the system, the greater the overall efficiency of the tribological system [1].
Overall, tribology is found in various industrial and medical applications (*e.g.*, understanding joint mechanics and chemistry) [18]. In addition, the field of application encompasses a vast range, spanning from nanotechnology to earthquake dynamics [19, 20]. It is, therefore, not surprising that tribology is an interdisciplinary science. It requires the collaboration between mechanical engineering, materials science, physics, chemistry, medicine, and biology to understand tribological processes [21]. This combination makes tribology a diverse and interesting field of research with many applications. Consequently, tribology represents an engaging, diverse, and fascinating research field with a wide array of practical uses. Its primary goals include enhancing the efficiency of tribological systems and extending the lifespan of components [1, 21]. By adopting novel tribological technologies (like anti-wear

and anti-friction additives [22]), industries can significantly reduce energy consumption, operational costs, and CO_2 emissions [23]. The latter is particularly urgent in the context of climate change [24]. In medicine, analyzing the physical-chemical interactions of the human body with an implant and wear particle formation in artificial joints could decrease the need for revision surgeries caused by wear-related complications, improving outcomes for millions of patients and reducing their suffering [25, 26, 27, 28]. Therefore, exploring tribology is not only scientifically fascinating but also crucial from economic, environmental, and social (medical) perspectives.

Studies have shown that thin material layers are formed between all the interacting surfaces as a result of chemical and physical interactions [29, 30, 31]. These layers significantly influence tribological behavior and are known as tribomaterial or third-bodies [29, 32]. The tribomaterial may differ significantly in structure and chemical composition from the initial surfaces and surrounding medium [29, 33]. Since tribomaterial formation is crucial for the performance of the system, it finds relevance in biomedical and mechanical applications. For instance, in modular hip implants, tribomaterial formation involves complex interactions of the metals with biological fluids, influencing friction and wear behavior [34, 35, 36]. Similarly, in engineered systems, the tribomaterial plays a pivotal role in determining the performance of solid-state lubricants such as molybdenum disulfide (MoS_2) [37, 38]. While the former highlights the challenges of tribology under physiological conditions, the latter explores tribological optimization for industrial applications. Despite this centrality of tribomaterial in both domains, significant knowledge gaps remain in understanding the structural-chemical composition of tribomaterial formed during tribological contact. Closing these knowledge gaps is not just important - it is essential for focused optimization!

To achieve this, a detailed and spatially resolved analysis of the tribomaterial is crucial. Employing confocal Raman spectroscopy, an incredibly effective technique utilizing inelastic light scattering, revolutionizes the ability to gain detailed information about the molecular structure and chemical composition of the tribomaterial [34, 39, 40, 41]. This non-destructive method not only provides insights into the structural-chemical properties but also spatially localizes them on the surface using optical microscopy [42, 43]. It can identify various molecules, functional groups, and larger structural elements, such as a protein's secondary structures [44, 45, 46]. The capability to identify specific chemical bonds and phases plays a pivotal role in tribology, especially in recognizing tribochemical reactions (*e.g.*, oxidations) [34, 47]. This thesis employs Raman spectroscopy to uncover microstructural changes and mechanical-chemical reaction products caused by tribological contact, paving the way for advancements in modular hip implants and MoS_2 tribosystems.

In modular hip implants, which are widely used in clinical practice to treat arthritis, tribomaterial is formed in the taper junction due to gross-slip fretting [48, 49, 50, 51]. This process involves interactions with components of synovial fluid so that a metal-organic tribomaterial may be formed. Such a material can improve the implant's friction and wear behavior. Currently, it is only assumed that this tribomaterial consists of compounds from both the synovial fluid and the wear particles of the implant materials [52, 53, 54]. To this day, its structure, composition, and distribution within the tribologically loaded area remain unclear. Moreover, parts of the tribomaterial may migrate from the contact area into surrounding tissue. This migration can trigger adverse biomedical responses, including osteolysis, perivascular lymphocytic reactions, or metal hypersensitivity [49, 55, 56, 57]. While these biomedical consequences of fretting corrosion have been extensively studied,

the fundamental microstructural characteristics and adsorption mechanisms of the metal-organic biotribological material in the taper junction are barely fathomed.
To address these challenges, this thesis aims to systematically investigate the formation and structure of metal-organic compounds and the associated formation of tribomaterial (Chapter 4). Therefore it is important to analyze the microstructural features, molecular alterations, and adsorption processes of the biotribological material on orthopedic alloys as a function of the fretting time. In order to achieve this, two different biomedical grade metal alloys are compared: low-carbon cobalt alloy pins (CoCr29Mo6C0.03) and Co- and Ni-free austenitic high-nitrogen steel pins (FeCr18Mn14Mo3CN0.9), both pressed against a Ti6Al4V cylinder. The thesis simulates the tribological contact conditions found in real-life scenarios through *in vitro* gross-slip fretting tests using a bovine calf serum solution (BCS). Results indicate that the hydrophilicity of the metals significantly influences the adsorption of organic components from the BCS and the secondary structures of the adsorbed proteins. Even more significantly, the work uncovers the formation of amorphous carbon and a surprising nanocrystalline-amorphous cobalt sulfide tribomaterial. The insights gained from these analyses may necessitate a re-evaluation of the material selections and designs for hip joint implants. For example, CoS_x may be used in the future as a robust anti-wear film. Ultimately, this knowledge aims to improve implant integration into the human body, extending implant longevity and improving patient outcomes.
An additional focus of this thesis is the study of the tribomaterial in tribosystems, where a steel counter body is tested against molybdenum disulfide coatings (Chapter 5). In mechanical applications, such a coating is one option to reduce friction and optimize tribological performance [31, 58, 59]. Thereby, MoS_2 exhibits particular advantages under extreme conditions, such as high pressure or vacuum [58, 60, 61]. However, its effectiveness is greatly diminished by humidity [62, 63, 64]. A potential solution to mitigate this humidity sensitivity is the modification of MoS_2 with a transition metal X. This modification can enhance tribological properties, likely due to changes in microstructure and crystallite orientation [65, 66]. The lubricating mechanism of solid lubricants such as modified MoS_2 is fundamentally based on material transfer [31, 59]. The term transfer material refers to the material that is transferred from the main to the counter body (and vice versa) [15, 67]. This transfer material belongs to the tribomaterial and it may undergo structural and chemical changes [68, 69]. Existing structural investigations have primarily concentrated on the evaluation of the tribomaterial present on the initial coated body (here: main body) [70, 71, 72]. However, to fully understand the entire tribological system, it is crucial to additionally analyze the tribomaterial (transfer material) existing on the counter body. Regrettably, there is a notable absence of such studies in the existing literature. This thesis addresses this gap by characterizing the spatial distribution of the tribomaterial - particularly the transfer material - revealing its structural and chemical features and their alterations. Furthermore, the role of transition metals within the MoS_2:X lubrication layer is examined to gain a deeper understanding of their impact on tribological performance. The findings show the unexpected formation of Mo_4O_{11}, a Magnéli-phase, instead of the simpler MoO_3 that one might expect. Remarkably, both tensile and compressive strains can be detected in the transfer material through the E_{2g} and A_{1g} vibrational modes characteristic of MoS_2. Additionally, the splitting of the E_{2g} mode indicates the breaking of the degeneration due to this strain. Overall, this study allows for evaluating the functionality of modified MoS_2 as a solid lubricant and for predicting material failure already at the microscopic level.

A further thematic focus of this work is the determination of the layer thickness of MoS_2 coatings. As mentioned earlier, these coatings are known for their capability to significantly enhance the effectiveness and durability of mechanical tribological applications by providing low-friction surfaces and resistance to wear [73, 74, 75, 76]. However, the thickness of the coating is a decisive factor that can greatly influence its tribological characteristics [77, 78, 79, 80]. Conventional methods to ascertain this thickness often involve the destruction of the relevant component, typically through mechanical rupture, followed by cross-sectional analysis of the fracture surface [81]. For this analysis, techniques such as scanning electron microscopy (SEM) and energy-dispersive X-ray spectroscopy (EDS) are commonly employed [72, 82, 83]. SEM offers high-resolution images of the cross-sectional surface, while EDS provides insights into the chemical composition of the layers, enabling a detailed characterization [84]. Additionally, the calotte grinding method, frequently used in tribology, is another approach for layer thickness measurement [85, 86]. However, these analytical approaches come with a disadvantage; they destroy the component being tested and struggle with intricate, curved surfaces. Beyond tribological applications, the measurement of coating thickness is also relevant in fields like medicine [87, 88, 89, 90, 91], optics [92, 93], and even lacquer or paint applications [94, 95, 96]. Consequently, there are several non-destructive methods for measuring coating thickness, including ellipsometry and terahertz radiation techniques. While ellipsometry requires a customized model for accurate measurements - which is particularly difficult with metallic surfaces - terahertz radiation presents its own limitations, as it is reflected by metals. Overall the majority of these techniques encounter difficulties when attempting to ascertain the layer thickness of tribological coatings on metallic materials with highly curved geometries. In addition, tribology studies usually use measurement methods that unfortunately lead to the component becoming unusable for its intended application. This thesis aims to develop a novel minimal-invasive method, named ablation-Raman coating thickness analysis (ARCTA), for measuring coating thickness, here specifically for MoS_2 coatings (Chapter 5). The method utilizes a pulsed high-energy laser to ablate a part of the coating in the micrometer range. Following ablation, a Raman spectrum is recorded using a continuous wave laser. The Raman spectrum is employed for the purpose of verifying or falsifying the presence of the MoS_2 coating. If the coating is still detectable, further ablation is performed with the pulsed laser, and afterward, another Raman spectrum is recorded. This iterative process is continued until the signals from the substrate can be observed in the Raman spectrum, effectively counting the number of laser pulses required to ablate the MoS_2 layer. To ensure accuracy, the ARCTA technique is calibrated using a well-established method, namely scanning electron microscopy cross-section analysis. For this calibration, flat surfaces coated with up to 5 µm of MoS_2 are used. This calibration serves as the foundation for subsequent measurements on curved surfaces, thereby illustrating the versatility and adaptability of ARCTA for diverse geometries. While there is a minor drawback regarding the potential re-deposition of the ablated material - which may lead to less precise measurements of thicker coatings - the overall performance as a minimal-invasive alternative is promising. Because the measurements are performed adjacent to the tribologically active surface, the ARCTA technique can preserve the functionality of coatings, enabling further usage.

Chapter 2

Fundamental Theory

The findings of this thesis are primarily based on inelastic light scattering, specifically Raman scattering, which represents a potential light-matter interaction. In Section 2.1, these interactions, particularly light scattering, are presented. The derivations and descriptions are based on the publications [39, 40, 41, 97, 98, 99, 100, 101, 102]. Employing the non-destructive optical technique of Raman spectroscopy, molecular vibrations can be analyzed, providing information about various materials' chemical composition and structural properties. It is important to note that certain selection rules must be fulfilled for Raman activity to occur. Taking these selection rules into account, the Raman activity of the structure under consideration can be evaluated by applying group theoretical principles. Accordingly, Section 2.2 outlines the fundamentals of group theory, relying on textbooks [103, 104, 105, 106, 107, 108, 109, 110, 111].
Since proteins play a crucial role in this study, Section 2.3 addresses their three-dimensional structural organization, while Section 2.4 explores their adsorption behavior at solid-liquid interfaces. Subsequently, Section 2.5 discusses the Raman signals of the two principal materials under consideration in this thesis: Molybdenum disulfide (MoS_2) and bovine serum albumin (BSA) protein. The two materials are employed in industrial (MoS_2) or biomedical (BSA) applications or simulations as a lubricant in a tribological system. This thesis focuses on the structural and chemical characteristics of the tribomaterial formed by the tribological contact. To provide an introduction to the field of tribology, Section 2.6 explains the terminology and the basic concepts of tribology, as presented in textbooks [112, 113, 114, 115, 116, 117].

2.1 Light-Matter Interactions

The interaction of light with matter is a fundamental phenomenon crucial to numerous physical processes and technological applications. This section will elaborate on the three principal interactions between electromagnetic radiation and matter: absorption, emission, and scattering.

1. Absorption:
Light absorption describes the process by which the energy E_0 of the incident light, represented by the equation $E_0 = \hbar\omega_0$, is absorbed by a medium. Here, the reduced Planck constant, represented by the symbol $\hbar$, and the angular frequency of the incident light, represented by the symbol ω_0, are involved. The incident light energy is converted into internal energy (*e.g.*, thermal energy) by electronic excitation within the medium. In such an absorption process, an electron in the quantum mechanical state i with the energy E_i be-

comes excited through the absorption of the incident photon (light particle) with the energy E_0. This electron transitions to the state f with an energy $E_\mathrm{f} = E_0 + E_\mathrm{i}$. The absorption probability of a photon through the medium is described by the Einstein coefficient $B_{\mathrm{i}\to\mathrm{f}}$. So, the number of particles in the low-energy state, denoted by n_i, are subject to a change according to the differential

$$\frac{\mathrm{d}n_\mathrm{i}}{\mathrm{d}t} = -n_\mathrm{i} B_{\mathrm{i}\to\mathrm{f}} \rho(\omega_0), \tag{2.1}$$

where $\rho(\omega_0)$ represents the density of the incident radiation and t represents the time. This phenomenon of absorption is employed, for example, in the field of absorption spectroscopy to identify an unknown sample. The sample is successively illuminated with different wavelengths of known intensity, and the intensity of the light emerging from the sample is subsequently measured.

2. Emission:
Emission is the process by which an electron transitions in the medium from a high energy quantum mechanical state to a lower one, resulting in the emission of a photon (light). A distinction is made between spontaneous and stimulated emission. In spontaneous emission, a spontaneous electronic transition occurs randomly from an excited state with energy E_f to a low energy state E_i (*e.g.*, the ground state). The remaining energy, $E_\mathrm{f} - E_\mathrm{i}$, is emitted in the form of a photon with angular frequency ω_e, given by the relation $E_\mathrm{f} - E_\mathrm{i} = \hbar\omega_\mathrm{e}$. In this case of spontaneous emission, the phase and direction of the emitted photon are random.
In contrast, stimulated (induced) emission relies on an external influence. A photon of a specific energy $\hbar\omega_\mathrm{e}$, which correlates with the energy of an electronic transition ($E_\mathrm{f} \to E_\mathrm{i}$), interacts with the medium in the excited state with the energy E_f. This incident photon triggers the electronic transition ($E_\mathrm{f} \to E_\mathrm{i}$), thereby initiating a new photon. The frequency, polarisation, and direction of propagation of these new photons are consistent with those of the incident wave, indicating that the incident and created photons are coherent. Lasers represent a particularly expansive field of application, commencing with spontaneous emission and operating based on stimulated emission. The probability of spontaneous and stimulated emission of a photon is described by the Einstein coefficients $A_{\mathrm{f}\to\mathrm{i}}$ and $B_{\mathrm{f}\to\mathrm{i}}$, respectively. Accordingly, the particle number, denoted as n_f, in the excited state f for spontaneous emission is subject to the following change:

$$\frac{\mathrm{d}n_\mathrm{f}}{\mathrm{d}t} = -n_\mathrm{f} A_{\mathrm{f}\to\mathrm{i}}\,. \tag{2.2}$$

The change in particle number for the spontaneous emission is given by:

$$\frac{\mathrm{d}n_\mathrm{f}}{\mathrm{d}t} = -n_\mathrm{f} B_{\mathrm{f}\to\mathrm{i}} \rho(\omega_0)\,. \tag{2.3}$$

The three transition probability Einstein coefficients, namely $B_{\mathrm{i}\to\mathrm{f}}$, $A_{\mathrm{f}\to\mathrm{i}}$, and $B_{\mathrm{f}\to\mathrm{i}}$, are specific quantities for the medium and the incident radiation. These coefficients are independent of each other [97].

3. Scattering:
The phenomenon of light scattering can be defined as the deflection and/or frequency change of incident photons due to interactions with the irradiated medium. A scattering process can also be described as the absorption of the initial incident light quantum with energy $\hbar\omega_0$ and the simultaneous emission of another photon with energy $\hbar\omega_e$. In this context, a distinction is made between elastic and inelastic scattering. In the case of elastic scattering, the energy of the scattered photon is equal to that of the incident photon. Conversely, this equality does not apply to inelastic scattering, as part of the energy is used for electronic and/or vibronic excitation, for example. This work focuses on inelastic light scattering, which is discussed in more detail in the following Sections.

2.1.1 Light Scattering - A Localized Electric Dipol

When electromagnetic radiation, which is an oscillating electric and magnetic field propagating in space, encounters a medium (atom, molecule, crystal lattice, etc.), the medium can interact with the electric and/or magnetic field. The charge, designated as $\mathfrak{Q}$, at a specific location $\mathbf{r}$, with a mass m, within the medium can interact with the incident monochromatic [1] electric field $\mathbf{E}(t) = \mathbf{E}_0 \cos(\omega_0 t)$, where $\mathbf{E}_0$ is the amplitude. The interaction between the charge and the time-varying electric field $\mathbf{E}(t)$ results in a charge shift. The charge itself within the irradiated medium $\mathfrak{Q}$ at location $\mathbf{r}$ can be represented by a constant charge $\mathfrak{Q}_0$ and/or an oscillating charge $\mathfrak{Q}_1$ with angular frequency Ω. Therefore, the charge can be expressed as $\mathfrak{Q} = \mathfrak{Q}_0 + \mathfrak{Q}_1 \cos(\Omega t)$. In an actual system, the oscillation of the charge can be caused, for example, by a phonon (a bosonic quasiparticle used to describe quantized lattice oscillations) of energy $\hbar\Omega$. The inhomogeneous linear differential equation

$$m\frac{\mathrm{d}^2}{\mathrm{dt}^2}\mathbf{r}(t) = -k\mathbf{r}(t) + \mathfrak{Q}\mathbf{E}(t) \tag{2.4}$$

describes this time-dependent process of charge displacement. In this context, the term $-k\mathbf{r}(t)$ represents the restoring force resulting from the deflection of the charge from its equilibrium position. Similar to a mechanical oscillator with the spring constant k. When the $\mathbf{E}$ field acts solely along the x-axis and $\Omega \ll \sqrt{k/m}$, the solution to the differential Equation 2.4 is given according to Ref. [40] by

$$\begin{aligned} x(t) = &\frac{\mathfrak{Q}_0 E_0}{m(\omega_\mathrm{h}^2 - \omega_0^2)} \cos(\omega_0 t) + \\ &+ \frac{\mathfrak{Q}_1 E_0}{m(\omega_\mathrm{h}^2 - (\omega_0 + \Omega)^2)} \cos((\omega_0 + \Omega)t) + \frac{\mathfrak{Q}_1 E_0}{m(\omega_\mathrm{h}^2 - (\omega_0 - \Omega)^2)} \cos((\omega_0 - \Omega)t)\,, \end{aligned} \tag{2.5}$$

where $\omega_\mathrm{h} = \sqrt{k/m}$ denotes the natural frequency of a harmonic oscillator. The forced oscillation of the charge gives rise to the generation of secondary radiation. These electromagnetic waves with frequencies of ω_0 and $\omega_0 \pm \Omega$ are the results of the scattering interaction between

[1] It is possible to measure the energy change of the scattered light with greater accuracy when the incident light is monochromatic, which allows the specific vibrational modes of the molecules or the crystal structure to be identified. In the absence of a monochromatic light source, this would be a more challenging endeavor, though not an impossible one. Indeed, Raman himself employed filters and sunlight in his investigations [118].

the incident radiation and the medium. If the secondary light wave has the same frequency as the incident wave ω_0 (first term in Equation 2.5), this radiation is designated elastic Rayleigh scattered light. However, if the frequency of the scattered wave differs from that of the initial wave, as in the last two terms in Equation 2.5, this describes inelastic Raman scattering with the frequencies $\omega_0 \pm \Omega$. There is a distinction between a Stokes and an anti-Stokes Raman process, each involving a phonon. But in a Stokes process, a phonon with an energy of $\hbar\Omega$ is generated by utilizing a portion of the energy $\hbar\omega_0$ brought into the system by the incident radiation for this excitation.
As a result, the Stokes-Raman radiation is comparatively low-energy $\hbar(\omega_0 - \omega)$. In contrast, in an anti-Stokes process, an existing elementary excitation of energy $\hbar\Omega$ is annihilated, resulting in the emission of anti-Stokes Raman radiation. The energy of the anti-Stokes Raman radiation is with $\hbar(\omega_0 + \Omega)$ higher than the energy of the incident ratiation $\hbar\omega_0$ or the Stokes-Raman radiation ($\hbar(\omega_0 - \omega)$). The probability of these two Raman processes is related to the probability of generating or annihilating an elementary excitation, i.e. a phonon. The average number of phonons n with the energy $\hbar\Omega$ at temperature T is given by the Bose-Einstein distribution function, $n = (\exp(\frac{\hbar\Omega}{k_\mathrm{B}T}) - 1)^{-1}$ [119]. In this context, the Boltzmann constant k_B is the quantity that controls the conversion of temperature into thermal energy. In a Stokes process, a phonon of energy $\hbar\Omega$ is created, resulting in a change of the number of phonons from n to $n+1$ ($n \rightarrow n+1$.). In an anti-Stokes process, the change is due to the annihilation of a phonon $n+1 \rightarrow n$. This leads to an intensity ratio of the Stokes I_S to the anti-Stokes I_aS scattered light intensity of [120]

$$\frac{I_\mathrm{S}}{I_\mathrm{aS}} = \left(\frac{\omega_0 - \Omega}{\omega_0 + \Omega}\right)^4 \cdot \frac{n+1}{n} = \left(\frac{\omega_0 - \Omega}{\omega_0 + \Omega}\right)^4 \cdot \exp\left(\frac{\hbar\Omega}{k_\mathrm{B}T}\right) . \tag{2.6}$$

In this equation, the first term is approximately equal to 1 ($^{(\omega_0 - \Omega)}/_{(\omega_0 + \Omega)} \approx 1$), given that $\Omega \ll \omega_0$. In reality, the probability of an elementary excitation being present in the medium is low, so the occurrence of the anti-Stokes process is rare. Moreover, it should also be noted that the Equation 2.6 only applies to non-resonant Raman scattering.

2.1.2 Inelastic Light Scattering - Raman Effect

In the preceding Section, the intensity ratio of the Stokes to the anti-Stokes scattered light is calculated (see Equation 2.6). However, this equation does not address the question of the radiation intensity scattered throughout the whole space (4π), given an incident electric field of

$$\mathbf{E} = \mathbf{E}_0 \exp(-i\omega_0 t) + \mathbf{E}_0^* \exp(i\omega_0 t) \tag{2.7}$$

for a specific electron transition from the initial energy state i to the final state f. According to quantum mechanical scattering theory [2], the intensity of the scattered radiation is given by

$$I_\mathrm{if} = \frac{2^3\pi}{3^2 c^4} I_0 (\omega_0 + \omega_\mathrm{if})^4 \sum_{\varrho,\sigma} \left| \left(\alpha_{\varrho\sigma}\right)_\mathrm{if} \right|^2 , \tag{2.8}$$

where c is the speed of light, $I_0 = {}^{c}/_{2\pi}|\mathbf{A}|^2$ is the intensity of the incident light, $\omega_\mathrm{if} = \omega_\mathrm{i} - \omega_\mathrm{f}$ is the frequency difference between the two energy levels, and $\left(\alpha_{\varrho\sigma}\right)_\mathrm{if}$ is the scattering tensor

[2] ω_0 does not correspond to an electron eigenfrequency.

for the transition i → f [98, 99, 100, 101]. The latter is given by the expression:

$$\begin{aligned}\left(\alpha_{\varrho\sigma}\right)_{\mathrm{if}} &= \langle\Psi_{\mathrm{f}}|\hat{\alpha}_{\varrho\sigma}|\Psi_{\mathrm{i}}\rangle \\ &= \frac{1}{\hbar}\sum_{\mathrm{r}}\left(\frac{\langle\Psi_{\mathrm{f}}|\hat{m}_{\varrho}|\Psi_{\mathrm{r}}\rangle\langle\Psi_{\mathrm{r}}|\hat{m}_{\sigma}|\Psi_{\mathrm{i}}\rangle}{\omega_{\mathrm{ri}}-\omega_0}+\frac{\langle\Psi_{\mathrm{f}}|\hat{m}_{\sigma}|\Psi_{\mathrm{r}}\rangle\langle\Psi_{\mathrm{r}}|\hat{m}_{\varrho}|\Psi_{\mathrm{i}}\rangle}{\omega_{\mathrm{rf}}+\omega_0}\right) \\ &= \frac{1}{\hbar}\sum_{\mathrm{r}}\left(\frac{(M_{\varrho})_{\mathrm{rf}}(M_{\sigma})_{\mathrm{ir}}}{\omega_{\mathrm{ri}}-\omega_0}+\frac{(M_{\sigma})_{\mathrm{rf}}(M_{\varrho})_{\mathrm{ir}}}{\omega_{\mathrm{rf}}+\omega_0}\right),\end{aligned} \tag{2.9}$$

wherein the Dirac notation $\langle\Psi_{\mathrm{f}}|\hat{m}_{\varrho}|\Psi_{\mathrm{i}}\rangle = \int\Psi_{\mathrm{f}}^{*}\hat{m}_{\varrho}\Psi_{\mathrm{i}}\mathrm{d}r$ is employed and the symbols ϱ and σ are used to independently represent the Cartesian coordinates x, y or z [97]. The incident electromagnetic field introduces an additional potential, which perturbs the system and is described by the electronic (induced) dipole moment operator $\hat{m} = \sum_{\mathrm{k}}\mathfrak{Q}_{\mathrm{k}}\mathbf{r}_{\mathrm{k}} + \sum_{\mathrm{j}}\mathfrak{Q}_{\mathrm{j}}\mathbf{r}_{\mathrm{j}}$. The electric charges are denoted by $\mathfrak{Q}$ and the position vectors by $\mathbf{r}$. It should be noted that the sum over k represents the contribution of the electrons, while the sum over j corresponds to the contribution of the nuclei [3]. The transition frequency for the electron transition from the initial state i (denoted by wave function Ψ_{i} and energy E_{i}) to an intermediate state r (denoted by wave function Ψ_{r} and energy E_{r}) is given by $\omega_{\mathrm{ri}} = \frac{1}{\hbar}(E_{\mathrm{r}} - E_{\mathrm{i}})$. The transition frequency for the electron transition r → f is denoted by ω_{rf}.
The elements of the scattering tensor are considered in detail below, as Raman scattering is only possible if $\left(\alpha_{\varrho\sigma}\right)_{\mathrm{if}} \neq 0$. The wave functions in Equation 2.9 can be represented by a product of the electronic wave function for state i (denoted by $\psi_{\mathrm{i}}(\mathbf{r}, \mathbf{Q}_m)$) and the vibrational wave function $\phi_{v_m}(\mathbf{Q}_m)$ [4] with normal coordinates $\mathbf{Q}_m$ using the zeroth order of the Born-Oppenheimer approximation [5]. In this context, the quantum numbers v_m, v'_m and v''_m refer to the levels of vibration $\mathbf{Q}_m$, which are associated with the corresponding levels k, n and r. The Schrödinger equation with the electronic Hamiltonian, represented by the operator $\hat{\mathcal{H}}(\mathbf{r}, \mathbf{Q}_m)$ for the electronic part, is given by

$$\hat{\mathcal{H}}(\mathbf{r}, \mathbf{Q}_m)\ \psi(\mathbf{r}, \mathbf{Q}_m) = \left[-\frac{\partial^2}{\partial r^2} + V(\mathbf{r}, \mathbf{Q})\right]\psi(\mathbf{r}, \mathbf{Q}_m) = W\,\psi(\mathbf{r}, \mathbf{Q}_m)\,. \tag{2.10}$$

Consider that the electronic Hamiltonian is almost independent of the motion of the nuclei, the Hamiltonian can be formulated as a Taylor series around the vibrational mode at the equilibrium position of the nucleus $\mathbf{Q} = 0$:

$$\hat{\mathcal{H}}(\mathbf{r}, \mathbf{Q}_m) = \hat{\mathcal{H}}(\mathbf{r}, \mathbf{Q}_m = 0) + \left(\frac{\partial\hat{\mathcal{H}}}{\partial Q_m}\right)_{Q_m=0}\cdot\mathbf{Q}_m + \ldots\,. \tag{2.11}$$

[3] In the following considerations, however, only the electronic contribution will be considered, given that the nuclei have greater inertia due to the difference in mass. Consequently, in many cases, the charge displacement in the nucleus is negligible. This is not necessarily the case for infrared radiation.

[4] Incorporating the rotational wavefunction $\vartheta(J, M)$ (M: magnetic quantum number, J: rotational quantum number) allows for the description of rotational Raman transitions. This results in the following expression: $\Psi_{\mathrm{i}} = \psi_{\mathrm{i}}(\mathbf{r}, \mathbf{Q}_m)\phi_{v_m}(\mathbf{Q}_m)\vartheta(J, M)$

[5] Generally not valid if the electronic state i is degenerate.

The electronic wave function can then be written, using first-order perturbation theory, as

$$\begin{aligned}\psi_{\mathrm{i}}(\mathbf{r},\mathbf{Q}_m) &= \psi_{\mathrm{i}}(\mathbf{r},\mathbf{Q}_m=0) + \sum_{\mathrm{t}\neq\mathrm{i}} \frac{\left\langle \psi_{\mathrm{t}}^0 \middle| \left(\frac{\partial\hat{\mathcal{H}}}{\partial Q_m}\right)_{Q_m=0} \mathbf{Q}_m \middle| \psi_{\mathrm{i}}^0 \right\rangle}{E_{\mathrm{i}}^0 - E_{\mathrm{t}}^0} \psi_{\mathrm{t}}^0 , \\ &= \psi_{\mathrm{i}}^0 + \sum_{\mathrm{t}\neq\mathrm{i}} h_{\mathrm{ti}}^{Q_m} \cdot \mathbf{Q}_m \cdot \psi_{\mathrm{t}}^0 \end{aligned} \tag{2.12}$$

where the equilibrium position of the nucleus $\mathbf{Q}=0$ is written with a superscript 0. Presume that all wave functions are real ($(M_\varrho^0)_{\mathrm{ri}} = (M_\varrho^0)_{\mathrm{ir}}$ and $h_{\mathrm{tr}}^{Q_m} = h_{\mathrm{tr}}^{*Q_m}$) and the space of vibronic wave functions is closed [6]. For an element of the scattering tensor, this results in

$$\begin{aligned}\left(\alpha_{\varrho\sigma}\right)_{\mathrm{i},v_m;\mathrm{f},v'_m} &= \frac{1}{\hbar}\sum_{\mathrm{r}} \left[\frac{\left(M_\sigma^0\right)_{\mathrm{ir}} \left(M_\varrho^0\right)_{\mathrm{rf}}}{\omega_{\mathrm{r},v''_m;\mathrm{i},v_m} - \omega_0} + \frac{[\varrho \leftrightarrow \sigma]}{\omega_{\mathrm{r},v''_m;\mathrm{f},v'_m} + \omega_0} \right] \\ &\quad \left\langle \varphi_{v_m}(\mathbf{Q}_m) \mid \varphi_{v'm}(\mathbf{Q}_m) \right\rangle + \left\langle \varphi_{v_m}(\mathbf{Q}_m) \left|\mathbf{Q}_m\right| \varphi_{v'_m}(\mathbf{Q}_m) \right\rangle \\ &\quad \left[\sum_{\mathrm{t},Q} \frac{h_{\mathrm{tr}}^{Q_m} \left(\left(M_\sigma^0\right)_{\mathrm{ir}} \left(M_\varrho^0\right)_{\mathrm{ft}} + \left(M_\varrho^0\right)_{\mathrm{rf}} \left(M_\sigma^0\right)_{\mathrm{i\,t}} \right)}{\omega_{\mathrm{r},v''_m;\mathrm{i},v_m} - \omega_0} \right. \\ &\quad \left. + \frac{[\varrho \leftrightarrow \sigma]}{\omega_{\mathrm{r},v''_m;\mathrm{f},v'_m} + \omega_0} \right] + \text{ terms in } h_{\mathrm{tf}}^{Q_m}, h_{\mathrm{ti}}^{Q_m} + \ldots , \end{aligned} \tag{2.13}$$

where the abbreviation $\omega_{\mathrm{r},v''_m;\mathrm{i},v_m} = \omega_{\mathrm{r},v''_m} - \omega_{\mathrm{i},v_m}$ is used. If the equation is to include not only the vibronic coupling of the states i and f but also that of r, the terms h_{tf}^Q and h_{ti}^Q are added.

The first term in the Equations 2.13 describes the Franck-Condon overlap of the vibronic wave functions associated with the electronic states i and f. If the distance between the vibronic modes of the electronic states i, r, and f is comparable, the first term will contribute when $v'_m = v_m$. This term contributes considerably much more to the element of the scattering tensor $\left(\alpha_{\varrho\sigma}\right)_{\mathrm{i},v_m;\mathrm{f},v'_m}$ that corresponds to the transition from state i to state f with v_m and v'_m, respectively because the terms $h_{\mathrm{tr}}^{Q_m}$, $h_{\mathrm{tf}}^{Q_m}$, and $h_{\mathrm{ti}}^{Q_m}$ are relatively small. This term thus corresponds to a pure electronic transition, which corresponds to intense Rayleigh scattering in the Raman spectrum. The contribution of the second term is only present if $\left\langle \varphi_{v_m} \middle| \mathbf{Q}_m \middle| \varphi_{v'_m} \right\rangle \neq 0$. Assume again that the vibronic modes of the electronic states i, r, and f are situated at the same distance from each other [7], a contribution is made only if $v'_m = v_m \pm 1$. Consequently, radiation with an energy $\hbar\left(\omega_0 \pm \omega_{v_m,v'_m}\right) = \hbar\left(\omega_0 \pm \omega\right)$ is emitted, representing the Raman scattering [8]. The strength of the Raman scattering contribution also depends on the contributions $h_{\mathrm{tr}}^{Q_m}$ and $\left(M_\sigma^0\right)_{\mathrm{ir}}$, which are, in turn, determined by the symmetry properties of the scattering material point group. In possible

[6] $\sum_{v''} \left\langle \varphi_{v_m}(\mathbf{Q}_m) \mid \varphi_{v''_m}(\mathbf{Q}_m) \right\rangle \left\langle \varphi_{v''_m}(\mathbf{Q}_m) \mid \varphi_{v'_m}(\mathbf{Q}_m) \right\rangle = \left\langle \varphi_{v_m}(\mathbf{Q}_m) \mid \varphi_{v'_m}(\mathbf{Q}_m) \right\rangle$

[7] If this condition does not hold, deviations are possible and for example n, $v'_m = v_m \pm 2 \leftrightarrow \mathrm{k}, v_m$ transitions are measurable.

[8] $\omega_0 \pm \Omega$ is a first-order Raman process, i.e. the interaction with one fundamental vibrational mode. In addition, second-order, third-order, and so on Raman effects are also possible, representing a combination or overtones of two, three, and so on fundamental modes.

further considerations, these symmetry properties are taken into account to calculate the elements of the scattering tensor. However, this calculation is not carried out in this thesis since the fundamental selection rules can be derived from the preceding considerations.

Selection Rules

For Raman scattering to occur, it is not sufficient that $v'_m = v_m \pm 1$. Moreover, it is crucial that the terms of the form M^0_{ir} and $h^{Q_m}_{\mathrm{tr}}$ (see Equation 2.13) are non-zero. Or more generally, the scattering tensor/polarisability of the structure must undergo a change when the transition i $\rightarrow$ f occurs $((\alpha_{\varrho\sigma})_{\mathrm{if}} \neq 0)$ [9]. All these terms can be expressed in the form of an integral, specifically as an integral of products of functions, as follows: $\int f_{\mathrm{a}} f_{\mathrm{b}} f_{\mathrm{c}} \mathrm{d}r$. Given that the integral is performed over the entire space, it will only yield a non-zero result if the integrand is invariant under all operations of the symmetry group of the structure in investigation. Furthermore, the integral will not vanish if the integrand is formulated as a sum and one term is invariant.
In the following, the simplified integral $\int f_{\mathrm{a}} f_{\gamma} \mathrm{d}r$ is considered. Let the integrand be invariant under all symmetry operations. In this case, $f_{\mathrm{a}} f_{\gamma}$ forms a basis for the totally symmetric reducible representation, denoted by $\Gamma_{\mathrm{a}\gamma}$. Furthermore, let f_{a} be a basis for the irreducible representation Γ_{a} and f_{γ} be a basis of Γ_{γ}. Further fundamental details on symmetry operations and reducible or irreducible representations are provided in Section 2.2 on group theory in Raman spectroscopy. Section 2.2 also introduces Equation 2.27, which is used to express the representation $\Gamma_{\mathrm{a}\gamma}$ as a sum of irreducible representations. If this sum contains the fully symmetric representation, designated as Γ_1, with the character $\chi_1 = 1 \,\forall\, \hat{R}$, the integral is not equal to zero. In this case, the representation Γ_1 is a_1 times contained in the representation $\Gamma_{\mathrm{a}\gamma}$, and a_1 can be calculated as follows:

$$a_1 \overset{2.27}{=} \frac{1}{h} \sum_{\hat{R}} \chi_{\mathrm{a}\gamma}(\hat{R}) = \frac{1}{h} \sum_{\hat{R}} \chi_{\mathrm{a}}(\hat{R}) \chi_{\gamma}(\hat{R}) \overset{2.25}{=} \delta_{\mathrm{a}\gamma}\,, \tag{2.14}$$

Consequently, Γ_1 can only be included once, leading to another statement that is of greater importance concerning Raman activity. Namely, the representation $\Gamma_{\mathrm{a}\gamma}$ contains the fully symmetric representation only if $\Gamma_{\mathrm{a}} = \Gamma_{\gamma}$.
For the case of the integral with three functions $\int f_{\mathrm{a}} f_{\mathrm{b}} f_{\mathrm{c}} \mathrm{d}r$, the integral will not vanish unless the representation of the direct product of two functions has the same representation as the third function or contains it. Based on this general integral consideration the basic selection rule for a Raman activity can be derived:
For Raman activity, $(\hat{\alpha}_{\varrho\sigma})_{if}$ must be unequal to 0 $((\hat{\alpha}_{\varrho\sigma})_{if} \neq 0)$, so the direct product $(\Gamma_i \otimes \Gamma_{\hat{\alpha}})$ must contain the irreducible representation of the final state Γ_f.

[9] The scattering tensor $(\alpha_{\varrho\sigma})_{\mathrm{i},v_m;\mathrm{i},v'_m}$ can be expressed as a function of the polarizability tensor α_{ii}, given that the vibronic wave functions ψ are confined within a closed space [6] and the operator $\hat{m}$ only acts on the electronic wave functions:

$$(\alpha_{\varrho\sigma})_{\mathrm{i},v_m;\mathrm{i},v'_m} = \left\langle \phi_{v'_m}(\mathbf{Q}_m) \left| (\alpha_{\varrho\sigma})_{\mathrm{ii}} \right| \phi_{v_m}(\mathbf{Q}_m) \right\rangle$$

$$(\alpha_{\varrho\sigma})_{\mathrm{ii}} = \frac{1}{\hbar} \sum_{\mathrm{r}} \left[\frac{\langle \psi^0_{\mathrm{i}} | \hat{m} | \psi^0_{\mathrm{r}} \rangle \langle \psi^0_{\mathrm{r}} | \hat{m} | \psi^0_{\mathrm{i}} \rangle}{\omega_{\mathrm{r},v''_m;\mathrm{i},v_m} - \omega_0} + \frac{[\varrho \leftrightarrow \sigma]}{\omega_{\mathrm{r},v''_m;\mathrm{i},v_m} + \omega_0} \right].$$

The following considerations aim to use this group-theoretical selection rule to obtain information about whether the oscillations of any symmetry class Γ_{vib} of a point group are Raman active or Raman "forbidden". For this purpose, it is useful to consider the symmetry properties of the second-order scattering tensor α. Under a symmetry operation $\hat{R}$ ($\hat{R}$ is orthogonal), the transformation takes place

$$\begin{aligned} \alpha' &= \hat{R}^{-1}\alpha\hat{R} \\ \alpha'_{xx} =& R_{xx}^2\alpha_{xx} + R_{xy}^2\alpha_{yy} + R_{xz}^2\alpha_{zz} + 2R_{xx}R_{xy}\alpha_{xy} + 2R_{xx}R_{xz}\alpha_{xz} + 2R_{xy}R_{xz}\alpha_{yz} \\ \alpha'_{xy} =& R_{xx}R_{yz}\alpha_{xx} + R_{xy}R_{yy}\alpha_{yy} + R_{xz}R_{yz}\alpha_{zz} + \left(R_{xx}R_{yy} + R_{xy}R_{yx}\right)\alpha_{xy} \\ &+ \left(R_{xx}R_{yz} + R_{xz}R_{yx}\right)\alpha_{xz} + \left(R_{xy}R_{yz} + R_{xz}R_{yy}\right)\alpha_{yz} \end{aligned} \tag{2.15}$$

When the same symmetry operation $\hat{R}$ is applied to a vector $\mathbf{r}$, the result is

$$\begin{aligned} \mathbf{r}' &= \hat{R}\mathbf{r} \\ x'^2 =& R_{xx}^2x^2 + R_{xy}^2y^2 + R_{xz}^2z^2 + 2R_{xx}R_{xy}xy + 2R_{xx}R_{xz}xz + 2R_{xy}R_{xz}yz \\ x'y' =& R_{xx}R_{yz}x^2 + R_{xy}R_{yy}y^2 + R_{xz}R_{yz}z^2 + \left(R_{xx}R_{yy} + R_{xy}R_{yx}\right)xy \\ &+ \left(R_{xx}R_{yz} + R_{xz}R_{yx}\right)xz + \left(R_{xy}R_{yz} + R_{xz}R_{yy}\right)yz \end{aligned} \tag{2.16}$$

A comparison of these two equations reveals that the transformation properties of α are identical to those of a general quadratic function $(x^2, y^2, z^2, xy, yz, xz)$. The transformation properties of these basis functions are also listed in the character tables of the point groups. It can thus be ascertained directly from the character table the number and nature of the potential Raman-active vibration modes (compare with Equation 2.30).

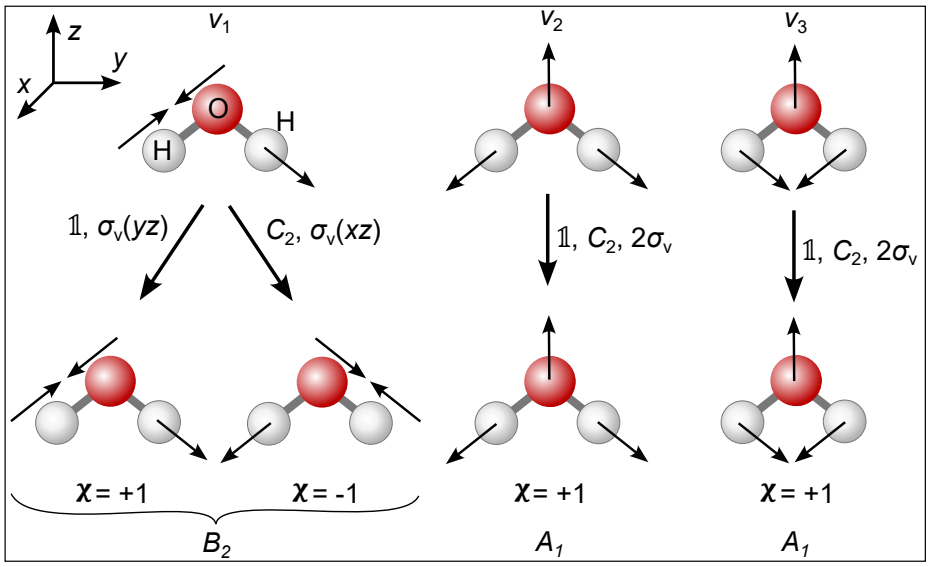


Figure 2.1: All symmetry operations transform the vibrational normal modes v_2 and v_3 of H_2O back into themselves. Consequently, the characters are $\chi(\mathbb{1}, C_2, 2\sigma_v) = +1$. Whereas the vibrational normal mode v_1 is asymmetric, when C_2 and $\sigma_v(xy)$ are applied, so that $\chi(C_2, \sigma_v(xy)) = -1$. Adapted from textbook [121]

In the case of the water (H_2O) molecule, all vibration modes (according to Equation 2.30 the three modes $2A_1$ and B_2) are Raman active, as they correspond to the transformation properties of the quadratic functions x^2, y^2, z^2 and xz (see Table 2.3). Accordingly, this group-theoretical selection rule can predict whether a vibrational mode will manifest in the Raman effect - even without knowing its atomic movement. A more detailed analysis of the shape of the vibration and its behavior under the symmetry operations of the group allows each elementary vibration to be assigned to a symmetry class (see Figure 2.1 for the H_2O molecule). This also demonstrates that each vibrational normal mode forms the basis of an irreducible representation of the point group of H_2O.
For the second-order Raman spectrum [8], the selection rule dictates that measurement is possible only if $\Gamma_\mathrm{i} \otimes \Gamma_\mathrm{j}$ contains irreducible representations that are Raman active [122]. In the case of harmonics of frequency $\approx 2\omega_\mathrm{i}$ [10], the resulting modes are inherently Raman active. Consequently, certain modes that are typically "Raman forbidden" can be observed in the second-order spectrum.

Spectral Position of a Raman Signal

The intensity of the scattered Raman radiation can be calculated by using the Equation 2.8. Nevertheless, questions remain regarding the frequency of specific phonon modes. To address this, the Raman shift, denoted as $\Delta\nu$, is assumed to be approximately given by the expression [42, 123]

$$\Delta\nu \propto \frac{1}{d}\sqrt{\frac{W}{m_\mathrm{red}}}\,. \tag{2.17}$$

Where d is the bond length of the atoms involved in the phonon mode, W is the coupling strength, and $m_\mathrm{red} = {m_1 * m_2}/{m_1 + m_2}$ is the reduced mass of the interacting atoms. To facilitate the comparison of Raman spectra recorded at different excitation wavelengths, the Raman shift of a phonon mode is typically expressed in relative inverse length and calculated using the following formula:

$$\Delta\nu = {1}/{\lambda_0} - {1}/{\lambda_\mathrm{m}}, \tag{2.18}$$

where λ_0 is the excitation wavelength of the incident laser light and λ_m is the wavelength of the inelastically scattered light.

2.2 Fundamentals of Group Theory for Raman Spectroscopy

Various problems related to the structure of the material under consideration can often be simplified by analyzing the symmetry properties. A crystal or molecule is symmetric if it can be transformed into indistinguishable orientations through certain operations, such as rotations, reflections, or inversions, that leave its overall structure and spatial arrangement unchanged. This symmetry is defined by symmetry elements - like planes, axes, or centers of symmetry - that dictate the possible operations and determine the overall symmetry of the crystal or molecule. In some cases, however, the entire structure, particularly in

[10] To excite harmonics or combination modes, a perturbation is usually necessary, which also leads to slight changes in the frequencies of these modes.

amorphous or nanocrystalline materials, does not have global symmetry. Instead, local symmetry often exists within specific regions of the structure. It is beneficial to consider these regions of local symmetry because they significantly influence the properties of the entire structure. For example, many of the properties of a free benzene ring are almost identical to the properties of a phenyl ring bound to a larger molecule [124].
Symmetry operations describe transformations that map the crystal or molecule back onto itself, preserving its overall orientation. To denote these symmetry operations, Schoenflies notation or Hermann-Mauguin notation is typically employed, with this thesis using the Schoenflies notation. Table 2.1 lists the different symmetry operations. The Hermann-Mauguin notation can be found in literature (for example, in [105, 106, 107, 109]).

Table 2.1: List of symmetry operations.

Symbol	Symmetry operation
$\mathbb{1}$	Identity, an object is left unchanged.
C_n	n-fold rotation symmetry axis exists, where a rotation by the angle $\varphi = {}^{2\pi}/_{n}$ is a transition into itself.
S_n	There is an n-fold rotation-reflection axis (also called improper rotation axis), in which a rotation by the angle $\varphi = {}^{2\pi}/_{n}$ with subsequent reflection of all atoms on a plane perpendicular to this axis produces a transition back into itself.
I	An inversion center I exists in which a point reflection of all atoms at this center produces a self-image.
σ	There is a mirror plane on which a reflection of all atomic coordinates transforms the structure back into itself.
σ_h	There is a horizontal mirror plane which means there is a σ perpendicular to the principal axis (axis with highest symmetry).
σ_v	There is a vertical mirror plane which means there is a σ parallel to the principal axis (axis with highest symmetry).
σ_d	There is a dihedral mirror plane which means there is a σ_v that bisects the angle between two C_2 axes.

For a H_2O molecule there are four symmetry operations ($\mathbb{1}$, C_2, two σ_v), which are shown schematically in the Figure 2.2. Note that a symmetry plane is often noted with a Cartesian orientation. The convention is that the axis C_n with the largest n (principal axis) is placed along the z direction. For the H_2O molecule, this notation leads to $\sigma(xz)$ or $\sigma(yz)$. In this figure, the individual atoms in the H_2O molecule are labeled, and the backs of the atoms are shown slightly darker to indicate the new orientation. Since the atoms are indistinguishable in reality, the shown symmetry operation transforms the H_2O molecule by rotation (C_2) or mirroring ($\sigma_v(xz)$, $\sigma_v(yz)$) to a position that is indistinguishable from the original position.

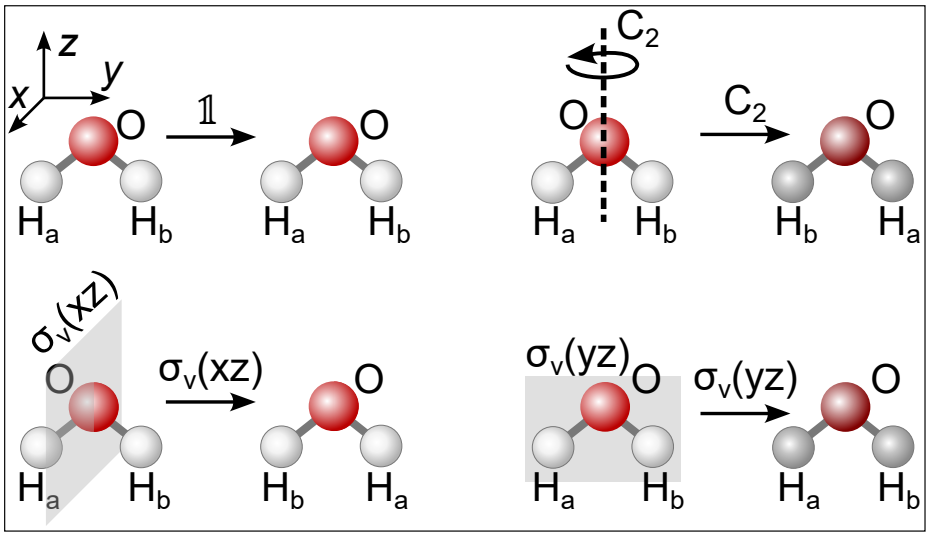


Figure 2.2: Symmetry operations and elements of the H_2O molecule.

Mathematically, these symmetry operations can be described using group theory. A group is a finite or infinite set $\mathcal{G} = \{A, B, C, ...\}$ together with an operation $\cdot$ ($\cdot : \mathcal{G} \cdot \mathcal{G} \rightarrow \mathcal{G}$), if the following rules hold [125, 126]:

1. Closure: $\forall A, B \in \mathcal{G} \quad \exists\, C \in \mathcal{G}$, so $A \cdot B = C$.
2. Associativity: $(A \cdot B) \cdot C = A \cdot (B \cdot C) \quad \forall A, B, C \in \mathcal{G}$.
3. Identity element: $\exists! \mathbb{1} \in \mathcal{G}$, so $A \cdot \mathbb{1} = \mathbb{1} \cdot A = A \quad \forall A \in \mathcal{G}$.
4. Inverse element: $\forall A \in \mathcal{G}\ \exists!\, A^{-1}$, so $A^{-1} \cdot A = A \cdot A^{-1} = \mathbb{1}$.

After identifying all symmetry operations of a given structure (molecule or crystal), it is necessary to verify that these operations satisfy the four criteria of a mathematical group. Such a verification can be accomplished through the use of a multiplication table, as illustrated in Table 2.2, using the example of the H_2O molecule.

Table 2.2: Group multiplication table for the point group C_{2v}.

C_{2v}	$\mathbb{1}$	C_2	$\sigma_v(xz)$	$\sigma'_v(yz)$
$\mathbb{1}$	$\mathbb{1}$	C_2	$\sigma_v(xz)$	$\sigma_v(yz)$
C_2	C_2	$\mathbb{1}$	$\sigma_v(yz)$	$\sigma_v(xz)$
$\sigma_v(xz)$	$\sigma_v(xz)$	$\sigma_v(yz)$	$\mathbb{1}$	C_2
$\sigma_v(yz)$	$\sigma_v(yz)$	$\sigma_v(xz)$	C_2	$\mathbb{1}$

The symmetry operation in the first row is applied first, followed by the symmetry operation in the first column. If the resulting product of two symmetry operations is also a symmetry operation in the set, the closure has been proven. The second rule is fulfilled if products of symmetry operations can be calculated, to which the associative law applies. The symmetry operation $\mathbb{1}$ automatically satisfies the third rule for mathematical groups. Finally, there must be proof that every group element has an inverse. The following applies

to the individual symmetry operations (compare with Table 2.1):

$$\mathbb{1} \cdot \mathbb{1} = \mathbb{1}, \qquad (C_n)^m \cdot (C_n)^{n-m} = \mathbb{1}, \qquad I \cdot I = \mathbb{1}, \qquad \sigma \cdot \sigma = \mathbb{1}$$

and for the improper rotation S_n^m a distinction must be made as to whether n and/or m are even or odd:

$$\begin{aligned} &n \text{ even:} && (S_n)^m \cdot (S_n)^{n-m} &&= \mathbb{1} \\ &n \text{ odd; } m \text{ even:} && (S_n)^m \cdot (C_n)^{n-m} &&= \mathbb{1} \\ &n \text{ odd; } m \text{ odd:} && (S_n)^m \cdot (S_n)^{2n-m} &&= \mathbb{1} \end{aligned}$$

The symmetry operations listed in Table 2.1 can satisfy the four rules of mathematical groups. Consequently, it is possible to select some of these symmetry operations, which comprise a part of the symmetry operations and reflect the symmetries of a given crystal or molecule. Thus, a group forms that can be represented in a multiplication table and has all properties of mathematical groups. Such groups are known as point groups. The term point groups originates within the fact that in these groups, at least one point remains when the different symmetry operations of the group are applied. The number of symmetry operations (elements) in the group denotes the order h of the group. For example, the molecule H_2O is assigned to the point group C_{2v} with the order $h = 4$ due to the four symmetry operations (see Figure 2.2). In total, a number of 32 crystallographic point groups compatible with a space lattice can be defined. However, there are infinitely many other non-crystallographic point groups. Some are used in molecular symmetry, quasicrystals, or to describe proteins or viruses. Figure 2.3 shows a flow chart for determining the point group in Schoenflies notation [12]. The assignment of a given molecule or crystal to a point group is not only important for the symmetry description but also provides information about certain physical properties, such as optical activity, piezoelectricity, or pyroelectricity [128]. Still, these point groups do not reflect the overall symmetry of a crystal, since translational symmetry in the form of helical and slip reflections are not included as symmetry operations. In total, there are 230 crystallographic space groups that fully describe all possible crystal symmetries. More detailed information on space groups can be found in literature, such as in Ref. [129, 130, 131]. Mathematically, these groups can be represented by matrices that reflect the multiplication tables of each group through matrix multiplication. The following 3×3 matrices can be assigned to the symmetry operations of the Table 2.1:

$$\begin{aligned} \mathbb{1} &: \begin{bmatrix} 1 & 0 & 0 \\ 0 & 1 & 0 \\ 0 & 0 & 1 \end{bmatrix} \quad C_n : \begin{bmatrix} \cos\varphi & \sin\varphi & 0 \\ -\sin\varphi & \cos\varphi & 0 \\ 0 & 0 & 1 \end{bmatrix} \\ I &: \begin{bmatrix} -1 & 0 & 0 \\ 0 & -1 & 0 \\ 0 & 0 & -1 \end{bmatrix} \quad S_n : \begin{bmatrix} \cos\varphi & \sin\varphi & 0 \\ -\sin\varphi & \cos\varphi & 0 \\ 0 & 0 & -1 \end{bmatrix} \\ \sigma(xy) &: \begin{bmatrix} 1 & 0 & 0 \\ 0 & 1 & 0 \\ 0 & 0 & -1 \end{bmatrix} \quad \sigma(xz) : \begin{bmatrix} 1 & 0 & 0 \\ 0 & -1 & 0 \\ 0 & 0 & 1 \end{bmatrix} \quad \sigma(yz) : \begin{bmatrix} -1 & 0 & 0 \\ 0 & 1 & 0 \\ 0 & 0 & 1 \end{bmatrix}. \end{aligned} \tag{2.19}$$

[12] A flow chart for assigning a structure to the 32 crystallographic point groups in Hermann-Mauguin notation is shown in Ref. [127].

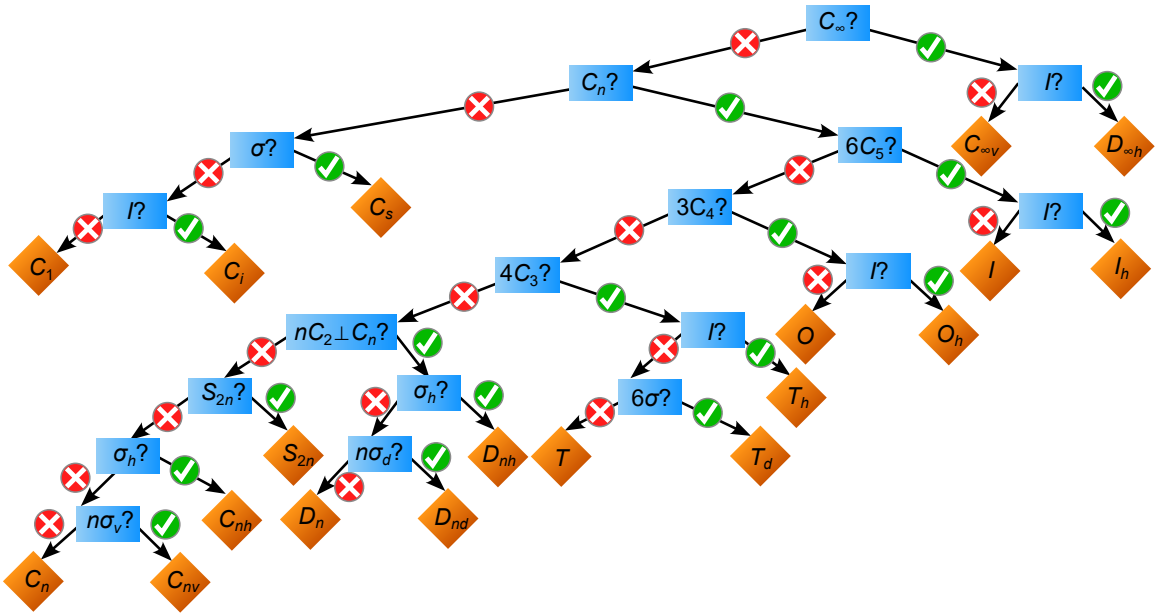


Figure 2.3: Flow chart for determining the point group of a structure through symmetry operations. The blue boxes with question marks indicate decision points where the presence of specific symmetry operations (as detailed in Table 2.1) must be evaluated. A green tick indicates that the operation preserves the structure, allowing the path to progress to the right, while a red cross signifies that the operation does not maintain the structure and the path is continued to the left. The example of the H_2O molecule is analyzed to illustrate this process, beginning with the assessment of a C_∞ axis [11]. The absence of this axis leads to a check of the C_n rotational axes with $n \geq 2$ since $n = 1$ corresponds to a 360° rotation. As shown in Figure 2.2, H_2O has a C_2 axis. Further checks for higher symmetry axes, including $6C_5$, $3C_4$, and $4C_3$, reveal their absence. This process reaches the $nC_2 \perp C_n$ box, where the number of the highest symmetry axis $n = 2$. After confirming the lack of $2C_2$ axes perpendicular to the principal axis (C_2), as well as the absence of a S_{2n} and a σ_h symmetry element, the check for $2\sigma_v$ planes (see Figure 2.2) confirms the point group of H_2O as C_{2v}. Adapted from textbook [121].

A relatively simple approach to creating these matrices would be to describe the spatial position of each atom in the structure under consideration. For the H_2O molecule, this results in four 9×9 matrices describing the symmetry operations and fulfilling the rules of the multiplication table 2.2. However, the matrices quickly become very large with this type of description of the symmetry operations, especially for larger molecules or crystals. Therefore, this type of representation is not the most efficient. Depending on the choice of the basis, there are many other ways to represent a given group of points. The most compact representation of a group that contains all the fundamental properties is the irreducible representation. To achieve this, the matrices $A, B, C, ...$ are transformed with similarity transformations

$$Q^{-1} \cdot A \cdot Q = A' \tag{2.20}$$

into block diagonal matrices $A', B', C', ...$, which also satisfy the multiplication table ($A \cdot B = C \iff A' \cdot B' = C'$) and thus represent the same symmetry operation of the group. The

following applies to the matrix multiplication of block diagonal matrices:

$$\begin{bmatrix} A'_1 & & 0 \\ & A'_2 & \\ 0 & & A'_3 \end{bmatrix} \cdot \begin{bmatrix} B'_1 & & 0 \\ & B'_2 & \\ 0 & & B'_3 \end{bmatrix} = \begin{bmatrix} C'_1 & & 0 \\ & C'_2 & \\ 0 & & C'_3 \end{bmatrix} . \tag{2.21}$$

Where each of these blocks/submatrices $A'_i, B'_j, C'_l;\ i,j,l \in \{1,2,3\}$ with $A'_i \cdot B'_i = C'_i$ fulfills the original multiplication table. Consequently, these submatrices also constitute a representation of the group.
Through the application of similarity transformations, the submatrices are further converted into block diagonal matrices. This reduction process is iteratively performed until only 1×1 matrices or $l_i \times l_i$ matrices remain, which can no longer be simplified by similarity transformations. At this stage, the resulting matrices correspond to the i-th irreducible representation associated with the R-th symmetry operation of the group. This is where the name of the i-th irreducible representation originates:

$$\Gamma_i(R) = \begin{bmatrix} \Gamma_i(R)_{1\,1} & \Gamma_i(R)_{1\,2} & \dots & \Gamma_i(R)_{1\,l_i} \\ \Gamma_i(R)_{2\,1} & \Gamma_i(R)_{2\,2} & \dots & \Gamma_i(R)_{2\,l_i} \\ \vdots & & & \vdots \\ \Gamma_i(R)_{l_i\,1} & & \dots & \Gamma_i(R)_{l_i\,l_i} \end{bmatrix} .$$

Nonetheless, some of these matrices may be transformed into each other using similarity transformations ($Q^{-1} \cdot A \cdot Q = B$). Then, the matrices A and B are called conjugates. A complete set of operations conjugated with one another forms a class.
To simplify the description of a group, the trace of the matrices

$$\chi_i(R) = \sum_m \Gamma_i(R)_{mm} \tag{2.22}$$

is used, called the character of the irreducible representation. An essential property of the character is that it does not change by similarity transformations, which means that conjugate matrices also have the same character. These characters and irreducible representations have some fundamental and beneficial properties:

1. The number of irreducible representations equals the number of classes κ of the group.

2. The sum of the squares of the dimensions of the irreducible representations is equal to the order of the group. The character under $\mathbb{1}$ always indicates the dimension of the irreducible representation.

$$\sum_i l_i^2 = h \quad \text{if } l_j = \chi_j(\mathbb{1}) : \sum_j \left[\chi_j(\mathbb{1})\right]^2 = h \tag{2.23}$$

3. It is possible to define h dimensional vectors, represented by the symbol $\boldsymbol{\Gamma}_{i,\,mn} = (\Gamma_i(R_1)_{mn}, \Gamma_i(R_2)_{mn}, \dots, \Gamma_i(R_h)_{mn})^\top$, which are orthogonal to each other. This is known as the "Great Orthogonality Theorem":

$$\boldsymbol{\Gamma}_{i,\,mn} \cdot \boldsymbol{\Gamma}^*_{j,\,m'n'} = \sum_R \left[\Gamma_i(R)_{mn}\right] \left[\Gamma_j(R)_{m'n'}\right]^* = \frac{h}{\sqrt{l_i l_j}} \delta_{ij} \delta_{mm'} \delta_{nn'} . \tag{2.24}$$

4. The character system of irreducible representations forms κ dimensional orthogonal vectors $\boldsymbol{\chi}_i = (\sqrt{\beta_1}\chi_i(R_1), \sqrt{\beta_2}\chi_i(R_2), \ldots, \sqrt{\beta_\kappa}\chi_i(R_\kappa))^\top$, where β_j is the number of operations in the j-th class. In addition, the sum of the squares of the characters of an irreducible representation is equal to the order of the group:

$$\boldsymbol{\chi}_i \cdot \boldsymbol{\chi}_j^* = \sum_R \chi_i(R)\chi_j^*(R) = h\,\delta_{ij}\,. \tag{2.25}$$

5. The vectors $\boldsymbol{\chi}_i$ span the vector space of the characters for all representations of the group. A reducible representation $\boldsymbol{\chi}$ can contain the irreducible representation a_i times:

$$\boldsymbol{\chi} = \sum_i a_i \boldsymbol{\chi}_i\,. \tag{2.26}$$

   The composition of a reducible representation $\chi(R)$ is unique. How often $\chi(R)$ contains an irreducible representation $\chi_i(R)$ can be determined by:

$$a_i = \frac{1}{h}\sum_R \chi(R)\chi_i(R)\beta_i(R)\,. \tag{2.27}$$

Proofs of these properties are given in [103, 105, 108]. As mentioned earlier, there are many ways to represent matrices. Since their characters are always the same, only the characters are typically used.

Table 2.3: Character table for C_{2v} point group.

C_{2v}		$\mathbb{1}$	C_2	$\sigma_v(xz)$	$\sigma_v'(yz)$		
Γ_1	A_1	1	1	1	1	z	x^2, y^2, z^2
Γ_2	A_2	1	1	-1	-1	R_z	xy
Γ_3	B_1	1	-1	1	-1	x, R_y	xz
Γ_4	B_2	1	-1	-1	1	y, R_x	yz

A list of the characters of all irreducible representations concerning all symmetry operations is called the character table of the point group. The C_{2v} point group, to which the H_2O molecule belongs, has four irreducible representations (Γ_1 to Γ_4). The corresponding character table is given in Table 2.3. The first row of a character table contains the symmetry operations R. The irreducible representations Γ_i of the corresponding point group are listed in the first column. In literature, however, it is common to use the Mulliken symbols [13], which contain symmetry information about the irreducible representation. See Table 2.4 for a rough explanation of the concept of Mulliken symbols. The following columns in Table 2.3 list the characters of the corresponding irreducible representation for all elements/classes of the group. In the final columns, the table also depicts "base functions", which can be employed to generate matrices that represent the symmetry elements of a given irreducible representation. In other words, Table 2.3 lists the rotations R_x, R_y, R_z around the x-, y-, z-axis and the linear/square functions that have the same transformation properties as Γ_i.

[13] This notation was first proposed by Robert S. Mulliken in the early 1930s [132] and is named in his honor. Robert S. Mulliken was awarded the Nobel Prize in Chemistry in 1966 "for his fundamental work concerning chemical bonds and the electronic structure of molecules by the molecular orbital method" [133]

Table 2.4: Mulliken symbols for the irreducible representations. Within this table C_n refers to the principal axis.

Dimension of representation	Character under symmetry operation $\mathbb{1}$	C_n	i	σ_h	$C_2 \perp C_n$ or σ_v	Symbol			
1	1	1				A			
	1	-1				B			
2	2					E			
3	3					T			
			1			A_g	B_g	E_g	T_g
			-1			A_u	B_u	E_u	T_u
				1		A'	B'		
				-1		A''	B''		
					1	A_1	B_1		
					-1	A_2	B_2		

2.2.1 Application of Symmetry in Raman Spectroscopy

Knowing the point group symmetry of a crystal or molecule, along with the corresponding character table, provides information about the fundamental (normal) vibrations. Therefore, the $3N$ degrees of motional freedom of an N atomic structure must be determined first. A coordinate system is assigned to each atom to capture all atomic motions. These $3N$ vectors form the basis of a point group representation. In case of the H_2O molecule, this results in the 9×9 matrices mentioned above. It is, however, not necessary to explicitly construct the transformation matrices, as the symmetry properties alone are sufficient to determine the character associated with each symmetry operation within the group. Only the diagonal elements of these matrices contribute to the character of a given symmetry operation (see Equation 2.22). Notably, these diagonal entries are nonzero only when the symmetry operation leaves an atom in its original position, indicating invariance of that atomic site under the operation. This alignment between diagonal contributions and unchanged atomic positions is key to identifying the character of the operation without detailed matrix construction. For the H_2O molecule, this means that all atoms remain in place during the operation $\mathbb{1}$ (see Figure 2.2). This leads to character 9, since the three 3×3 $\mathbb{1}$ matrices (see Equation 2.19) on the diagonal have each character 3. In the C_2 operation, only the O atom remains in place (see Figure 2.2). Consequently, there is only one 3×3 C_2 matrix from the Equation 2.19 on the diagonal leading to the character -1. For the whole H_2O molecule, the following reducible representation is examined:

$$\begin{array}{c|cccc} C_{2v} & E & C_2 & \sigma_v & \sigma_v' \\ \hline \Gamma_{\text{tot}} & 9 & -1 & 3 & 1 \end{array} . \tag{2.28}$$

According to the Equation 2.26, it consists of 9 irreducible representations

$$\Gamma_{\text{tot}} = 3A_1 + A_2 + 2B_1 + 3B_2 \, . \tag{2.29}$$

This methodology facilitates a determination of the $3N$ degrees of freedom (irreducible representations) for each N-atomic symmetric structure. To isolate the vibronic degrees of

freedom Γ_{vib}, which correspond to the normal vibrational modes relevant for spectroscopic analysis, it is essential to subtract the translational Γ_{trans} and rotational Γ_{rot} degrees of freedom. These latter representations can be determined using the appropriate functions listed in the character table for the symmetry group. For the H_2O molecule, the character Table 2.3 leads to:

$$\begin{aligned} \Gamma_{\text{trans}} &= A_1 + B_1 + B_2 \\ \Gamma_{\text{rot}} &= A_2 + B_1 + B_2 \\ \Rightarrow \Gamma_{\text{vib}} &= \Gamma_{\text{tot}} - \Gamma_{\text{rot}} - \Gamma_{\text{trans}} = 2A_1 + B_2 \,. \end{aligned} \tag{2.30}$$

Therefore, there are three normal vibrations for the H_2O molecule, of which all further vibrations are composed. Each of these normal modes serves as a basis for an irreducible representation of the molecule's point group, reflecting the underlying symmetry of the structure [14].

2.3 Three-Dimensional Structural Organization of Proteins

There are many structural variations of amino acids. They are all called amino acids because they have one amine (NH_2) and one carboxyl (COOH) unit in common. The amino acids are classified according to the position of the amino group in relation to the carboxyl group, as schematically illustrated in Figure 2.4.

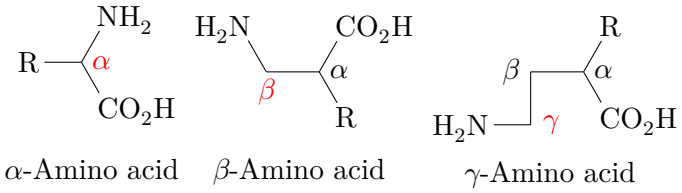


Figure 2.4: Amino acids are categorized based on the relative positioning of the amino group (NH_2) to the carboxyl group (CO_2H). In α-amino acids, the amino group is attached to the carbon atom (called the α-carbon) directly adjacent to the carboxyl group. In contrast, β-amino acids are characterized by having two carbon atoms between the amino group and the carboxyl group, with the amino group attached to the β-carbon. γ-amino acids have the amino group on the γ-carbon. Although additional amino acids can be synthesized following this positional framework, α-amino acids are particularly noteworthy as they serve as the essential building blocks of proteins.

Of particular biological importance are about 20 α-amino acids, which built the basis of proteins from which all living organisms are formed [135, 136]. Depending on the chemical properties of the side chains (R-group), these α-amino acids can be roughly classified as [137, 138]:

- hydrophobic (non-polar side chains) aliphatic:
  Alanine, Glycine, Isoleucine, Leucine, Methionine, Proline, Valine

[14] In the same way, all the wave functions for normal vibrations in their ground state also form a basis for the symmetric representation of the point group of the structure [134]

- hydrophilic (polar side chains):
  Asparagine, Cysteine, Glutamine, Serine, Threonine
- uncharged hydrophilic charged:
  Arginine, Aspartate, Glutamate, Histidine, Lysine
- Aromatic:
  Non-polar side chain: Phenylalanine, Triptophan,
  Charged polar side chain: Tyrosine.

Figure 2.5 (a) shows examples of the aromatic α-amino acids phenylalanine, tryptophan, and tyrosine, along with the hydrophilic α-amino acid cysteine.

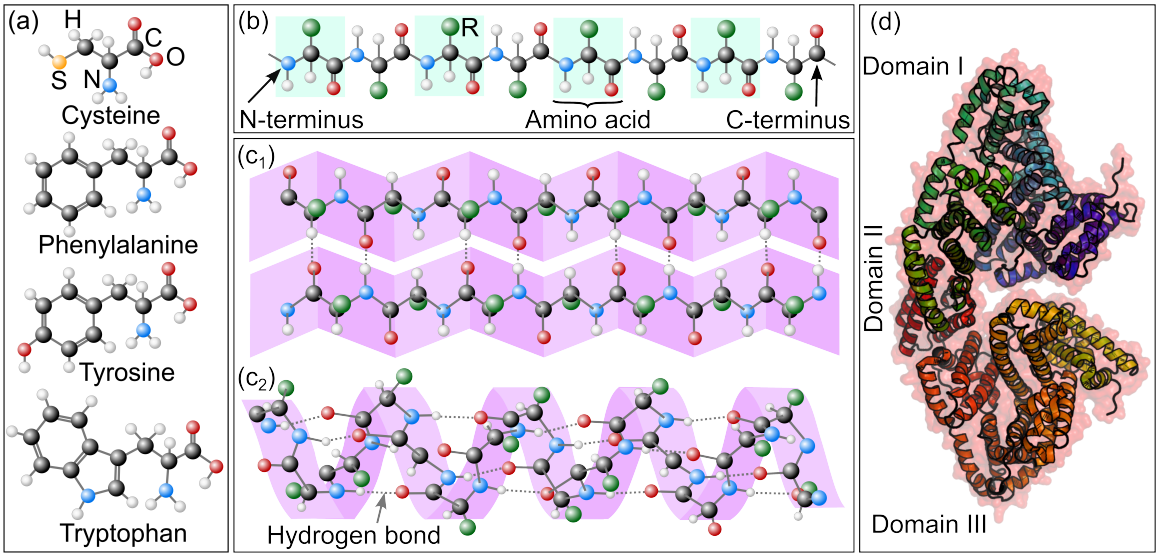


Figure 2.5: In any protein, three structural levels are identifiable. The primary structure (b) is a polypeptide chain consisting of different α-amino acid residues (four α-amino acids are shown as examples in (a)) that make up the protein by peptidic bonding. The formation of the secondary structure, particularly the β-sheet (c_1) and the α-helix (c_2), is contingent upon how individual hydrogen bonds are established between amino acid residues. The tertiary structure (d), in this case of a BSA protein, describes the entire three-dimensional, stable native structure of the protein. The tertiary structure formes due to hydrogen bonding, hydrophobic interaction, ion bonding and disulfide bonds.

Amino acids can link together to form a chain through a reaction, in which a water molecule is released as the amine group of one amino acid residue bonds with the carboxyl group of another. This covalent linkage, known as a peptide bond, results in the formation of a polypeptide chain, often referred to as a protein. The chain of peptide bonds without the side chains (R) is known as the polypeptide backbone. Such a chain has a free amine group (N-terminus) at one end and a free carboxyl group (C-terminus) at the other end, as can be seen in Figure 2.5 (b). For clarity, this figure illustrates the side chains of the amino acid residues as an R group. Each peptide chain is characterized by a specific sequence of amino acid residues, referred to as its primary structure. Furthermore, the peptide bond (C=N) exerts a structural influence due to its 50 % double bond character (C-atom sp^2 hybridization), as illustrated in Figure 2.6. Consequently, the amide unit is predominantly planar, and most peptide bonds exhibit a trans-relationship [139]. Nevertheless, a rotation

around the $C_{\alpha'}-C$ (θ) and $C_{\alpha}-N$ (ζ) bonds is possible, as indicated in Figure 2.6. This rotation is significantly influenced by the side chains of the individual amino acids, thereby allowing for a diverse range of conformations.

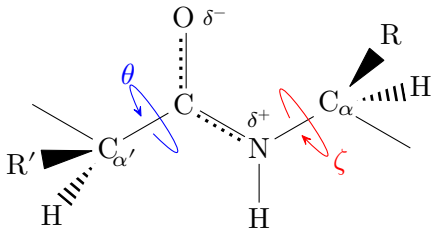


Figure 2.6: Illustration of the peptide bond, highlighting the possible rotation angles around the $C_{\alpha'}-C$ (θ) and $C_{\alpha}-N$ (ζ) bonds. In a peptide chain, the planar nature of the peptide bond between C=O and N=H restricts rotation around the C=N axis. However, rotation is permitted around the $C_{\alpha'}-C$ and $C_{\alpha}-N$ bonds, which define the backbone dihedral angles θ and ζ, respectively. These rotations influence the secondary structure of peptides, with specific angle values correlating to structures such as α-helices and β-sheets.

A common conformation is the ***β*-sheet**. This folded surface structure is formed when two peptide chains align closely, enabling the formation of intermolecular hydrogen bonds. These bonds occur between the partially positive (δ^+) hydrogen atom on the amide nitrogen (N) of one peptide chain and the partially negative (δ^-) oxygen atom on the carbonyl (C=O) group of an adjacent chain. Figure 2.5 (c_1) schematically shows such a β-sheet. The C- and N-termini of the two peptide chains can be on the same side, which is called a parallel β-sheet ($\theta = -120\,°$ and $\zeta = 115\,°$). In nature, however, the antiparallel β-sheet ($\theta = -139\,°$ and $\zeta = 135\,°$) is more common, where the C- and N-termini are opposite of each other [140].
Another conformation frequently found in nature is the ***α*-helix** with average rotational angles of $\theta = -(64 \pm 7)\,°$ and $\zeta = -(41 \pm 7)\,°$ [140, 141]. Within this helical structure, intramolecular hydrogen bonds stabilize the helix along its axis. Specifically, these hydrogen bonds form between the H atom attached to the amide nitrogen (N) of the n-th amino acid residue and the O atom of the carbonyl group on the $n + 4$-th residue, progressing toward the N-terminus. An ideal α-helix contains 3.6 amino acid residues per complete helical turn [15].
These locally organized conformations are referred to as secondary structures. However, many regions within proteins lack a defined, regular secondary structure and are instead described as **random coil** regions. In these disordered regions, rotation around the dihedral angles *and* results in a non-uniform orientation of amino acid residues, making hydrogen bond formation comparatively more difficult than in well-defined structures like α-helices or β-sheets.
The various secondary structures thus describe local (α-helix up to 35 and β-sheet up to 15 amino acid residues [141]) structural (bending and folding) conformations within a protein, which are created depending on the hydrogen bonds of the amino acid residues. Several secondary structures are called domains when the corresponding contiguous amino acid

[15] In addition to the α-helix, the less common 3.10-helix and the π-helix have been observed in proteins. More information can be found in [140].

sequences exhibit a relatively independent functionality. A protein domain typically comprises 40 to 700 amino acid residues [140, 141], which fold into a distinct three-dimensional conformation driven by the chemical and physical interactions among the side chains of the amino acids. This folding results in an architecture where hydrophobic residues are predominantly situated within the core of the domain, while hydrophilic residues are positioned on the exterior. This hydrophilic exterior of the domains facilitates interactions with the aqueous environment [141, 142]. The entire three-dimensional configuration of a protein, known as its tertiary structure, comprises these consecutive protein domains. This tertiary structure is often stabilized by various interactions, including ionic bonds, hydrophobic-hydrophilic interactions, hydrogen bonds, salt bridges, and covalent disulfide bonds [143]. Furthermore, the linkages between domains enable some proteins to exhibit dynamic behaviors, such as conformational changes and movement, which are particularly important for enzymes in facilitating binding and catalysis. Figure 2.5 (d) shows an example of the structure of BSA in a Richardson diagram [141, 144], where the domains are labeled.
Despite that, many proteins are not composed of a single, continuous polypeptide chain. Instead, they consist of multiple polypeptide chains (subunits). The chains assemble to form the functional protein complex through hydrogen bonds, hydrophobic interactions, disulfide bonds, and van der Waals forces [145]. When a protein has this overarching structure, it is called the quaternary structure of the protein. Still, the primary structure of the protein determines the three-dimensional native form into which the protein spontaneously folds due to hydrophobic forces to maximize the entropy. Since the amino acids differ quite significantly in their physicochemical properties (*e.g.*, polarity, aromaticity, conformational flexibility, hydrogen bonding ability, chemical reactivity), a wide range of protein properties is possible.
In addition to the hydrogen bond stabilization of the secondary, tertiary, and quaternary structure, some proteins are stabilized by disulfide bonds. For this, the amino acid residue of cysteine must be present several times in the primary structure. By oxidizing the thiol group (S–H, see the structure of cysteine in Figure 2.5 (a)), it is then possible for two cysteine residues to form a covalent disulfide bond. The resulting chemical compound is called cystine, and the reaction is shown schematically in Figure 2.7.

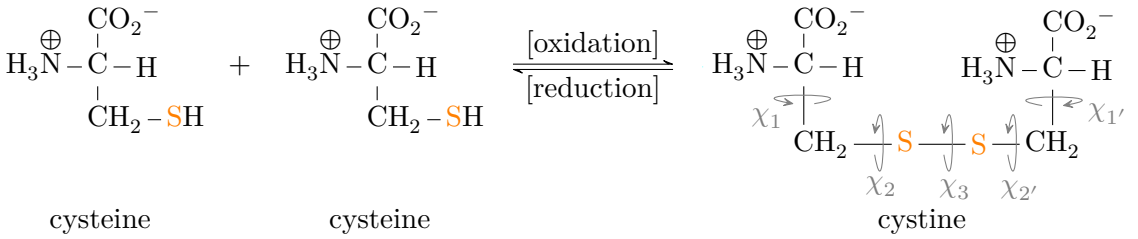


Figure 2.7: The schematic representation shows a cystine complex formation from two cysteine amino acids. The reaction illustrates the oxidation process in which the thiol groups (–SH) of two cysteine residues interact to form a covalent disulfide bond (–S–S–), resulting in the dimeric structure of cystine. In addition, these cystine complexes can adopt various orientations, which are defined by the dihedral angles χ_1, χ_2, χ_3, $\chi_{2'}$, and $\chi_{1'}$. These disulfide linkages and angles are involved in the stabilization of protein structures and the influence of their three-dimensional conformation.

Depending on the number of cysteine residues, several cystine complexes are possible within a protein structure. Even so, exactly one configuration corresponds to the native form of the protein. Since disulfide bonds can be either intramolecular or intermolecular, analogous to hydrogen bonds, they are crucial for the structure and activity of peptides and proteins [146, 147]. In addition, these cystine side chains, like the backbone (see Figure 2.6), can adopt specific orientations. This orientation is described by the dihedral angles χ_1, χ_2, χ_3, $\chi_{2'}$, and $\chi_{1'}$, as illustrated in Figure 2.7. Notably, three configurations are of particular importance: the trans-gauche-trans (tgt), gauche-gauche-trans (ggt), and gauche-gauche-gauche (ggg) arrangements. The corresponding dihedral angles for each configuration are provided in Table 2.5. Certain angle combinations are energetically favored over others [141, 151, 152].

Table 2.5: Dihedral angles for trans-gauche-trans (tgt), the gauche-gauche-trans (ggt), and gauche-gauche-gauche (ggg) conformations of the cysteine complex [141, 148, 149, 150].

Configuration	χ_2	χ_3	$\chi_{2'}$
tgt	180°	±90°	180°
ggt	±90°	±90°	180°
ggg	±90°	±90°	±90°

The cystine complex usually adopts the trans-gauche-trans configuration when the distance between the $C_\alpha - C_{\alpha'}$ of the cysteine residues is relatively large ($\approx 7\,\text{Å}$) and the angle χ_1 or $\chi_{1'}$ are both either 60° or 180°. While at shorter distances ($\approx 5\,\text{Å}$), the gauche-gauche-gauche configuration is preferred (χ_1 or $\chi_{1'}$ around $-60°$) with either a left-handed or right-handed spiral or hook geometric configuration [141].

2.4 Protein Adsorption at Solid-Liquid Interfaces

Adsorption refers to a physical process where substances (molecules, proteins) in liquid or gaseous phase adhere to the interface/surface of another solid substance (implant) and accumulate on its surface. Such adsorption processes occur at the first contact of the solid surface with the biological fluids and tissues so that the surface is covered within seconds [153, 154]. However, it can take several hours until the final protein layer accumulates/adsorbs on the surface [153, 154]. This interfacial protein layer that forms on the surface is the layer that cells recognize. For this reason, it is assumed that the reaction of the cells to the foreign body depends on this layer [155, 156, 157]. It is, therefore, necessary to study the formation and composition of this protein layer.
Proteins or molecules reach the surface through diffusion or convection, depending on their concentration and diffusion coefficient, before adsorbing onto the surface [143, 158, 159, 160]. The surrounding environment significantly influences diffusion rates; for instance, elevated temperatures can accelerate diffusion. Various factors impact the adsorption process itself. Key influences include the solution composition - particularly the adsorption affinity, structural stability of the proteins, and protein concentration. Additionally, surface characteristics play a critical role in adsorption. These factors and their effects on the adsorption process are discussed in the following section.

2.4.1 Protein Interactions with the Surface

How the protein layer is formed, and the amount of adsorbed proteins on the surface depends on several factors. One important factor is related to the surface properties, especially its **wettability**. As explained in Section 2.3, proteins have hydrophobic, hydrophilic, positively and negatively charged regions that interact with their environment and the surface. Contact with the hydrophobic surface causes the proteins to unfold so that the hydrophobic amino acid residues present in the native structure (see Section 2.3) can bind to the surface. In contrast, if the surface is neutrally hydrophilic, the hydrophilic amino acid residues, which are in the native structure on the protein surface, are more likely to bind to the solid surface. In this case, the protein structure is less altered. For this reason, adsorption to neutral hydrophilic surfaces is relatively weak, whereas adsorption to hydrophobic surfaces is strong and often irreversible [158]. It is therefore not surprising that hydrophobic surfaces frequently bind more proteins than hydrophilic surfaces [161].
Protein adsorption on a charged surface depends, among other things, on how the proteins is charged, which depends on the pH value of the environment [162, 163, 164]. If the protein is in a more acidic environment (pH < 7), the α-amino group (NH_2) ionizes to $NH_3{}^+$. If the environment is more basic (pH > 7), the α-carboxyl group (CO_2H) ionizes to $CO_2{}^-$. In addition to these changes in the protein backbone, the side chains of some amino acids, especially the basic (lysines, arginines, histidines) or acidic (aspartates, glutamates) ones, can also ionize [135]. Due to a change in pH value, these chemical changes can cause denaturation of the proteins and thus significantly impair their function [164, 165, 166].
In the human body, blood exhibits a slightly alkaline pH value of approximately 7.4 [167, 168]. The pH value of normal synovial fluid is similar to that of blood, typically also around 7.4 [167], but possibly slightly higher, reaching 7.8 [168] [16]. This pH value is further reduced by metal ions that may be released from the metal surface, especially in the synovial fluid. For example, a pH value of about 7.6 [169], or about 7.1 in chronic prosthetic joint infection, or about 7.3 in aspectic failure has been observed in revision surgery [170]. Consequently, proteins in this pH value range (7-8) tend to be negatively charged and then preferentially adsorb to positively charged surfaces via **polar or ionic interaction**.
In addition to the various possible interactions, the **chemical structures** of the proteins and the surface also influence adsorption. Most proteins are not homogeneous but consist of different domains, each of which can be hydrophilic/hydrophobic/charged. For example, human serum albumin, like bovine serum albumin, consists of three domains (see Figure 2.5 (d)). Domains I and II are negatively charged, and domain III is weakly positively charged [171, 172]. Furthermore, the first loop in domain I is slightly hydrophobic [171, 172]. This results in a different adsorption behavior depending on which domain is in contact with the surface. These properties are influenced by the pH value [166]. Additionally, the surface may also have domains that interact differently with the proteins [161]. Consequently, a non-uniformity of the proteins and the surface ensures that each encounter has an individual interaction energy, resulting in different degrees of adsorption and possibly denaturation [171].
Another important factor influencing protein adsorption is the **topography of the surface**. A rougher surface effectively provides a larger contact area with the surrounding

[16] However, the pH value changes when disease/inflammation (rheumatoid arthritis or osteoarthritis) occurs. Study-dependent pH values of around 7.2 [167], 7.6 [168] or 7.8 [169] are then reported.

liquid, resulting in an increased number of binding sites available for proteins on the metal surface. As a result, protein adsorption is significantly affected by surface topology, where not only the dimensions and precise morphology of individual roughness features are critical, but also their spatial distribution [173]. The distribution of topographical features can lead to preferential binding sites that may selectively attract certain proteins [156, 174, 175, 176]. Moreover, different proteins exhibit varying responses to surface topography. For example, studies using silica spheres of differing diameters show that highly curved surfaces can induce the denaturation of bovine fibrinogen while stabilizing the structure of bovine serum albumin [177]. Such opposite responses illustrate that the nature of the interactions between proteins and surfaces, as well as any resulting structural changes in the proteins, is contingent upon protein shape and flexibility. Thus, the interaction between surface topography and protein characteristics complicates the adsorption process, a challenge that is particularly pronounced in *in vivo* applications due to the presence of numerous diverse biomolecules [173].

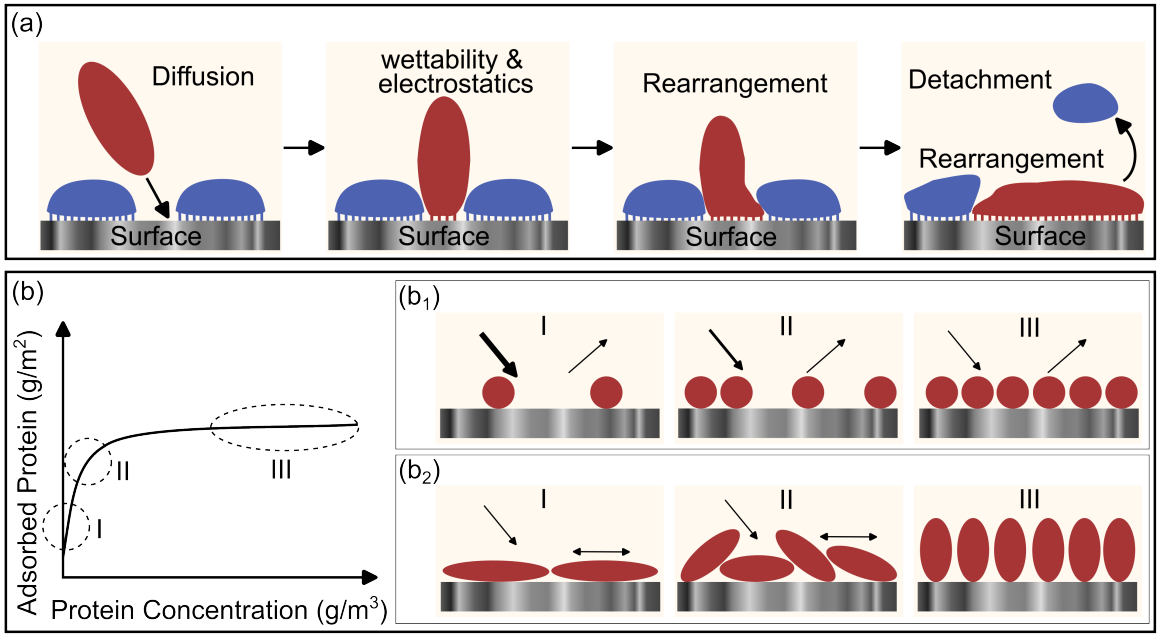


Figure 2.8: The Vroman effect, illustrated in panel (a), describes a process where an initially adsorbed protein is displaced by a subsequent protein that exhibits greater affinity for the surface than the protein that is already adsorbed. The Langmuir adsorption isotherm curve, shown in panel (b), can be interpreted in the context of true Langmuir adsorption behavior (b_1), which occurs under conditions where the adsorption process is reversible (involving both adsorption and desorption), binding sites are equivalent, and the solute behaves as a non-interacting ideal gas. Conversely, the same adsorption curve (b) displays a typical irreversible protein adsorption behavior. In this scenario, at low solution concentrations, the adsorbed proteins have more time to spread across the surface (b_2), resulting in a Langmuir-like adsorption process.

2.4.2 Competitive Adsorption

In addition to this multitude of factors that influence and determine adsorption, the choice of material and the composition of the biological fluid are crucial [157, 178]. The adsorption process becomes competitive when the fluid is a mixture of proteins (for example, blood contains far beyond 1000 proteins [179, 180]). As soon as the metal surface comes into contact with the protein mixture, proteins that reach the surface by diffusion or convection adsorb to it [143, 158, 159, 160]. Initially, the proteins with the highest mobility (typically small, low molecular weight proteins) reach the surface and adsorb there [181]. Over time, these adsorbed proteins may undergo partial replacement by subsequently arriving proteins (less mobile, high molecular weight), provided these later-arriving proteins exhibit greater surface affinity than those initially adsorbed [182, 183]. This adsorption process is called the "Vroman effect" [184], as is displayed schematically in Figure 2.8 (a). Due to this high affinity of certain proteins, there is an enrichment of these proteins in the adsorption layer. However, there is still a large variety of proteins within this layer. The final composition depends on which proteins are present in how high of a concentration in the protein mixture, their diffusion dynamics, the individual adsorption affinity of a protein, the individual desorption character of the proteins, and the surface properties. This adsorption often leads to a structural rearrangement of the proteins (see Figure 2.8 (a)). However, the extent of the structural change depends on the structural stability of the proteins. A distinction is made between "soft" (low conformational stability) and "hard" (high conformational stability) proteins, with the adsorption of "soft" proteins being more likely because they can have more binding sites [143, 162]. Due to this structural rearrangement of the proteins, there are more binding sites for the protein at the surface. So, in summary, the adsorption, which is significantly influenced by the hydrophobic, hydrophilic, and electrostatic (polar, Coulomb) interactions as described, is usually an irreversible process [158, 185, 186, 187, 188].

2.4.3 Concentration Dependent Adsorption

In addition to the individual components of the biological fluid, the concentration of these components in the fluid also influences the adsorption process. This impact of protein concentration on adsorption is particularly pronounced when examining solutions consisting of a single protein rather than a mixture of proteins. Then, the amount of protein adsorbed per unit area is observed as a function of the protein concentration in the solution, as displayed in Figure 2.8 (b). This curve corresponds to the Langmuir adsorption model[17] (see Figure 2.8 (b_1)), which assumes reversible and isothermal adsorption and that the rules of an ideal gas apply to the adsorbent [190]. However, as described earlier, protein adsorption is usually irreversible, and proteins are also not an ideal gas. For this reason, calculations based on Langmuir adsorption cannot be used [191]. The observable, so-called Langmuir-like adsorption process for proteins can be explained by the fact that the adsorbed proteins have more time to spread on the surface when the protein concentration in the solution is low, as shown schematically in Figure 2.8 (b_2) I. Many binding sites are already saturated by a protein, resulting in a relatively low surface concentration. If, on the other hand, a high protein concentration is used, the binding sites are saturated with other proteins, so that

[17] Irving Langmuir was awarded the Nobel Prize in Chemistry in 1932"for his discoveries and investigations in surface chemistry" [189].

the proteins do not have time to spread out on the surface, and more proteins adsorb on the same surface (see Figure 2.8 (b_2) II and III) [191, 192]. At a certain protein concentration in the solution, saturation occurs (0.1-0.5 mg/cm^2) [191, 193], so that the curve does not rise any further, as can be seen in Figure 2.8 (b_2) in region III. In addition to this saturation, a slight increase in adsorbed protein per unit area is occasionally observed with increasing protein concentration in the solution. This relationship is then described by the Freundlich isotherm [160, 191, 193].

2.4.4 Metal-Protein Complex Formation

In addition to the effect on the pH value described in Section 2.4.1, metal ions can also contribute to the formation of metal-protein complexes [194]. A metal ion (*e.g.*, Zn^{2+}, Cu^{2+}, Co^{2+}, Cr^{2+}, Fe^{3+}, Ni^{2+}, Mg^{+2}) binds to a specific position on the polypeptide chain, with certain binding sites being preferred. For example, the side chains of some amino acids (Glu, Tyr, Cys, His, Arg, Lys, Asp, and Met), the N-terminus of proteins, or the amide/carboxyl groups of the protein backbone are often identified as components of a protein that bind to the metal ions [195, 196]. In particular, the amino acids histidine and cysteine are known for their affinity for metal ions. This phenomenom is also being used in technical applications to filter out a specific protein from a mixture of different proteins (for example, immobilized metal affinity chromatography is based on this principle) [194, 195, 196, 197]. The tripeptide [18] glutathione, which consists of the amino acids glutamate, cysteine, and glycine, plays an essential regulatory and protective role in nearly all eukaryotic and prokaryotic cells, mainly due to its oxidative capacity [198]. In particular, glutathione acts as an antioxidant, protecting cells from damage caused by reactive oxygen species and toxic heavy metals by undergoing oxidation more readily than cellular components [198]. This protective function is primarily facilitated by the sulfhydryl group of the cysteine residue, which readily binds to metal ions, as shown in Figure 2.9.

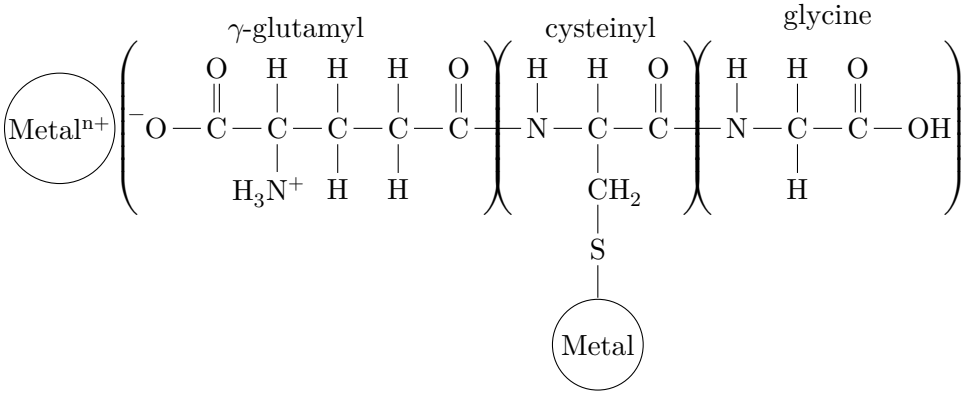


Figure 2.9: The tripeptide glutathione, comprising the amino acids glutamate, cysteine, and glycine, has binding sites for metal ions. In particular, the sulfhydryl group of the cysteine residue provides a binding site to metal ions. This interaction plays a significant role in glutathione's function as an antioxidant, thereby protecting cellular components from damage.

[18] The term tripeptide is actually not quite correct, as the two amino acids glutamates and cysteines are bound via C_γ and not via C_α as is usual with a peptide bond (see Section 2.3).

Furthermore, the ability of proteins to form metal complexes is not only a protective property against damage but also an important biological property for the distribution of essential transition metal ions in the human body. For example, the protein human serum albumin (HSA) is fundamental for the transport and distribution of Cu^{2+} and Zn^{2+} [199].

2.5 Raman Signals of Selected Materials

This section describes the materials and their Raman signals, which are primarily discussed in this thesis. For this reason, Section 2.5.1 first identifies the Raman signals of crystalline molybdenum disulfide based on the symmetry observations (point group) and discusses the Raman shifts of two characteristic Raman modes due to structural changes. It is common to refer to the modes measured in the Raman spectrum as the corresponding vibrational modes because of their symmetry properties. In organic materials, in contrast to the MoS_2 crystal, there are typically only local symmetries, so individual functional groups give rise to the Raman signals. For this reason, Section 2.5.2 will first present some characteristic group frequencies of specific functional groups commonly found in organic materials. Followed by a discussion of the structure of BSA and the associated Raman signals.

2.5.1 Raman Signals of Molybdenum disulfide (MoS_2)

Molybdenum disulfide (MoS_2) is part of the class of transition metal dichalcogenides (TMDC). TMDC monolayers consist of a layer of transition metal atoms Mo (groups 4-12 of the periodic table) sandwiched between two layers of chalcogen atoms S (group 16 of the periodic table), forming a covalently bonded three-layer structure. This three-layer structure forms a so-called monolayer of MoS_2 or 2D material. By stacking these monolayers a MoS_2 bulk crystal is formed. The layers are held together by van der Waals interactions. The resulting structure is depicted in Figure 2.10 (a).

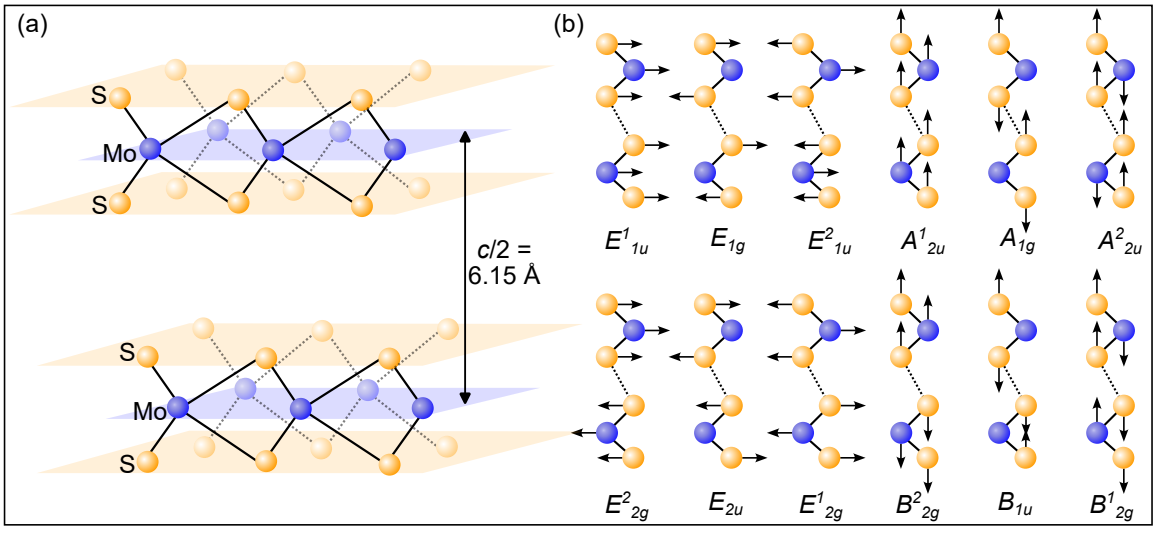


Figure 2.10: (a) Three dimensional representation of the structure of 2H-MoS_2. The lattice parameter c is taken from [200]. (b) Sketch of the vibrational modes of bulk MoS_2.

Bulk TMDCs can exist in three structural polymorphs $1T$, $2H$, and $3R$ [19], where MoS_2 exists in two crystal forms (hexagonal and rhombohedral). However, the hexagonal 2H-MoS_2 form is the most common [201], which is assigned to the D_{6h} point group because of its symmetry [202].
The unit cell contains six atoms, resulting in 18 normal modes Γ_{tot}. According to group theoretical considerations, as in Section 2.2.1, using the Equation 2.30 for the lattice vibrations of the bulk MoS_2 at the Γ point leads to the irreducible representation [203]

$$\Gamma_{\text{vib}} = A_{1g} + 2A_{2u} + 2B_{2g} + B_{1u} + E_{1g} + 2E_{2g} + 2E_{1u} + E_{2u}\,. \tag{2.31}$$

These 12 irreducible representations correspond to the bulk MoS_2 vibrational modes, which are illustrated schematically in Figure 2.10 (b), where a distinction is made between in-plane and out-of-plane modes. From the character table of the D_{6h} point group (see for example [103, 109, 204]), it follows that the vibrational modes A_{1g}, E_{1g} and $2E_{2g}$ satisfy the selection rules in Section 2.1.2 for Raman activity. In a non-resonant Raman spectrum, these four first-order Raman-active modes can be observed in bulk MoS_2, as listed in Table 2.6. Nevertheless, a minor limitation exists in backscattering experiments, wherein the c-axis of the MoS_2 crystal is parallel to the laser beam propagation. Due to symmetry considerations in these experiments, the E_{1g} Raman mode is forbidden [205, 206, 207].

Table 2.6: Frequency shifts for Raman active modes for monolayer, bilayer, trilayer, quadrilayer, and bulk MoS_2 with 532 nm excitation laser wavelength. The data for the Raman shifts is taken from Reference [44] and for the intensity ratio from reference [208].

mode	monolayer	bilayer	trilayer	quadrilayer	bulk
	Raman shift (cm^{-1})				
E^2_{2g}					32
E_{1g}					286
E^1_{2g}	384.7	382.5	382.4	382.4	383
A_{1g}	402.7	404.9	405.7	406.7	407.8
$I(A_{1g})/I(E^1_{2g})$	1.05	0.80	0.78	0.76	0.75

Further Raman spectroscopic investigations have revealed a systematic correlation between the number of MoS_2 layers and the frequency of the E^1_{2g} mode and, in particular, the A_{1g} mode [44, 208, 209]. Table 2.6 lists the redshift of approximately 2 cm^{-1} of the E^1_{2g} mode and the blueshift of approximately 5 cm^{-1} of the A_{1g} mode with an increasing number of layers. From the atomic motion of the A_{1g} vibrational mode, as schematically illustrated in Figure 2.10 (b), it is obvious that an interaction of the sulfur atoms of neighboring layers is possible within a multilayer MoS_2 crystal. Therefore, the vibration is influenced by an additional coupling or binding force between the neighboring sulfur atoms, which leads to a stiffening of the A_{1g} mode with an increasing number of MoS_2 layers. Similarly, for the E^1_{2g} mode, the atomic movement during vibration (see Figure 2.10 (b)) suggests that a stiffening would also occur with an increasing number of layers. However, the opposite is observed, namely that the long-range restoring Coulomb force becomes weaker with an

[19] The letter indicates the symmetry trigonal (T), hexagonal (H), rhombohedral (R), and the number indicates the amount of layers in the unit cell.

increasing number of layers. This behavior can be explained by the dielectric screening properties, which depend on the number of MoS_2 layers and are particularly pronounced for molybdenum atoms [210].
The band structure and the associated electronic properties also depend on the number of MoS_2 layers. Of particular interest is the gradual transition from an indirect band gap (1.23 eV[211]) in bulk MoS_2 to a direct band gap (1.90 eV[212]) semiconductor in a monolayer MoS_2. Due to the band structure, MoS_2 is an intriguing candidate for several optoelectronic and magneto-optical applications within the field of semiconductor physics, including spin and valleytronics [213, 214, 215]. In addition, this dependence of the electronic structure on the number of MoS_2 layers can also explain the relationship between the ratios of the Raman intensities $I(A_{1g})/I(E^1_{2g})$, which decrease with increasing layer thickness, and the number of MoS_2 layers, also listed in the Table 2.6 [208, 209]. These correlations allow the number of MoS_2 layers to be deduced from the Raman shift or intensity ratio.
In addition to this thickness-dependent change in vibrational frequencies, the application of tensile or compressive stress can also cause a structural change in the sample in form of tensile or compressive strain. For example, under tensile stress, atoms are pulled apart along the stress direction, causing the chemical bonds to lengthen. Conversely, compressive stress (pressure) shortens these chemical bonds. According to the Equation 2.17, this leads to a Raman shift of the individual phonon modes, whereby longer chemical bonds give rise to a redshift of the vibronic mode and shorter bonds cause a corresponding blueshift. Due to the geometry and spatial symmetry of the E^1_{2g} and A_{1g} phonon modes of MoS_2, it is possible to show a relationship between strain and Raman shift of the modes. At compressive stress (pressure) along the *c*-axis, the chemical bond lengths along this axis are shortened significantly more than those within the basal plane[20] [216], so that the A_{1g} phonon mode, which represents a vibration along the *c*-axis (compare with Figure 2.10 (b)), is affected to a significantly greater extent than the E^1_{2g} mode. Thus, up to a pressure of 2 GPa a linear relationship between Raman shift and compressive stress was observed, with the A_{1g} mode increasing by about 3.8 cm^{-1} and the E^1_{2g} mode is shifted by about 1.8 cm^{-1} per 1 GPa [217, 218]. With a further increase in compression pressure, the linear relationship between Raman shift and pressure no longer holds, despite a further blueshift of both modes [217, 219, 220].
In contrast, a tensile strain within the basal plane[20] of the MoS_2 structure has little effect ($-0.4\,cm^{-1}$ per % tensile strain) on the frequency of the A_{1g} mode. This is again due to the geometry and spatial symmetry of the A_{1g} phonon mode. Still, the tensile strain has a significant impact on the Raman shift of the E^1_{2g} mode, since the motion of the atoms is applied along to the basal plane. The Raman shifts observed in literature range from approximately $-7.4\,cm^{-1}$ to $-1.7\,cm^{-1}$ per 1 % tensile strain [221, 222, 223]. Additionally to these changes in the Raman shift, the spectra themselves demonstrate alterations when tensile strain modifies the MoS_2 structure. For instance, at a tensile strain exceeding 1 %, the symmetry of the MoS_2 crystal breaks, resulting in the removal of the double degeneracy of the E^1_{2g} vibration. Consequently, the E^1_{2g} mode splits into two singlet sub-bands $E^{1,-}_{2g}$ ($E^{1,\parallel}_{2g}$) and $E^{1,+}_{2g}$ ($E^{1,\perp}_{2g}$), as reported in literature [222, 224, 225]. The phonon mode

[20] In MoS_2, the basal plane refers to the surface aligned parallel to the atomic layers within the MoS_2 crystal structure. More details on the basal plane are provided in Section 2.6.6.

designated as $E_{2g}^{1,-}$ ($E_{2g}^{1,\parallel}$) describes the motion of the atoms in a direction parallel to the applied stress. Correspondingly, the atoms move perpendicular to the strain direction in the $E_{2g}^{1,+}$ ($E_{2g}^{1,\perp}$) phonon mode. In addition, the tensile strain affects the frequencies of these non-degenerate modes. For the $E_{2g}^{1,-}$ mode, Raman shifts of $-2.5\,\mathrm{cm}^{-1}$ to $-4.6\,\mathrm{cm}^{-1}$ per 1 % tensile strain have been observed [222, 224, 225]. In contrast, the maximum Raman shift identified for the $E_{2g}^{1,+}$ mode was $-1\,\mathrm{cm}^{-1}$ per 1 % tensile strain [222, 224, 225].
Furthermore, the compressive or tensile strain, along with its direction, influences the intensity ratio $I(A_{1g})/I(E_{2g}^1)$. With increasing compressive stress parallel to the *c*-axis, the intensity ratio $I(A_{1g})/I(E_{2g}^1)$ increases [226]. In contrast, the intensity ratio decreases when the tensile strain, oriented parallel to the basal plane, is applied (within the xy plane) [224, 227]. The intensity ratio is ≥ 1, which can be attributed to the stronger coupling of the A_{1g} mode to the excited d_{z^2} states [218]. These correlations allow the type (compressive or tensile) and amount of strain and orientation relative to the MoS_2 crystal structure to be inferred from the Raman shift and/or intensity ratio. Moreover, studies have demonstrated that these Raman modes also depend on the temperature [228, 229]. Consequently, an increase in temperature results in a redshift of the E_{2g}^1 mode and, particularly, of the A_{1g} mode [228, 229].
In the scope of this thesis MoS_2 crystals are not considered, but sputtered MoS_2 coatings, which are structurally more like microcrystalline MoS_2 with varying defect density, orientation (basal or columnar), and grain size. These perturbations (defects or grain boundaries) can excite other modes such as acoustic phonons like $LA(M)$ as well as harmonics or combination modes, as mentioned in Section 2.1.2. The perturbations also cause slight changes in the frequencies of the modes.

2.5.2 Raman Signals of Organic Materials

Organic substances typically have very pronounced intensities in the C−H stretching region from $2800\,\mathrm{cm}^{-1}$ to $3100\,\mathrm{cm}^{-1}$ and in the spectral region from $750\,\mathrm{cm}^{-1}$ to $1800\,\mathrm{cm}^{-1}$. The latter is frequently designated as the "fingerprint region" as this spectral region is characteristic of an organic substance. It is thus possible to distinguish between different organic substances based on the fingerprint region. Table 2.7 lists some of the main frequency assignments of the Raman spectra of organic compounds. It is common practice to abbreviate stretching vibrations with ν, bending vibrations with δ, and rotations with ρ. A detailed examination of Table 2.7 reveals that the Raman shift depends on the bond order: $\nu(\mathrm{C{-}C}) < \nu(\mathrm{C{=}C}) < \nu(\mathrm{C{\equiv}C})$. Furthermore, it is noticeable that vibrations involving H atoms exhibit a higher frequency. In addition, the frequency of stretching vibrations is higher than that of bending vibrations within the same structural group (*e.g.*, $\delta(\mathrm{CC}) < \nu(\mathrm{CC})$). These observations can be explained by Equation 2.17, since the coupling strength W increases with the bond order [230]. In addition, structures with light atoms (such as H) have a smaller reduced mass m_{red}, which comparatively increases the vibrational frequency [21]. The stretching vibrations are shifted to a greater extent than the bending vibrations since stretching changes the length of the chemical bond, which requires a greater input of energy than the angular change associated with the bending vibration.

[21] It is noteworthy that inorganic compounds usually contain heavy atoms, such as iron or molybdenum, resulting in comparatively smaller Raman shifts (see also the Raman shifts of MoS_2 in Table 2.6). This allows for the distinction between inorganic and organic materials to be made.

Table 2.7: The table presents the assignment of bands to functional groups in the Raman spectra of organic materials. For a comprehensive list of band assignments and organic-related Raman signals, please refer to [45, 46, 231]. The assignments presented in this table are taken from these references.

Vibration	Abbreviation	Raman shift (cm^{-1})
Symmetric bending of aliphatic chains (C_n with $n = 3 ... 12$)	δ_{sym} (CC)	$150 - 425$
C−C stretch of aliphatic chains and cycloalkanes	ν(C−C)	$950 - 1150$
C=C stretch of alkenes	ν(C=C)	$1450 - 1750$
C≡C stretch of alkynes	ν(C≡C)	$2100 - 2250$
CC stretch of aromates ((substituted) benzene molecules)	ν(CC)	≈ 1000, ≈ 1450, ≈ 1500, ≈ 1580, ≈ 1600
CH_2 in phase twist	$\delta(CH_2)$	$1295 - 1305$
Symmetric CH_3 bend	$\delta_{sym}(CH_3)$	≈ 1380
CH_2 bending vibrations, antisymmetric CH_3 bend	$\delta(CH_2), \delta_{asym}(CH_3)$	$1400 - 1470$
Amide III band (30 % CN stretch, 30 % NH bend, 10 % CO stretch, 10 % O=C−N bend, rest other)	Amide III β-sheet Amide III random Amide III α-helix	$1225 - 1235$ $1240 - 1255$ $1270 - 1300$
Amide II band (≈60 % NH bend, 40 % CN stretch)	Amide II	≈ 1565
Amide I band (≈80 % CO stretch, ≈10 % CN stretch, ≈10 % NH bend)	Amide I α-helix Amide I random Amide I β-sheet	$1645 - 1655$ $1660 - 1670$ $1665 - 1675$
CH stretch	$\nu_{sym}(CH_2)$, $\nu_{sym}(CH_3)$, $\nu_{asym}(CH_2)$, $\nu_{asym}(CH_3)$	$2750 - 3100$

The amide bands listed in Table 2.7 are of significant importance for the identification and elucidation of the tertiary structure of organic material. As indicated in the Table 2.7, several vibrations within the amide structure are involved in the spectral appearance of the Raman amide bands. The Raman signal results from the interaction of these vibrations, meaning that individual bond vibrations in the amide structure are not considered separately. Nevertheless, it is possible to determine the presence of an α-helix, β-sheet, or random coil structure, in particular, based on the Raman shift of the amide I and amide III bands. Therefore, these two modes are considered to be the most important Raman-active vibrations of this functional group. For example, the first structural studies of BSA using Raman spectroscopy showed that the structure was predominantly α-helical, based on the Raman shift of the amide III band [232]. But the determined proportion of about 60 % [232] differs from the value of 74 % known today [233].

Structural Features and Raman Activity of Serum Albumin

Serum albumin (SA) is the most abundant multi-domain protein of blood plasma found in all mammals [233, 234, 172]. Albumins are distinguished from other proteins by a low proportion of the amino acids tryptophan and methionine in their primary structure, coupled with a high proportion of the amino acids cysteine, aspartic acid, glutamic acid, lysine, and arginine. Because of its flexibility (soft protein), SA can bind a diverse range of materials, often through hydrophobic interactions. Thus, the SA protein acts as both a depot and a carrier for many endogenous and exogenous compounds [22]. Among other things, SA is used to transport a variety of metabolites, drugs, nutrients, metals (especially Ca^{2+} and Mg^{2+}), short-chain fatty acids and other molecules [172, 233, 234, 235].

Table 2.8: This table summarizes the occurrence of each amino acid in bovine and human serum albumin, along with the helical content, calculated net charge at a pH value of 7, and molecular weight for both proteins [172, 233, 236].

Amino acid	Bovine	Human
Aspartic acid	40	36
Asparagine	14	17
Threonine	33	28
Serine	28	24
Glutamic acid	59	62
Glutamine	20	20
Proline	28	24
Glycine	16	12
Alanine	47	62
Valine	36	41
Cysteine	35	35
Methionine	4	6
Isoleucine	14	8
Leucine	61	61
Tyrosine	20	18
Phenylalanine	27	31
Lysine	59	59
Histidine	17	16
Tryptophan	2	1
Arginine	23	24
Total	583	585
Helical content	74 %	67 %
Calculated net charge, pH 7	-18	-15
molecular weight	66.5 kDa	66.5 kDa

[22] This diverse binding property of the multifunctional SA protein is also of interest for a wide range of clinical, pharmaceutical, and biochemical applications, including the detection and treatment of various diseases. For further details, see reference [234] and the references therein.

The mature plasma protein SA is a macromolecule with a molecular weight of approximately 66 kDa. It has a heart-shaped tertiary structure [23] comprising three helical domains, as illustrated in Figure 2.5 (d). Table 2.8 lists the occurrences of individual amino acids within the primary structure of BSA and human serum albumin (HSA), which consist of 583 and 585 amino acids, respectively. As indicated in Table 2.8, the primary structure of the protein is predominantly comprised of negatively charged amino acids, resulting in a net negative charge at a pH value of 7. This enhances the solubility of SA. The exact sequence of the individual amino acids and a comparison of this sequence between BSA and HSA is given in reference [233]. This shows that the amino acids are not distributed homogeneously across the domains, with a higher proportion of charged amino acids present in a given domain. Consequently, the protein is not uniformly charged. At a pH value of 7 for the BSA [HSA] proteins, the net charge of domain I is -10 [-9], domain II -8 [-8] and domain III 0 [+2] [172]. In addition, the sequence of BSA and HSA shows that these two albumins share 75.6 % sequence homology [233]. The 35 cysteine residues form 17 cystine complexes through disulfide bridges. In most cases, one cysteine residue remains unbound, presumably protected from oxidation by steric factors, resulting in a free thiol group (Cys34 in BSA and HSA) [24]. The orientation of the 17 disulfide bonds affects the folding of the BSA and HSA molecules, contributing to their stability and organization into a series of nine loops [172, 236, 241]. Since a protein's function depends on its conformation, these 17 cystine complexes are crucial for its function.

Table 2.9: Characteristic Raman Lines of Aromatic Amino Acids.

Aromatic amino acids	Raman lines (cm^{-1})	Reference
Phenylalanine	622, 1004, 1033, 1207, 1586, 1605	[242]
Tryptophan	760, 878, 1340, 1360, 1553	[243]
Tyrosine	643 , 829, 852, 1177, 1207, 1605, 1617	[244]

These cystine complexes can adopt three stable conformations, as discussed in more detail in Section 2.3. Each of these conformations exhibits a characteristic Raman signal: ggg at 510 cm^{-1}, ggt at 525 cm^{-1}, and tgt at 540 cm^{-1} [148, 149, 245]. Raman studies of N-form BSA show that most ($\approx$ 10) of the 17 disulfide bridges adopt the ggg conformation, while the remaining ones adopt the ggt conformation [236, 241]. The conformation of the disulfide bridge, as well as the whole tertiary structure of the protein, depend on external factors such as pH value [23]. In addition to these α-amino acid cysteine, the primary structure of BSA and HSA proteins contains the aromatic α-amino acids phenylalanine (Phe), tryptophan (Trp) and tyrosine (Tyr). These π-conjugated amino acids exhibit particularly

[23] The tertiary structure may deviate from this heart-shaped structure when the environmental conditions change. This heart-shaped N-form is identified at a neutral pH value of approximately 7. It should be noted, however, that the A-form (pH$\approx$5.5), B-form (pH$\approx$9.3), E-form (pH$\approx$2.7), and F-form (pH$\approx$3.8) also exist [237]. Other conformational changes are also possible, for example, as a result of thermal denaturation processes [238] or as a consequence of urea or guanidine hydrochloride induced unfolding [239, 240].

[24] It should be noted that not all SA molecules contain a free thiol group. In healthy adults, 25-30% of HSA proteins are bound in the form of a mixed disulfide. Furthermore, Csy34 can act as a radical scavenger or as a binding site for a variety of endogenous ligands, metal ions, or drugs. In addition to this modification, many other changes are possible, so not all SA proteins are exactly the same [234].

high Raman activity and are sensitive to their surrounding environment [246]. Table 2.9 lists the characteristic Raman lines of these aromatic amino acids. Particular to note is the narrow-band Phe ring breathing mode at $1004\,\mathrm{cm}^{-1}$, which is independent of the Phe conformation and is suitable for normalizing the Raman spectra [247].

2.6 Tribology

The term tribology originates from the Greek language and the literal translation is "science of rubbing". After the economic importance of friction and wear was studied in 1966 [25], tribology has been systematically and scientifically studied. It is, therefore, a comparatively young scientific discipline and describes the combination of friction, wear, and lubrication. Every property of a tribological system is determined by the interaction of the entire system. This system consists of two active surfaces, an intermediate medium (*e.g.*, lubricant), and the surrounding medium (*e.g.*, air), rather than by individual materials. This section provides a fundamental understanding of tribology by gradually exploring its key principles and processes. Insights into these processes are crucial, as they demonstrate that tribological processes are seldom static. Instead, they depend on intricate interactions that significantly influence system behavior. Two of these processes, that occur in any tribological system, are friction and wear and are discussed in Section 2.6.1. Furthermore, the contact situation influences the tribological behavior, thus necessitating an analysis of contact problems, such as ball-on-disc and cylinder-on-disc, within the framework of Hertzian contact mechanics, as will be undertaken in Section 2.6.2. This analysis allows the initial Hertzian pressure to be calculated based on parameters such as the normal force. Such a calculation helps determine the maximum stresses and deformations at the contact surface, which is essential for designing tribologically involved components. Section 2.6.3 examines tribology at different scales, from macrotribology to micro- and nanotribology. This multi-scale approach offers insight into the unique, scale-dependent characteristics of friction and wear, enriching the understanding of tribological behavior across various applications. Moreover, the tribological material, formed in a tribological process, significantly influences the friction and wear properties, as well as the stability and durability of the tribological system. Section 2.6.4 discusses the formation of this tribological material, with particular emphasis on tribofilms and transfer films that develop between contact surfaces. These films play a crucial role in modifying the friction and wear properties and influence the stability and durability of the system. Finally, Section 2.6.5 deals with grain boundary segregation, affecting material structure and surface properties.

2.6.1 Friction and Wear

When a body moves relative to the contacted surface of another body or through a medium (*e.g.*, oil, water, or air), **friction** acts as the force that opposes this motion. While friction is essential for the transmission of mechanical energy, it can also pose drawbacks, such as impeding the movement of a body. The desired frictional behavior of the two bodies in contact varies based on the application. For instance, high friction is advantageous in braking

[25] Original definition: "Tribology is the science and technology of interacting surfaces in relative motion and related subjects and practices" [3].

systems to ensure effective deceleration. Conversely, in motors and gearboxes, minimizing friction is critical to prevent the conversion of energy into forms that do not fulfill their intended function.
Upon tribological interaction between the body and the counter body, they come into direct contact with one another only on a surface that is referred to as the "true contact surface" [26]. Interactions between the bodies or the lubricant occur at this true contact surface, for example, in the form of an adhesion-induced interfacial bond. In context of tribological systems, the requisite force for breaking these adhesive bonds, which are continuously formed at varying locations in the contact zone, represents a part of the overall frictional force [9].
Furthermore, tribological loading gives rise to elastic and plastic deformation of surface areas at the microscopic level, which, when accumulated, are observed at the macroscopic level. Additionally, furrowing may also occur. Some of the energy introduced into the system from the outside is absorbed by the system itself, for example, in form of lattice deformations, the formation of residual stresses, or tribochemical reactions. Alternatively, it may be dissipated or emitted through thermal processes. This illustrates that the friction process is inherently intricate, encompassing a variety of physical and chemical interactions that facilitate energy transfer and conversion. Additionally, friction can manifest in several types, each with distinct characteristics and effects on the performance and durability of the materials involved.
The type of friction process depends on the aggregate states involved and is therefore differentiated:

1. Dry fiction: Between two solid surfaces.

2. Lubricated friction: A (liquid or solid) lubricant separates two solid surfaces.

3. Fluid friction: Between two viscous fluids.

In the case of dry friction between two solid bodies, the ratio of the frictional force F_{F} and the normal force F_{N} can be described by the empirical law of friction

$$\mu = \frac{F_{\mathrm{F}}}{F_{\mathrm{N}}} \tag{2.32}$$

proposed by Amontons and Coulomb. This ratio remains constant and is defined by the coefficient of friction μ (COF) [7, 8]. Nevertheless, the linear relationship is not universally valid; it may be influenced by several factors, including temperature variations [248], high sliding velocities [249], and the viscoelastic behavior of materials [250]. Despite these limitations, this linear approximation remains accurate for many practical applications, particularly those involving metal-on-metal contacts [251]. In laboratory tests, the COF is often determined in simple tribological systems. These include the ball-on-disk tribometer tests with an initial contact situation, described in more detail in Section 2.6.2 on the tribological contacts.

[26] As a consequence of the roughness profile, contact is only established at discrete micro-contacts, named asperities, (see Figure 2.13), which are capable of undergoing deformation as a result of tribological loading.

During tribological contact, physical and chemical interactions cause damage to the surface, resulting in the formation of particles (or debris) that can leave the tribological system. Such a material loss is referred to as **wear**, resulting in a change in the shape and surface structure of the friction body or bodies. Ultimately, this may result in a loss of function of the affected component. Various methods (*e.g.*, transmission electron microscopy [34], 3D profilometry [252], wear measurements using radionuclide technology [253]) and units are used to quantify the wear of a tribological system. The wear coefficient k according to Archard's wear law or the wear rate w [10, 11]

$$k = \frac{V}{F_\mathrm{N} s}, \quad w = \frac{V}{s}, \tag{2.33}$$

which relates the volume loss V to the wear path s (and the normal force F_N), is often given. Depending on the wear rates or wear coefficients, the wear is categorized as severe wear ($w \geq 10^{-2}\,\mathrm{mm^3\,m^{-1}}$), mild wear ($10^{-3}\,\mathrm{mm^3\,m^{-1}} \leq w \leq 10^{-4}\,\mathrm{mm^3\,m^{-1}}$) and ultra-mild wear ($w \leq 10^{-4}\,\mathrm{mm^3\,m^{-1}}$) [27] [254, 255]. However, it should be noted that the boundaries of these categories are not entirely clear. Rather, the categorization of wear depends on several factors, including the specific tribological circumstances, the load, and the sliding speed, as well as the morphology of the worn surfaces and the number and size of the wear particles [256, 257].
It is possible to distinguish between several wear processes depending on how the two tribological bodies move relative to one another to enable different applications [258]:

1. Sliding wear: They are in sliding contact.
2. Fretting wear: A very small, oscillating, and sliding movement between two contact surfaces.
3. Rolling wear: The two bodies roll against each other.
4. Rolling-sliding wear: The movement of the bodies is a superposition of sliding and rolling.
5. Abrasive wear: Material removal caused by the mechanical action, often involving hard particles or rough surfaces.
6. Erosive wear: A liquid or gas containing abrasive particles.

Only four main wear mechanisms, tribochemical reactions, surface fatigue, abrasion, and adhesion [6], are responsible for all wear processes. The mechanisms are listed in Figure 2.11, along with the associated sub-mechanisms. In a tribological system, these four mechanisms can occur simultaneously and contribute to wear. However, it is frequently the case that one particular wear mechanism is the dominant factor [6, 259, 260].
The wear mechanism known as tribochemical reactions involves chemical interactions initiated by tribological processes between the two contacting bodies, the intermediate medium (such as a lubricant), and the surrounding environment (*e.g.*, atmosphere). These reactions

[27] The specified limit value for the wear rate in the ultra-mild wear regime is unsuitable for the majority of applications in mechanical engineering. The wear rates required for these applications must be $w \leq 10^{-7}\,\mathrm{mm^3\,m^{-1}}$ [34].

are the consequence of an increase in energy at the interfaces, which is a tribologically induced phenomenon. To minimize this energy, chemisorption, and various chemical reactions may occur, which are often accelerated by the frictional heat [10, 261]. As a result, the reaction products formed typically exhibit altered physical and chemical properties due to their modified chemical composition. For instance, in metal-metal sliding contacts, oxidation frequently occurs at the interface surfaces of the metal bodies [12, 13, 14]. Under tribological load, this brittle oxide layer cannot withstand the load and often fractures, causing metal oxide particles to detach from the surface.

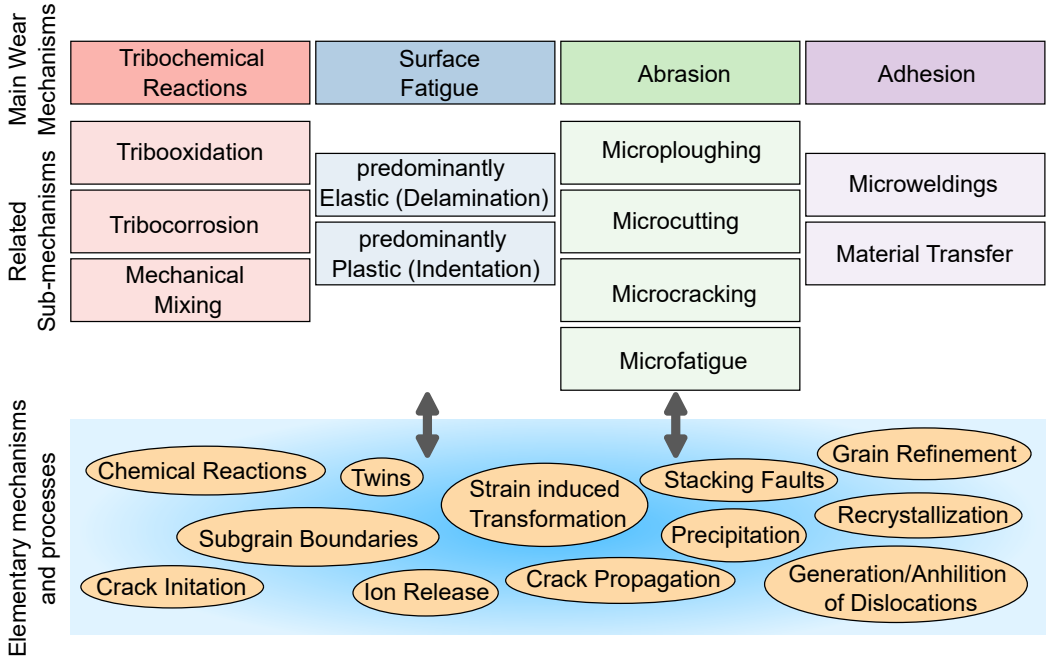


Figure 2.11: Main four wear mechanisms and sub-mechanisms. Adapted from textbook [34].

In addition, as previously mentioned, the forces occurring in the tribological contact are transmitted through the micro-contacts. Cyclic mechanical loading and the resulting elastic and plastic deformations of these contacts induce tensile, compressive, and shear strain. Such multi-axial strain variations lead to damage accumulation and initiate crack formation, a wear mechanism known as surface fatigue. Surface fatigue is determined in particular by the load amplitude and the number of cycles [10, 261].
Tribologically induced abrasion occurs when one friction body is harder than the other. For example, the roughness peaks of the harder body can remove material from the softer body, or hard (wear) particles may cause material removal. In contrast, adhesion is the transfer of material from one body to the other, where atomic and molecular forces play a decisive role. Adhesion is influenced by the totality of the microcontacts, the microstructure itself, and the structure of the surfaces [10, 16, 262].

2.6.2 Contact Problem - Hertzian Contact

Considering the initial contact in a ball-on-disk tribometer test without friction, a normal force F_N acts between the base and the counter body in the z-direction, with a pressure

distribution $p_z(x, y)$ on a circular contact surface $A = \pi a^2$ with a contact radius a, as shown in Figure 2.12. If only the effect of F_N in z-direction on an elastic medium is considered, the medium will deform along the z-axis. This deformation is given by

$$d_\mathrm{z}(r) = \frac{1-\nu^2}{\pi\mathfrak{E}}\frac{1}{r}F_\mathrm{N} = \frac{1-\nu^2}{\pi\mathfrak{E}}\int\int p_z(x,y)\frac{1}{r}\mathrm{d}y\,\mathrm{d}x\,, \tag{2.34}$$

as described by Landau and Lifschitz [263], where the elastic behavior of the deformed elastic medium is described by Young's modulus $\mathfrak{E}$ and Poisson's ratio ν.

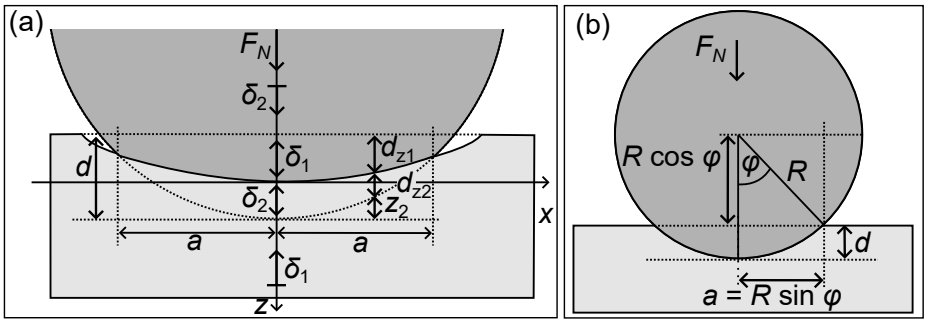


Figure 2.12: (a) Schematic representation of a Hertzian contact between an elastic sphere and an elastic plane. Panel (b) provides a schematic illustration of Hertzian contact between a rigid sphere and an elastic half-space.

Now, a tribological contact between two elastic bodies with the origin of the coordinate system in the middle of the contact area is considered, as illustrated in Figure 2.12 (a). The deformation of each body under the impact of the normal force F_N results in a total displacement that depends on the radial distance r, and is given by

$$d_\mathrm{z}(r) = \frac{1}{\pi}\underbrace{\left(\frac{1-\nu_1^2}{\mathfrak{E}_1}+\frac{1-\nu_2^2}{\mathfrak{E}_2}\right)}_{=:\,1/\mathfrak{E}^*}\int\int p_z(x,y)\frac{1}{r}\mathrm{d}y\,\mathrm{d}x\,. \tag{2.35}$$

Assuming a Hertzian pressure distribution [264]

$$p(x,y) = p_0\sqrt{1-\frac{x^2}{a^2}-\frac{y^2}{a^2}} = p_0\sqrt{1-\frac{r^2}{a^2}}\,, \tag{2.36}$$

within the circular contact area of radius a, with a maximum pressure p_0 at the center of the contact area, the vertical displacement is given by [28]:

$$d_\mathrm{z}(r) = \frac{1}{\mathfrak{E}^*}\frac{p_0}{4a}(2a^2-r^2)\,. \tag{2.37}$$

The total force or normal force acting on the contact area can be calculated by integrating the pressure (Equation 2.36) over the contact area

$$F_\mathrm{N} = \int_0^a p(r)2\pi r\mathrm{d}r = \frac{2\pi p_0}{3}a^2\,. \tag{2.38}$$

[28] Comprehensive and detailed calculations can be found in Ref. [265].

The contact situation is analyzed geometrically, as shown in Figure 2.12 (b), to determine the maximum pressure p_0 and the radius a of the contact surface as a function of the known material constants and dimensions. For simplicity, the limiting case is considered that the sphere is so rigid/hard that only the plane is deformed under the effect of the normal force F_N in z-direction. Furthermore, it is assumed that the sphere with a radius R does not significantly penetrate the other body ($a \ll R$), allowing for a small-angle approximation to be made. The depth of penetration or deformation can be calculated as follows

$$a = R\sin\phi \approx R\phi\,, \quad d = R(1-\cos\phi) \approx R(1-1+\frac{\phi^2}{2}) \Rightarrow d_\mathrm{z}(r) = d - \frac{r^2}{2R}\,, \tag{2.39}$$

which must correspond to the deformation in Equation 2.37, resulting in:

$$a = \frac{\pi p_0 R}{2\mathfrak{E}^*}\,, \quad d = \frac{\pi a p_0}{2\mathfrak{E}^*}\,. \tag{2.40}$$

By employing Equation 2.38, the following can then be calculated:

$$a = \sqrt[3]{\frac{3F_\mathrm{N}R}{4\mathfrak{E}^*}} \quad p_0 = \sqrt[3]{\frac{6F_\mathrm{N}\mathfrak{E}^{*2}}{\pi^3 R^2}} \tag{2.41}$$

where a and p_0 depend only on the known material properties and the radius of the sphere R. In the case of initial frictionless contact between a cylinder of radius R and length L and a flat surface, the resulting equations differ slightly from those previously presented due to the different geometry and, hence, different integration limits. When a Hertzian pressure distribution, as given in Equation 2.36, is used, but only in the x-direction, the resulting total force and the maximum pressure are given by [265]

$$F_\mathrm{N} \approx \frac{\pi}{4}\mathfrak{E}^* L d\,, \quad p_0 = \frac{2F_\mathrm{N}}{\pi L a} \approx \sqrt{\frac{\mathfrak{E}^* F_\mathrm{N}}{\pi L R}}\,. \tag{2.42}$$

2.6.3 Tribology Across Scales

Tribological processes are relevant in various applications or phenomena, encompassing many orders of magnitude. For instance, tribological processes range from plate tectonics, where large tectonic plates of the Earth's lithosphere interact over kilometers, leading to seismic activity (earthquakes), over mechanical applications such as engines, to nanoelectronics. The nano-, micro-, and macroscales that tribology encompasses can thus be understood in terms of Hertzian contact size. For example, a macroscopic sliding contact involves millions of asperities. In contrast, nanotribology may consider only a single asperity contact, as shown in Figure 2.13. Thus, most tribological processes can be considered at all of these scales. These fields of tribology are discussed in more detail below.

Macrotribology deals with the development, design, and realization of a large amount and diverse range of technical applications for the transmission of forces (*e.g.*, clutches), energy (*e.g.*, gears), and/or motion (*e.g.*, joints). The aim is to minimize:

1. Transmission losses:
   A usable energy reduction is linked to inefficiencies in power transmission, where a portion of the total energy is converted into forms that are no longer accessible to the system - such as heat - due to factors like misalignment, friction, or vibration.

2. Tribological losses:
   A portion of the total energy is converted into other forms, including thermal, acoustic, chemical, and material deformation energy, due to friction and wear at contact surfaces. As a result, the available usable energy within the system is reduced.

Minimizing these losses may enhance the overall energy efficiency of mechanical systems and prolong the service life of components.
The variety of applications for macrotribological systems results in a high level of diversity and complexity in tribological systems. To investigate the tribological properties of a tribological system in a laboratory setting, it is common practice to consider geometrically simple tribological systems (see Figure 2.13), such as ball-on-disc tribometers (see Section 3.2.3 and Figure 3.3). Nevertheless, a thorough investigation of the tribological processes leading to component failure cannot be accomplished through a macroscopic perspective alone, as it does not provide a comprehensive understanding of the phenomenon. A more in-depth analysis of the tribologically loaded area and the structural characteristics of the tribological bodies is necessary to achieve this understanding.

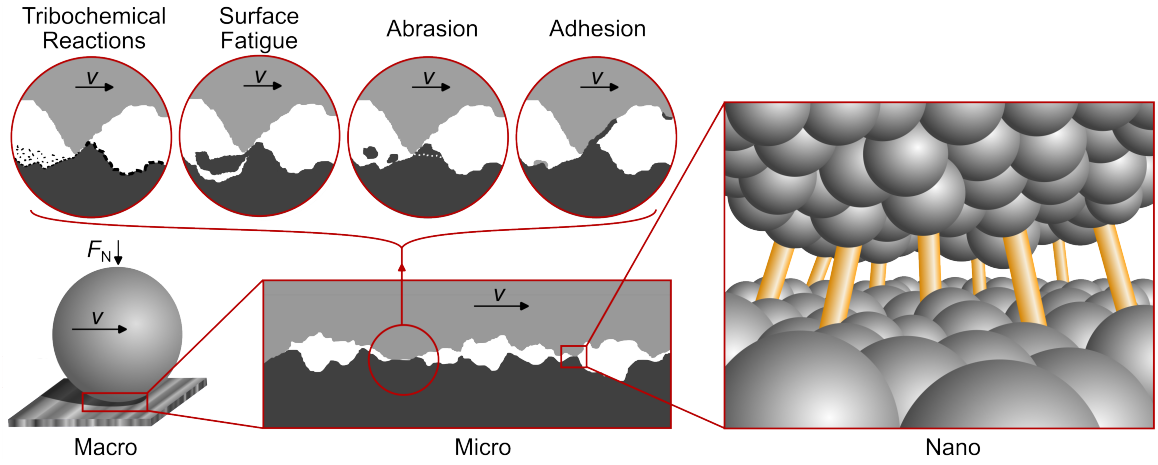


Figure 2.13: Schematic representation of a geometrically simple ball-on-disc tribological system illustrating the multi-scale nature of tribology. The actual contact area is much smaller than would be expected geometrically because of the micro-contacts created by the roughness. One of these micro-contacts is used to illustrate the four main wear mechanisms caused by the nanostructure. Adapted from [10, 266].

It is important to note that, regardless of the degree of smoothness achieved in the polishing of the macroscopic surface, the material surface will always exhibit a degree of roughness on a microscopic scale. Such a microscopic roughness is characterized by the presence of sharp, rough or rugged projections, termed “asperities”. During a tribological contact, micro-contacts (touching asperities from the tribological bodies) are distributed randomly, spatially, and temporally within the contact area, where the tribological processes occur, as

illustrated in Figure 2.13. Furthermore, the metal's physical properties exert a considerable influence on the macroscopic tribological process. For example, the hardness of a material provides information on how resistant it is to abrasion, which is crucial for applications such as milling. However, excessively hard materials can become brittle and may break under loads, which must be taken into account when selecting the material for a tool.

The field of **microtribology** studies microcontacts and the microstructure of tribological bodies and materials, with a particular focus on the changes induced by tribological contact. Understanding the structure of a technical surface is essential to understand and categorize the tribological processes leading to wear and friction.
The surface is the outermost or uppermost layer of a physical object or space and thus represents the interface between two distinct phases. In technical applications, the surface is between a solid material and the (liquid) lubricant, the surrounding atmosphere, or another solid material. Furthermore, the surface often exhibits crystallographic differences from the bulk material. Due to defects and the reduced number of neighboring atoms on the surface, the surface atoms can occupy more energetically favorable positions through surface reconstructions and recombinations. In the presence of a lubricant or an atmosphere, chemisorption and/or physisorption result in further alterations to the surface composition and/or structure. For instance, in the case of metals, the oxygen present in the atmosphere typically oxidizes the outermost layer during the manufacturing process or subsequent transportation. However, this oxidation does not affect the strength and ductility of the material [267, 268, 269] and represents the outermost boundary/layer of the material, with a thickness of maximal about 10 nm [262]. It may contain oxidations, adsorptions, and contaminations, as illustrated in Figure 2.14 (a). This surface layer is, the initial component of a tribological body that is in direct contact with the counter body and/or the lubricant.

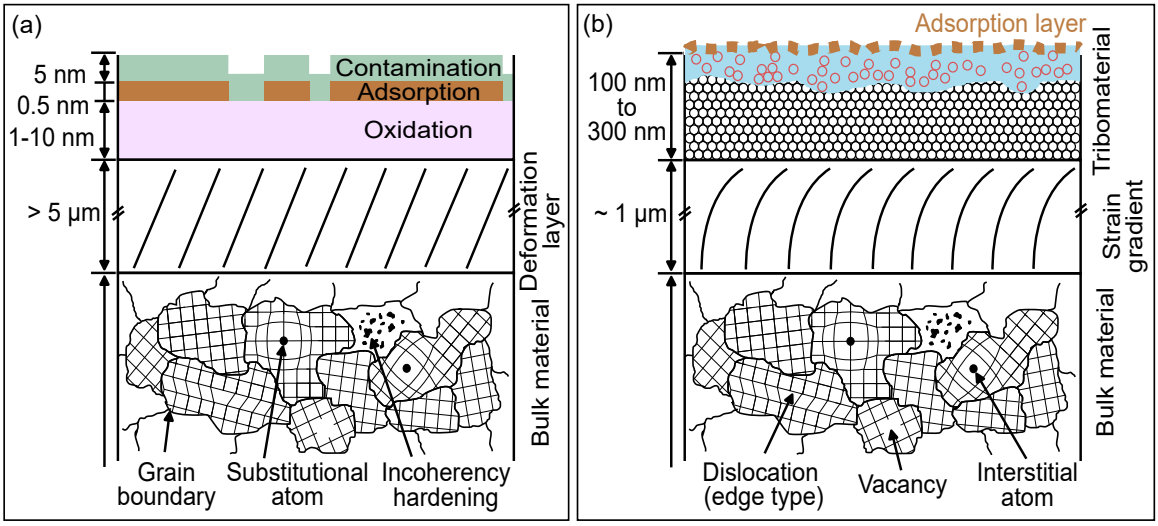


Figure 2.14: Schematic representation of the cross-section of a technical metal surface without tribological load (a) and after tribological load (b), where particles and lubricant represent the constituents of the generated tribomaterial. Additionally, the representation of the bulk material incorporates certain metal-physical characteristics of the material microstructure, which may also be present in the hole material. Adapted from [35, 262].

The manufacturing process exerts a significant influence on both the surface roughness and the material structure. For instance, residual stresses may be introduced, which can subsequently affect the load-bearing capacity of the material. Further influences of the manufacturing process on the material structure and the associated physical and chemical properties are not addressed in this thesis; in case of further interest, refer to the "Fertigungsverfahren" compendium [261, 270, 271, 272, 273]. The structural alterations introduced by the manufacturing process (residual stresses, deformations, hardening, etc.) typically extend several micrometers into the solid body, forming the deformation layer, as depicted in the cross-section of a metal surface in Figure 2.14 (a).
The mentioned layers within the illustration are referred to as the technical surface, as they represent the boundary layer area, which differs from the subsequent base material in composition and structure. The base material does not possess a single-crystal structure; rather, it is comprised of discrete grains, as will be explained in Section 2.6.5. In a manner analogous to the thermodynamically favored accumulation of specific alloy atoms at grain boundaries (see Section 2.6.5), oxidation may occur at the material surface at this boundaries [274, 275]. Such an oxidation may result in embrittlement, which may lead to cracking in tribological contact due to internal stresses or external forces [275, 276]. This is one of the forms of wear that microtribology addresses. The wear phenomenon is then used to categorize the wear mechanism on which the tribological system is based. As already mentioned in Section 2.6.1, a fundamental distinction is made between the four main wear mechanisms: tribochemical reactions, surface fatigue, abrasion, and adhesion. Figure 2.13 schematically shows the effects of these main wear mechanisms on the microcontacts as a result of tribological loading.

The field of **nanotribology** is concerned with studying individual micro- to nano-scale tribological contacts to gain a deeper understanding of the fundamental tribological processes at the interface. In particular, the adhesion effect is of crucial importance, as adhesion represents one of the essential mechanisms of friction. Nanotribology also plays an important role in nanotechnology [29] applications and its micro/nanoelectromechanical systems, including magnetic memory devices, quantum dot transistors, or single-walled carbon nanotube chemical sensors. Atomic force microscopy [30] can be used to simulate and analyze atomic friction contacts. A pointed (single-atom) tip is brought into contact with the material surface, and the surface is scanned.
Depending on the tip, micro, nano, and atomic frictional contacts can be simulated, and the resulting frictional and adhesive forces can be determined in the nN range. These measurements allow conclusions to be drawn about contact formation and forces. In addition to these experimental investigations, nanotribology also involves theoretical investigations in the form of simulations such as molecular modeling.

[29] Nanotechnology covers scales from 100 nm to one atom (≈ 1 Å) [277]. The birth of the idea was a visionary lecture by Richard P. Feynman [278], who was awarded the Nobel Prize in Physics in 1965 "for their fundamental work in quantum electrodynamics, with profound consequences for the physics of elementary particles" [279].

[30] The atomic force microscope was developed in 1985 by Gerd Binnig, Calvin Quate, and Christoph Gerber [280]; Gerd Binnig and Heinrich Rohrer had previously received the 1986 Nobel Prize in Physics "for their design of the scanning tunneling microscope" [281].

2.6.4 The Tribomaterial - The Third-Bodies

Due to the tribological contact between bodies, a thin layer of tribomaterial forms in the space between and/or at the interface of these bodies, as illustrated in Figure 2.14 (b). The thickness of this layer - which can range from a monolayer to several micrometers [32] - is subject to variation in both spatial and temporal terms, depending on the load. This tribomaterial is generated at an early stage of the wear process [282, 283]. Its composition is dependent on several factors, including the material of the body and counter body, in particular their technical surface consisting of contaminations, adsorptions, oxidations and the deformation layer as described in the previous section and illustrated in Figure 2.14 (a). Furthermore, the composition of the tribomaterial depends on the interfacial medium (*e.g.*, lubricant), the physical and chemical properties of the tribological bodies and the interfacial medium, as well as the interactions between them and the environment [33]. In accordance with Godet [32], this tribomaterial is also designated as "third-bodies" and is constituted of wear particles from both tribological bodies, chemical reaction products (*e.g.*, oxidations) and the lubricant, if one has been utilized. Thereby, a differentiation is drawn between artificial and natural third-bodies.
Artificial third-bodies are defined as a substance that is intentionally introduced into a tribological system to modify the friction and wear properties. Such a substance can be a solid and/or liquid lubricant or a special coating, which reduces direct contact between the mechanically relevant components, thereby decreasing friction and wear. In contrast, natural third-bodies are always formed during the tribological process, even in the absence of lubricants. Their formation is driven by various sub-mechanisms of the main wear mechanisms. For example, in the case of abrasive wear in a tribological system with a lubricant, small particles of a solid body (wear particles) may enter the lubricant by microploughing. Once in the lubricant, these particles may undergo further wear processes, such as tribochemical reactions, especially the sub-mechanism mechanical mixing, takes place. So the particles are mixed with other particles or the lubricant and may react with them, but also reactions induced by the environment are possible. Consequently, the tribomaterial is not only structurally but also chemically distinct from the bulk material. For instance, a natural tribomaterial may comprise particles detached directly from the tribological bodies, oxides, contaminants, or particles formed from components of the lubricant. These particles are trapped between the interface of the two contacted tribological bodies. If the debris is harder than either of the bodies, it can cause a significant increase in friction and wear due to abrasion [2, 284]. Nevertheless, the debris may also roll (in practice, approximately 10 % [2]), which could still lead to abrasion. Alternatively, the debris may reduce friction, in a manner analogous to that of a rolling bearing [2].
In addition to the generation of wear particles - which influence tribological behavior and form an essential component of the tribomaterial - the rheological properties of the tribomaterial also significantly impact tribological performance. Rheological properties encompass the material characteristics that define its flow and deformation response when subjected to applied stress or strain. These properties are crucial in tribological systems, as the tribomaterial acts as an intermediate medium between two surfaces in relative motion, transmitting forces and modifying frictional responses at the interface. Characterizing the flow and deformation behavior and, thus, the tribological effectiveness of the tribomaterial requires a detailed understanding of their elastic, viscous, and plastic properties:

- Elastic properties allow the material to temporarily deform under stress and return to its original state once stress is removed. In tribological contexts, elasticity helps to absorb contact-induced stresses, mitigating surface fatigue and wear by reducing energy transfer to rigid surfaces.

- Viscous properties, or the resistance to flow, are particularly significant in lubricants, as they influence the material's ability to maintain a film between contact surfaces. An appropriate viscosity enables the formation of a lubricating film that prevents direct contact between the main and counter body, reducing friction and wear. If the viscosity is too low, the lubricant film may be inadequate, allowing surfaces to come into direct contact and resulting in higher friction and wear. Conversely, excessive viscosity may hinder fluid movement and reduce energy efficiency, by energy transfer (*e.g.*, generating heat).

- Plastic properties enable the material to undergo permanent deformation without fracturing under high stress. In tribological applications, plastic deformation can be beneficial by allowing the tribomaterial to adapt under high loads, distributing stress over a larger area, and reducing localized wear.

Tribological material is an essential component of the contact surface and, therefore, influences the tribological behavior, which in turn determines the performance and lifetime of the tribological system. Thereby, the tribomaterial has four main functions [29]:

1. Transmission of the normal force (*e.g.*, load distribution across the contact area between two surfaces, preventing localized stress.)

2. Separation of main and counter body

3. Speed equalisation

4. Transformation of kinetic energy into heat, which can then dissipate via the bodies

It is concluded that the phenomena of friction and wear can be understood in terms of the following: the generation and subsequent transport of tribomaterial out of the system characterize wear, whereas the rheological properties of the tribomaterial are the cause of friction.

Tribofilm and Transferfilm

The tribomaterial generated during the tribological process may agglomerate on the surface of one or both tribological bodies. The thin solid film of tribomaterial formed in this way is called a tribofilm if it extends over a significant part of the tribological contact area. It differs from the surface to which it adheres in its chemical composition, structure, and tribological behavior. This tribofilm has a significant influence on both friction and wear behavior [285]. In particular, the tribofilm frequently serves as a protection of the body's surfaces, which can also reduce friction and wear [286, 287, 288, 289, 290].
In the majority of cases, the material is transferred from the softer tribological body (*e.g.*, soft metals (*e.g.*, aluminum (Al) [291], copper (Cu) [292], magnesium (Mg) [293]), soft coatings (*e.g.*, molybdenum disulfide (MoS_2) [294], diamond-like carbon (DLC) [295]), or

polymers (*e.g.*, polytetrafluoroethylene (PTFE), polyvinyl chloride (PVC)) [296]) to the surface of a comparatively harder tribological body when they slide against each other. The formation of the transfer film is initiated by the accumulation of damage at the microcontacts due to the continuous cyclic tribological load and the associated plastic deformations, particularly in the softer material. In this manner, a part of the softer material may adhere (adhesively) to the harder material and remain in position, thereby forming the transfer layer. During the tribological sliding process, it is also possible that part of the transferred material is transferred back again, possibly with components of the harder base material (mechanical mixing), thus forming a dynamic equilibrium between back-and-forth transfer [67]. Similarly, the chemical and physical properties of a transfer layer are also crucial in determining the tribological properties of the system, just as they are for a general tribological film. In particular, most solid lubricants primarily function through the formation of a transfer film.

2.6.5 Metal Structure and Grain Boundaries

The structure of metals fundamentally impacts their behavior in tribological contexts, as it determines how a material will respond under friction, wear, and lubrication conditions. Amongst other factors, grain boundaries within this structure are crucial, influencing mechanical properties, surface interactions, and the overall tribological performance of the material. As explained in Section 2.6.3, oxidation may occur at grain boundaries. The specific oxide formed may protect the underlying material [12, 297, 298] or cause embrittlement [275, 276], depending on the circumstances. In addition, grain boundaries can act as sites for crack initiation, potentially increasing wear [299, 300, 301]. However, grain boundaries may also be advantageous, as they impede dislocation movement, thereby increasing the hardness of the material (Hall-Petch effect) [302]. Hard materials typically offer higher wear resistance, as they can endure more contact pressures with reduced plastic deformation than soft materials. The influence of grain size on tribological behavior is equally noteworthy. Particularly in fine-grained materials, grain boundary sliding may occur [303, 304]. This sliding can cause grains to shift relative to one another, potentially increasing the wear rate under certain loading conditions. Nonetheless, grain boundaries in fine-grained structures can sometimes serve as reservoirs for lubricants or additives, enhancing the lubrication and improving wear resistance [305]. Many tribological coatings and surface treatments are designed to provide this reservoir function, optimizing the tribological performance of the material [306, 307]. These few examples illustrate how grain boundaries and sizes are critical for optimizing tribological behavior. Depending on the application, selecting an appropriate grain structure can enhance performance by balancing hardness, wear resistance, and lubrication capacity.
Grains are formed as the metal undergoes crystallization from the melt. As the molten metal cools, additional atoms crystallize around a nucleus, causing the crystal to grow. However, the growth of this crystal is impeded by the presence of other growing crystals, which act as a barrier to further expansion. This process results in the formation of irregularly shaped contact boundaries known as grain boundaries. Structural defects often occur during the growth of such a grain. For example, the metal lattice may contain vacancies, substituted and/or interstitial foreign atoms, step dislocations, and/or screw dislocations, which may be different in individual grains [4, 308]. The aforementioned structural defects

give rise to lattice distortions, which in turn affect the physical properties. Consequently, the grains may be composed of a single material or a mixture of materials, exhibiting either a monocrystalline or a polycrystalline structure. Figure 2.14 schematically displays some of these metal physical properties within the bulk material. It is crucial to emphasize that the entire metallic solid body exhibits this grain structure. Near the surface, the grain structure is influenced by several factors, such as strain, oxidation, and adsorption. For clarity, only the alterations in the upper layers are illustrated in Figure 2.14.
Moreover, most engineering materials are alloys, which can cause the concentration of any element in the material to vary not just randomly but systematically, especially near grain boundaries. This phenomenon, known as grain boundary segregation, occurs due to misorientation in the crystal lattice at the boundaries, which gives rise to atomic rearrangement, including the formation of dislocations. Such increased atomic misalignment at the grain boundary regions causes relatively high energy compared to the bulk material [308]. To minimize this energy, the grain boundaries can interact with alloy atoms, resulting in an accumulation of alloy atoms at the grain boundaries. As a consequence of interfacial segregation, embrittlement may ensue; however, it can also result in strengthening of the grain boundaries. In addition to grain boundary segregation, surface segregation can also occur. Surface segregation refers to the process where certain atoms or elements in a material preferentially migrate to the surface or interface of the material, causing a change in the chemical composition near the surface compared to the bulk material. This typically occurs during the manufacturing process or as a consequence of subsequent heat treatment. Thermodynamic and statistical mechanical models can be used to describe the segregation of atoms at interfaces.

Thermodynamics of Grain Boundary Segration

The following section considers a bicrystal comprising atoms of types $\mathfrak{A}$ and $\mathfrak{B}$ within the context of the grand canonical ensemble. In consideration of the interface, it is assumed that each "lattice site", denoted as i, is occupied by atom $\mathfrak{A}$ or $\mathfrak{B}$. However, it should be noted that the lattice sites are not fixed. If the site is occupied by an $\mathfrak{A}$ atom, the occupation number o_i is set to zero ($o_\mathrm{i} = 0$), whereas for a $\mathfrak{B}$ atom, it is set to one ($o_\mathrm{i} = 1$). Therefore, the time average $\langle o_\mathrm{i} \rangle = c_\mathrm{i}$ represents the equilibrium occupation of site i and can be interpreted as the concentration of $\mathfrak{B}$ atoms. To ascertain the equilibrium distribution of the atoms $\mathfrak{A}$ and $\mathfrak{B}$ in the vicinity of the interface at a given temperature T and pressure p, it is beneficial to consider the grand potential

$$\begin{aligned} \Omega &= U - TS - \mu_\mathfrak{A} N_\mathfrak{A} - \mu_\mathfrak{B} N_\mathfrak{B} \\ &= F - TS_\mathrm{c} - \mu_\mathfrak{A} N_\mathfrak{A} - \mu_\mathfrak{B} N_\mathfrak{B} \text{ with } F = U - TS_\mathrm{v} \,. \end{aligned} \tag{2.43}$$

In this context, F denotes the Helmholtz free energy, which includes the internal energy U and the vibrational entropy S_v, but not the configurational entropy S_c. The number of atoms $\mathfrak{A}$ and $\mathfrak{B}$ is accordingly given by $N_\mathfrak{A} = \sum_\mathrm{i}(1 - c_\mathrm{i})$ and $N_\mathfrak{B} \sum_\mathrm{i}(c_\mathrm{i})$. If it is assumed that the atoms do not interact (Bragg-Williams approximation), then the entropy can be expressed as follows:

$$S_\mathrm{c} = -k_\mathrm{B} \sum_\mathrm{i} c_\mathrm{i} \ln(c_\mathrm{i}) + (1 - c_\mathrm{i}) \ln(1 - c_\mathrm{i}) \,, \tag{2.44}$$

where the Boltzmann constant k_B is used [308]. If the equilibrium minimization, expressed as $\partial\Omega/\partial c_\mathrm{j} = 0$ is formed, the result is

$$\frac{\partial F}{\partial c_\mathrm{j}} + k_\mathrm{B}T \cdot \ln\left(\frac{c_\mathrm{j}}{1-c_\mathrm{j}}\right) = \mu_{\mathfrak{B}} - \mu_{\mathfrak{A}}\,. \tag{2.45}$$

This condition must also be satisfied at an atomic site b, situated at a considerable distance from the interface and within the bulk of one of the two crystals. It can be concluded that:

$$\begin{aligned}\frac{c_\mathrm{j}}{1-c_\mathrm{j}} &= \frac{c_\mathrm{b}}{1-c_\mathrm{b}} \exp\left(-\frac{1}{k_\mathrm{B}T}\left(\frac{\partial F}{\partial c_\mathrm{j}} - \frac{\partial F}{\partial c_\mathrm{b}}\right)\right) \\ &= \frac{c_\mathrm{b}}{1-c_\mathrm{b}} \exp\left(-\frac{\Delta F_\mathrm{seg}}{k_\mathrm{B}T}\right)\,,\end{aligned} \tag{2.46}$$

where ΔF_seg denotes the free energy of segregation. This is the well-known Langmuir-McLean isotherm for the segregation of alloy atoms (here $\mathfrak{B}$ atoms) at interfaces. c_j indicates the concentration of $\mathfrak{B}$ atoms within the interface, while c_b indicates the concentration of $\mathfrak{B}$ atoms within the bulk crystal [309]. Nevertheless, the Langmuir-McLean isotherm is limited since it does not account for interactions between the atoms and only considers a single type of site at which segregation occurs. Therefore, several alternative models have been proposed to describe the segregation of atoms at interfaces. Furthermore, no exact solution in three-dimensional scenarios is known for calculating the entropy, necessitating approximate solutions (*e.g.*, Monte Carlo). For further information on interfacial segregation and models, see Ref. [308, 310].

2.6.6 Tribological Properties of Selected Materials

This section provides a more detailed examination of the fundamental tribological properties of the materials discussed in this thesis. First, the solid lubricant MoS_2 is discussed in more detail, focusing on its tribological properties and the factors leading to its degradation under humid conditions. Moreover, a strategy for mitigating humidity-induced failure, such as modifying MoS_2 with additional elements to enhance its stability and performance in diverse conditions, is introduced. Second, the tribological properties of a standardized bovine calf serum solution, which serves as an analog for human synovial fluid in artificial hip joint simulations, are outlined. In addition, the impact on the tribological behavior of various environmental factors, such as temperature and pH value, and synovial fluid components like globulin, hyaluronic acid, and lubricin are discussed. Particular emphasis is placed on BSA proteins, which may promote tribofilm formation on implant surfaces, potentially providing boundary lubrication that mitigates wear during joint motion.

Solid Lubricants - MoS_2

Solid lubricants are defined as materials in solid form that are utilized as lubricants in tribological contact situations to reduce friction and wear. They present an alternative to liquid lubricants and can be employed in many applications, particularly in extreme conditions where liquid lubricants may prove inadequate. These include, for instance, vacuum, high pressures due to extreme loads, exceedingly high temperatures, or cryogenic environments [58, 60, 61]. The solid lubricants can be classified into four distinct groups [31, 58, 59]:

1. Materials with layered grid structure (such as transition metal dichalcogenide compounds (such as MoS_2), carbon-based materials (such as graphite and diamond like coatings), or hexagonal boron nitride (hBN))
2. Oxidic and fluoridic compounds of transition and alkaline earth metals (such as CuO, MoO_3, WO_3, ZrO_2, TiO_2)
3. Soft metals (such as Au, Pb, Ag, Cu, Sn)
4. Polymers (such as PTFE, Polyimid)

One of the most commonly utilized lubricants is molybdenum disulfide (MoS_2), renowned for its resilience to high temperatures and exceptional sliding properties. The lubricating properties of MoS_2 are related to its lamellar structure, which is associated with low shear strength [37, 38] and the ability to form a transfer film, as previously mentioned in Section 2.6.4. In tribological applications, components are, for example, coated with a thin MoS_2 layer using plasma-based coating techniques, which ensures the requisite lubrication. The coating process employed in this thesis is outlined in Section 3.2. The tribological performance of MoS_2 is highly sensitive to humidity, with the coefficient of friction increasing to a range of 0.1 to 0.2 under humid conditions. In contrast, under vacuum conditions, the frictional values decrease by approximately two orders of magnitude [62]. This increase in friction under humid conditions is primarily attributed to the adsorption and diffusion of water molecules, which enhances the shear strength [63, 64]. Furthermore, the generated wear particles can more easily leave the tribological contact area due to the adsorption of water on these particles, which results in a loss of their ductility [311]. Thus, the tribological behavior of MoS_2 (coatings) is a complex function of both intrinsic structural properties and environmental factors. This emphasizes the need to tailor MoS_2 (coatings) to specific operational environments to achieve optimal performance.

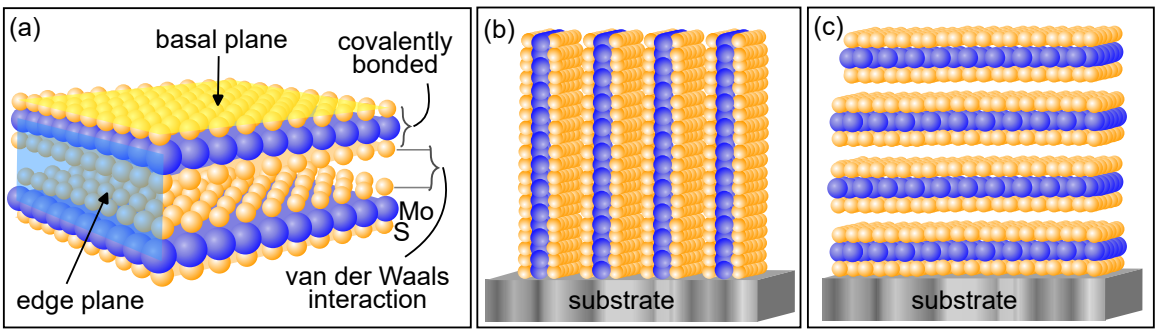


Figure 2.15: The model (a) of a MoS_2 crystal, which highlights the edge and basal planes, also elucidates the potential crystallographic orientations that may emerge from the synthesis of MoS_2 films. The basal plane can be oriented either perpendicular (b) or along/parallel (c) to the substrate surface. Adapted from [312, 313].

As explained in Section 2.5 and illustrated in Figure 2.15 (a), MoS_2 has a layered structure. This layered structure gives rise to two distinct potential crystalline orientations that can form during the MoS_2 film growth process. In one instance, the (002) basal planes can be oriented parallel to the substrate surface, as shown in Figure 2.15 (b). Conversely, the

(100) edge planes can be parallel to the substrate surface as illustrated in Figure 2.15 (c). However, these two orientations differ in their chemical reactivity and thus in their tribological properties. The atoms in the basal plane are saturated and therefore chemically less reactive compared to the atoms in the edge plane, which are unsaturated [314, 313, 315]. Consequently, the edge-plane atoms are highly susceptible to humid conditions, which in turn leads to a deterioration in tribological behavior [63, 64, 316, 317]. It should be noted that in a film growth process, these two crystallographic orientations may coexist, or the grown film may have a completely amorphous structure [123]. However, this edge plane orientation with sulfur defect site favoring adsorption is often observed in sputtered MoS_2 thin films [123, 315, 314]. In addition, water molecules can diffuse between the layers, further degrading the frictional properties [318].
To improve the tribological properties, a promising approach is to modify the MoS_2 layers with additional elements [65, 66]. This has an immediate effect on the structure and may promote the formation of MoS_2 crystalline structure with a preferred orientation along the basal plane. Because the MoS_2 layers shear easily between basal planes, the tribological properties could thus be improved. The reason for this improvement is that the MoS_2 layers are held together only by the relatively weak van der Waals forces. In addition, the tribological properties can be improved under humid conditions because there are fewer free bonds in the basal orientation. The dopants are incorporated into the layered structure of MoS_2 in different ways: The dopant atoms can substitute Mo or S atoms (*e.g.*, tungsten (W) [319]), they can occupy interstitial sites (*e.g.*, copper (Cu) [65]), or they can be intercalated between layers (*e.g.*, vanadium (V) [320]). How a dopant is integrated into the MoS_2 lattice depends on the dopant itself, its concentration, and the synthesis process. Moreover, the structural and tribological properties are contingent upon these parameters [321, 322]. For example, it has been demonstrated that the presence of additional lead (Pb) targets during the deposition process leads to a rearrangement of the deposited MoS_2 planes and the formation of nucleation sites favoring basal crystallite growth [323]. The incorporation of V may lead to a horizontal stacking [324]. It was also noted that, due to the incorporation of nickel (Ni), the MoS_2 crystallite growth is interrupted during the film growth, because a poorly ordered NiO_x layer of few atoms thickness is formed at the edges of the MoS_2 crystallites. This layer acts as a nucleation barrier, preventing the formation of crystallites beyond a certain size [325]. Similar effects are achieved by synthesizing a layered structure, where a periodic deposition of metal layers between the MoS_2 layers causes predominantly (002) basal-oriented MoS_2 crystallites. The presence of multilayers suppresses or interrupts the competitive nucleation and the growth of the (100) edge-planes, since a new nucleation starts on each layer. The first few nanometers of the growing film are typically (002) basal-oriented, which results in a (002) basal-plane orientation for the complete film [326, 327, 328].
Incorporating elements such as titanium (Ti) [329, 330, 331, 332, 333], zirconium (Zr) [334], or chromium (Cr) [333] into MoS_2 films results in microstructural densification, effectively reducing friction by limiting the diffusion of water molecules into the film [329, 333, 335, 223]. However, as the concentration of these modifying elements increases, the film transitions from a crystalline to a nanocrystalline or even amorphous structure. Thus, after exceeding a critical amount of the incorporated element, the tribological properties are impaired [329, 332, 333]. Additionally, integrating gold (Au), a soft metal with inherent lubricating properties, further enhances tribological behavior. Au-modified MoS_2 thin films

show high columnar packing density, leading to increased cohesion between the crystallites and reducing the amount of generated wear particles [336].
The mentioned studies display that the incorporation of additional elements into a MoS_2 thin film provides great potential to adjust the structure, especially the crystallite orientation, and thus to reduce the sensitivity of the tribological properties on humidity. Nevertheless, the effect is strongly dependent on the type of the element with respect to its own properties.

Bovine Calf Serum

The International Organization for Standardization (ISO) has established international standards for the simulation of the synovial fluid of the human body and the provision of a fluid test medium for artificial implants. In these standards, bovine serum is used as the basis for the lubricant solution, as it contains the primary synovial protein, albumin. However, the test fluids for hip and knee joints differ slightly. For the former, bovine calf serum (BCS) is used, diluted with deionized water to achieve a protein mass concentration of $(30 \pm 2)\,\mathrm{g\,L^{-1}}$ (ISO 14242-1:2014). In contrast, the simulated knee fluid does not specify whether bovine calf serum (BCS), bovine serum albumin (BSA), or fetal bovine serum (FBS) [31] should be used to dilute with deionized water to a protein mass concentration of $20\,\mathrm{g\,L^{-1}}$ (ISO 14243-3:2014). These protein concentrations are recommended because the wear mechanisms and wear rates are comparable to physiological ones for several materials. In addition, there is a maximum level of BSA content to act as an effective lubricant [337].

In test setups for artificial joints, the pseudo-synovial fluid, which contains the biological macromolecule BSA, provides lubrication and exhibits boundary lubrication properties [337, 338, 339]. This boundary lubrication is possible because some of the proteins in the fluid adsorb to the implant surface. The adsorption process depends on the physicochemical properties of the surfaces, which, in contrast to the minor influence of the viscosity of the fluid or the speed, significantly determine the boundary lubrication [340]. These adsorbed BSA proteins are usually denatured and/or partially degraded [341] and protect against wear of the surfaces of metal joint implants [342]. In addition, friction tests of metallic surfaces lubricated with BSA have shown low coefficients of friction throughout the entire test period [343]. However, the formation of such a protective and lubricating tribofilm also depends on the load [344].
In addition, amorphous carbon structures formed from the carbon of albumin have been identified on metal-on-metal hip replacements retrieved from patients [48]. Carbon-based materials are a known solid lubricant (as mentioned in the previous Section 2.6.6) that can improve the tribological properties of artificial hip joints. Further studies have demonstrated that the tribological behavior of a natural or artificial joint does not depend on albumin alone. In addition, three other components of the synovial fluid, globulin, hyaluronic acid, and lubricin, influence the thickness of the tribofilm, the coefficient of friction, and the wear

[31] Bovine serum albumin (BSA) is a protein that has been purified from bovine serum. In contrast, fetal bovine serum (FBS) and bovine calf serum (BCS) contain several additional substances, including growth factors, hormones, $\alpha-$, $\beta-$, and $\gamma-$globulins. However, the primary component in all three cases is the protein BSA. Despite this commonality, there are notable differences in their exact composition. For example, BCS has a higher protein content and more immunoglobulins than FBS.

rate [345]. Nevertheless, the impact of each component is contingent upon its concentration. However, as with all tribological systems, the entire system is crucial. In the case of human joints, the properties of the frictional bodies (*e.g.*, metal implant, cartilage, bone), their surface wettability [346] as well as external influences such as temperature [347] and pH [348] are also crucial. In conclusion, this results in a complex and variable tribological contact situation in the human body, which is also individual because every person has a slightly different composition of synovial fluid. In addition, the lubrication process of an artificial hip joint with BSA alone, and especially with denatured BSA, is not yet fully studied and understood.

Chapter 3

Experimental Details

This chapter presents the sample preparation techniques and experimental setups employed in this thesis. The first Section 3.1 provides an overview of the spatially resolved confocal Raman setup, which is consistently used across all experimental procedures. This setup enables the non-destructive examination of structural and chemical changes within various tribological systems. Here, two distinct sample systems are investigated. On the one hand, (modified) MoS_2 solid lubricants are studied. Their synthetisation process, the modifications to the general Raman setup, and the tribological experiments performed with these solid lubricants are discussed in Section 3.2. On the other hand, metal samples that have undergone fretting experiments within a simulated modular metal-on-metal hip joint are subjected to analysis. The experimental details of these fretting experiments, along with changes made to the general Raman setup, are discussed in the final Section 3.3.

3.1 Confocal Raman Scattering Setup

The general Raman setup, upon which all results presented in this thesis are based, is shown schematically in Figure 3.1 (a). As explained in Section 2.1, Raman spectroscopy uses a monochromatic light source, which is in this case a single-frequency continuous wave (CW) laser (Samba 100 532 nm, Cobolt) with a wavelength of $\lambda = 532\,\text{nm}$. The laser beam first passes through an achromatic Galilean beam expander (coated (400 nm-650 nm) and magnification $5\times$, Thorlabs) to increase the beam diameter d. On the one hand, this expansion reduces the divergence θ of the laser beam, which is given according to the diffraction theory for Gaussian beams by [349]

$$\theta = \frac{2\lambda}{\pi d}\,. \tag{3.1}$$

On the other hand, an expanded beam (diameter d) can be focused using a lens, objective, or similar tools (focal length f) to a smaller spot with diameter [349]

$$d_\text{S} \geq \frac{4\lambda f}{\pi d}\,. \tag{3.2}$$

In addition, a wider beam is easier to shape and correct with optical elements, and the power density is lower, so the subsequent optics are not exposed to high laser light power. The power of this broadened laser beam is then regulated by a neutral density filter (ND filter) in the vast majority of measurements in this thesis so that no sample changes (*e.g.*, oxidation) are induced. The laser light power used is specified for each experiment in the following sections. The laser beam passes through a beam splitter to an objective that

focuses the beam onto a small sample volume. Table 3.1 presents the two objectives used in this work including their specifications. The light scattered by the sample is collected again with the same objective (180 ° backscattering Raman spectroscopy setup) and is sent through the beam splitter on its way to detection. At this point, a CMOS camera can also be brought into the beam path via a beam splitter, enabling the capture of monochromatic images of a sample region, along with the laser spot. This way, before and after each exposure of a sample area to the laser light, a microscopic check is made to ensure that no optically detectable sample changes (*e.g.*, optical brightening or darkening) have been induced.

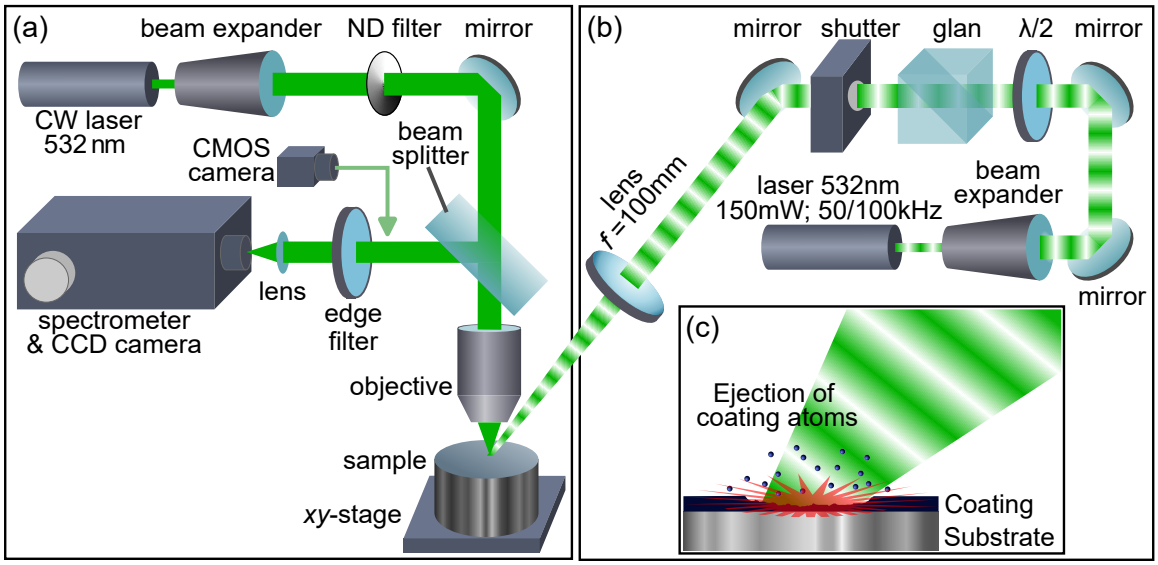


Figure 3.1: Panel (a) displays a schematic of the confocal Raman microscope system setup used for recording all Raman spectra presented in this thesis. It is adapted from [350] with modifications. Panel (b) shows an extension of the Raman setup to enable layer thickness measurements using laser ablation. In panel (c), the idea of laser ablation is represented schematically.

The intensity of the laser or Rayleigh scattered light remaining in the scattered light is reduced by several orders of magnitude using an edge filter (532 nm RazorEdge, Semrock). This allows the scattered light to predominantly contain the Stokes-shifted Raman scattered light. This "adjusted" scattered light is then directed into the spectrometer (0.75 m focal length; Acton Spectra Pro SP-2750, Princeton Instruments). In front of the spectrometer is a lens that focuses the scattered light coming from the focal plane of the objective onto the entrance slit of the spectrometer (width=100 µm). This setup with the entrance slit in front of the spectrometer is the main feature of confocal Raman spectroscopy, which significantly improves the depth resolution. More details on confocal Raman spectroscopy are given in reference [39]. Inside the spectrometer, an optical grating with a periodic structure serves as a dispersive element, diffracting the Stokes-shifted light. Different gratings can be used to achieve the desired spectral resolution or to cover the desired spectral range. In this work, either a 300 groove/mm or 600 groove/mm grating is used, depending on the experiment as specified in the following sections. Both gratings have a blaze angle of 500 nm and are thus adapted to the laser wavelength and the scattered light. The first

diffraction order of the grating is converted into a digital signal by the front-illuminated Si chip (2048 Pixels × 512 Pixels) of the nitrogen-cooled ($T = 120\,°C$) charge-coupled device (CCD) camera (PyLoN 2KF, Princeton Instruments). The sample is placed on a high-precision motorized xy-stage that allows spatial Raman scattering mappings of the sample to be recorded. The sample is moved along the lateral x- and y-direction, and a Raman spectrum is recorded at each position.

Table 3.1: Specifications (magnification M, numerical aperture NA, working distance WD, and applicable wavelength range λ) of the objectives used in this work (UPLFLN20× or LMPLFLN50×, Olympus).

M	NA	WD/mm	λ/nm
20	0.5	2.1	400 – 700
50	0.5	10.6	400 – 700

3.1.1 Material Penetration Depth of 532 nm Laser Light

In Raman experiments, the elastically scattered light of a sample irradiated with laser light is detected and analyzed. This raises the question of how much of the sample volume is involved in the scattering process, i.e., how far the light can penetrate the sample. For reasons of continuity, it is clear that the light always penetrates the sample. However, to answer this question quantitatively, it makes sense to determine the electric field E of an electromagnetic wave propagating in time t and space in the x-direction with the angular frequency ω [351]

$$\begin{aligned} E(x,t) &= E_0 \exp\left(-i\left(\omega t - \frac{\omega}{c} n x\right)\right) \\ &= E_0 \exp\left(-i\left(\omega t - \frac{\omega}{c} n_\mathrm{r} x\right)\right) \cdot \exp\left(-\frac{\omega}{c} n_\mathrm{i} x\right) . \end{aligned} \tag{3.3}$$

Where E_0 is the amplitude of the E field, c is the speed of light, and $n = n_\mathrm{r} + i n_\mathrm{i}$ is the complex refractive index of the medium with normal refractive index n_r and extinction coefficient n_i. This equation shows that the temporal and spatial propagation of the wave in the medium results in absorption, indicated by the exponential decrease in Equation 3.4. The intensity $I(x) \propto |E|^2$ of the laser light entering the sample has its maximum at the interface ($x = 0$). At a distance of

$$\delta_\mathrm{P} = \frac{c}{2\omega n_\mathrm{i}} = \frac{\lambda}{4\pi n_\mathrm{i}} , \tag{3.4}$$

the intensity has decreased to $\exp(-1)$ times the maximum value. This distance is called the penetration depth of the laser light into the sample.
Using the Equation 3.4, the penetration depth of the 532 nm laser light (2.33 eV) utilized in this work for Raman scattering experiments can be calculated across a wide variety of materials by employing the wavelength-dependent extinction coefficient. Table 3.2 lists the calculated, widely varying penetration depths for various materials, some of which

are important to this work [1]. It is particularly striking that organic compounds such as tyrosine [355] or blood [356] have rather small extinction coefficients that the 532 nm laser light passes through a thin organic layer (<5 µm) practically undisturbed. In contrast, the penetration depth in metals is the lowest out of all materials that were considered, with a penetration depth of about 10 nm. However, alloys such as Ti6Al4V, low carbon cobalt alloys (CoCr29Mo6C0.03), or high nitrogen steels (FeCr18Mn14Mo3CN0.9) are investigated in this work, where the exact penetration depths are unknown. The assumption is hierin, however, that they are of the same order of magnitude as the penetration depth of pure metals.

Material	n_i	δ_P (nm)	Reference
Al	5.10	8.3	[357]
amorphous carbon (a-C)	0.85	49.8	[358]
blood	$1 \cdot 10^{-3}$*	$42.3 \cdot 10^3$	[356]
Co	3.74	11.3	[352]
CoS_2	1.4	30.2	[359]
Co_3O_4	1.04	40.7	[360]
Cr	3.33	12.7	[352]
Fe	2.92	14.5	[352]
Fe_2O_3	0.56	75.6	[354]
Fe_3O_4	0.09	470.4	[354]
graphite	$8 \cdot 10^{-3}$	$5.3 \cdot 10^3$	[361]
Mo	7.19	5.9	[353]
MoS_2	1.16	36.5	[362]
MoO_2	$13 \cdot 10^{-3}$	$3.3 \cdot 10^3$	[363]
MoO_3	$9 \cdot 10^{-3}$	$4.7 \cdot 10^3$	[364]
Ti	3.35	12.6	[352]
tyrosine	$3 \cdot 10^{-6}$**	$14.1 \cdot 10^6$	[355]
V	4.35	9.73	[353]

Table 3.2: Penetration depth δ_P of 532 nm laser light radiation (2.33 eV) at normal incidence into various materials. The δ_P is calculated using Equation 3.4. The required extinction coefficients n_i are taken from the listed references[1]. In two cases, to the best of my knowledge, no extinction coefficient is given for irradiation with 532 nm laser light. *: The value given for n_i was determined at a wavelength of 2 µm. **: The value given for n_i is at a wavelength of 0.32 µm.

[1] It should be noted that in the literature there are different specifications for the extinction coefficient for 532 nm irradiation of a material. For example, in Ref. [352] an extinction coefficient of $n_i = 2.92$ for Fe is given in Ref. [353] but $n_i = 5.65$ and in Ref. [354] again $n_i = 3.14$, so that slightly different penetration depths are always calculated. For this reason, the values given here are more of an estimate than an exact value.

3.2 Sample Preparation - Solid Lubricants

This section begins with an overview of the physical vapor deposition method, which is used to produce thin MoS_2 films [2]. Subsequently, the modification of the Raman setup is discussed in more detail in order to determine the thickness of the different MoS_2 coatings. Finally, the tribological ball-on-disk experiments are presented, which are conducted to investigate the transfer material that is characteristic of MoS_2 coatings using Raman spectroscopy.

3.2.1 Physical Vapour Deposition (PVD)

The partially modified MoS_2 solid lubricants investigated in this work are prepared by high-power impulse magnetron sputtering (HiPIMS), a variant of physical vapor deposition (PVD). Ions or atoms from the gas phase are deposited as a thin film (0.5 µm to 6 µm) on a substrate (here: 16MnCr5 steel disk (AISI 5115) and/or silicon wafer) without a chemical reaction, which is different from chemical vapor deposition (CVD). The deposition chamber is evacuated ($< 10^{-4}$ mbar) and heated ($> 100\,°C$) to prevent environmental contamination of the coating. The principle of PVD is explained below. The PVD system used in this thesis is then described in more detail.

Principle of PVD

The targets, which contain the starting material for the coating, and the substrates to be coated are positioned within the deposition chamber of the PVD system, as illustrated schematically in Figure 3.2. The inert working gas argon (Ar) is introduced into the chamber for the coating process (pressure: $3 \cdot 10^{-3}$ mbar). A negative voltage U_P is applied to the target so that free electrons e^- are accelerated and collide with Ar atoms. These collisions produce argon ions (Ar^+) and additional free electrons.
The Ar^+ ions are also accelerated by the electric field E created by the voltage, but in the opposite direction, toward the target material (cathode). When the Ar^+ ions hit the surface of the target, they can transfer their kinetic energy to the target atoms. During this energy transfer, if the atom has enough kinetic energy to overcome its binding energy to the cathode, it can be ejected from the target. This process is shown schematically in Figure 3.2 (a) and is known as sputtering. As this sputtering process causes the target to heat up, cooling with water is necessary to avoid melting.
In addition to the E field, there is a magnetic field B generated by permanent magnets in the volume between the target and the substrate (see Figure 3.2 (a)). This B field is responsible for the action of the Lorentz force on charged particles (specifically, Ar^+ and e^-), with the force being strongest near of the substrate's surface. The E field exerts a Coulomb force on the charged particles (Ar^+, e^-). The Coulomb force is orthogonal to the Lorentz force due to the experimental design. Both forces are superimposed and act on the charged particles, forcing them into a spiral path. This increases the probability of collisions and associated ionisation, and the particle or plasma density is highest in front

[2] The samples used in this thesis were produced at the Institute of Materials Engineering, Chair of Materials Technology (LWT), within the PVD Technologies department at TU Dortmund University (44227 Dortmund, Germany).

of the target. This sputtering process with a B field is called magnetron sputtering. The atoms, ions, or molecules sputtered from the target adsorb or condense from the gas phase onto the substrate surface to form a homogeneous layer. The bias voltage U_B applied to the substrate accelerates the deposition process.

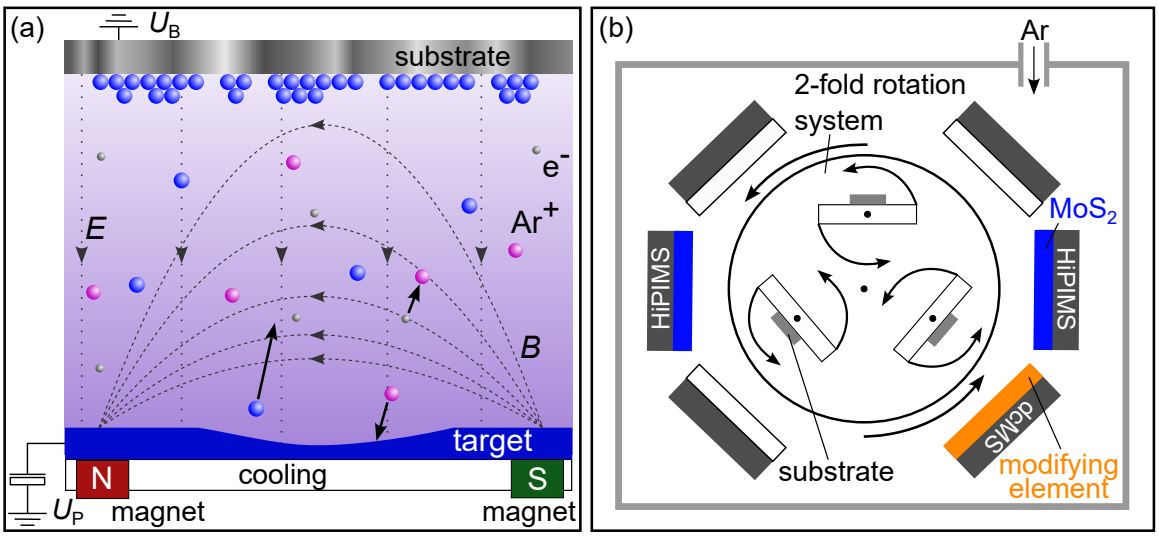


Figure 3.2: (a) Schematic representation of the fundamental principles underlying magnetron cathode sputtering. (b) Schematic illustration of the configuration of cathodes (targets) within the coating chamber of the PVD coating system, utilized for the synthesis of PVD thin films.

To reduce the heating of the taget [365] and to increase the plasma density [366], a pulsed voltage U_P can be used in the coating process. As a result, a distinction can be made between different PVD variants depending on the power supply. If the voltage does not vary during the coating process, it is called direct current magnetron sputtering (DCMS). If an alternating voltage is applied, a distinction is made between high-frequency magnetron sputtering (HFMS; $\approx$ 13.56 MHz) and medium-frequency magnetron sputtering (MFMS; 10 kHz – 200 kHz), depending on the frequency applied. Alternatively, unipolar negative voltage pulses can be used on the cathode. The high power magnetron impulse sputtering (HiPIMS) PVD variant is based on this method, where short unipolar pulses (30 µs – 100 µs) are applied with an adjustable frequency of 50 Hz to 1 kHz.

PVD – Sample Preperation

The modified MoS_2:X coatings studied in this thesis were deposited using a PVD system (CC800/9 Custom, CemeCon AG) equipped with six cathodes. Out of these, four cathodes support operation in either DCMS or MFMS modes. The remaining two cathodes can be used in DCMS or HiPIMS modes, as shown in Figure 3.2 (b). For the synthesis of the modified MoS_2 layers, two MoS_2 targets (purity 99.99 %, size 200 mm^2 × 88 mm^2) are used as HiPIMS cathodes and a further target containing the respective modification element X (X=Cr, Cu, V, or Zr, purity 99.99 %, size 200 mm^2 × 88 mm^2) is used in DCMS mode. The two MoS_2 targets are each mounted on opposite sides, and the X target is adjacent to a MoS_2 target, as shown in Figure 3.2 (b). At the center of the system is a dual rotation

system to which the substrates intended for coating are attached. The substrates (16MnCr5 steel disks and silicon wafers) are mounted in the center of the deposition chamber on a two-fold rotation system. During the coating process, the substrates two-fold rotate to achieve a more uniform coating as the substrates move and tilt to the individual targets. Before the actual coating process begins, the substrates are cleaned in an ultrasonic bath with ethanol to remove coarse, production-related impurities. The substrates are then heated and plasma etched to remove impurities and contaminants. Any oxides and impurities on the target surfaces are also removed by heating and etching prior to the deposition process. For the subsequent synthesis of the element-modified MoS_2:X film, the three targets are sputtered simultaneously. The two MoS_2 HiPIMS cathodes are each operated with an average cathode power of 3 kW, a pulse frequency of 1 kHz and a pulse duration of 200 µs. A DC power is applied to the DCMS cathode of the modifying element so that 20 at. % of the modifying element is in the deposited layer.
The unmodified MoS_2 coatings were grown in the same PVD system as the modified MoS_2:X coatings. However, only the two MoS_2 cathodes operated in HiPIMS mode are in the deposition chamber. An average cathode power of 3 kW, a pulse frequency of 1 kHz, a pulse duration of 200 µs, $U_B = -100$ V, and a Ar chamber pressure of 400 mPa is used.

3.2.2 Layer Thickness Measurements

The coatings are produced using HiPIMS, as described in Section 3.2.1. Silicon wafers, micro milling cutters, and steel rods are coated with an intermediate silicon (Si) layer, followed by the deposition of a MoS_2 layer on top. The Si interlayer is incorporated due to its favorable Raman scattering properties, exhibiting a distinct Raman signal around 520.5 cm^{-1}, which is well separated from the signals associated with MoS_2 and any Mo or S oxide species.
To measure the thickness of the MoS_2 layers, the Raman setup presented in Section 3.1 is extended as illustrated schematically in Figure 3.1 (b). In this extended setup, a pulsed 532 nm laser (BLS6, Spectra-Physics) with adjustable repetition frequencies (set to 50 kHz or 100 kHz) is used. The pulsed laser light beam is expanded with an achromatic Galilean beam expander (400 nm-650 nm coating and 5 × magnification, Thorlabs) for the reasons mentioned earlier in Section 3.1. To stabilize the average pulsed laser light power at (150 ± 1) mW, a $\lambda/2$ wave plate combined with a Glan-Taylor prism is employed. The sample is then irradiated for 0.1 s with the pulsed laser light using a shutter – correspondent to 5,000 [10,000] laser light pulses at a repetition frequency of 50 kHz [100 kHz]. For beam focusing, a lens with a focal length of 100 mm was positioned in front of the sample, creating an irradiated area of approximately $(5136 \pm 250)\,\mu m^2$. The peak power of a laser light pulse delivered to the sample at a repetition frequency of 50 kHz [100 kHz] is approximately 115 W [58 W]. The MoS_2 layer is partially ablated by these high energy laser pulses as schematically displayed in Figure 3.1 (c).
The coating thickness is determined using this experimental setup by sequentially recording a Raman spectrum of the sample. In the Raman setup depicted in Figure 3.1 (a), a 50× objective and a 600 grooves/mm grating (blazed at 500 nm, silver-coated), which diffracts and spectrally disperses the scattered light, are used. The CW laser light power is set to about 1.5 mW with the ND filter to prevent sample alterations.
Initially, a Raman spectrum was recorded, and the sample was then irradiated with pulsed

laser light via a shutter, partially ablating the MoS_2 layer with high-energy laser light pulses. Subsequently, another Raman spectrum is recorded at the same sample position. The sample is then irradiated again with the pulsed laser, followed by recording a Raman spectrum, and so on. The recorded Raman spectra are characteristic of specific compounds in the irradiated area and can be used to identify which compounds are present in this area. When the Raman spectra identify MoS_2, Mo or S oxides, then the MoS_2 layer is still present at the measurement region. In contrast, the detection of the substrate or interlayer signal (here, Si) indicates that the MoS_2 layer is fully ablated in that area.

3.2.3 Transfer Material Experiments and Tribometer

Part of this thesis is concerned with the analysis of tribologically loaded MoS_2:X coatings applied to a case-hardened steel ball (100Cr6 (AISI 52100)), which was neither lubricated nor coated. The MoS_2:X coatings themselves were synthesized on a 16MnCr5 (AISI 5115) steel substrate ((52 ± 1) HRC hardness, (3.1 ± 0.6) nm average roughness) using the PVD system described in Section 3.2.1. The MoS_2:X films have a thickness of 2 µm – 2.5 µm.

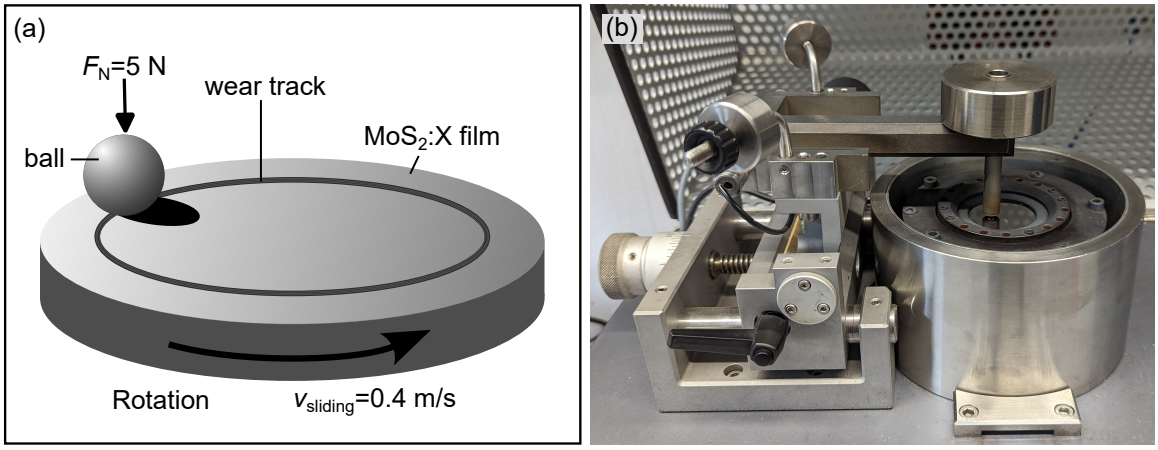


Figure 3.3: (a) Scheme of the tribological ball-on-disc setup showing the MoS_2:X film (main body) and the steel sphere (counter body). Panel (a) is adapted from [367] with slight modifications. The photograph (b) of the actual configuration was taken by Nelson Filipe Lopes Dias, and with his permission, it is included in this thesis.

The MoS_2:X films were tribologically tested under ambient conditions using a ball-on-disc tribometer (CSM-Instruments, Switzerland). The experimental setup of the ball-on-disc tribometer is sketched in Figure 3.3 (a), with a photograph of the tribometer shown in Figure 3.3 (b). The base body is a disc coated with MoS_2:X, against which the counter body, an uncoated 100Cr6 steel sphere (diameter: 6 mm, hardness: (11.3 ± 0.2) GPa), is pressed with a normal force F$F_N = 5$ N. According to Equation 2.41, this results in a maximum Hertzian contact pressure of $p_0 \approx 1.12$ GPa, assuming an elastic modulus of $\mathfrak{E} = 210$ GPa and a Poisson's ratio $\nu = 0.29$ for both the ball and the disc. During testing, the disc undergoes translational motion relative to the counter body (ball) at a sliding speed of $v_{\text{sliding}} = 0.4\,\text{m}\,\text{s}^{-1}$. By measuring both the tangential and normal forces, the software calculates the coefficient of friction. For each film composition, both the main body and counter body are subjected to tribological testing for 5000 circular rotations.

The contact area (wear track) of the main body and, in particular, the counter body of the tribologically loaded surfaces are investigated in more detail using Raman scattering spectroscopy, as described in Section 3.1. Therefore, the laser light power is adjusted to about 1.5 mW to avoid sample damage. The used wavelength of 532 nm avoids resonance effects in MoS_2 and possible tribochemical compounds like Mo oxides as reported in references [47, 226, 368]. The laser light is focused with a 20× magnification microscope objective onto a spot of about 2 µm diameter on the sample.

3.3 Fretting Experiments – Artificial Hip Joints

In modular metal-on-metal hip replacements, fretting contact occurs at the tapered junction between the femoral head and neck, as schematically illustrated in Figure 3.4 (a). To simulate this contact, high nitrogen FeCr18Mn14Mo3CN0.9 stainless steel pins[3, 4] or low carbon CoCr29Mo6C0.03 pins[5] were run against Ti6Al4V cylinders[6] in tribological fretting tests[7] as shown in Figure 3.4 (b). The Ti6Al4V cylinder (⌀13 mm) moves with an amplitude of 50 µm, while the pins (⌀12 mm × 7 mm) remain in position and pressed with a normal force of $F_N = (18.5 \pm 0.4)$ N against the lateral surface of the Ti6Al4V cylinder. Both pins are made of either Co-alloy or high nitrogen steel. The number of fretting cycles n_c is varied between 50 and 5×10^4. Meanwhile, the pins and cylinder are surrounded by a standardized (ISO 14242-1:2014) bovine calf serum (BCS) based lubricant and kept at a temperature of 37 °C. This maintains physiological conditions and simulates human body fluids surrounding and lubricating the artificial hip joint (see Section 2.6.6). BCS is a widely used and suitable substitute for these body fluids because bovine and human serum albumin are similar, as explained in Section 2.5.2. The preparation of this BCS solution is the dissolution of a certain amount of newborn calf serum (NBCS) in 1 L of deionized water. The amount of NBCS required to achieve the desired protein concentration of 30 g L^{-1} varies from batch to batch as the protein concentration in the batch is batch-dependent. To also simulate the physiological salt concentration, 3.7 g NaCl is added to the BCS solution. In addition, 82.4 g ethylenediaminetetraacetic acid (EDTA) is added to the solution to prevent calcium phosphate complexation, and 11.12 g tris(hydroxymethyl)aminomethane (Tris) to buffer the pH value. In addition, HCl is added to bring the pH value to that of blood or synovial fluid (pH = 7.4; see Section 2.4.1). The main natural component of this BCS solution is a mixture of various biological substances, i.e. NBCS contains bovine serum albumin (BSA), globulins, lipids, carbohydrates, carotenoids, growth factors, free amino acids, urea, inorganic substances, hormones, vitamins [386, 387]. Figure 3.4 (c) shows a photo of the fretting test setup, with a drop of BCS solution still visible on the pin surface. The pins and cylinder are then sonicated (Branson 5800, Branson Ultrasonics, Brookfield CT, USA)

[3] Co- and Ni-free austenitic high-nitrogen steel is rarely employed in routine clinical procedures. Nonetheless, it has demonstrated exceptional corrosion resistance, wear resilience, and biocompatibility [369, 370, 371, 372, 373, 374, 375, 376, 377, 378].

[4] 1.4452 FeCr18Mn14Mo3CN0.9, similar to ASTM F2229-02 and ISO5832-9, 0.08 C, 18 Cr, 14 Mn, 3.5 Mo, 0.88 N balanced by Fe, see also [377, 378, 379].

[5] 0.034 C, 0.19 Fe, 0.38 Si, 0.6 Mn, 5.7 Mo, 27.6 Cr and balanced by Co, ISO5832-12.

[6] ASTM F 136, 0.02 C, 6 Al, 3.88 V, 0.13 Fe balanced by Ti.

[7] Comparison of the wear appearance and underlying wear mechanisms of fretting corrosion from the retrieval studies [380, 381] and the test rig demonstrated the similarities between the *in vitro* tests and *in vivo* conditions [35, 382, 383, 384, 385].

in 70/30 ethanol for 10 min. Finally, the samples are dried with nitrogen gas and stored under a normal atmosphere in a plastic box lined with laboratory wipes.
Confocal Raman scattering spectroscopy is then used to analyze the tribomaterial formed on the surface of the pins and cylinders tribologically tested by this fretting contact. The confocal Raman scattering spectroscopy setup is described in Section 3.1. Here are only some specifications given regarding the setup and measurements. The power of the laser light is reduced by the ND filter so that the power on the sample is below 0.1 mW to exclude laser-induced changes. The recording time of a Raman spectrum is several hours to obtain a suitable signal-to-noise ratio. The laser light is applied to the sample using a 20× objective (spot size: 2 µm). The Stokes-shifted, inelastically scattered light is dispersed with a 300 grooves/mm grating (blazed at 500 nm, silver coated).

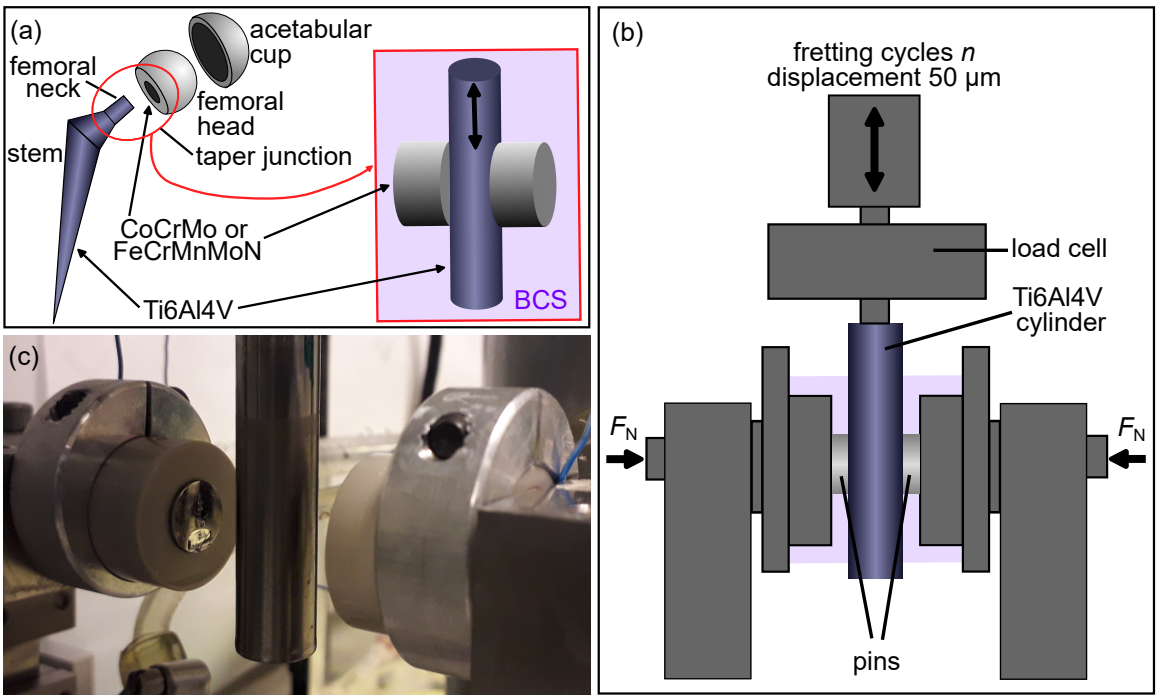


Figure 3.4: Within a modular metal-on-metal hip implant, as schematicly shown in (a), the femoral head is fixed on the femoral neck via a tapered junction. At this junction *in vivo* fretting occurs, which is simulated by *in vitro* fretting corrosion tests (b). By pressing ($F_N = (18.5 \pm 4.0)$ N) two pins made of either a Co-alloy (CoCr29Mo6C0.03) or a high-nitrogen steel (FeCr18Mn14Mo3CN0.9) against a Ti6Al4V cylinder. The cylinder is moving at 50 Hz with an amplitude of 50 µm. The number of fretting cycles n was varied. The human body fluid was simulated by BCS acting as the tribologically third-body which surrounded permanently the cylinder and pins. (c) depicts the actual experimental configuration, captured by Christian Beckmann and utilized in this theses with his consent. Panels (a) and (b) are adapted from [350] with modifications.

In addition, Raman spectroscopy was used to analyze the fretting track of the tribologically highly loaded ($n_c = 4 \times 10^4$) low-carbon Co-alloy. In these measurements, however, a laser light power below 0.5 mW was used without causing any laser-induced changes. The recording time of a single Raman spectrum is also comparatively shorter. One spectrum is recorded by accumulating ten Raman spectra (10 s exposure time for each spectrum).

In addition, laser-induced oxidation was selectively induced within the fretting track. The resulting oxidations can be used to indirectly identify compounds (third-bodies) produced by the tribological contact. In order to have a correlation between the signals before and after oxidation, Raman spectra are first recorded at 0.5 mW excitation power. The laser light power is then increased to 5 mW and applied to the same area of the sample for a few seconds. A Raman spectrum at 0.5 mW laser light power is then recorded at the same position. A 600 grooves/mm grating (blazed at 500 nm, silver coated) is used to diffract the scattered light.

Chapter 4

Protein-Metal Interactions and CoS_x Tribofilm Formation at Hip Implant Taper Junctions: *In vitro* Analyses

Artificial hip joints represent one of the most promising treatment options for patients suffering from endstage osteoarthritis or rheumatoid arthritis in the hip. In the United States, over 1.5 million hip and knee replacement surgeries are performed each year, and this number is expected to rise in the future [25, 26]. Since 1980, the frequency of total hip replacement surgeries has been on a steady ascent, influenced by factors such as a demographic trend of an aging population and increasing levels of body mass index (BMI) [388, 389, 390, 391]. Additionally, the expectations of older adults have shifted, with a growing emphasis on achieving a better quality of life and greater mobility in their later years [392]. Approximately 10 % of these surgeries are revision surgeries, necessitated by issues like infections, instability, aseptic loosening, and trunnionosis [27, 393, 394], which arises from the release of wear debris at the head-stem taper junction [395, 396, 397, 398, 399, 400, 401]. Currently, around 40,000 patients are impacted by trunnionosis annually, with the earliest cases reported back in the 1970s [402, 403]. In addition to wear-related revision surgeries, several other factors necessitate surgical intervention in hip implants, as illustrated in Figure 4.1.

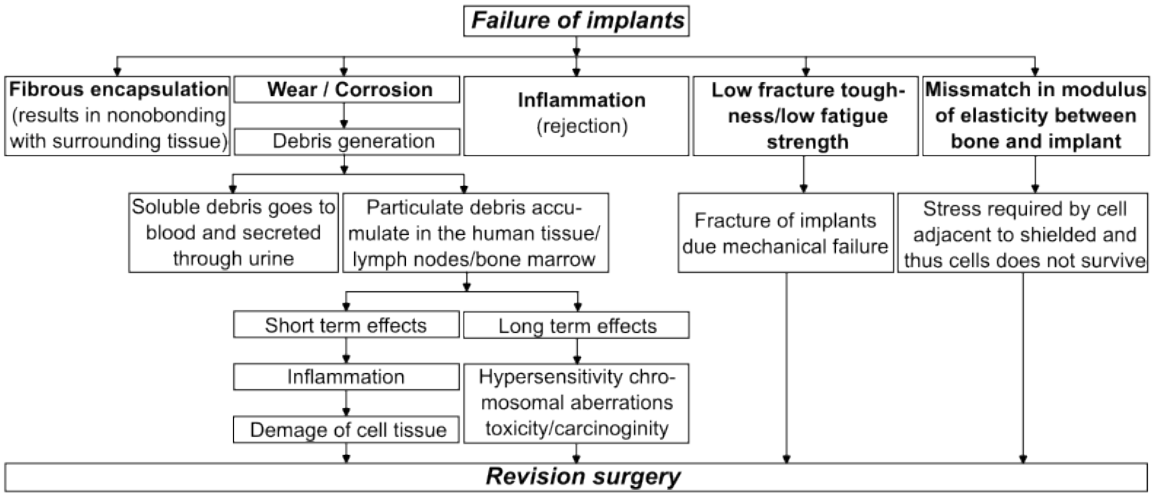


Figure 4.1: Causes for failure of implants. Adapted from [404]

One factor is the elastic modulus $\mathfrak{E}$ of the metals or alloys employed in the implant, such as Ti6Al4V with an approximate modulus of $\mathfrak{E} \approx 114\,\text{GPa}$ [405] and CoCrMo with $\mathfrak{E} \approx 248\,\text{GPa}$ [406]. These values are significantly higher than the elastic modulus of natural porous cortical bone, which ranges from 5 GPa to 30 GPa [407]. This considerable discrepancy results in inadequate loading of the surrounding bone, leading to stress shielding, bone resorption, and ultimately, premature implant failure [408, 409, 410]. Additionally, mechanical failure, while rare, may occur due to the presence of impurities in the implant's manufacturing process, rather than due to external factors like the patient's BMI or physical activity levels [411, 412, 413].
Another factor is the human body's response to the foreign material (implant) in the form of a fibrous tissue layer around the foreign body, which may give rise to complications (see flowchart in Figure 4.1). While a certain degree of fibrous encapsulation is expected, it may impede osteoinductivity and osteoconductivity at the implant-bone interface. This encapsulation can prevent proper bonding between the implant and the bone, potentially leading to implant loosening and dislocation [414, 415, 416]. Moreover, bacterial contamination introduced during the surgical procedure can lead to inflammation [417, 418, 419]. Among the causative agents, *Staphylococcus* species are the most prevalent, accounting for approximately 80 % of infections associated with orthopedic implants [420]. In rare cases, allergic reactions to implant materials - specifically nickel, cobalt, chromium, and bone cement - can also induce inflammatory responses, leading to further complications [421, 422].
Aseptic loosening, accounting for approximately 60 % of revision surgeries, remains the most common cause for implant failure [28, 423, 424]. This failure is often linked to factors outlined in the flowchart in Figure 4.1. Nevertheless, the role of tribological processes and the wear particles generated, along with various biological responses and interactions with the human body, are considered to be the primary contributors to the phenomenon of aseptic loosening [425].
In the evolution of hip arthroplasty, many different models and materials have been developed and analyzed over time. Modular hip joints, for example, offer remarkable mechanical properties, corrosion resistance, and the potential for customization. Current femoral stems are primarily made from Ti6Al4V, while the head may be composed of a low- or high-carbon cobalt alloy or ceramic material. This diverse material combination enhances adaptability to patient-specific needs, improving fixation, increasing fracture resistance, and enhancing wear performance, which explains the wide range of modular designs available commercially [426, 427].
In modular bearings, beyond the primary articulation contact between the head and cup, there exists at least one additional cone-like contact between the head and the stem taper. During normal activities, slight relative movements may occur within this interface [428], leading to fretting corrosion [396, 429, 430]. During fretting corrosion, the surfaces of the head and stem taper react chemically and mechanically with the synovial fluid, while reaction products may be released into the surrounding fluids and tissues [401]. Additionally, when an artificial hip joint is implanted, components of synovial fluid, including proteins and lipids, adsorb onto the implant's surface [431, 432]. The characteristics of this adsorption process and the resulting film are influenced by several physico-chemical factors, as described in Section 2.4. This adsorption process, in conjunction with the wear particles, influences the implant's biocompatibility [432]. Additionally, metal-protein complexes [49, 433] may be formed, which, together with the generated wear particles [50, 384, 434, 435,

436], may raise biocompatibility issues such as osteolysis, perivascular lymphocytic tissue responses, and metal hypersensitivity [49, 55, 56, 57]. Thus, the clinical consequences of wear and adverse reactions are known. *Despite this, a fundamental understanding of the structural characteristics and adsorption mechanisms of metal-organic and, correspondingly, biotribological material at the taper junction of hip implants remains limited. In particular, the interaction between human body fluids and various implant alloys during fretting corrosion poses significant open questions in the field of biotribology for orthopedic alloys and artificial hips. Additionally, the molecular-structural effects of these interactions on proteins, which are essential for their proper functioning in the human body, require further investigation. Among the open questions is the impact of the physico-chemical conditions and the nature of the interactions (e.g., ionic or van der Waals, hydrophobicity) between body fluids and implant materials on the properties of the adsorbed biotribomaterial. Additionally, there are critical gaps in knowledge regarding the role of various proteins, including albumin and other serum components, in the formation of tribological layers.*

Alongside absorption processes and wear particle generation, additional factors contribute to the tribological behavior and longevity of artificial hip joints. Numerous retrieval analyses as well as laboratory experiments that simulated the coarse fretting corrosion caused by Ti6Al4V in conjunction with various Co-alloys, austenitic high-nitrogen steels or zirconium dioxide ceramics (ZTA) have shown that – in addition to the main body, the counter body, the lubricant and the environment – the tribological material (also called third-bodies, see Section 2.6.4) influences the friction and wear behavior of the implant. The research of Godet [52, 437, 438], Rigney [439, 440], and more recently Greiner [53, 54, 441] has led to the hypotheses that this tribomaterial may be a nanostructured metal-organic(-ceramic) composite. This metal-organic tribomaterial is expected to be formed from components of the human body fluid surrounding the joint and wear products from the contacting surfaces. Generated within the sliding interface, the tribomaterial may act as a lubricant. Thus, this tribomaterial may be capable to withstand the extreme shear forces caused by the rotation of nano-grains or their clusters [34, 36, 439, 442].

The varying chemical compositions and alterations of the tribomaterial may be explained by sub-mechanisms of tribochemical reactions, with mechanical mixing being a primary factor [12, 34, 35, 50] [1]. Additionally, couples of Co-alloy and Ti6Al4V create mechanically mixed layers through a sub-mechanism of abrasion characterized by microploughing [6]. Moreover, the Co-alloy side of the contact experiences immediate tribocorrosion, another sub-mechanism of tribochemical reactions, resulting in the release of metal ions into the surrounding fluid [35, 50]. When the surfaces are separated, they may repassivate via tribooxidation, another sub-mechanism of tribochemical reactions [12, 443]. All these mechanisms generate wear products that may contribute to the tribomaterial. The amount of tribomaterial remaining at the interface can differ by several orders of magnitude from the amount of metal ions released [35, 382, 385]. Furthermore, the tribomaterial demonstrates significant load-bearing capacity within the interface [35, 382, 383]. These observations support the protective role of the tribomaterial, as proposed in the 1980s [444]. Proteins, such as albumin, may be incorporated into the tribomaterial. In the primary articulating area of the hip joint, they may undergo denaturation and decomposition.

[1] An overview of the four main wear mechanisms and their associated sub-mechanisms is given in Section 2.6.1.

The denaturation and decomposition of albumin have been linked to several factors, including possible decreases in the pH-value [445] at the interface, significant increases in temperature due to frictional heating [446, 447], and the extreme local contact pressures and shear stresses involved [448]. Additionally, it was suggested that the release of abundant Co or Cr ions might trigger the denaturation and decomposition of albumin. However, the release of Mo ions appears to specifically induce the denaturation of albumin, while also facilitating the formation of a tribofilm [449]. Moreover, the decomposition of albumin has been shown to lead to the formation of amorphous carbon layers in thin patches [48], which may provide protective effects under boundary lubrication conditions. It is conceivable that, in addition to the organic tribomaterial (amorphous carbon), metal-organic compounds may also form during the fretting contact at the implant surface. These metal-organic species may contribute to developing adverse local tissue reactions and, thus, implant failure.
Existing research has primarily focused on the biological effects of metal ions in synovial fluid and surrounding tissues. This issue is a primary concern for metal-on-metal artificial hip replacementss [450, 451, 452]. However, complications may arise from the synergistic effects of organic and inorganic components. The interactions of these components remain largely underexplored. Chromium phosphate is the only matal-organic compound identified on implant surfaces [453, 454, 455]. Additionally, while metal ion binding to serum albumin (such as Co^{2+} binding to serum albumin) has been observed [456, 457, 458], its role in the context of implants remains insufficiently studied. *Despite these first steps taken to investigate the structural properties of the metal-organic tribomaterial, there remains a significant gap in understanding their origin, structure, and composition. Consequently, a comprehensive and systematic analysis of these metal-organic compounds and their reaction products is crucial to elucidate the tribological behavior of biomedical alloys and potentially optimize their performance. The identification and in-depth characterization of metal-organic compounds, and tribochemical reaction products represent a significant interdisciplinary challenge, as well as an experimental one in terms of instrument sensitivity, spatial resolution, and signal-to-noise ratio.*
A gross-slip fretting corrosion test rig, as described in Section 3.3, is used to investigate adsorption processes and the tribologically induced mechanical-chemical reaction products. This test rig reflects the fretting corrosion and loading conditions of hip joint taper junctions within a periprosthetic environment. To analyze and characterize the tribomaterial and wear products, confocal Raman scattering spectroscopy is mainly employed. It is well-suited for identifying and characterizing proteins (see Section 2.5.2) and several reaction products, including oxides [459, 460, 461, 462, 463]. The confocal Raman setup used for the measurements is described in detail in Section 3.1. It enables detailed spatial analysis of the tribomaterial and wear products, including adsorbed proteins and mechanical-chemical reaction products.
A topographical investigation (Section 4.1) is conducted to identify the predominant wear mechanisms by analyzing the wear patterns. The analysis shows that the tribologically loaded area could be divided into two distinct regions. On the one hand, the fretting track (FT), situated at the center of the contact area. On the other hand, the area adjacent to the FT represents a potential site for tribomaterial and wear particle agglomeration. This latter area is designated the accumulated wear products (AWP) region. In the following Sections of this chapter, these two regions are analyzed separately, as the elevated pressures present in the FT region may lead to other mechanical-chemical reaction products.

Section 4.2 analyzes the AWP region, focusing on the metal-protein interactions. For this purpose, the initial state of the samples is determined by recording the Raman spectra of pure BCS and unworn pin surfaces (Section 4.2.1). These spectra will serve as a reference for later analyses. In Section 4.2.2, the Raman spectra of the AWP region are examined in the low-wavenumber range, where metal oxides typically exhibit characteristic bands. Such an approach permits tribochemical reaction products (*e.g.*, metal oxides) to be identified and characterized. In contrast, Section 4.2.3 investigates the high-wavenumber range of the AWP Raman spectra as a function of the number of fretting cycles n. This investigation aims to understand adsorption behavior and structural characteristics, including fretting-induced structural changes, of BCS components. Special attention is given to alterations in the amide band, allowing for an in-depth examination of the secondary structure. Furthermore, the adsorption behavior of short- and long-chained organic compounds on both material surfaces is assessed. This aspect is crucial, as the adsorption characteristics significantly impact biocompatibility, wound healing, and long-term implant stability. Understanding these interactions may lead to advancements in implant surface engineering and improved material performance in biomedical applications.
An in-depth analysis of the Raman spectra recorded from the FT region is presented in Sections 4.3 and 4.4. Whereby, Section 4.3 addresses the products that can be identified on both pin materials, while Section 4.4 is dedicated to the unique products found solely on the Co-alloy pin. In this context, a metal-organic compound CoS_x is identified. A combination of confocal Raman scattering spectroscopy and scanning transmission electron microscopy (STEM) is utilized to investigate the origin, structure, composition, and formation process of CoS_x. This analytical approach allows for a comprehensive understanding of the compound's characteristics and behavior under the conditions encountered in the fretting contact. Finally, this chapter concludes with a summary of the results (Section 4.5). The results presented in this chapter are the subject of two publications [350, 464].

4.1 Topography of Tribologically Loaded Pins and Cylinders Surface

In this Section, the topographic details of the surfaces of pins and cylinders that have been exposed to a certain number of fretting cycles n are examined using optical and microscopic techniques. Figure 4.2 illustrates the optical micrographs (taken with a 4× microscope objective) of the surfaces of the pins and cylinders as a function of the number of fretting cycles n. The first row (a)–(d) depicts the surfaces of the FeCr18Mn14Mo3CN0.9 pins. The second row (f)–(i) presents the microscope images of the surfaces of the CoCr29Mo6C0.03 pins. Most of the pin surface appears rather light/light gray under the microscope. This region shows the bare pin surface, which was polished before the fretting tests. It is referred to here as the outer region, where usually no organic components can be detected by Raman spectroscopy. The elongated, clearly darker region runs parallel to the axis of movement during the fretting tests and imply adsorbed material or changes on the surface compared to the outer region and corresponds to the tribologically involved region.
As expected for both pin materials, the size of this worn surface area increases with the number of fretting cycles. An explicit difference between both pin materials is already observed comparing the pin surfaces after 500 fretting cycles (n_{mid}): In contrast to the Co-

alloy pin (Figure 4.2 (g)), the high-nitrogen steel pin surface exhibits a larger tribologically involved region (Figure 4.2 (b)). This observation becomes even more obvious, as shown in Figure 4.2 (c) and (h) for high-nitrogen steel and Co-alloy respectively, when the number of fretting cycles is increased to $n = 5000$. The same behavior remains valid for $n \geq 4 \times 10^4$. Furthermore, the tribologically involved region of the high-nitrogen steel pin is more elongated than that of the Co-alloy pin. From the mechanical point of view, the Co-alloy pin seems to be more robust against wear than the high-nitrogen steel pin likely due to an enhanced hardness which amounts to (340 ± 28) HV10, for CoCr29Mo6C0.03, and (270 ± 12) HV10, for FeCr18Mn14Mo3CN0.9 [371].

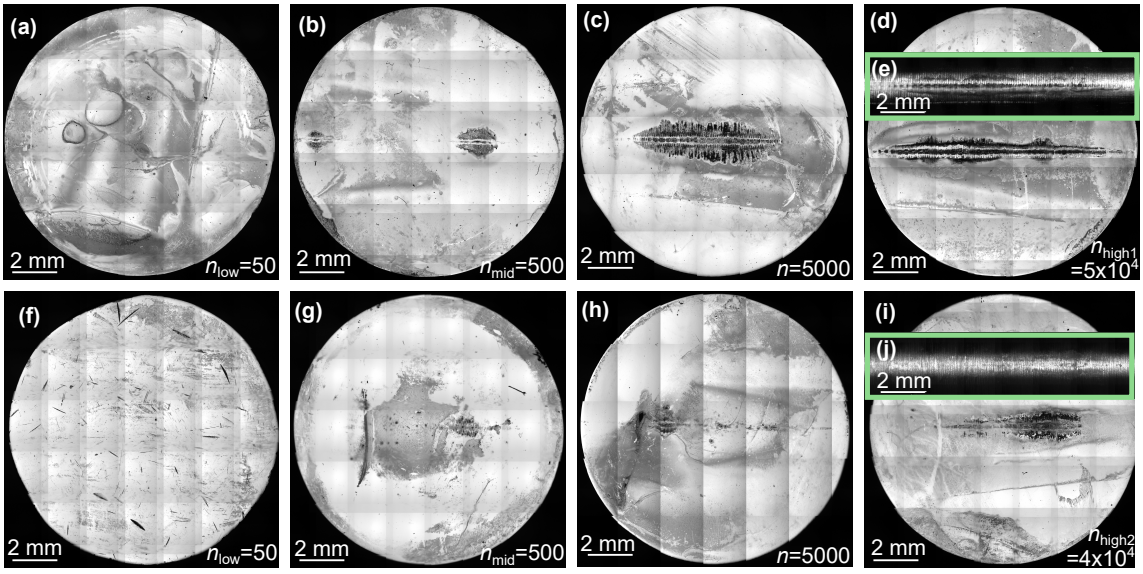


Figure 4.2: Stitched images (taken with a 4× microscope objective) of the pins and cylinders which were run for 50 (n_{low}), 500 (n_{mid}), 5000, 4×10^4 (n_{high2}), or 5×10^4 (n_{high1}) fretting cycles. (a)–(d) show FeCr18Mn14Mo3CN0.9 pins and the images of the CoCr29Mo6C0.03 pin surfaces are depicted in (f)–(i). The microscopic image in (e) [(j)] depicts the Ti6Al4V cylinder which was run against the pin made from FeCr18Mn14Mo3CN0.9 [CoCr29Mo6C0.03] shown in (d) [(i)]. The shape of the wear area at the cylinder surface corresponds to the wear area at the pin surface. Images (a), (b), (d), (e), (f), (g), (i), and (j) are reproduced from [350], while images (c) and (h) are newly presented in this work.

It is also noteworthy to mention the tribologically affected areas of the Ti6Al4V cylinder surfaces. These are presented as illustrative examples for n_{high} in Figure 4.2 (e) and (j). The optical appearance of the tribologically loaded area of the Ti6Al4V cylinder surface, which has been subjected to contact with the high-nitrogen steel pin (d) or the Co-alloy pin (i), is illustrated in (e) and (j), respectively. It is worthy of note that the tribologically loaded areas of the cylinder surfaces and the pin surfaces are almost identical in optical appearance, exhibiting a mirror-image symmetry. This observation shows that, as one might have expected, the fretting tracks are shaped by the geometry of the pin and cylinder.
Since optical differences can already be seen in Figure 4.2, it is also interesting to further investigate the tribologically loaded area. Figure 4.3 (a) provides a microscopic image taken with 20× magnification of a part of the worn surface area of the high-nitrogen steel

pin, which is shown in Figure 4.2 (d). In the middle of the tribologically involved region, a fretting track (FT) along the tribological contact area of the pin and cylinder can be identified.

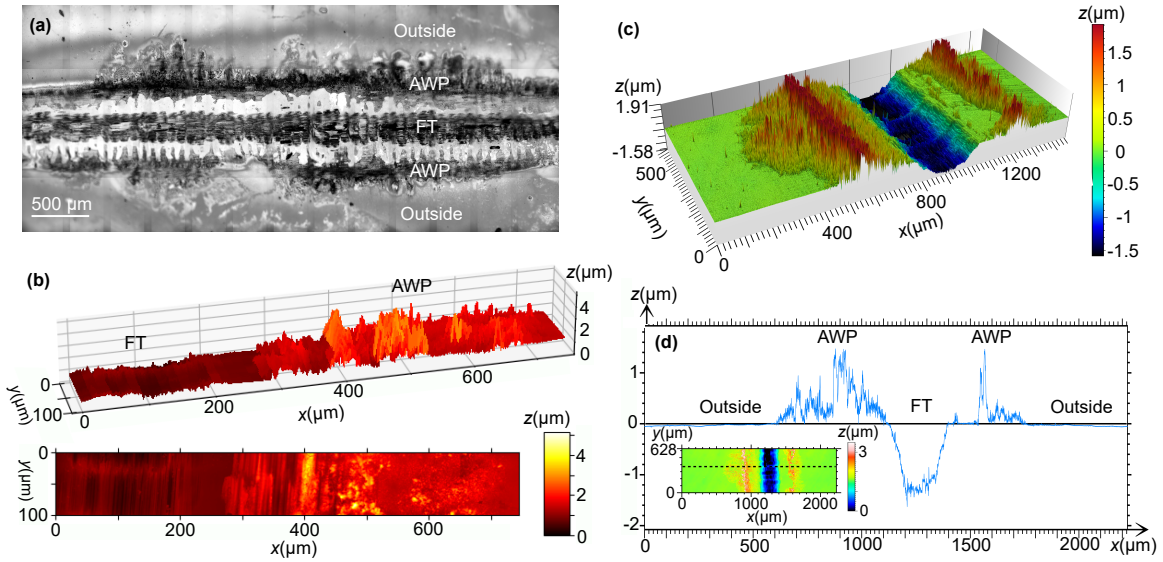


Figure 4.3: (a) A magnified stitched image (taken with a 20× microscope objective) of the tribologically affected area shown in Figure 4.2 (d). Three main areas can be distinguished: an outer region, a region of agglomeration of wear products (AWP), and the fretting track (FT). An atomic force microscope image (b) and a white-light interferometric image (c) visualize the 3D height profile of a high-nitrogen steel and Co-alloy pin surface that has been worn by n_{high} fretting cycles, respectively. The cross-section of the white-light interferometric 3D height profile at $y \approx 367\,\mu\mathrm{m}$ is shown in (d). Panels (a), (c), and (d) are reproduced from [350], while panel (b) is presented here for the first time.

On both sides of the FT, a dark gray to black, irregularly shaped surface area can be identified. To analyze this area and the entire topography of the tribologically loaded area in more detail, an atomic force microscope (AFM) scan, shown in Figure 4.3 (b), and a white light interferometer image, shown in Figure 4.3 (c) and (d), are taken. It is important to note, however, that the height data obtained from these two measurement methods should not be regarded as accurate. This lack of accuracy observed in the AFM image presented in Figure 4.3 (b) can be attributed to the fact that 10 individual AFM scans were necessary to obtain the image shown. Each scan has a maximum area of $100\,\mu\mathrm{m} \times 100\,\mu\mathrm{m}$. The scans were recorded with an approximate overlap of 30 µm and were subsequently combined. However, due to hysteresis effects, it is not always feasible to compare the scans of the individual areas with each other, which may result in discrepancies in the height data across the scans. In contrast, the lack of accuracy in the height measurements obtained through white light interferometry can be attributed to the distinct optical properties of the organic material and the loaded or unloaded metal surface. In conclusion, both methods yield comparable results and the measurements demonstrate that the wear particles departed from the FT laterally accumulated on its side. These accumulated wear products are discernible in the AFM and white light interferometry images and exhibit an increase in the height of a few micrometers adjacent to the FT.

The AFM, white light interferometry, and even micriscope images demonstrate that the FT is comprised of deepened grooves created by microploughing. Moreover, the FT is widest (approximately $\approx 300\,\mu m$) for FeCr18Mn14Mo3CN0.9 with the highest number of fretting cycles $n_{high1} = 5 \times 10^4$. Both the FT as well as the AWP are displayed in a dark grey to black tone in the optical images (Figure 4.3 (a)). This optical phenomenon can be attributed to the variations in height (variations in roughness), as the grooves in the FT are less illuminated by white light. The dark coloration of the AWP can be attributed to alterations in the refractive index and extinction coefficient, which result in modifications to the absorption and reflectivity of the surface when exposed to visible light. These phenomena are the result of the adsorption of molecules from the BCS solution and material mixing processes that alter the size and composition of the wear particles on the surface. The wear particles, which are particularly agglomerated on the sides of the FT, consist of the organic material from the BCS mixed with metal ions released from the pin and cylinder material.

4.2 Raman Spectra of the AWP at the Co-Alloy and High-Nitrogen Steel Pin Surfaces

To facilitate a comparative analysis of the Raman spectra of the AWP recorded on the CoCr29Mo6C0.03 and FeCr18Mn14Mo3CN0.9 pins, it is first necessary to assign the measurable Raman signals to specific components of the BCS or particular parts of the incorporated proteins. This assignment is made in the next Section 4.2.1. The subsequent Sections focus on the alterations in the biotribological material induced by fretting, which can be identified through Raman spectroscopy. In particular, the conformational changes identified by the amide bands and the varying adsorption behaviors of short- and long-chain organic compounds are examined.

4.2.1 Reference Spectrum of Pure BCS and of Unworn Pin Surfaces

Prior to a comparative analysis of the Raman spectra of the AWP measured on the high-nitrogen steel and Co-alloy pins, an investigation of the Raman spectrum of dried pure BCS is conducted within a spectral range from $450\,cm^{-1}$ to $1700\,cm^{-1}$ in relation to the laser line at $0\,cm^{-1}$. The aim of this discussion of the dried BCS spectra is to improve the comparability and to gain insight into the BCS signals without an tribological impact. The Raman spectrum of the dried pure BCS is presented in Figure 4.4 (a). As previously stated in Section 3.3, BCS is comprised of a variety of components, with the primary component being bovine serum albumin (BSA) proteins. As previously outlined in Section 2.5.2, the mature BSA protein comprises 583 amino acids, with the aromatic amino acids exhibiting Raman activity in particular. Additionally, the Raman signals of the cystine complex are contingent upon the three potential conformations of the disulfide bonds (see Section 2.3). The Raman spectrum of the dried pure BCS, as illustrated in Figure 4.4 (a), exhibits a distinct Raman signal at $509\,cm^{-1}$, accompanied by a minor shoulder at $524\,cm^{-1}$. These two signals confirm the presence of disulfide bonds in the cystine complexes, primarily gauche-gauche-gauche, with only a minor proportion exhibiting gauche-gauche-trans conformation. This finding is in accordance with the predictions outlined in Section 2.5.2. These 17 cysteine complexes stabilize the protein structure, as previously outlined in Section 2.3, and

thus play an important role in the activity and functionality of the proteins. The secondary structure of the BCS solution can be identified by analyzing the amide bands of the Raman spectra, as outlined in Section 2.5.2. Since the amide I band is at about 1657 cm^{-1} and the amide III band is at about 1279 cm^{-1}, it can be concluded that the secondary protein structure is predominantly α-helical. This finding aligns with the expected helical content of BSA, which is reported to be 74 % [233]. Lipids are another component of the BCS solution and can also lead to Raman scattering signals. In particular, the Raman signals identified in Figure 4.4 (a) at 670, 895, 1065, 1084, 1103, 1127, 1157, 1382, 1420, 1449, and 1464 cm^{-1} are presumed to originate from lipids [46].

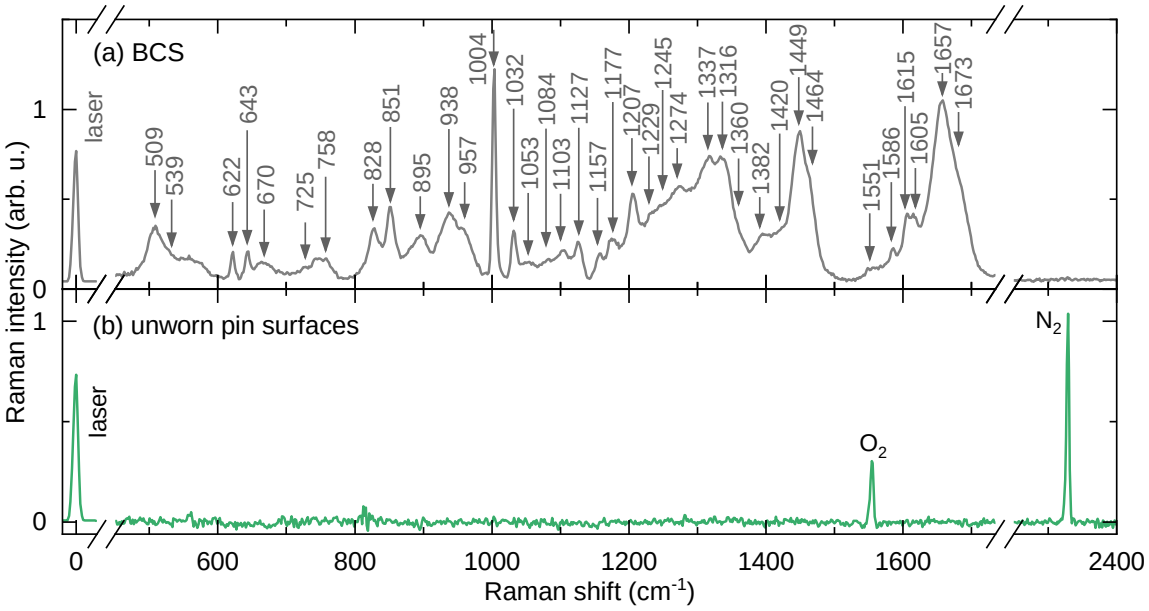


Figure 4.4: (a) The background-corrected Raman spectrum of dried BCS reveals the vibrational modes listed in Table 4.1 with their possible assignments. In panel (b), a representative Raman spectrum of the unworn pin surfaces is depicted, showing the presence of surficial adsorbed O_2 and N_2 molecules. These spectra have been previously published in [350].

In addition to understand the Raman signals of dried BCS, it is crucial to identify the Raman signals from tribologically unloaded metal surfaces to facilitate comparison with the recorded Raman spectra after tribological testing. Figure 4.4 (b) displays the Raman spectrum measured on unworn pin surfaces made of high-nitrogen steel or Co-alloy. These unworn (blank) pin surfaces exhibit Raman signals at approximately 1554 cm^{-1} and 2336 cm^{-1}, which are attributed to surface-adsorbed oxygen (O_2) and nitrogen (N_2) molecules from the surrounding atmosphere [465, 466]. All measured Raman signals and their potential assignments are summarized in Table 4.1.

Table 4.1: Summary of Raman scattering lines obtained from dried BCS and worn CoCr29Mo6C0.03 and FeCr18Mn14Mo3CN0.9 pin surfaces. Phonon modes and organic compound assignments are listed along with the estimated uncertainty of the Raman shift, derived from peak widths. Adapted from [350].

Raman shift (cm^{-1})	Phonon mode	Organic compound	Reference
509 ± 10	S–S stretch ggg	Cys	[148, 149, 245]
539 ± 5	S–S stretch tgt	Cys	[148, 149, 245]
622 ± 5	phenyl ring breathing	Phe	[242]
643 ± 5	phenol ring breathing	Tyr	[244]
670 ± 10	C=O–C def.	fatty acids	[46]
725 ± 30	choline stretch	phospholipids	[46]
758 ± 8	indole ring	Trp	[243, 467]
829 ± 8	Fermi doublet Tyr	Tyr	[244]
851 ± 5	Fermi doublet Tyr	Tyr	[244]
895 ± 10	C–O–O skel.	lipids	[46]
921 ± 15	ring breathing, C–C stretch α-helix	Pro, proteins	[245, 468]
938 ± 10	C–N–C stretch α-helix, C–C stretch		[469, 232]
957 ± 10	C–C stretch		[469, 232]
1004 ± 5	phenyl ring angular bending vib.	Phe	[242]
1032 ± 5	C–C stretch coup. C–C–H def.	Phe	[242]
1053 ± 5	C–N stretch		[469, 232]
1065 ± 20	C–C stretch	lipids	[46]
1084 ± 5	P–O stretch	phospholipids	[46]
1103 ± 8	C–C stretch	lipids	[46]
1103 ± 8	C–N stretch	albumin	[470]
1127 ± 5	C–C stretch, indole ring	lipids, Trp, desmethyl carotenoids	[46, 467, 471]
1157 ± 5	C–C stretch	carotenoide	[471]
1157 ± 5	C–C stretch	lipids	[46]
1177 ± 8	phenol ring H displacement	Tyr	[244]
1207 ± 5	phenyl, phenol ring	Phe, Tyr	[242, 244, 472]
1229 ± 10	amide III, β-sheet	proteins	[473]
1245 ± 10	amide III, random chain	proteins	[473]
1274 ± 10	amide III, α-helix	proteins	[45]
1316 ± 8	CH_2/CH_3 twist.	proteins	[474]
1337 ± 8	Fermi doublet	Trp	[243, 467]

Continued on next page

Table 4.1 – continued from previous page

Raman shift (cm^{-1})	Phonon mode	Organic compound	Reference
1360 ± 8	Fermi doublet	Trp	[243, 467]
1382 ± 5	CH_3 sym. def.	lipids	[45]
1420 ± 10	CH_2 bend.	fatty acid	[46]
1449 ± 8	CH_2/CH_3 scis.	lipids, proteins	[46, 475]
1464 ± 8	CH_2/CH_3 bend.	lipids, proteins	[46, 475]
1551 ± 5	indole ring, O–O stretch	Trp, O_2	[243, 465, 467]
1586 ± 5	phenyl ring stretch.	Phe	[242]
1605 ± 5	phenol, phenyl ring	Tyr, Phe	[242, 244]
1615 ± 5	phenol ring	Tyr	[244]
1657 ± 20	amide I, α-helix	proteins	[473]
1673 ± 20	amide I, β-sheet/turns	proteins	[473]
2852 ± 10	sym. stretch CH_2	aliphatic chains	[45]
2877 ± 10	sym. stretch CH_3	aliphatic chains	[45]
2936 ± 10	asym. stretch CH_2	aliphatic chains	[45]
2968 ± 10	asym. stretch CH_3	aliphatic chains	[45]
3062 ± 15	C–H stretch	carbon ring of aromatic amino acids	[45]

4.2.2 Identification of Oxidized Transition Metal Compounds

To facilitate a more detailed analysis and comparison of the AWP Raman spectra recorded on the CoCr29Mo6C0.03 and FeCr18Mn14Mo3CN0.9 pins, the spectral range from 200 cm^{-1} to 985 cm^{-1} is considered first. This low-wavenumber region contains, in particular, the Raman signals of transition metal oxides, which will be discussed in this Section.
For a spectra comparison with the low-wavenumber Raman signals of pure, dried BCS, its spectrum is shown in Figure 4.5 (a). The typical low-wavenumber Raman spectra recorded on the CoCr29Mo6C0.03 and FeCr18Mn14Mo3CN0.9 pin surfaces are presented in Figure 4.5 (b) and (c), respectively. The broad and intense Raman signals observed in this spectral region are comparable on the pin surfaces that have been run for different numbers of fretting cycles. Thus, only a typical Raman spectrum is provided in Figure 4.5 (b) and (c).
At the low-wavenumber spectrum of the AWP probed at the Co-alloy an intense and broad Raman band at about 535 cm^{-1} is quite obvious. This peak is not solely attributable to the organic constituents of the BCS, as a comparable Raman signal is absent in the spectra obtained for the dried BCS. However, the three potential conformations of the disulfide bond in cystine complexes may contribute to this Raman signal. Nevertheless, the Raman band likely originates from chromium (III) compounds, while the peak observed at approximately 800 cm^{-1} is characteristic of chromium (IV) compounds. It is also possible that the latter contains a superposition of Raman signals of the choline stretching mode of Trp, as well as the Fermi doublet of Tyr (see Table 4.1).
Moreover, the Raman signals at about 826, 860, and 915 cm^{-1} on the Co-alloy surfaces are

particularly noteworthy. These signals cannot be explained by the organic components of the BCS either, as comparable Raman signals are absent in the spectra obtained for the dried BCS. Since low-carbon Co-alloys (and nickel-free austenitic high-nitrogen steel) form an oxygen-rich passivation layer on their surface [476, 477, 478, 479], the Raman signals originate most probably from corresponding oxides [476, 478]. Cr oxides with high oxidation states contribute to the measured Raman lines: On the one hand, Cr_3O_8 demonstrates intense Raman peaks at 478, 886, 902, and 968 cm^{-1} with the most intense Raman mode at 902 cm^{-1} [480], and on the other hand Cr_2O_5 as well as Cr_8O_{11} have their most pronounced Raman lines at 884–900 cm^{-1} [480, 481]. Additionally, chromates based on CrO_4 may also be formed whose Cr – O stretching modes range from 750 to 950 cm^{-1} [482, 483, 484]. Thus, the recorded broadened Raman peaks fall in this spectral region and, in turn, may indicate the presence of chromates within the tribological contact. For example, sodium chromate (Na_2CrO_4)[476] could form due to a tribochemical reaction between the BCS solution and the pin surface. The line broadening highlights a disordered or amorphous structure of the chromates. Due to this inhomogeneous structure of the chromates, the O – Cr – O bending modes, whose Raman scattering intensities are already weak for crystalline chromates, are not observed in the spectral range from 200 to 550 cm^{-1} [482, 483, 484].

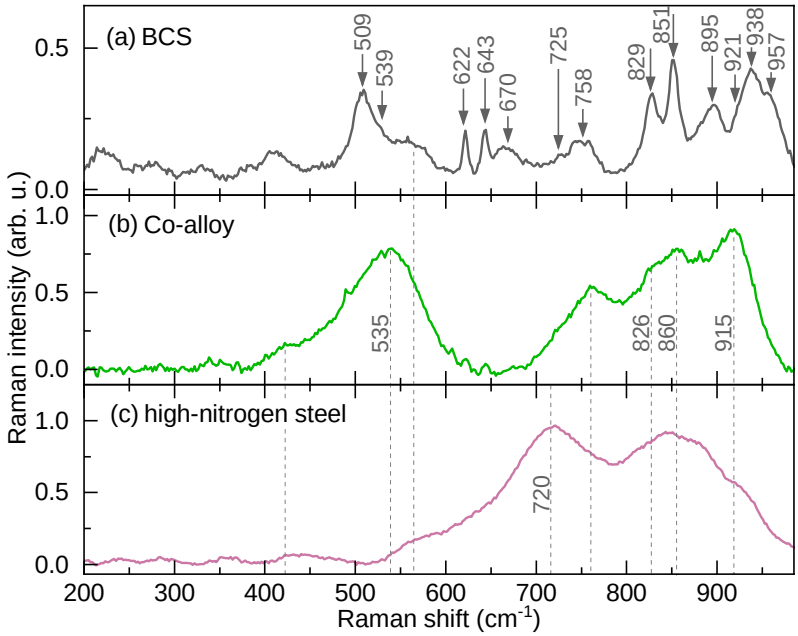


Figure 4.5: Comparison of the low-wavenumber range Adapted(200 to 985 cm^{-1}) of typical Raman spectra: dried BCS (a), AWP region on Co-alloy surfaces (b), and AWP region on nitrogen-rich steel surfaces (c). Arrows indicate prominent Raman signals of BCS (see Table 4.1), while dashed lines represent signals from tribochemical reaction products. Adapted from [350].

In addition, chromium phosphate $CrPO_4$ may have formed as a result of the tribological fretting contact at the Co-alloy surface and contribute to the Raman signals at about 350, 430, and the broad Raman band at about 535 cm^{-1} [485, 486]. Furthermore, since the pin material also contains Mo, Mo oxides may cause the broad peaks at 826, 860, and 915 cm^{-1}. Orthorhombic MoO_3 yields a Raman line at 820 cm^{-1}, while for a metastable monoclinic

modification of MoO_3 a band at 848 cm^{-1} is Raman active [487, 488]. Owing to the small concentration of Mo in the Co-alloy, MoO_3 may only weakly contribute to the Raman band observed.
However, a typical Cr-involved tribo-oxidation leads to the formation of Cr_2O_3. Its Raman modes nominally show Raman shifts of 305, 348, 397, 524, 550, 610, and 826 cm^{-1} [481, 489]. Thus, the peak at 826 cm^{-1} may correspond to the Raman peak observed in the spectra; however, the other phonon modes are not observed. Accordingly, it is unlikely that the observed Raman line indicated the presence of Cr_2O_3. A pressure-induced change in the Raman bands of Cr_2O_3 resulting even in the disappearance of specific low-frequency phonon modes is also unlikely to occur [489]. It can thus be assumed that chromates and Cr oxides with high oxidation states have formed on the Co-alloy surface.
A comparison of the Raman spectra in Figure 4.5 (b) and (c) shows that both the tribologically loaded Co-alloy surfaces and the high-nitrogen steel surfaces in the AWP region exhibit similarly broad Raman bands above 800 cm^{-1}. It can be inferred that the origin of these signals is the same as that previously discussed. They are likely composed of a few Raman bands, derived from amorphous chromates and other Cr oxides with high oxidation states.
In addition, weak Raman signals below 600 cm^{-1} and an intense and broad Raman band at approximately 720 cm^{-1} are also observed on the nickel-free high-nitrogen steel surfaces. As previously stated, an oxygen-rich passivation layer also forms on these surfaces, which allows for the possibility of Raman signals from iron oxides, for example. However, the Raman modes of iron oxides are typically narrow-band, intense, Lorentzian-shaped signals. The Raman signals of magnetite and hematite, in particular, the strong Raman signals at about 670 cm^{-1} and 1320 cm^{-1} are characteristic (see Section 5.1.3). Given the recorded broad Raman band at about 720 cm^{-1}, it is probably composed of multiple Raman signals. It is possible that various iron oxides and organic compounds, including the choline stretching mode of Trp, the C=O–C deformation vibration, and also the idol ring of Tyr, may be involved. Nevertheless, a more comprehensive and spatially high-resolution investigation of the fretting-induced oxidation of the transition metals is necessary. For example, the chemical composition and oxidation state could be analyzed using X-ray photoelectron spectroscopy (XPS). However, the following Sections will examine the changes in the biotribological material in greater detail.

4.2.3 Fretting Induced Changes in the Biotribological Material

This Section examines the Raman spectra of the Co-alloy and high-nitrogen steel pin surfaces within the AWP region, specifically within the spectral range of 985 cm^{-1} to 1735 cm^{-1}. This high-wavenumber region is dominated by Raman modes of organic compounds, which will be discussed in further detail here. The corresponding Raman spectra for the Co-alloy and the high-nitrogen steel pin are shown, as a function of the number of fretting cycles, n, in Figure 4.6 (b) and (c), respectively. Figure 4.6 (a) represents the Raman spectrum of dried BCS in the high-wavenumber region, as previously discussed in Section 4.2.1, to facilitate a more straightforward comparison. On the tribologically loaded surfaces, broadened BCS-related Raman lines are identified on both pin materials. These signals are similar to the Raman scattering signatures obtained from pure BCS. Furthermore, for n_{low}, the Raman lines are narrower than those for n_{high}.

To illustrate, the broadening observed for the Trp indole-ring vibration (W3) at 1553 cm^{-1}, which represents the $C_2{=}C_3$ stretching mode [490], is dependent on the number of fretting cycles n. This broadening can be explained by the fact that the oscillation frequency depends on the torsion angle around the $C_2{=}C_3{-}C_\beta{-}C_\alpha$ bond [467]. Consequently, a spatially inhomogeneous distribution of the mechanical load may result in variations of the torsion angle, which may give rise to a line broadening.

A further illustration of this broadening phenomenon is the lipid-induced asymmetric C–C stretching vibrations at about 1065 cm^{-1}. The dispersion may be attributed to the distortion of the C–C bond, as a consequence of the tribological load. In accordance with Equation 2.17, this results in a different Raman shift for the individual C–C bond, which in turn causes a broadening in the collective. Furthermore, as indicated by Equation 2.17, a variation in the coupling strength of the bound carbon atoms can also cause a broadening. When analyzing the C–C stretching oscillations, it is noticeable that the symmetrical C–C stretching oscillation at approximately 1127 cm^{-1} is detected at high fretting cycles on both pin surface materials. This symmetric mode is typically more robust than the asymmetric mode due to a high interaction constant. Thus, the occurrence of this symmetric mode identifies the duration of the fretting process as a critical factor for the adhesion and probability of formation of C–C bonds on the pin surfaces. Since lipids have low polarity, they are (weakly) attracted to both pin materials in a similar way. The dispersion in the aforementioned linewidth indicates spatially distributed structural inhomogeneities of the interatomic vibrations. These are caused by thermomechanical stress and tribochemical reactions during the fretting process.

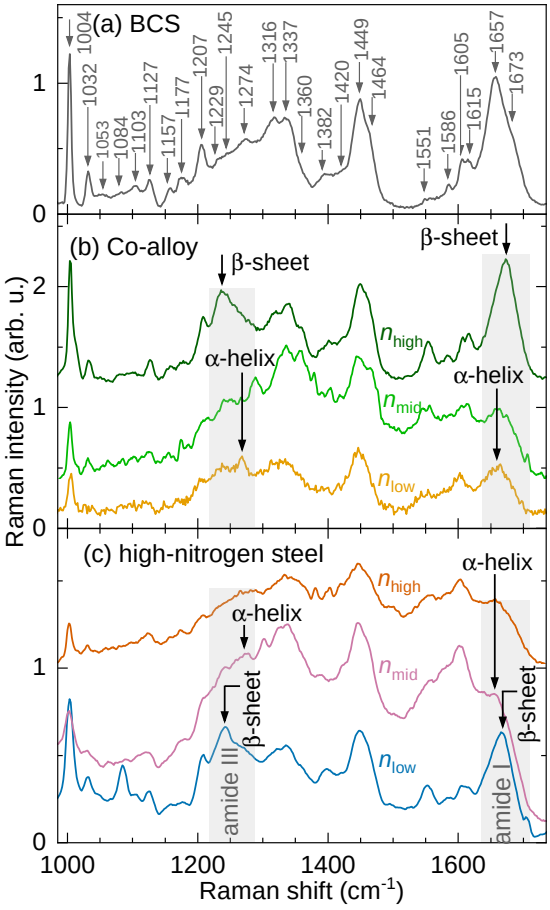


Figure 4.6: Depicted in (a) is the high-wavenumber Raman spectrum of BCS dried on a pin surface, with marked peaks (arrows) specified in Table 4.1. Panels (b) and (c) illustrate the typical Raman spectra measured in the AWP region at Co-alloy and high-nitrogen steel pin surfaces after different numbers of fretting cycles. The presented spectra represent an accumulation of 40 ± 5 individual spectra, each measured in the AWP region. The observed shifts in the amide I and III bands indicate differences in the secondary structure of the adsorbed proteins. Adapted from [350].

In addition, the Raman signals of the organic constituents tend to be more pronounced for n_{high} compared to n_{low}. This intensity enhancement of Raman scattering signals is attributed to an increasing amount of organic matter adsorbed at the surfaces with a rising number of fretting cycles. However, the

Raman signal at 1553 cm^{-1} represents a notable exception, exhibiting comparatively high intensity in the pins that were run for 50 cycles. The weakening of this Raman scattering line can be attributed to the fact that, at this Raman shift, both the vibration of the indole ring of tryptophan (Trp) and the presence of superficially adsorbed atmospheric O_2 [465] can be identified. As the number of layers, n, increases, O_2 becomes increasingly covered by organic layers, leading to a significant weakening of its Raman scattering line compared to the growing Raman signals of the organics, including Trp. However, the superposition of these two Raman signals does not influence the previously described broadening, as the line width of the surface-adsorbed oxygen remains unchanged. In the following Sections, the spectral differences that arise with an increasing number of fretting cycles n are discussed in more detail.

Amide Bands: Conformational Changes in the Biotribological Material

Protein adsorption frequently leads to conformational changes, which can be further influenced by thermal and mechano-chemical conditions in the tribological fretting contact. Given that the functionality of proteins is closely linked to their structural integrity, it is essential to analyze these structural changes. This Section provides a more in-depth examination of the secondary structure of proteins, depending on the number of fretting cycles n. As mentioned earlier in Section 2.5.2, the Raman scattering bands of amide I and amide III are particularly suitable for investigating changes in protein structure, as they are sensitive to the overall conformation of the protein. The amide I band, which is detected between 1648 cm^{-1} and 1680 cm^{-1}, primarily results from the stretching vibration of the carbonyl (C=O) group within the peptide backbone. The amide III band, which appears between 1230 cm^{-1} and 1300 cm^{-1}, is largely generated by the coupling of the C–N stretching vibration and the N–H bending vibration associated with the peptide bonds [473, 491]. By analyzing variations in these amide modes, different secondary structures – such as α-helices, β-sheets, and random coil configurations – each yield distinct Raman shifts can be identified (see Table 4.1).

Typical Raman spectra obtained from the Co-alloy pins, for n_{low} and n_{high}, are shown in Figure 4.6 (b). The amide I mode is centered, for n_{low}, at about 1657 cm^{-1}, while it is blue-shifted to 1673 cm^{-1}, for n_{high}. A similar change is also recognized for the amid III mode. There is a comparatively weak peak at 1279 cm^{-1}, for n_{low}, which has a slight shoulder at about 1229 cm^{-1}. This shoulder is the main peak for n_{high} and possesses a shallow flank at the high relative wavenumber side.

Both shifts within the amide I and III bands indicate a change in the secondary structure of the adsorbed proteins, namely from the α-helix (n_{low}) to the β-sheet or random-coil configuration (n_{high}). The proteins natively possess the α-helix structure [2]; thus, the shift of the amide Raman bands with increasing n indicates an unfolding, denaturation or (partially) degradation of the proteins into the β-sheet or random coil structure. These conformational changes are attributed to several factors related to the fretting experiments. One factor is local heating due to the fretting contact [492]. In addition to that, compressive and shearing frictional forces and the associated stresses also affect the protein conformation and

[2] As mentioned in Section 2.5.2, the native structure of BSA is predominantly α-helical, which is in accordance with the findings presented in Section 4.2.1, which are based on the spectral position of the amide bands of dried BCS.

aggregation [493]. However, unfolding may already take place when the protein adsorbs to the surface, as these structural changes may be energetically advantageous or may passivate the metallic surface [143, 493]. However, no such structural change was identified by the reference measurements (see Section 4.2.1) of dried BCS dropped onto the bare metal surfaces. Therefore, the tribological fretting contact and duration are critical factors for the extent to which proteins unfold, denature, or undergo (partial) decomposition.
The amide bands in the Raman spectra recorded in the AWP region on the high-nitrogen steel pin surfaces show an opposite shift compared to the Co-alloy pins. As shown in Figure 4.6 (c), the amide III mode is blue-shifted, and the amide I mode is red-shifted with an increasing number of fretting cycles. These shifts indicate a conformational change from β-sheets and/or random coil to α-helices, or it may indicate that the initial α-helix structure of BSA remains unchanged even after prolonged fretting tests. Although the fretting conditions are consistent for both pin materials, the interaction mechanisms between the protein and surface must differ. The high-nitrogen steel is more hydrophilic and exhibits better wettability [3] than the Co-alloy surface [494, 495]. Consequently, this increased wettability leads to more adsorption sites, resulting in a relatively uniform protein coverage on the high-nitrogen steel surface [494]. Furthermore, the long-range Coulomb-like coupling allows a multi-stacked proteinaceous system (several layers of proteins) on the high-nitrogen steel surface to be formed. As the fretting duration increases, the thickness of the protein layer (or cluster size) increases, acting like an elastic entity (cushion) that absorbs and dissipates thermal and mechanical energy from the fretting contact. As a result, the top layer of BSA proteins, predominantly in the α-helix conformation, experiences thermal and mechanical stimuli that are insufficient to induce any conformational changes. Additionally, ionic forces may prompt a conformational shift from the α-helix to a β-sheet or random-coil configuration when the proteins initially contact the high-nitrogen steel surface. This layer of denatured BSA proteins traps the ionic forces, resulting in a subsequent layer of BSA proteins retaining the α-helix structure.
In addition to BSA proteins, BCS includes globulins, which possess a higher proportion of β-sheets in their secondary structure than BSA proteins. This suggests that globulins might first adhere to the high-nitrogen steel surface, followed by the accumulation of BSA proteins on top, as indicated in Ref. [496]. However, this study used a hydrophilic glass plate rather than a metal. In another study, investigating the adsorption of globulins and albumins on a glass plate coated with CH_3, it was observed that globulins adsorb first and are then replaced by albumins as they are present in higher concentration in the solution than the globulins [497]. The polarity of CH_3 is comparable to that of the hydrophobic Co-alloy surface, whereas the high-nitrogen steel pin surface considered here is more hydrophilic. Thus, the argument for a multi-stacked proteinaceous system seems more plausible. Nonetheless, it remains unproven whether at n_{low} mainly globulins are adsorbed, while the adsorption of albumins only occurs after many fretting cycles.
Notably, the Raman lines observed in the AWP at the high-nitrogen steel surface exhibit a broadened shape, whereas the lines for the Co-alloy become narrower as the number of fretting cycles increases. The structural configurations of the AWP related to β-sheet and/or random-coil structures yield narrow Raman signatures, which suggests a degree of stability of these structures. These β-sheet and/or random-coil configurations are inherently of low

[3] Further details on the wettability of the two pin surfaces are provided in the subsequent Section 4.2.3.

structural order and thus may be less sensitive to the strains induced by the tribological fretting contact. This may be crucial in understanding the performance of BCS under load. Conversely, the Raman lines associated with the α-helix structure observed in the Co-alloy are notably broad for n_{high}, indicating their sensitivity to mechanical stress.

CH_2 and CH_3 Stretching Modes: Different Adsorption Behavior of Short- and Long-Chained Organic Compounds

This Section presents a discussion of the Raman signals that can be measured in the spectral range of 2800 cm^{-1} to 3120 cm^{-1} on both pin materials within the AWP region. Figure 4.7 (a) and (b) illustrate the Raman spectra measured on the Co-alloy and high-nitrogen steel pins, respectively, as a function of the number of fretting cycles n. As discussed in Section 2.5.2 and listed in Table 4.1, these signals arise from the stretching vibrations of hydrocarbons. For both pin materials, the asymmetric stretching of CH_2 bonds, observed around 2936 cm^{-1}, exhibits always the highest intensity $I_{\mathrm{CH_2,asym}}$ irrespective of n.

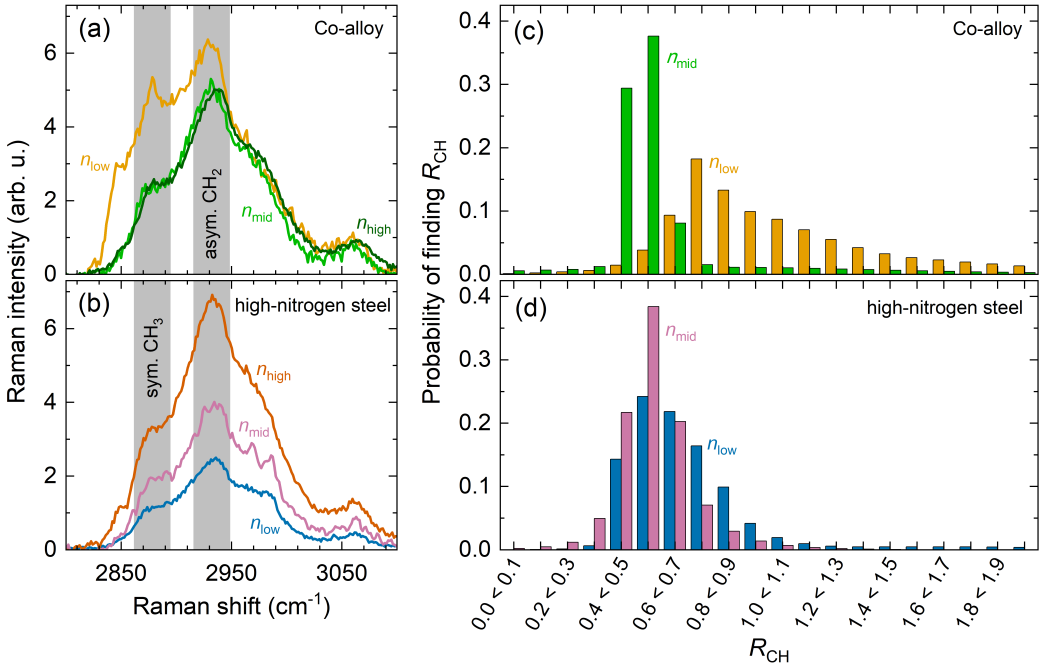


Figure 4.7: Raman spectra depicting hydrocarbon vibrations detected on (a) CoCr29Mo6C0.03 and (b) FeCr18Mn14Mo3CN0.9 pin surfaces subjected to n_{low} or n_{mid} fretting cycles. The associated probabilities of specific intensity ratios $R_{\mathrm{CH}} = I_{\mathrm{CH_3,sym}}/I_{\mathrm{CH_2,asym}}$ for hydrocarbon stretching vibrations for n_{low} and n_{mid} at the Co-alloy and high-nitrogen steel pins are represented in panels (c) and (d), respectively. Note that although the vertical bars are displayed side by side, they correspond to the same value ranges. Reproduced from [350].

In contrast, for the symmetric CH_3 stretching vibration around 2877 cm^{-1}, particularly at the Co-alloy surface, as illustrated in Figure 4.7 (a), a correlation between the intensity $I_{\mathrm{CH_3,sym}}$ and n is evident. This dependence is further elucidated when the intensity ratio, defined as $R_{\mathrm{CH}} = I_{\mathrm{CH_3,sym}}/I_{\mathrm{CH_2,asym}}$, is taken into account. To quantitatively evaluate

the variations in R_{CH} and analyze the associated structural changes, probability distributions for specific ratios are examined as a function of the number of fretting cycles. For this analysis, Raman spectra are recorded at various locations in the AWP region on both pin material surfaces. The intensities of the asymmetric CH_2 and symmetric CH_3 Raman modes are determined through Gaussian fitting. These intensities (not the areas) are then employed to compute R_{CH}. It is assumed that the R_{CH} values follow a normal distribution, implying that the standard deviation can serve as a measure of uncertainty for the ratio. Numerical integration over intervals of 0.1 widths is performed for each normal distribution. By analyzing a total of 67 spectra, the probability of measuring particular intensity ratios can be derived.
The probabilities of specific R_{CH} values are illustrated as histograms in Figure 4.7 (c) and (d), revealing distinct differences between the CoCr29Mo6C0.03 and FeCr18Mn14Mo3CN0.9 pin surfaces. For the Co-alloy at n_{low}, the most probable intensity ratio (18.2 %) falls between 0.7 and 0.8. When the number of fretting cycles is increased tenfold (n_{mid}), the most likely intensity ratio jumps to 37.6 %, and ranges from 0.5 to 0.6, with a noticeably narrower probability distribution. For the high-nitrogen steel pin, the most probable intensity ratio remains between 0.5 and 0.6 for both n_{low} (24.2 %) and n_{mid} (38.4 %), with only a slight narrowing of the probability distribution for n_{mid}.
The shift of the probability distribution to low values of R_{CH}, for Co-alloy with increasing n, indicates an intensity enhancement of the CH_2 stretching mode compared to that of the CH_3 vibration. To explain this change, it is necessary to be aware that polypeptides usually contain a greater number of CH_2 groups than CH_3 groups, given that their structure is based on the peptide bond (please refer to Section 2.3 for further details) and the majority of amino acid side chains contain multiple CH_2 groups. In contrast, CH_3 groups are typically present in the side chains of certain amino acids, such as alanine or valine. However, overall, CH_3 groups are less abundant in the chain than CH_2 groups. Therefore, the observed shift/decrease in R_{CH} likely indicates an increase in the length of the aliphatic chain or the number of carbon atoms [498, 499, 500]. Consequently, small R_{CH} values suggest a higher prevalence of long-chain structures on the pin surface than shorter ones. When comparing the R_{CH} ratios for both pin materials at the early stages of fretting (n_{low}), it is evident that the organic moieties adsorbed onto the Co-alloy surface feature shorter aliphatic chains than those on the high-nitrogen steel surface. However, as the number of fretting cycles increases, this distinction diminishes, and the adsorbed molecules on both pin materials exhibit similarly long chain lengths.
The presence of short-chained molecules on the Co-alloy surface may be attributed to the nature of the interaction between the hydrocarbons and the pin materials. Therefore, it is essential to consider the surface and hydrocarbon polarities, which can significantly influence the observed adsorption behavior of the two materials.The degree of polarity and, in turn, the hydrophilic or hydrophobic behavior of a surface is particularly determined by the chemical structure of the pin material and its surface recombination as well as the surface topography. This property, referred to as surface wettability (see Section 2.4.1), is measured by the contact angle of a water droplet on the surface. The mean contact angle for polished high-nitrogen steel surfaces ranges from 61° to 75° depending on the nitrogen concentration within the steel [501, 502]. In contrast, Co-alloy surfaces show a much larger contact angle, between 97° and 117°, indicating that Co-alloy surfaces are considered weakly polar (hydrophobic) [494, 495]. Additionally, hydrocarbons and C−H bonds are largely regarded

as non-polar due to their minimal electronegativity differences ($\approx$ 2.55 for C, $\approx$ 2.20 for H) [503]. Therefore, ionic interactions (see Section 2.4.1) between both CH_2 and CH_3 and the weakly polar Co-alloy surface can be ruled out.
Consequently, the adsorption of organic components or hydrocarbons on the Co-alloy surface is driven by van der Waals forces. The strength of these forces F depends on the distance r between the adsorbate and the Co-alloy surface ($F \propto r^{-6}$). To enhance the strength of these van der Waals bonds, it is essential to reduce the distance to the metal surface, but only up to a certain limit [4]. For these reasons, a flat arrangement may be preferred for low densities of organic components and hydrocarbons. This is particularly the case with short-chain constituents, which result in a higher number of CH_3 chain ends compared to CH_2 chain links. Accordingly, the probability distribution is pronounced at high R_{CH} values for the Co-alloy. Moreover, short-chained molecules have smaller volumes, allowing for increased movement and diffusion on the Co-alloy surface [504, 505]. This also contributes to the observation of $R_{CH} > 1$. Sections 2.4.3 and 2.4.2 discuss additional factors that may influence this adsorption process.
In contrast, organic components can adsorb on the polar FeCr18Mn14Mo3CN0.9 surface through a more Coulomb-like coupling, whereby a more direct orientation is favored. Consequently, the long-chained organic components, whose bonds are more flexible, also adsorb to a greater extent than short-chained ones. As a result, steric effects exert a more pronounced influence on the adsorption process on the high-nitrogen steel pin surface than on the adsorption on the Co-alloy surface. Accordingly, the probability distributions shown in Figure 4.7 (d) are narrower for the high-nitrogen steel pin than the Co-alloy (Figure 4.7 (c)). Furthermore, the maxima of the probability distributions in Figure 4.7 (d) are well below $R_{CH} = 1$ and are similar for different number of fretting cycles.
The various components of the BCS solution diffuse onto both pin material surfaces at differing rates (refer to Sections 2.4.3 and 2.4.2). However, components of BCS that have already adsorbed are replaced by subsequently arriving components with long aliphatic chains. These long-chain molecules are more flexible and adsorb more readily to pin surfaces than short-chained molecules. This phenomenon is referred to as the Vroman effect, further detailed in Section 2.4.2. As a result, the ratio R_{CH} decreases at n_{mid}, especially for the Co-alloy. For instance, albumin is a "soft" protein, as discussed in Section 2.5.2, which may readily adsorb to both hydrophobic and hydrophilic surfaces. Similarly, the diffusion coefficient of BSA on PMMA has been found to be independent of the adsorption duration but is contingent upon the surface concentration of albumin [506]. Based on the microscopy images and the overall increase in Raman scattering intensity illustrated in Figures 4.2 and 4.6, the amount of adsorbed molecules increases with increasing n. The ratio is likely to shift further towards low values with increased fretting cycles due to a high concentration of long-chained organic components.
It is also noteworthy that CH_2 stretching from the carbon rings of aromatic molecules produces a Raman line near 3062 cm^{-1}. The intensity of this line, relative to that of the asymmetric CH_2 stretching, is roughly 0.2 in every spectrum, suggesting that aromatic molecules, due to their relatively small volume, are adsorbed onto both pin surfaces prior to the assembly of compounds with long aliphatic chains. Consequently, the surface inter-

[4] Once this distance limit is exceeded, the repulsive interactions, such as those arising from Pauli repulsion, where electrons in overlapping orbitals experience a force that pushes them apart, dominate.

action properties of the two pin materials play a role mainly in the adsorption of chain-like molecules but have no role in the adsorption of aromatic molecules. For the Co-alloy, van der Waals forces dominate the adsorption, favoring a flat arrangement of short-chained molecules. On the contrary, the more Coulomb-like interactions on the polar, nitrogen-rich steel surface lead to a non-flat arrangement of the flexible long-chained organic components, resulting in the different R_{CH} distributions. However, as the number of fretting cycles increases, these differences disappear, and the Vroman effect contributes to a decrease in the R_{CH} values, especially for the Co-alloy, and an increase in the number of adsorbed long-chained organic molecules.

4.3 Raman Spectra of the FT at the High-Nitrogen Steel and Co-Alloy Pin Surfaces

This Section presents an analysis of the FT spectra characteristic of both pin materials after many fretting cycles ($n_{\mathrm{high}} \geq 4 \times 10^4$). Upon analysis of the measured Raman spectra, three distinct spectral shapes emerge[5]. Among these, the FT spectra correspond to the shape depicted in Figure 4.4 (b). At these measurement positions, the surface of the pin in its original, unaltered state is observed. This surface may have been exposed by microploughing. So only the Raman signals of surficial adsorbed O_2 and N_2 are observed. The remaining spectral shapes are illustrated as examples in Figure 4.8. The spectra are characteristic of the FT of both pins (Figure 4.8 (a) and (b)) and the Ti6Al4V cylinder (Figure 4.8 (c)), which was paired with a high-nitrogen steel pin. The shape of the measured Raman spectra is strongly dependent on the spatial measurement position within the FT. The following Sections will provide a more detailed discussion of these spectral shapes.

4.3.1 Secondary Structure of BCS within the FT at Both Pin Materials

This Section presents an analysis of the spectrum represented in Figure 4.8 (a). The spectrum is analogous to the BCS spectra that were previously discussed in detail in Section 4.2, thereby demonstrating the presence of proteins as well as lipids in the FT on both pin materials. The position of the amide III band at approximately $1244\,\mathrm{cm}^{-1}$ suggests the presence of a secondary protein structure comprising primarily β-sheets and random coils [473]. Furthermore, the amide I band at $1665\,\mathrm{cm}^{-1}$ also indicates the presence of a β-sheet secondary structure [473]. Therefore, the secondary structure of the proteins adsorbed within the FT after n_{high} is dominated by β-sheets and/or random coils, irrespective of the pin materials. Given that the native structure of BSA is predominantly α-helical (see Section 2.5.2 and Section 4.2.1), it can be inferred that an unfolding, denaturation or partial degradation of the proteins into β-sheet and/or random coil structures must have occurred within the FT. This conformational change is due to tribological contact and the associated mechanical stresses and heating, as previously explained in Section 4.2.3.
A comparison of the secondary structure of the adsorbed organics measured within the FT with that in the AWP region (see Section 4.2.3) reveals differences between both pin materials. On the Co-alloy pin surfaces, after a high number of fretting cycles, a β-sheet and/or

[5]Moreover, an additional spectral shape has been identified on the n_{high} Co-alloy surfaces, but not on the high-nitrogen steel pin surfaces. This finding is discussed in greater detail in Section 4.4.

random coil secondary structure is consistently identified, irrespective of the measurement region (FT or AWP). In contrast, an α-helix structure was identified after n_{high} within the AWP region on the high-nitrogen steel pins, as previously outlined in Section 4.2.3. Accordingly, the secondary structure of the adsorbed organics differs on the high-nitrogen steel pins in the AWP region (α-helix) and FT (β-sheet and/or random coil). This discrepancy may be explained by the high tribological load within the FT (see the Hertzian pressure in Section 2.6.2), which precludes the formation of proteinaceous multi-stacked structures in the FT, whereas such structures are possible in the AWP region (see Section 4.2.3). Moreover, the elevated tribological load within the FT facilitates the fretting-induced unfolding, denaturation, or partial decomposition of the adsorbed proteins. This explains the identified conformational changes of the secondary structure within the FT on both pin materials.

4.3.2 Formation of sp^2 Hybridized Amorphous Carbon Within the FT

In addition to the previously discussed spectra in Section 4.3.1, further spectra are also measurable within the FT, which are comparable to the spectrum depicted in Figure 4.8 (b). In this spectrum, two broad Raman bands are discernible at approximately $1353\,\text{cm}^{-1}$ and $1550\,\text{cm}^{-1}$. The intensity of these bands is markedly higher than that of the Raman signals from the BCS. However, the measured Raman signals from the hydrocarbons in the spectral range from $2800\,\text{cm}^{-1}$ to $3100\,\text{cm}^{-1}$ seems to be the same. Nevertheless, comparing the Raman signals measured within the FT on both pins (Figure 4.8 (a) and (b)) reveals that the hydrocarbon signals are markedly weaker when the two broad Raman bands are present.
The spectrum recorded within the FT on a Ti6Al4V cylinder is also characterized by two broad and intense Raman bands at approximately $1353\,\text{cm}^{-1}$ and $1596\,\text{cm}^{-1}$, with no discernible signal observed within the hydrocarbons spectral range (compare with Figure 4.8 (c)).
The emergence of this broad and intense Raman signals at specific measurement points suggests the formation of amorphous carbon within the FT. The signal at $1356\,\text{cm}^{-1}$ is designated the D-peak and originates from the breathing A_{1g} mode of carbon rings [507]. The broad Raman band at about $1550\,\text{cm}^{-1}$ ($1596\,\text{cm}^{-1}$) is caused by an in-plane bond stretching motion of sp^2 hybridized carbon atoms (E_{2g} mode) and is designated the G-peak [507]. The observed wavenumbers of the G-peak indicate the presence of amorphous carbon and defective graphite clusters within the FT.
Amorphous carbon and graphite have been known for a long time to be advantageous tribological materials, and their formation may reduce friction, corrosion, and wear, even in the presence of water [48, 82, 508]. As previously outlined in Section 2.6.6, the formation of amorphous carbon structures on metal-on-metal hip replacements retrieved from patients was identified. Given that high levels of shear stress are present within the fretting contact, it follows that denaturation and cleavage of the proteins will occur, as discussed previously. This will subsequently result in the release of carbon atoms, which will then form sp^2-hybridized clusters. In addition, a catalytic effect of the freshly exposed metal surfaces could contribute to generating this amorphous carbon structure [48].
The presence of D- and G-peaks detected at various, randomly selected FT positions on the pin and cylinder surfaces indicates that the creation of amorphous carbon is highly localized.

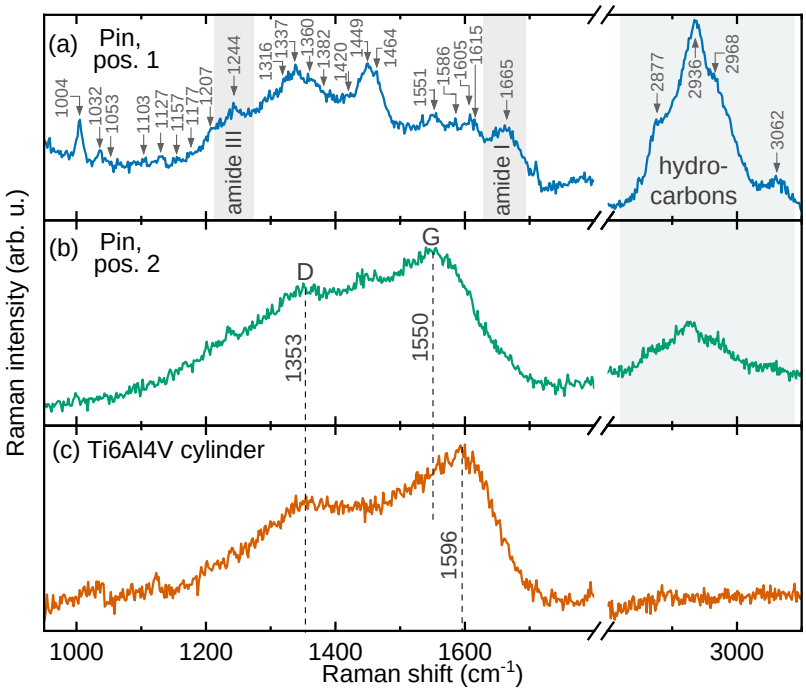


Figure 4.8: Typical Raman spectra recorded within the fretting track of both pin materials and Ti6Al4V cylinder after a high number of fretting cycles. The detection of D- and G-peaks suggests the formation of sp^2 hybridized amorphous carbon and defective graphite clusters. Adapted from [350].

Additionally, the Raman spectra recorded within the FT demonstrate a notable inhomogeneity in the biotribological material. This inhomogeneity is attributed to microploughing and the resulting surface grooves that can "trap" organic compounds. Interestingly, the degree of surface hydrophilicity does not seem to play a significant role in the generation of sp^2 hybridized amorphous carbon, as the Raman peaks corresponding to amorphous carbon are observed on all studied surfaces within the FT after n_{high} fretting cycles. The formation of amorphous or graphitic carbon should not cause biocompatibility problems [509], but the studies on the coating of implants with diamond-like carbon do not clearly show this [510].

4.4 Formation of a Nanocrystalline CoS_x Tribomaterial at Hip Implant Taper Junctions

This Section analyzes the metal-organic compounds identified exclusively within the FT at the highly worn Co-alloy surfaces. Energy-dispersive X-ray spectroscopy (EDS) is initially conducted on the Co-alloy pin surface using a scanning electron microscope (SEM). The analysis reveals the presence of a tribologically induced chemical reaction product between inorganic and organic components, although the specific material could not be identified. To further investigate this material, Section 4.4.2 presents the results of the Raman spectroscopic examination of the Co-alloy FT. But even the Raman peaks do not provide definitive evidence regarding the identity of the tribochemical compound that has formed. Neverthe-

less, the formation of CoS_x is confirmed through laser-induced oxidation, which is discussed in Section 4.4.3. To investigate the nanoscopic structure, composition, and thickness of the CoS_x tribomaterial adsorbed on the Co-alloy surface, the results of scanning transmission electron microscopy (STEM), STEM-EDS, and electron energy loss spectroscopy (STEM-EELS) are presented in Section 4.4.4. Finally, Section 4.4.5 explores the quantitative occurrence of CoS_x within the FT and examines the structure of CoS_x formed in the fretting contact in greater detail, using fitting calculations on the Raman spectra.

4.4.1 Elemental Concentrations and Spatial Distribution of Co-alloy Metals within the FT

The EDS elemental patterns in Figure 4.9 (a) allow for the identification of the presence and concentration of specific elements in the FT of the Co-alloy. This identification can be spatially resolved by combining EDS with SEM. As illustrated in Figure 4.9 (a), the EDS elemental pattern reveals a uniform distribution of cobalt (Co), the primary metallic component of the Co-alloy pin, within the FT. However, the elements molybdenum (Mo) and sulfur (S) are often observed in clusters or areas where they are approximately equally distributed. In contrast, the concentration of chromium (Cr) appears to be diminished in these areas where there is an enrichment of Mo and S.

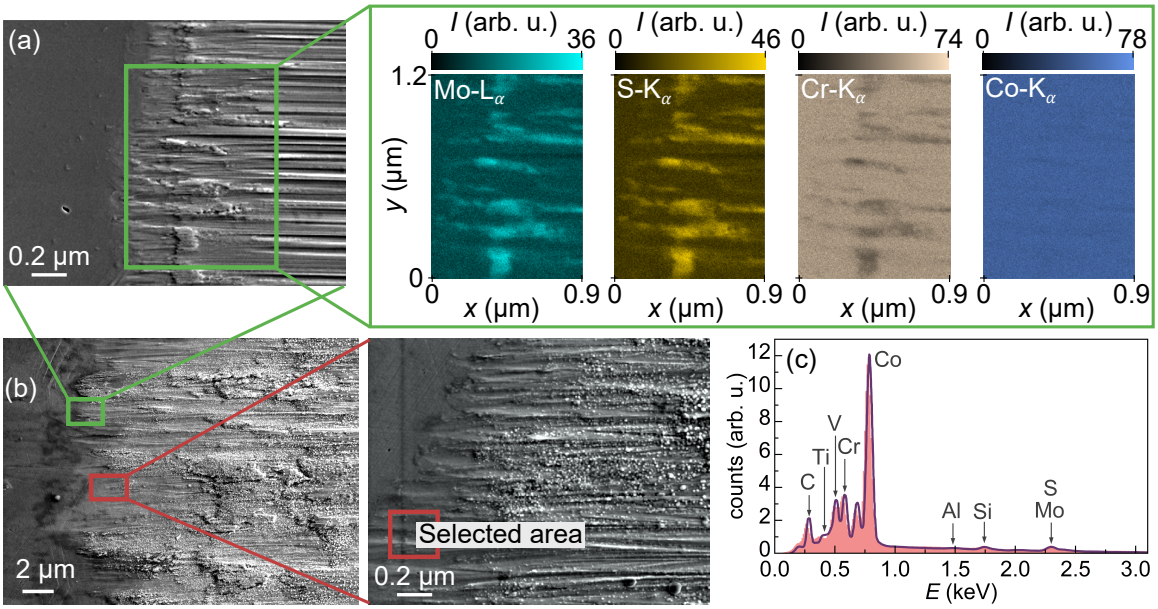


Figure 4.9: The EDS elemental pattern (a) illustrates the composition of the worn Co-alloy pin surface. The locations where the EDS measurements were conducted are indicated in the SEM image (b), which presents an overview of the FT of the Co-alloy, emphasizing the presence of fine and coarse grooves along with adsorbed tribomaterial. The EDS spectrum (c) from the marked area within the FT provides a detailed elemental analysis. Panel (a) is presented here for the first time, while panels (b) and (c) are adapted from [464].

As shown in the EDS spectra in Figure 4.9 (c), the Mo/Co ratio is approximately 0.21. In contrast, the composition of the Co-alloy, as detailed in Section 3.3, yields a Mo/Co ratio of 0.09. One potential explanation for this discrepancy is the enrichment of Mo at the

surface in the so-called σ phase [511, 512, 513]. The formation of the σ phase is a diffusion-driven process, analogous to grain boundary segregation, which is discussed in more detail in Section 2.6.5. However, this phase is localized, occurring only as segregation within sub-µm areas in forged alloys. Another possible explanation for the significantly higher Mo/Co ratio observed in the EDS spectrum is that the Mo peak may be superimposed with another peak, likely the S-K_α line, which overlaps with the Mo-L_α signal.
This leads to the assumption that a MoS_2-like structure has formed as a result of the tribological contact since the Mo ions (and not the Co or Cr ions) have been demonstrated to facilitate the denaturation of albumin [449]. Additionally, MoS_2 is recognized as an extreme pressure additive in lubricants. Consequently, MoS_2 (if formed) may act as a boundary lubricant in conjunction with the amorphous carbon structures derived from the carbon in the BCS solution, as discussed in Section 4.3.2. However, SEM-EDS does not allow for an unequivocal result when analyzing thin layers on metallic surfaces. At first, the quantitative numbers in such thin, mechanically mixed layers are small. Secondly, the background noise of Co, Cr, and Mo cannot simply be subtracted (at least not on a severely plastically deformed and mechanically mixed surface). Third and most crucial, the Mo and S signals overlap, further complicating the analysis. The following Sections present the results of the Raman spectroscopic and STEM investigations to identify the tribochemical reaction products in the FT on highly worn Co-alloy surfaces.

4.4.2 Spectral Appearance and Origin of the Raman Signals

The Raman spectra only obtained within the fretting track on CoCr29Mo6C0.03 pins subjected to $n_{\text{high}} \geq 4 \times 10^4$ fretting cycles are similar to the Raman spectrum shown in Figure 4.10 (a). In the higher wavenumber Raman spectral range three weak and relatively broad Raman bands at approximately 842, 920, and 1063 cm^{-1} are detected. These peaks are likely attributed to calcium phosphate and/or oxide [514, 515, 516].
Furthermore, four Raman signals at about 193, 292, 338, and 401 cm^{-1} can be identified in the lower wavenumber range Raman spectrum on the Co-alloy within the FT for n_{high}. These Raman bands do not match the Raman signals characteristic for the BCS solution, which are discussed in Section 4.2.1. In addition, the bare Co-alloy pin surface shows none of these Raman signals (compare with Figure 4.4 (b)). Furthermore, these signals are only measurable within the FT of highly worn CoCr29Mo6C0.03 pins and not in the AWP region nor on Co- and Ni-free FeCr18Mn14Mo3CN0.9 pin surfaces, compare with Section 4.3. The measured signals must therefore originate from newly formed metal-organic complexes, which are formed due to the fretting contact.
A literature review shows that pyrite-like compounds, characterized by a metal atom M covalently bonded to two S atoms (MS_2), frequently display a double peak structure in this spectral region. Consequently, the well-known solid lubricant MoS_2 comes to mind as a potential candidate, especially since MoS_2 was already a possible candidate in the previous EDS analysis (Section 4.4.1). In non-resonant Raman spectra (532 nm excitation) of bulk MoS_2 presented in Section 2.5.1, four peaks are typically identified at approximately 32 (E^2_{2g}), 286 (E_{1g}), 383 (E^1_{2g}), and 408 cm^{-1} (A^2_{1g}) [44, 205, 517]. While the E_{1g} mode could not be observed in backscattering experiments as performed in this thesis [44, 205, 517]. However, in defective MoS_2, other combination modes or Raman overtones are also active, whereby five peaks are usually observed at about 178 (A_{1g}—LA), 232 (LA), 286 (E_{1g}), 383

(E_{2g}), and 408 cm^{-1} (A_{1g}) in the relevant spectral range [205, 518]. In particular, the modes E^1_{2g} and A^2_{1g} as well as the longitudinal-acoustic (LA) phonon modes are intense. However, no red-shifts to approximately 338 cm^{-1} are observed for the E^1_{2g} mode, neither as a result of a change in the number of MoS_2 layers nor as a consequence of tensile or compressive stress (for further details, please refer to Section 2.5.1). Therefore, the observed Raman signals cannot be attributed to the presence of MoS_2.

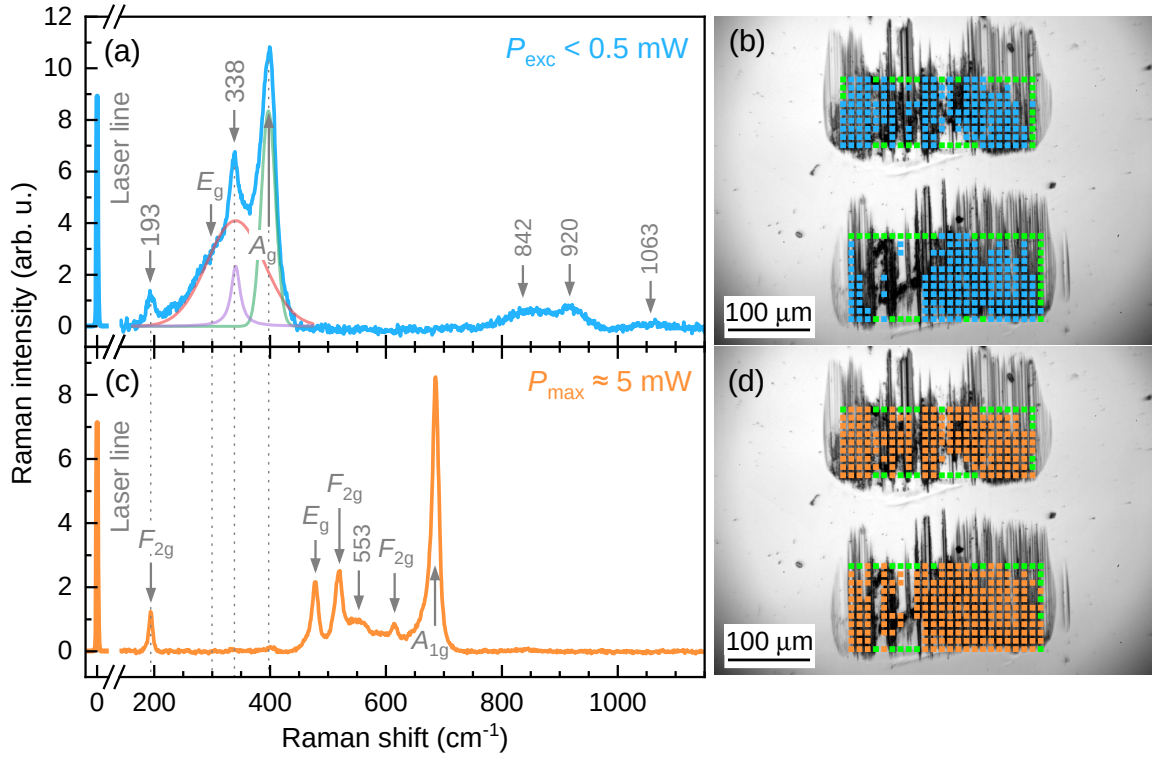


Figure 4.10: Within the FT on the Co-alloy, a laser power of $P_{exc} < 0.5$ mW can be used to non-destructively measure Raman spectra, which are comparable to the background corrected Raman spectrum in (a). A Raman mapping can identify the positions at which a spectrum similar to that in (a) is measured. In the microscope image (b), these positions are marked with blue squares, while green squares outline the mapping edge. After irradiating the surface with $P_{max} = 5$ mW, a Raman spectrum is again recorded with a laser power of $P_{exc} < 0.5$ mW at the same positions as before, as shown in (c). The positions where the spectra have a similar spectral shape are marked with orange squares in the microscope image (d). The difference in the shape of the spectra in (a) and (c) can be explained by the higher energy input of the laser, which induces local oxidation. Adapted from [464].

In addition, FeS_2 with Raman signals at 343 (E_g), 350 (T_g), 377 (T_g), 379 (A_g), and 430 cm^{-1} (T_g) [519, 520, 521] could contribute to the measured signals in Figure 4.10 (a). In particular, the most intense Raman modes E_g and A_g could contribute to the measured spectral shape. This is not surprising, although the Co-alloy contains little (< 1 %) Fe, there is plenty of it in the surrounding simulated body fluid: The BCS already contains about 1 ppm Fe transferred from the NBCS [522]. Besides FeS_2, the formation of CrS_2 is also a possibility, given that the CoCr29Mo6C0.03 pin comprises approximately 27.6 % Cr (see

Section 3.3). Furthermore, CrS_2 exhibits Raman modes at approximately 175, 252, 283, 346, and 359 cm^{-1}, with the modes at about 252 and 283 cm^{-1} being the most intense [523, 524]. Other chromium sulfides could also have formed, such as Cr_2S_3, which has Raman signals at 177, 254, 287, 305, 349, and 364 cm^{-1} [525, 526]. However, the typical Raman signals of FeS_2, CrS_2, or Cr_2S_3 are unable to account for the observed Raman spectrum in the low wavenumber range. Even when these structures are subjected to high tensile or compressive strain, which results in a shift and broadening of the Raman signals, they cannot be identified as the source of the measured signals. In particular, the intense and narrow-band peak at 401 cm^{-1} remains unexplained.
Another possible organic-inorganic composition that could have been formed by the tribological fretting contact and could also be the origin or contribute to the measured signals is CoS_2. This formation would be conceivable since the CoCr29Mo6C0.03 pin consists mainly of Co. CoS_2 has Raman signals at about 289 (E_g), 316 ($T_g(1)$), 395 (A_g), and 417 cm^{-1} ($T_g(2)$), whereas at room temperature the most intense Raman mode is the A_g mode at about 395 cm^{-1} [527, 528, 529]. And the second most intense Raman mode is the E_g at 289 cm^{-1} [527, 528]. However, this crystalline CoS_2 structure has only these two intense peaks in this spectral region, and their Raman shift differs from the one observed here. In addition, the measured Raman signals are broadened, which is known for disordered structure, as it is often observed in sputtered layers. Thus, a broadening of the signals was shown in magnetron sputtered CoS_2 layers [528]. However, this crystalline structure is unlikely to be the origin of the Raman signals. Kornienko et al. investigate spectroscopically amorphous cobalt sulfide (CoS_x) and observe Raman spectra similar to the presented spectra in this work [530]. Therefore, it can be assumed that the fretting contact does not form a stoichiometric crystalline CoS_2 structure but rather an amorphous/nanocrystalline CoS_x structure. This amorphous/nanocrystalline CoS_x structure may also explain why another Raman signal is measured at 190 cm^{-1} (compare with Figure 4.10 (a)), which is not measurable in a crystalline CoS_2 solid. This could be because, like the appearance of additional modes in amorphous carbon [531], this mode is forbidden in a CoS_2 crystal. However, further investigation and calculations are required to assign the peaks unambiguously.
In summary, it is plausible that the observed Raman spectrum represents a superposition of Raman signals from the materials discussed in this Section and listed in Table 4.2. Additionally, possible strain in these formed materials may influence and account for the observed Raman shifts [217, 221, 225, 532]. Moreover, the size of the crystallites and the degree of crystallinity influence the Raman shift [205, 533, 534, 535, 536], which could also elucidate the observed Raman shifts. However, the similarity between the measured spectra and those of CoS_x suggests that CoS_x is the dominant structure formed by a tribochemical reaction between Co and S. To elucidate the origins of the measured Raman signals, which may represent contributions from multiple materials or may be influenced by strain and degree of crystallinity, the following Section discusses further investigations.

4.4.3 Identification of CoS_x by Laser Induced Oxidation and Raman Spectroscopy

Combining Raman spectroscopy with laser-light induced oxidation represents a novel approach to identifying the chemical species formed from the metal and the organic material resulting from tribological contact. First, as shown in Figure 4.10 (a), a Raman spectrum is

recorded with an excitation laser power of $P_{exc} \leq 0.5\,mW$. The same sample position is then exposed to a laser power of $P_{max} = 5\,mW$. Afterward, a Raman spectrum is recorded again with $P_{exc} \leq 0.5\,mW$ at the same sample position, as shown in Figure 4.10 (c). The Raman signals have changed completely: Instead of Raman signals at 292, 338, and 401 cm^{-1} there are now relatively narrow peaks at 194, 478, 519, 615, and 685 cm^{-1}.
For a variety of materials, it has been reported that higher laser power can lead to laser-induced structural transformations [537, 538], oxidations [539, 540, 541] and/or a complete sample destruction [538, 542]. These structural-chemical changes are caused by local heating, where the temperature can rise by several hundred degrees [537, 540, 541]. Thus, to explain the Raman signals after irradiation with $P_{max} = 5\,mW$, it is reasonable to consider different oxides as well as transformations of the MS_2 structures.
By comparing with various Raman spectra, the Raman shifts of these five Raman signals have been found to agree well with the Raman shifts of Co_3O_4 phonon modes reported in the literature [543, 544, 545] and compared in Table 4.2. Moreover, the spectral shape of the Raman spectrum in Figure 4.10 (c) is also similar to the shapes shown in the literature [543, 544, 545]. It is therefore proven that Co_3O_4 is formed by local oxidation caused by laser heating. This supports the idea that a CoS_2-like structure was formed on the Co-alloy surface as a result of the fretting contact. This CoS_2-like structure oxidizes to Co_3O_4 as a result of the laser-light energy input. However, the Co content of the pin material itself is quite high at about 65 % (see Section 3.3), so it is possible that the Co_3O_4 signals are not caused by oxidized tribomaterial, but by oxidation of the CoCr29Mo6C0.03 pin itself.

Table 4.2: Measurable Raman signals with Raman shifts $\Delta\nu$ within the FT before and after illumination with intense laser light ($P_{max} \approx 5\,mW$). Prior to the intense laser light illuminating the surface, the observed Raman signals may have originated from different pytite-like MS_2 compounds, the Raman signals of which are listed. It was found that the high laser power caused oxidation. Adapted from [464].

Before irradiation with high laser-power P_{max}					After irradiation with P_{max}	
$\Delta\nu$ (cm^{-1})	$\Delta\nu$ [lit.] (cm^{-1})				$\Delta\nu$ (cm^{-1})	$\Delta\nu$ [lit.] (cm^{-1})
	MoS_2	FeS_2	CrS_2	CoS_2		Co_3O_4
193	178[a]	343[b]	175[c]	289[d]	194	194[e]
292	232[a]	379[b]	252[c]	316[d]	478	479[e]
338	286[a]		285[c]	395[d]	519	515[e]
401	383[a]		346[c]	417[d]	615	617[e]
	408[a]		359[c]		685	686[e]

References: a: [44, 205, 517], b: [519, 520, 521], c: [523, 524], d: [527, 528, 529], e: [543, 544, 545]

So, it is not yet clear whether these spectral shapes in Figure 4.10 (a) and (c) are correlated. Therefore, Raman mappings are performed where the sample is scanned in a raster with 10 µm steps in x- and y-direction. As previously outlined, Raman spectra are recorded at each position before and after the laser light illumination of the sample with $P_{max} = 5\,mW$ so that a spatially resolved comparison of these Raman spectra is possible. Figure 4.10 (b) shows a microscope image of the fretting track scanned with 480 measuring positions. The edge of the Raman mapping is marked with green squares. In addition, the positions where

a MS_2-like Raman spectrum is measured, similar to the spectrum in Figure 4.10 (a), are marked in blue. Figure 4.10 (d) shows the same microscope image of the fretting track, with the green marked edge of the mapping. Now, the positions where a Co_3O_4 Raman spectrum is measured after irradiation with $P_{max} = 5\,mW$ (similar to the spectrum in Figure 4.10 (c)) are marked with orange squares. Comparing these two mappings it can be seen that in 96.2 % of the measurement positions where a MS_2-like Raman spectrum (see Figure 4.10 (a) and (b)) is measured, a Co_3O_4 spectrum (see Figure 4.10 (c) and (d)) is measured after irradiation with P_{max}. There are 11 positions where MS_2-like spectra have been measured with no Co_3O_4 present after irradiation with the high laser power. Vice versa, there are also 83 (22.3 %) measurement positions where a Co_3O_4 spectrum is measured without a preceding MS_2-like spectrum. In addition, measurements outside the tribologically loaded area on the polished CoCr29Mo6C0.03 pin surface show that a laser power of $P_{max} = 5\,mW$ is not sufficient to induce oxidation. This can be taken as indirect evidence for the formation of a CoS_2-like tribomaterial within the fretting track on the CoCr29Mo6C0.03 surfaces, since in 96, 2 % of the cases where an MS_2-like spectrum is measured, Co_3O_4 is measured after laser-induced local heating and the bar pin surface doesn't oxidize even after laser irradiation with P_{max}.
However, there are also 11 measurement positions where CoS_2 was identified where Co_3O_4 is not measured after laser-induced heating. This can be explained by the fact that the sample was moved in the experiment using a *xy*-stage. Thus it can happen that the same positions are not always approached during the mapping. It is, therefore, possible that not the area where the sample was locally heated is measured, but a position minimally adjacent to it where no structural changes were induced. However, Co_3O_4 is detected at 83 measurement positions and CoS_2 was not measured before. This could be due to some CoO particles in the tribomaterial, which were then further oxidized to Co_3O_4. However, these CoO wear particles could not be identified within the spectra. This is not surprising, as the CoO Raman signals are comparatively weak and broad, so they disappear in the background [545, 546] or the amount of CoS_2 formed was too small to be identified and distinguished from the background noise by Raman spectroscopy. In addition, the inaccuracy of the *xy*-stage could also contribute to the discrepancy.

4.4.4 Identification CoS_x and Spatial Distribution of Different Elements within the Cross-Section of the Worn Co-alloy Surface by STEM

The combination of Raman spectroscopy and laser-induced oxidation enabled the microscopic detection of tribologically induced CoS_x formation in the FT on the Co-alloy surfaces. To analyze the nanoscopic structure and composition of this CoS_x tribomaterial, scanning transmission electron microscopy (STEM), STEM-EDS, and electron energy loss spectroscopy (STEM-EELS) are employed.
A bright-field STEM cross-section image of the Co-alloy pin, shown in Figure 4.11 (a) to (c), reveals a notable bright layer spanning the entire recording area (exceeding 3.5 µm). The thickness of this layer is approximately 15 nm, as observable in Figure 4.11 (b). This layer is the tribomaterial formed during the fretting contact, which still adheres to the Co-alloy surface. The Raman investigations conducted in the preceding Sections (4.4.2 and 4.4.3) have demonstrated that this tribomaterial is predominantly composed of CoS_x and is therefore named CoS_x layer.

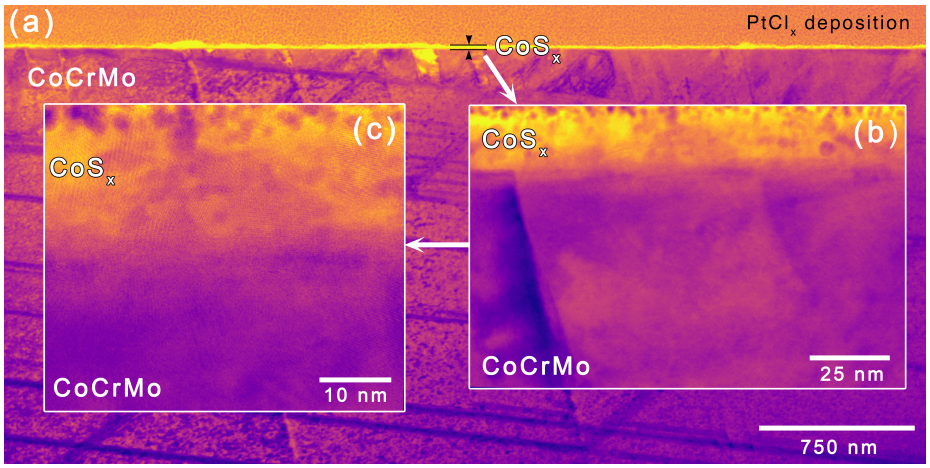


Figure 4.11: (a) An overview image of the cross-section after tribological loading of a Co-alloy pin, recorded using bright-field scanning transmission electron microscopy (BF-STEM). A bright line can be observed in the upper part of the image, representing the adhering tribomaterial and labeled here as CoS_x. The extended lines within the base material are indicative of stacking faults. At higher magnification (b), the approximately 15 nm thick CoS_x layer is observed to possess a substructure. Further increasing the resolution (c) reveals the presence of lattice fringes, indicative of a partially nanocrystalline CoS_x structure. Reproduced from [464].

As depicted in Figure 4.11 (c), the CoS_x layer exhibits a lattice fringe structure in certain areas, indicating that it has undergone partial nanocrystalline transformation during the tribological contact. This may enhance its adhesion to the underlying Co-alloy base material. STEM-EDS can be used to analyze the distribution of chemical elements within the CoS_x layer. A non-negative matrix factorization (NMF) of a STEM-EDS elemental image can be employed to investigate the spatial distribution of the first four components in conjunction with the corresponding EDS spectra at the nanoscopic level, as illustrated in Figure 4.12. The primary component, depicted in blue, is identified as a Co-alloy, corroborated by the EDS signals. The secondary component, represented in green, reveals EDS signals, including the Co-K_α and Co-K_β transitions, which overlap with those of the first component. However, a significant deviation is observed in the appearance of a novel EDS signal at approximately 2.3 keV in the second component spectra, alongside Cr-related signals disappear. This novel signal could correspond to either S-K_α or Mo-L_α transitions, considering the overlapping X-ray peaks of these elements. Furthermore, the Mo-K_α peak is also observed, which complicates the interpretation of the EDS spectra regarding the formation of CoS_x. However, the second component is assigned to the CoS_x layer in combination with the Raman results discussed above.
The third component (depicted in red in Figure 4.12) is attributed to a Ca-P-rich compound, as indicated by the X-ray peaks observed in the EDS spectra. This component does not appear to contain S or Mo. This corroborates the categorization of the observed Raman signals within the spectral range of 840 to 1070 cm^{-1} as calcium phosphate and/or oxide modes, as outlined in Section 4.4.2.
To further investigate the distribution of elements as a function of distance from the surface, X-ray spectra are recorded from line scans conducted across the interface. This approach provides additional depth-dependent information about the tribomaterial. The colored rect-

angles in Figure 4.13 (a) indicate the specific regions from which the line scan X-ray spectra were collected. These spectra are then averaged and presented in the corresponding colors in Figure 4.13 (b). A comparison of the two Figures 4.13 (a) and (b) reveals that the X-ray peak at approximately 2.3 keV is notably pronounced in the red to yellow spectra, which were captured in areas close to the surface. In contrast, the spectra obtained at greater distances from the surface (in the yellow to blue regions) show the emergence of the Cr-K_α signal, indicating that this region corresponds to a Co-alloy substrate.

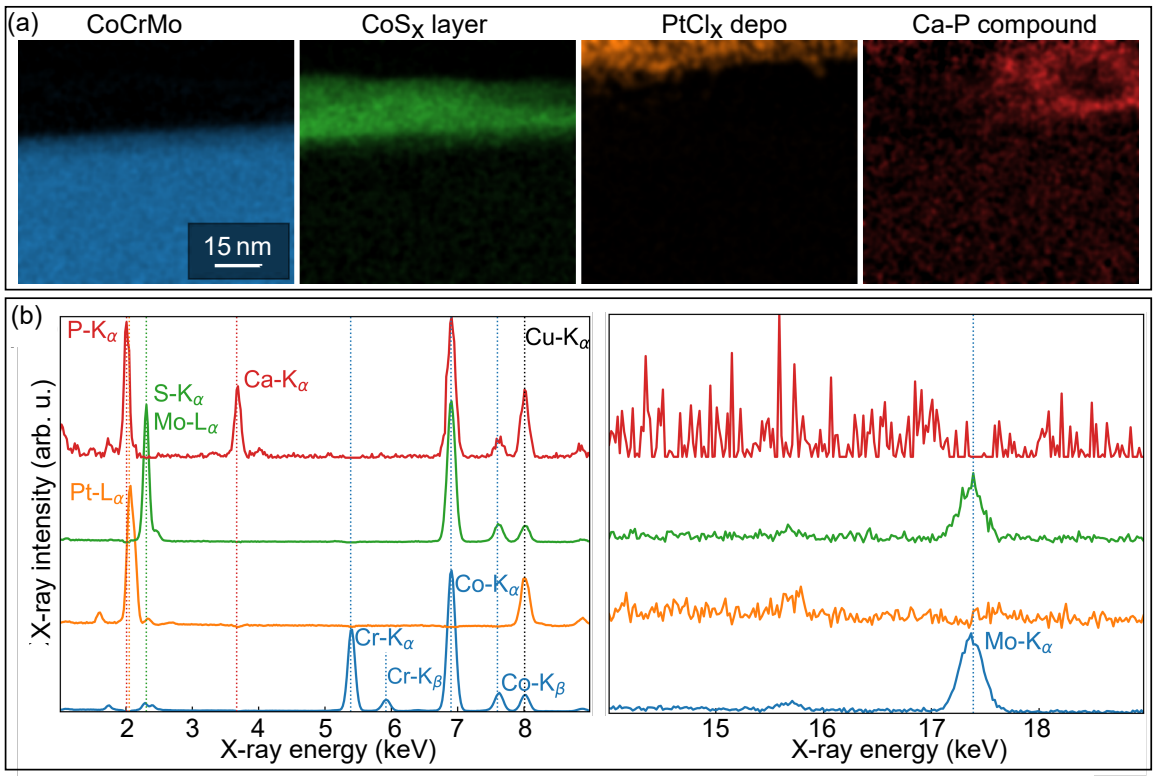


Figure 4.12: The elemental distribution analysis of the cross-section, conducted using STEM-EDS and NMF, identified four key components. (a) illustrates the spatial distribution of these components, as extracted from a STEM-EDS elemental image. The decomposition represents the Co-alloy base material (blue), the CoS_x layer (green), the $PtCl_x$ protective layer (orange), and a Ca-P compound (red). The corresponding EDS spectra are presented in (b). Adapted from [464].

Additionally, within the first few nanometers of the Co-alloy substrate, there is a marked decrease in signal intensity around 2.3 keV, accompanied by a slight shift toward the Mo-L_α line in the yellow to blue spectra. Conversely, the intensity of the Mo-K_α peak demonstrates only a minimal increase at the CoS_x Co-alloy interface. Collectively, these findings suggest that the superficial layer is primarily composed of CoS_x, with molybdenum accumulating at the interface. Furthermore, the EDS spectra indicate that the X-ray signal around 2.3 keV is most pronounced in areas close to the interface (yellow), where the Cr-K_α peak is not yet detected, and the sulfur concentration at the interface does not show an abrupt drop to zero. This observation supports the hypothesis of chemical mixing due to fretting contact, which facilitates the incorporation of sulfur atoms into the initial nanometers of the Co-alloy.

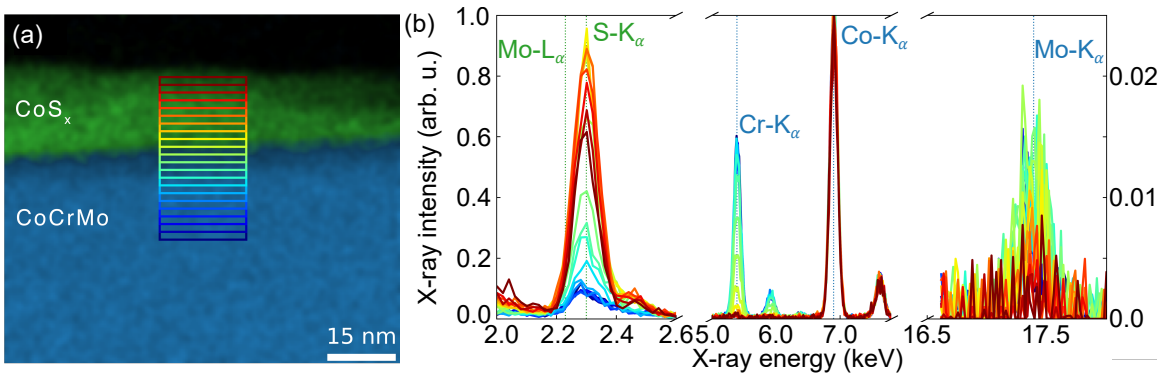


Figure 4.13: (a) Line scan regions indicated by rectangles for averaging EDS spectra presented in (b). The spectra show pronounced S-K$_\alpha$ peaks in the CoS_x layer (red to yellow) while the Mo-Kα peak increases towards the CoS_x Co-alloy interface, suggesting possible Mo enrichment. The rapid decay of the S-Kα peak into the Co-alloy substrate (yellow to blue) indicates the predominance of CoS_x, with S concentration decreasing, supporting the hypothesis of chemical mixing during tribological loading. Adapted from the Supporting Information of [464].

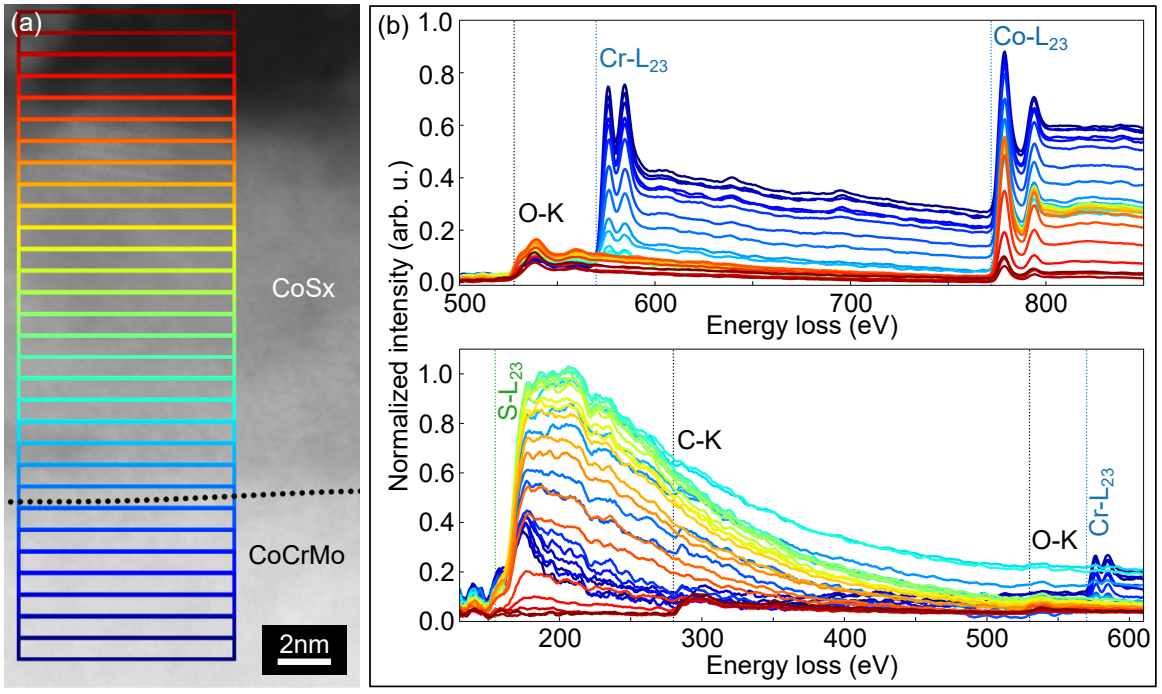


Figure 4.14: (a) ADF-STEM image with integration windows for the EEL spectra. (b) Energy loss ranges showing O-K, Cr-L23, and Co-L23 ionization edges, and S-L23 and Cr-L23 signatures. The red spectra at the top indicate oxygen and carbon signatures likely from sample handling. The rapid increase in S-L_{23} intensity (yellow to light green) within the CoS_x layer confirms sulfur presence. Despite transitioning into the Co-alloy (blue spectra), significant S-L23 signals are still detected, suggesting that sulfur is chemically mixed into the first few nanometers of the Co-alloy during fretting corrosion tests, consistent with STEM-EDS findings (see Figure 4.13). Adapted from [464].

The distribution of S observed based on the previously discussed STEM-EDS measurements can be confirmed using STEM-EELS measurements on the tribomaterial and its boundary area to the Co-alloy substrate. The integration windows of the EEL spectra employed in this study are indicated by colored squares in the annular dark-field STEM (ADF-STEM) image presented in Figure 4.14 (a). The corresponding colored spectra are presented in Figure 4.14 (b), with the two energy loss areas shown having been measured simultaneously and divided into two graphs for the sake of clarity. Upon initial examination of the spectra closest to the surface, plotted in red, it becomes evident that these exhibit signatures of both O and C, which are presumed to be the result of the preparation and transport processes.
Upon examination of the spectra recorded at a greater depth within the CoS_x layer (orange to light green), it becomes evident that the intensity of the S-L_{23} exhibits a notable increase. The blue spectra, which were measured in the Co-alloy, also exhibit these S-L_{23} signals, thereby corroborating the findings of the STEM-EDS measurements. A weak O-K peak is consistently observed in the CoS_x layer and the base metal alloy. However, it is also possible that this peak is a consequence of surface oxidation of the TEM sample during sample transfer.
In conclusion, the STEM, EDS, and EELS measurements indicate the incorporation of S atoms into the Co-alloy's surface through chemical mixing. These measurements also confirm the tribologically induced formation of an about 15 nm thick CoS_x layer. Furthermore, the STEM images evidence that the layer has at least a partial nanocrystalline structure.

4.4.5 Spatial Distribution of CoS_x Within the FT

The formation of CoS_x on the CoCr29Mo6C0.03 pin surfaces within the FT, resulting from tribological contact after a significant number of fretting cycles ($n_{\text{high}} \geq 4 \times 10^4$), has been demonstrated by Raman spectroscopy and STEM. The next question to address is the quantity of CoS_x that has formed.
To explore the spatial distribution of CoS_x on the Co-alloy pin surfaces in the FT, four Raman mappings were conducted at various positions across the sample surface, totaling 10,103 measurements. Figure 4.15 illustrates the areas covered by these mappings, with the specific regions of the four Raman mappings indicated within the FT. Furthermore, the measurement positions at which CoS_x can be identified are indicated with blue squares; this is the case in a total of about 12.2 % of the measurements. However, this identification of CoS_x in 12.2 % of the measurements is only an extrapolation based on a sample of 10,103 measurements. With this sample size, it follows that with a certainty of 95.56 % (confidence level 95.56 %, confidence interval 1 %) (12.2 ± 1) % of the fretting track of the CoCr29Mo6C0.03 sample surface is covered with CoS_x. This means that within the fretting track on the n_{high} CoCr29Mo6C0.03 surface, with a scanning distance of 100 µm and a sampling rate of 1 µm, CoS_x can be detected with a probability of 95 % at about 11 to 13 measuring positions. It should be noted, however, that although the areas in which the Raman mappings were made were randomly selected, the 10,103 measurements are not completely independent of each other, as neighboring points are considered.
To gain further insight into the tribologically formed CoS_x structure, fitting calculations were conducted using two Gaussian functions and a Lorentz function for the Raman signals at 292, 401, and 338 cm^{-1}, respectively. These fittings are illustrated in Figure 4.10 (a).

It was observed that the fit parameters of the Raman signals at approximately 292 and 338 cm^{-1} are strongly correlated; thus, only the signal of the mode at approximately 401 cm^{-1} is subjected to further analysis.

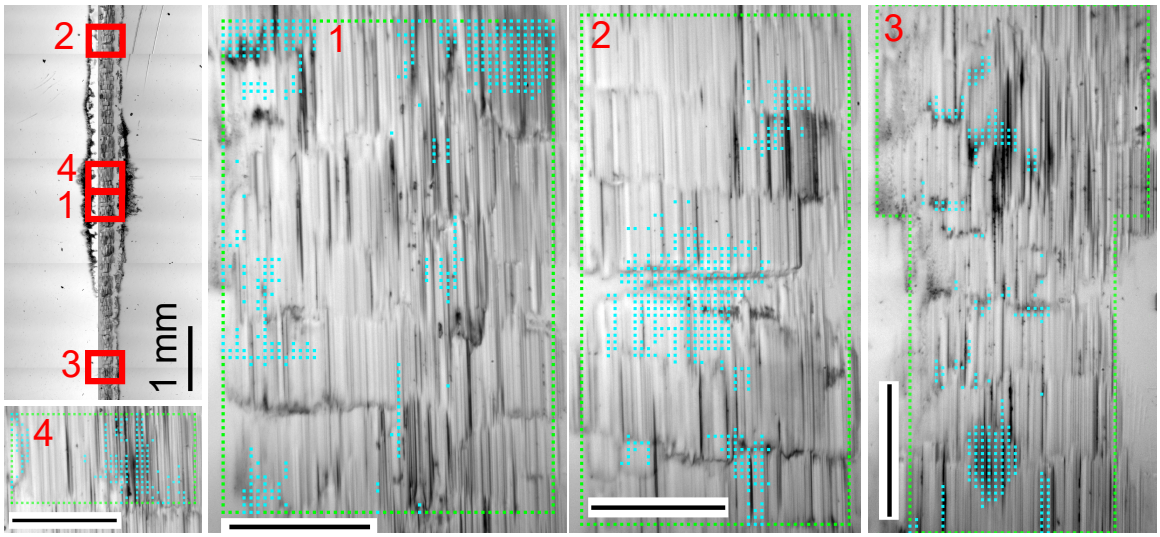


Figure 4.15: The locations where the four Raman mappings were conducted are indicated in the FT stitched image of the CoCr29Mo6C0.03 pin surface, captured with a 4× microscope objective. The individual areas in which the mappings are conducted are also depicted at a higher magnification (20×) and can be assigned to the overview image using numbering. The scale always corresponds to 100 µm. Furthermore, the edge of the Raman mappings is marked with green squares, while blue squares indicate that a CoS_x spectrum analogous to that depicted in Figure 4.10 (a) is obtained at this location. Mapping 1 encompasses 3,408 measurement points, with CoS_x identified at 12.1 % of these positions. Mapping 2 involved 3,157 measurements, revealing CoS_x at 13.4 %. In Mapping 3, CoS_x was detected at 8.4 % of 2,890 points, while Mapping 4 identified CoS_x at 23.1 % among 648 points. Adapted from [464].

For this purpose, the fit parameters (Raman shift, peak width, and intensity) are plotted in a heat map in Figure 4.16 and spatially correlated with the mappings within the fretting track (Figure 4.15). It can be observed in Figure 4.15 and 4.16 that the formation of CoS_x seems to occur mostly in clusters. Individual positions with CoS_x signals are only sporadically measurable, whereas neighboring measurement positions exhibit no CoS_x signals. This cluster formation may be attributed to the surface structure of the two contacting surfaces. Micro-contacts in these areas result in higher pressure and temperature, which may promote the formation of CoS_x. Additionally, a higher concentration of Co and S in these areas could also contribute to cluster formation. However, further studies are required to confirm these hypotheses.
An analysis of the spatial distribution of the Raman shifts, as illustrated in the second column of Figure 4.16, reveals no systematic within the mappings. It only seems that specific shifts are measured more frequently than others. To take a closer look at these distributions of Raman shifts within each mapping, they are plotted in histograms and shown in the last column in Figure 4.16. The most frequently occurring Raman shift is in the range of 400 cm^{-1} to 401 cm^{-1}, except the second mapping, which exhibits the most frequent Raman shift in the range 401 cm^{-1} to 402 cm^{-1}. Additionally, the distributions are slightly

asymmetric, broadening towards lower wavenumbers, likely due to the fitting procedure. The general spatial random distribution of the Raman shifts of CoS_x in the FT on the Co-alloy surface can be explained once more by the randomly distributed microcontacts, thus confirming the hypothesis of the formation of CoS_x at these contacts.
The full width at half maximum (FWHM) of the Raman signals observed in the four mappings, as illustrated in the third column of Figure 4.16, also appear to be distributed randomly. The most frequently measured FWHM ranges between 28 to 31 cm^{-1}. Nevertheless, a correlation between the line widths and the Raman shifts is discernible upon a comparison of the second (shift) and third (FWHM) columns in Figure 4.16. This comparison indicates that a higher Raman shift is associated with a narrower line width.
Furthermore, the measured signal intensity (rather than area) [6] is considered here and is shown for the corresponding mapping in the fourth column of Figure 4.16. The signal is typically most intense in the central regions of the areas/clusters where CoS_x is detected. This phenomenon is particularly evident in the third mapping illustrated in Figure 4.16. Furthermore, the highest intensities are observed at lower line widths, which is particularly clear in the fourth mapping illustrated in Figure 4.16. Given that a narrower line width is indicative of a more crystalline structure, it can be postulated that a more crystalline CoS_x structure is present in the center of the clusters. This also aligns with the hypothesis of CoS_x formation at the microcontacts, assuming, as with a Hertzian contact (for detail see Section 2.6.2), that the pressure is greatest in the center of the contact area. In accordance with the hypothesis presented here, this supports the formation of a more crystalline CoS_x structure.
Nevertheless, for crystalline CoS_2 a Raman shift of 395 cm^{-1} is observed for the most intense A_g Raman mode, as listed in Table 4.2. In contrast, the Raman signals with small linewidths, presumed to originate from a more crystalline CoS_x ($x \approx 2$), exhibit a shift to larger wavenumbers exceeding 400 cm^{-1}. This indicates that the A_g Raman mode of the structure here is blue-shifted in comparison to the literature value for crystalline CoS_2. A comparable blue-shift has previously been observed in a crystalline MoS_2 structure for the A_{1g} Raman mode when subjected to compressive strain (see Section 2.5.1). Given the structural similarities between CoS_2 and MoS_2, it is plausible that a compressive strain could also result in a blue-shift of the A_g Raman mode of the CoS_2 structure. Nevertheless, to the best of my knowledge, no studies on this topic can be found in the existing literature. However, it is assumed that a crystalline, maybe strained, CoS_x structure has formed in the cluster center, which becomes increasingly amorphous towards the edge of the cluster.

[6] In general, the measured intensities of the individual spectra cannot be compared with each other because, for example, the focal point may be slightly different from measurement point to measurement point, or the laser power may vary slightly from measurement to measurement.

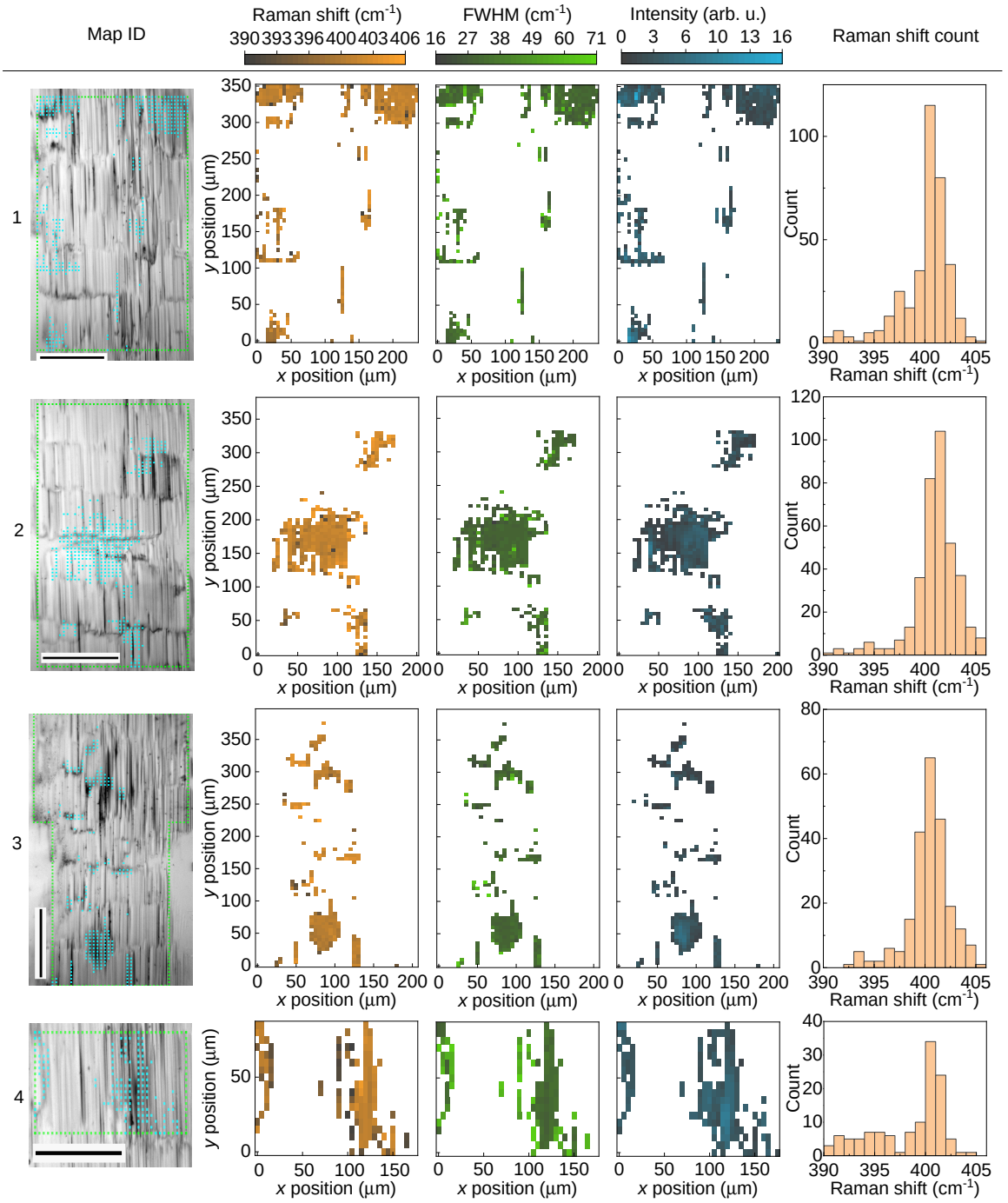


Figure 4.16: The Raman shift, width, and intensity of the CoS_x A_g vibration mode determined by fitting are shown according to the spatial position. To facilitate a better spatial correlation, the microscopic images of the FT areas in which Raman mappings were performed are also shown (see Figure 4.15). The scale in the images always corresponds to 100 µm. It can be observed that the formation of CoS_x seems to occur mostly in clusters, and the signal is typically most intense in the central regions of these clusters. Additionally, the most frequent Raman shift ranges between 400 cm^{-1} and 401 cm^{-1}. Adapted from [464] and the corresponding Supporting Information.

4.5 Conclusion

The taper junction of human hip implants is simulated by tribological gross-slip fretting corrosion experiments using Co-alloy or high-nitrogen steel surfaces in contact with a Ti6Al4V surface surrounded by BCS. Due to the metal-organic interactions biotribological wear particles are agglomerated near the fretting track and are microstructurally analyzed by confocal Raman scattering spectroscopy. Figure 4.17 schematically illustrates the tribomaterial identified in the AWP region. The thermomechanical conditions within the fretting contact result in the tribological oxidation of the metal. This releases ions from the Co-alloy (CoCr29Mo6C0.03) and the high-nitrogen steel (FeCr18Mn14Mo3CN0.9), leading to the formation of amorphous chromates and iron oxides in particular at some surface points, as illustrated in Figure 4.17. As the fretting experiments progress, these metal oxides and the non-oxidized surfaces of the pins become covered by organic moieties from the BCS. Coincidently, the microstructure of the organic compounds undergoes various changes depending on the number of fretting cycles. For example, the Raman lines related to the BCS show broadening that increases with the number of fretting cycles. Such a broadening indicates that the interatomic vibrations exhibit spatial inhomogeneity, which results from the thermomechanical stress and tribochemical reactions occurring during the fretting process.

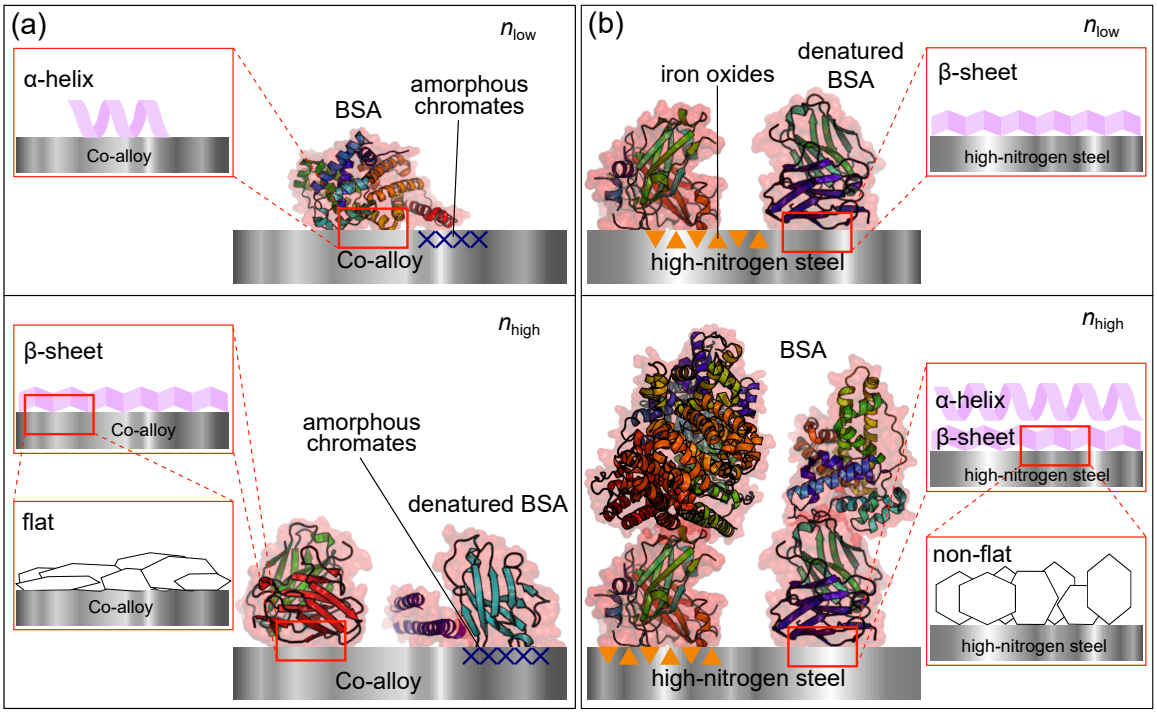


Figure 4.17: Schematic representation of the agglomerated tribomaterial detectable on the (a) CoCr29Mo6C0.03 and (b) FeCr18Mn14Mo3CN0.9 pin surfaces after a low (top) and a high (bottom) number of fretting cycles in the AWP region. The schematic is not to scale. Reproduced from [350].

Further details on the microstructural characteristics of the biotribological material formed in the fretting contact are evaluated by analyzing the asymmetric CH_2 and symmetric CH_3 vibrations at about 2900 cm^{-1}. Analysis of the probability distributions for the intensity

ratios of those vibrational modes indicates that the organic molecules adsorbed onto the Co-alloy feature shorter aliphatic chains than those on the high-nitrogen steel. However, this distinction diminishes as the fretting duration increases. Furthermore, due to van der Waals coupling short-chained organic moieties are arranged in a flat adsorption layer at the Co-alloy. By comparison, the more Coulomb-like coupling between the high-nitrogen steel and the hydrocarbons reduces surficial diffusion and favors a more directional alignment, so that predominantly flexible long-chained moieties are found at the high-nitrogen steel surfaces, independent of the fretting duration. The analysis of the Raman shifts of the amide I and III bands indicate that, for the Co-alloy, the secondary structure of the adsorbed proteins changes from the α-helix to the β-sheet or random-coil configuration with increasing number of fretting cycles. Conversely, for the high-nitrogen steel pins, a α-helix structure is identified after experencing a high number of fretting cycles, as shown in Figure 4.17. The enhanced wettability and hydrophilicity of the stainless steel facilitate the development of a proteinic multilayered structure at the AWP region, which includes more disordered proteins at the bottom. The long-range nature of the Coulomb-like coupling allows for efficient dissipation of thermal and mechanical energy, thus protecting the upper layer of α-helices of the BSA from undergoing denaturation.

The results of the Raman spectroscopy analysis of the FT indicate the presence of significant inhomogeneity in the tribological material within the FT, manifesting on both pin materials. On the one hand, organic material on both pin surfaces within the FT can be attributed to microploughing, which generates grooves that allow for the accumulation of organic matter. On the other hand, the freshly exposed metal surfaces may exert a catalytic effect in conjunction with shear stresses, facilitating the formation of amorphous carbon materials and defective graphite clusters on both pin surfaces. The latter process is driven by the release of carbon atoms through the cleavage of proteins.

Furthermore, following extensive gross slip fretting experiments, an metal-organic compound spanning hundreds of micrometers was identified in the FT of the Co-alloy surface. This compound underwent thermal oxidation to Co_3O_4 at elevated laser powers, leading to the identification of CoS_x. The measured Raman signals of the CoS_x layer differ significantly in both width and position from those of a crystalline CoS_2 structure. Consequently, it can be assumed that the CoS_x layer has a disordered or nanocrystalline structure. The BF-STEM images demonstrate that the CoS_x layer, which is approximately 15 nm thick, exhibits a partially nanocrystalline structure and adheres effectively to the Co-alloy base material. The recorded STEM-EDS and EEL spectra provide further evidence for the tribologically induced formation of a CoS_x film, which is associated with S enrichment in the CoS_x layer/tribomaterial. In addition, the spectra demonstrate that S was integrated into the first few nanometres of the base material through mechanical and chemical mixing. The S required to form these CoS_x compounds is derived from the disulfide bonds of the cysteine, which undergo denaturation and decomposition due to the tribological contact, as illustrated schematically in Figure 4.18. Additionally, Co ions are released from the alloy by tribocorrosion. These Co and S ions are capable of forming a bond with one another and creating a thin (≈ 15 nm), planar CoS_x tribofilm on the Co-alloy surface (see Figure 4.18 (c)). Raman mappings were employed to demonstrate the formation of CoS_x clusters, exhibiting a more nanocrystalline character in the center and becoming increasingly disordered toward the cluster edges. Additionally, it was estimated that this self-generated CoS_x tribofilm covers approximately (12.2 ± 1.0) % of the fretting track on the Co-alloy surface.

This entire tribomaterial, which has formed as a result of the in vitro gross slip fretting corrosion experiment in the tribological contact area (AWP region and FT) on both pin material surfaces, serves the dual function of lubricant and separator within a hip implant taper junction. Thus it prevents direct metal-on-metal contact and protects the surfaces from further oxidation and wear. In particular, the quasi-2D (laterally large, nanometre thin) nanocrystalline-amorphous CoS_x structure, generated by the tribosystem on the Co-alloy surfaces, acts as a lubricant capable of enduring extreme shear rates. Additionally, the electrical conductivity of CoS_x [547] may play a significant role in preventing charge accumulation, thereby enhancing triboelectric performance. The CoS_x layer demonstrates chemical stability, which may make it robust under acidic and alkaline conditions commonly found in hip joints. These unique properties of the transition metal dichalcogenide CoS_x, particularly its self-lubricating properties, contribute to the tribological advantages of its formation on medical Co-alloys. Nevertheless, the denatured proteins or CoS_x structure may potentially trigger an immunological defense reaction. Nevertheless, a hydrophilic surface, such as FeCr18Mn14Mo3CN0.9, could potentially mitigate this risk since increased hydrophilicity has been demonstrated to result in enhanced protein adsorption and the promotion of cell adhesion and growth [548, 549]. Previous studies have demonstrated that nitrogen-rich steel exerts a more favorable effect under inflammatory aspects than Co-alloys [370, 550, 551]. The length-scale bridging findings pre-

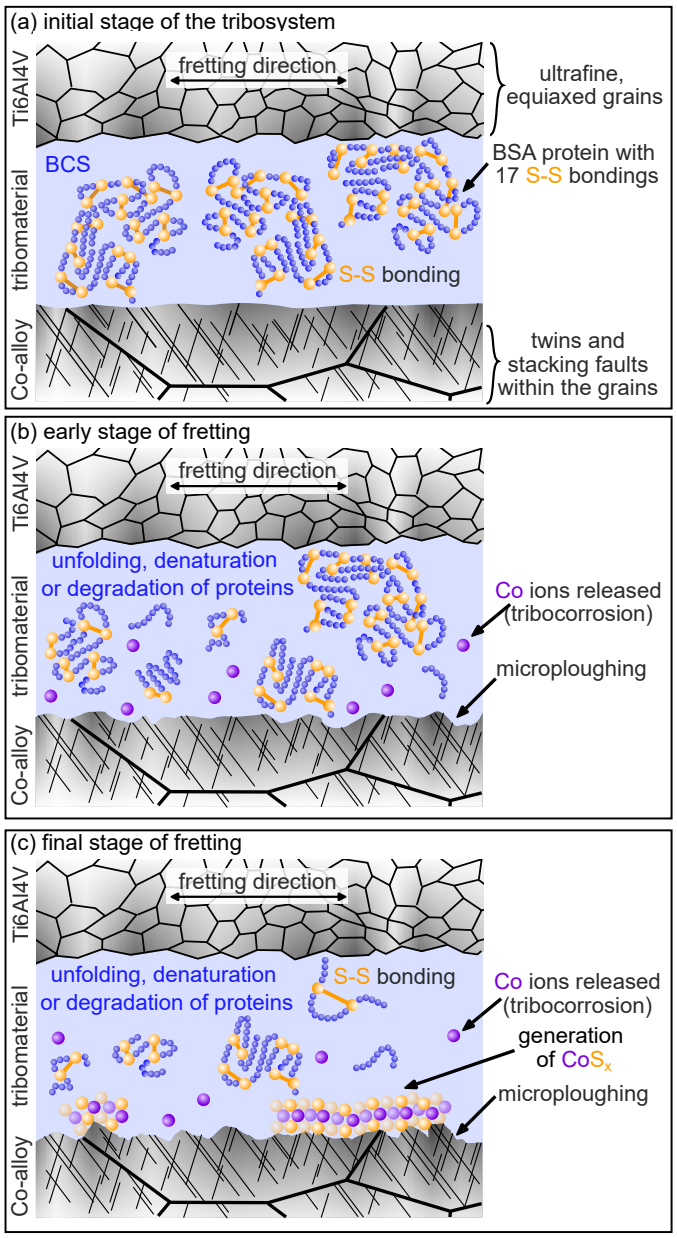


Figure 4.18: The schematic illustrates the formation of CoS_x on the surface of a Co-alloy during gross-slip fretting tests with a Ti6Al4V counter body. Through the fretting process, protein denaturation and tribocorrosion occurs, leading to the release of sulfur (orange) and cobalt ions (purple), respectively. In the final stage (c), a CoS_x layer on the surface of the Co-alloy is formed. Adapted from [464].

sented herein represent a significant contribution to the understanding and characterization of the adsorption mechanisms, structure, state, composition, and origin of the biotribological material and the metal-organic reaction products at the taper junctions of hip implants. These metal-organic reaction products may serve as a trigger for osteolysis, perivascular lymphocytic tissue reactions, or metal hypersensitivity in patients following implantation. This makes it possible to rethink the fabrication and choice of materials for hip joint implants and, if necessary, adapt them to improve their integration into the human body. This paves the way for the future provision of an even better artificial joint to patients with osteoarthritis or end-stage rheumatoid arthritis, significantly improving their quality of life and reducing the need for revision surgery. However, further research into the tribological mechanisms and the properties of the resulting tribomaterial is crucial for the development of innovations aimed at improving the performance and lifespan of artificial hip joints.

Chapter 5

MoS_2 Tribomaterial Characterization and Coating Thickness Measurement

The investigation of friction, wear, and lubrication mechanisms is of particular importance, as these mechanisms play a crucial role in the performance and longevity of tribological systems, exerting a significant influence on several natural and technical processes. Furthermore, approximately ($\approx 23\,\%$) of global energy consumption is attributable to friction and wear, associated with considerable costs and CO_2 emissions [23, 552]. A friction and wear reduction can result in significant cost savings and reduce CO_2 emissions, as demonstrated in Table 5.1 using four examples. Consequently, the objective of tribology is to minimize friction and wear. This may be achieved by optimizing existing lubricants or developing new methods or lubricants, which are then advanced to application maturity.

Table 5.1: Four examples from the field of vehicles & machinery are provided. These are supplied with energy by different fuel types, the proportion of which, designated as ΔF_f, is used to overcome friction. The application of novel technologies has the potential to markedly reduce friction and wear, leading in the long term (about 20 years) to significant annual global economic savings S and a notable decline in global CO_2 emissions $\Delta m(CO_2)$. The data presented here is from the referenced studies (Ref.).

Vehicles & machinery	Fuel types	ΔF_f (%)	S (bn €)	$\Delta m(CO_2)$ (m t)	Ref.
passenger cars	gasoline/diesel	33*	576	-960	[553]
trucks and buses	diesel	33	280	-530	[554]
mining industry		40	62.2	-290	[555]
paper machines	electric	32	4.2	-22.7	[556]

*: For an electric car, the amount is approximately half that of an internal combustion engine vehicle [553].

Fluid lubricants, such as oils or greases, are frequently employed in technical applications, as they enhance tribological performance and are straightforward to handle [557, 558]. Nevertheless, in specific instances, solid lubricants may be imperative, particularly when the conditions are too extreme for fluid lubrication [58, 60, 61]. Such extreme conditions include ultra-low temperatures (*e.g.*, in the aerospace industry), which render fluid lubricants ineffective due to solidification [559, 560], and vacuum, in which solid lubricants do not sublimate due to their low vapor pressure [60]. Furthermore, specific applications, such as those in the food industry, may prohibit the utilization of fluid lubricants due to the poten-

tial risk of contamination and the associated health hazards [561] [1]. The thickness of the coating is also a factor when using solid lubricants, as it often determines the load-bearing capacity, adhesion, and thus the tribological properties as well as the service life [79, 563, 564, 565, 566, 567].
One of these solid lubricants is molybdenum disulfide (MoS_2), which is of particular significance due to its lamellar structure, which is discussed in greater detail in Sections 2.5.1 and 2.6.6. In this context, MoS_2 can be employed by itself as a lubricant, as an additive to oils or greases, or as part of a composite coating [568]. In this thesis, only MoS_2 and modified MoS_2:X solid lubricant PVD coatings are considered.
This Chapter is divided into two Sections. The first Section 5.1 investigates the tribological behavior and induced changes of element-modified MoS_2:X films to gain a better understanding of the tribochemical and tribomechanical mechanisms and their interactions. The results presented in this Section 5.1 have already been published in reference [367]. The second Section 5.2 introduces a new method for measuring the thickness of coatings using the solid lubricant MoS_2 as an example coating. The motivation behind this novel approach arises from the limitations of conventional techniques in measuring thickness, particularly when applied to coated metallic samples featuring curved geometries. The results from this Section 5.2 will be published in reference [569].

5.1 Strain, Oxidation, and Formation of Few-Layer Graphene within the Tribomaterial in Steel-MoS_2:X Tribosystems

The efficacy and durability of MoS_2 as a lubricant is contingent upon the load and wear conditions, which encompass contact pressure, ambient humidity, and the chemical and physical structure of the synthesized MoS_2 films. As discussed in Section 2.6.6, the adsorption and diffusion of water molecules in particular lead to increased friction, and thus have a significant impact on the tribological performance of a MoS_2 layer. However, by modifying the MoS_2 layer, *i.e.* by incorporating additional elements, denoted as X, the structure and, in particular, the crystallite orientation can be influenced, resulting in a significant improvement in the performance of the modified MoS_2:X under humid conditions. In particular, the modification of MoS_2 by the transition metals X = Cr, Cu, V, or Zr appears promising. However, this effect is contingent upon the intrinsic properties of the modifying element, its integration into the MoS_2 structure, the concentration of the modifying element, and the synthesis process, as previously outlined in Section 2.6.6. It can therefore be concluded that the enhanced tribological properties are typically a result of alterations to the microstructure and crystallite orientation. However, the precise mechanisms and interactions that govern the tribological behavior of element-modified MoS_2:X films remain a topic of ongoing research.
The tribological behavior and effectiveness of the element-modified MoS_2:X films contingents upon a transfer film formation. This formation is typical for solid lubricants, as elucidated in Section 2.6.4. This Section, therefore, focuses on the transfer film in particular. To achieve this, a tribological system was constructed, comprising a main body coated with MoS_2:X via PVD (for further details on the PVD-based coating synthesis pro-

[1] There are fluid lubricants that are suitable for use with food, including edible oils and also hydraulic lubricants, which are employed in the food industry and comply with food regulations [562].

cess, please refer to Section 3.2.1), and an uncoated counter body made of case-hardened steel, with normal atmosphere serving as the ambient medium. A detailed description of the tribometer experiment conducted with these materials can be found in Section 3.2.3. It is typical for tribological contacts to result in not only material transfer but also the formation of tribomaterial in general. Subsequently, the tribomaterial is subjected to a more detailed analysis employing confocal, non-destructive Raman scattering spectroscopy on both bodies, as outlined in Sections 3.1 and 3.2.3. Mostly, the tribomaterial contains chemical reaction products in the form of oxide and sulfide compounds [570, 571]. It is also possible that wear particles may be formed, as discussed in Section 2.6.4. These wear particles can be subjected to several additional wear processes (for an overview of these processes, see Section 2.6.1). Therefore, they often differ from bulk materials in terms of their chemical reactivity, strain distribution, or degree of crystallization [70, 572, 573, 574, 575]. This indicates that the tribomaterial in general is not only structurally distinct from the bulk materials but also exhibits chemical differences.

To gain a more precise understanding of the mechanisms and their interaction, it is necessary to investigate the spatial distribution of the tribomaterial in greater detail and to determine its structural and chemical properties and phase transitions. These investigations have yet to be conducted for MoS_2:X coatings, and the influence of modification elements on transfer film formation remains to be elucidated. A detailed investigation of the spatial distribution of the tribological material on the counter body, which was tribological tested against a MoS_2:X film, as well as its structural and chemical properties, is still lacking. In this context, the question of how transition metals X in MoS_2:X can influence the material transfer from the main body to the counter body remains unanswered. Moreover, it would be advantageous to ascertain the potential chemical reaction products, such as oxides, and to elucidate their formation, as well as to categorize their impact on the tribosystem. In addition to these chemical changes, an investigation of the structural changes, such as strains, and their spatial distribution within the tribomaterial would also be of great interest. Furthermore, it would be beneficial to identify and structurally characterize the tribochemical and mechanically mixed tribomaterial with structural characteristics distinct from those of the underlying substrate or initial surface. In particular, it would be advantageous to analyze the significance of carbon in the steel counter bodies, as various tribologically advantageous carbon allotropes are known, possibly formed by the thermal and mechanical conditions in tribological contact.

The following Sections address these open questions. Firstly, the Raman spectra obtained from the main and counter body are subjected to a more detailed analysis, and a comparison is made between the two bodies. In addition, the coefficient of friction, the wear coefficient, the morphology, and the topography of the initial coating are discussed. The subsequent Section 5.1.2 presents a detailed analysis of the relative strain distribution caused by tribological contact in the MoS_2 transfer material based on Raman mappings. The third Section 5.1.3 employs Raman signals to identify tribochemically formed oxides with spatial resolution. Additionally, a thermodynamic analysis is conducted to elucidate their formation mechanisms. The final Section 5.1.4 presents a spatially resolved structural characterization of the few-layer graphene formed in the tribological contact.

5.1.1 Raman Scattering Spectra at Main and Counter Body and Impact of Doping Element on MoS_2

A representative Raman scattering spectrum taken from the main body and the MoS_2 transfer material on the counter body is shown in Figure 5.1 (a). The spectrum features prominent Raman bands at approximately 178, 232, 300, 378, and 411 cm^{-1}, which correspond to the Raman-active acoustic and optical phonon modes: $A_{1g}(M) - LA(M)$, $LA(M)$, $E_{1g}(M)$, $E^1_{2g}(\Gamma)$, and $A_{1g}(\Gamma)$ of multiple monolayers and/or bulk-like MoS_2 [205]. As previously demonstrated in Section 2.5.1 the $E^1_{2g}(\Gamma)$ mode is an in-plane mode in which the two sulfur atoms in the plane vibrate in phase with respect to the molybdenum atom. In contrast, the $A_{1g}(\Gamma)$ mode is an out-of-plane mode in which the two sulfur atoms vibrate out-of-phase concerning the molybdenum atom. Beyond this two first-order modes at the Brillouin zone center Γ, the $A_{1g}(M) - LA(M)$ mode at 179 cm^{-1} and the $LA(M)$ mode at 231 cm^{-1} are also significant within the Raman spectra. The $LA(M)$ mode represents longitudinal acoustic phonons at the M-point of the Brillouin zone, which correspond to in-plane collective movements of all the atoms in the MoS_2 lattice. In addition, the overtone $2LA(M)$ mode at 460 cm^{-1}, and the combination $A_{1g}(M) + LA(M)$ mode at 646 cm^{-1} can be identified. For the sake of clarity, the designation of the phonon modes will not include the points in the Brillouin zone in the following.

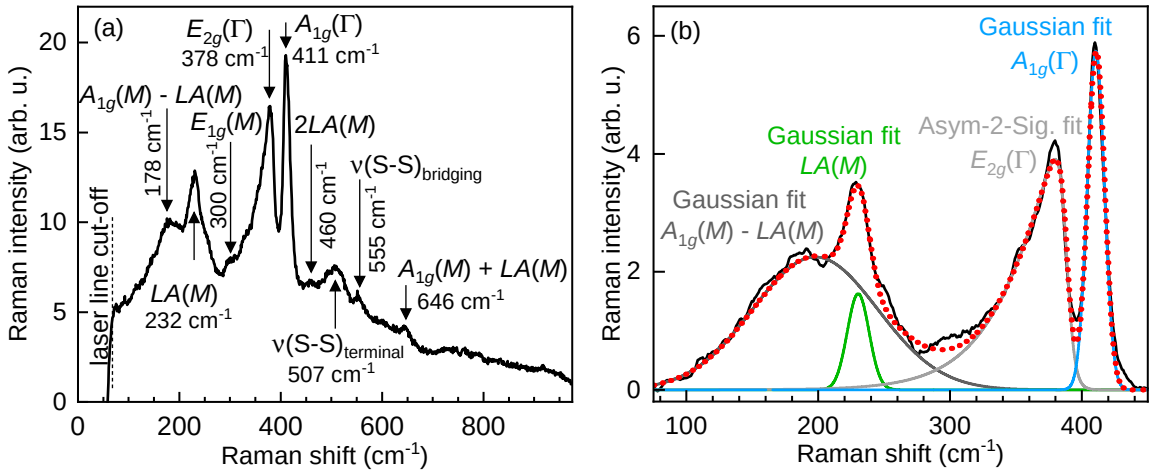


Figure 5.1: (a) depicts a representative Raman scattering spectrum of MoS_2 acquired on the transfer material on a steel ball in contact with the MoS_2:Cr film. Excitation was achieved through the use of a 532 nm laser light. The phonon modes characteristic for MoS_2 are indicated according to their Raman shift. The Raman shift, intensity, and width of these Raman signals can be determined using a fitting curve, as exemplified in (b). Thereby, the $A_{1g}(M) - LA(M)$, $LA(M)$, and $A_{1g}(\Gamma)$ Raman lines are fitted by Gaussian functions, while the asymmetric $E_{2g}(\Gamma)$ line is fitted by an asymmetric double sigmoidal function. Adapted from [367].

The subsequent discussion will focus on the longitudinal acoustic phonon mode LA (231 cm^{-1}) and the optical vibrational phonon modes E^1_{2g} (378 cm^{-1}) and A_{1g} (411 cm^{-1}), as they deliver insights into the atomic structure and structural changes can be regognized within the MoS_2 structure. Of particular interest in this context are the Raman shift, width and intensity. In order to obtain these peak parameters, equalization calculations are performed for

each Raman spectrum, whereby a background correction is carried out initially. Afterward, the $A_{1g} - LA$, LA, and A_{1g} mode were each fitted with Gaussian functions, and the E_{2g} mode with an asymmetric double sigmoidal function

$$I(\mathrm{E_{2g}}) = \frac{I_0}{1 + \exp\left(-\frac{x-\mu+\frac{\sigma_1}{2}}{\sigma_2}\right)} \cdot \left(1 - \frac{1}{1 + \exp\left(-\frac{x-\mu-\frac{\sigma_1}{2}}{\sigma_3}\right)}\right), \tag{5.1}$$

where μ is the Raman shift of the E_{2g} mode, I_0 indicates the intensity amplitude, σ_1 express the full width of half maximum, σ_2 represents the variance of low-energy side, σ_3 describes variance of high-energy side. These two fit functions were chosen because they particularly closely mimic the measured spectra, as exemplary shown in Figure 5.1 (b). To take into account both the contributions of the out-of-plane (A_{1g}) and the in-plane (E_{2g}) lattice vibrations when investigating the spatial distribution of MoS_2 on tribologically loaded surfaces, the intensity ratio $I_R[MoS_2] = I[A_{1g}]/I[E_{2g}]$ is considered. As previously outlined in Section 2.5.1, the intensity ratio can be employed to ascertain the number of MoS_2 layers or to determine the presence of compressive or tensile strain. Additionally, the texture of a nanocrystalline MoS_2 film can be characterized based on the intensity ratio [576]. Consequently, the intensity ratio offers a qualitative assessment of the structural characteristics of the tribologically loaded MoS_2:X films and the transfer material.
In order to investigate the tribological structure of the main body, spatially resolved Raman mappings over the wear tracks were recorded, as shown in Figure 5.2 (e) to (h). These mappings can be correlated with the scanning electron microscope (SEM) images of the tribological tracks at the main bodies with MoS_2:X (X = Cr, Cu, Zr, or V) surfaces, which are depicted in Figure 5.2 (a) to (d). In each of these SEM images, the wear track formed due to the ball-on-disc tribological test on the MoS_2:X coated surfaces can be identified in the center. Notably, the width of the wear track is typically approximately 200 µm, except for the MoS_2:V film, which is approximately twice this value. In the Raman mappings (Figure 5.2 (e) to (h)), the edge of the tribological track is visualized by a dashed line. Upon closer examination of the spatial distribution of the intensity ratio $I_R[MoS_2]$, a notable decrease is observed, from approximately $I_R[MoS_2] \approx 2.2$ in the unloaded region to around 1.3 within the wear track. This decrease of $I_R[MoS_2]$ by spatially moving into the wear track can be attributed to the influence of the tribological contact and the associated mechanical and thermal energy impact on the structure of the MoS_2 film. In particular, the induced tensile and compressive strains, as well as a realignment of the grains are responsible for the observed decrease in $I_R[MoS_2]$. In addition to the MoS_2 Raman signals, Fe oxides are discernible in the wear track of the MoS_2:Zr and particularly the MoS_2:V films (see Figure 5.2 (g) and (h), respectively), which are observed instead of the MoS_2 signals. The significantly wider tribological track and the detection of almost only Fe oxides in the tribological track alone demonstrate that the MoS_2:V lubricating film was almost completely removed during tribological contact. The detrimental tribological behavior of the MoS_2:V layer due to the modification with V is further evidenced by the coefficient of friction μ and the wear coefficient, which are thematized in the following Section.

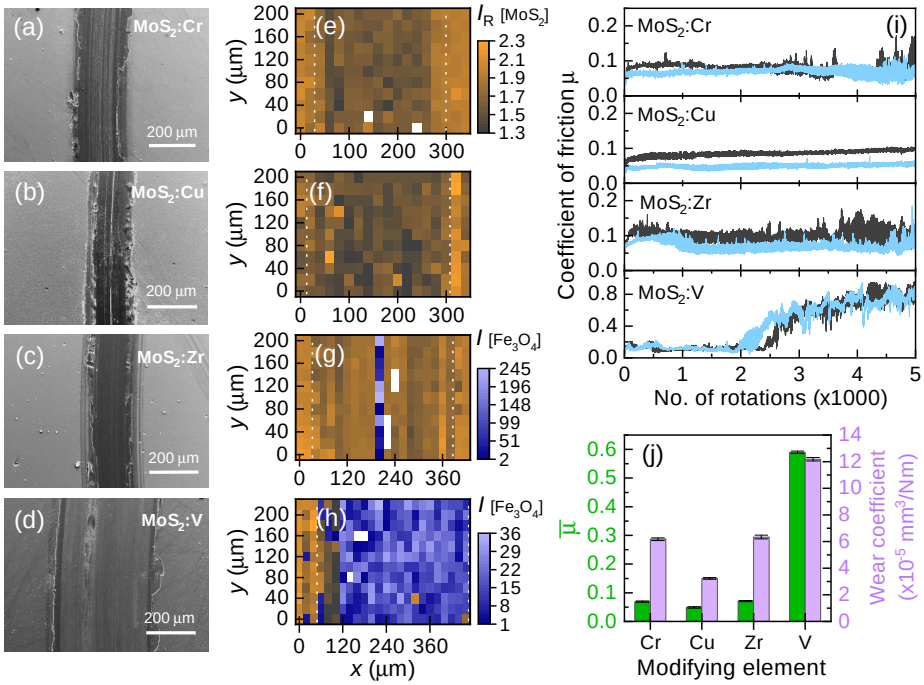


Figure 5.2: The scanning electron microscope (SEM) images of the tribological track (dark area) on the main bodies with MoS_2:X (X = Cr, Cu, Zr, or V) surfaces after ball-on-disc contact are presented in (a)–(d). The Raman mappings of these tribological tracks are given in (e)–(h), wherein the intensity ratio I_R and the Raman scattering intensity of the Fe_3O_4 A_{1g} mode at approximately 661 cm^{-1} are displayed. The dashed vertical lines indicate the edges of the tribological tracks. Furthermore, the friction coefficient measurements are presented as a function of the number of ball-on-disc rotations for the distinct MoS_2:X layers and the 10 mm (dark grey curves) and 12 mm (light blue curves) radius of the wear track in (i). The average friction coefficient $\bar{\mu}$ and wear coefficient resulting from the ball-on-disc tribometer tests are illustrated for the element-modified coatings in (j). Reproduced from [367].

Tribological Performance of Modified MoS_2 Films: Comparative Analysis of Coefficient of Friction and Wear Coefficients

The values of the coefficient of friction as the arithmetic mean value of three measurements $\bar{\mu}$ are illustrated in Figure 5.2 (j) and are for the Cr, Zr, and Cu-modified films below 0.1. Therefore, the modified films exhibit a comparatively lower coefficient of friction in a humid environment than non-modified MoS_2 films, whose average coefficient of friction is $\bar{\mu} = (0.151 \pm 0.011)$ [72]. As outlined in Section 2.6.6, the layered structure of MoS_2 endows it with advantageous lubricating properties. In particular, the facile shearing of the S–Mo–S layers, which hinges on the weak van der Waals forces between the S layers, is particularly important. This results in a increase in friction as the bond strength between these layers decreases [577]. An additional element, distinct from Mo or S, disrupts the ordered MoS_2 lattice structure, thereby influencing the friction properties. If the modifying element is incorporated into the van der Waals gap, the lattice expands in the (100) edge-plane direction. This expansion is associated with a reduction in the attraction between neighboring S planes [578] and a lowering in the bonding energy [577], which is linked to a decrease in friction.

Additionally, the diminished friction observed in the modified MoS_2:X film relative to the non-modified MoS_2 film may be explained by the (002) basal-plane orientation of the modified MoS_2:X film, which may impede the adsorption of water molecules, as previously discussed in Section 2.6.6. It has been demonstrated that water molecules enhance friction and wear [64, 579] and their reduced adsorption may contribute to a densification of the microstructure [38, 580, 581]. Therefore, the interaction with the surrounding water molecules from the environment and their penetration into the films may be reduced, contributing to lower friction than the unmodified MoS_2 film. However, none of the Raman spectra showed signals characteristic of water, which could be because the amount of water adsorbed is undetectable by Raman spectroscopy. The adsorbed water molecules do not only affect the friction by increasing the shear strength, but also by determining the properties and the flow of the generated wear particles. To investigate this effect, the wear coefficients, defined as the amount of removed film material from the sample surface, are calculated and shown in Figure 5.2 (j). The wear coefficients are significantly reduced for the Cr-, Cu-, and Zr-modified films in comparison to the non-modified MoS_2 film, with a value of $(7.66 \pm 0.08) \times 10^{-5}\,\mathrm{mm^3\,N^{-1}\,m^{-1}}$ [72].

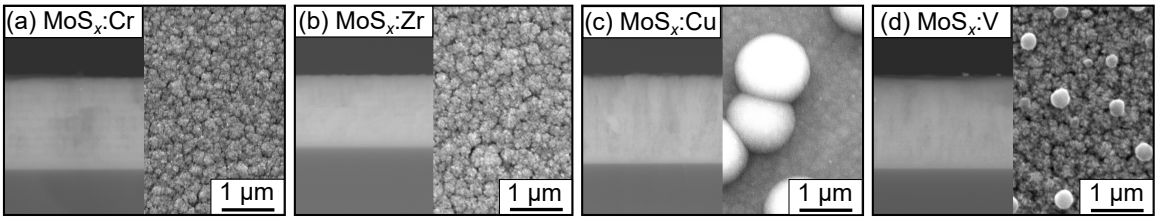


Figure 5.3: Morphology and topography of the element-modified MoS_2:X (X=Cr, Cu, V, and Zr) thin films. Compared to the non-modified MoS_2 film, which is characterized by a columnar microstructure (comparison Ref. [72]), all films exhibit a dense structure. The topography of the MoS_2:Cr (a) and MoS_2:Zr (b) film can be characterized as granular and cauliflower-like. The surface of the Cu-modified (c) and the V-modified (d) films is marked by the presence of isolated globular grains on a smoothed surface.

However, the MoS_2:V film exhibits markedly inferior tribological behavior compared to the other modified MoS_2:X films. The MoS_2:V film exhibits the highest average value of the coefficient of friction, with $\bar{\mu}$=(0.590 ± 0.004), as illustrated in Figure 5.2 (j). Furthermore, the curve of the coefficient of friction demonstrates an abrupt rise to approximately 0.8 after approximately 2000 rotations, which corresponds to the coefficient of friction observed in steel-steel contact. Furthermore, the MoS_2:V film exhibits the highest wear coefficient of $(12.18 \pm 0.13) \times 10^{-5}\,\mathrm{mm^3\,N^{-1}\,m^{-1}}$, as illustrated in Figure 5.2 (j). This finding supports the results from the Raman measurements, which indicate the presence of predominantly Fe oxides within the tribological track, and the observations made in the SEM images, which revealed the most extensive wear track in the V modification. All these results indicate that the MoS_2:V film is completely worn out by the tribological contact. This phenomenon may be attributed to the water adsorption capabilities of both polycrystalline V and various V oxides [582, 583]. Incorporating V into the MoS_2 structure increases water adsorption, which enhances the interaction between the film and the surrounding water molecules from the environment, facilitating their penetration into the film and contributing to high friction. Moreover, the flow of the generated wear particles is typically influenced by the ductility and

cohesion of the film material, which in turn is affected by the adsorbed water molecules [584]. An increased amount of water molecules leads to the agglomeration of wear particles, which become brittle and are more easily removed from the contact area.
In contrast, the MoS_2:Cu film exhibits the most favorable tribological properties of the solid lubricants under investigation. The MoS_2:Cu film demonstrates the lowest coefficients of friction, with a value of $\bar{\mu} = (0.049 \pm 0.003)$, and the lowest wear coefficient $(3.23 \pm 0.06) \times 10^{-5}\,\mathrm{mm^3\,N^{-1}\,m^{-1}}$. To ascertain the origin of this enhanced lubricity, it is beneficial to examine the morphology and topography of the MoS_2:X layers. As illustrated in Figure 5.3, all MoS_2:X films possess a dense structure, distinguishing them from unmodified MoS_2 films that exhibit a columnar microstructure [72]. The majority of films exhibit a granular and cauliflower-like topography. However, the surface of the V- and Cu-modified films represents a notable exception, exhibiting isolated globular grains comprising the respective modification element, as determined by EDX analysis. The formation of these V/Cu-enriched clusters is attributed to the segregation of V/Cu atoms when the incorporated concentration approaches the solubility limit in the MoS_2 matrix. Similar effects have been observed in Cu-modified DLC films [585]. It can thus be surmised that the Cu-enriched clusters on the surface of the film may be the reason for the improved tribological properties in comparison to the other modification elements. Since copper is a soft metal, it displays a lubricating effect itself due to its low shear strength [586]. Additionally, copper exhibits a cladding effect [587, 588], which, in conjunction with the higher columnar packing density observed in all MoS_2:X films, also increases the cohesion between the crystallites. This can reduce the amount of wear particles produced, as suggested for an Au modification [336].

Effects of MoS_2 Modification on Raman Spectra Recorded within the Tribological Loaded Area: Comparing Main and Counter Bodies

To investigate and compare the tribological structure of the main body and the counter body, spatially resolved Raman mappings are recorded over the wear tracks on the main and counter bodies. Equalization calculations are conducted on these spectra to ascertain the Raman shift of the A_{1g} and E_{2g} modes, in addition to the intensity ratio I_R, as outlined in Section 5.1.1. Consequently, the probabilities of the Raman shift and the intensity ratio of these modes for the specific tribological system can be calculated and are presented in Figure 5.4. Figure 5.4 (a) depicts the probability densities of the ball-on-disc tribosystem, which was lubricated using the MoS_2:Cr film. A comparison of the Raman shifts of the E_{2g} and A_{1g} modes measured on the main body and counter body, reveals that they fall within the same spectral range. This leads to the assumption that the tribological load on the tribological material is comparable for both bodies. In contrast, a discrepancy in the intensity ratio is observed. In most cases, the ratio exceeds 1.5 for the main body, whereas for the counter body, the ratio is typically less than 1.5. The low intensity ratio for the MoS_2:Cr transfer material suggests structural degradation. However, given that the Raman shifts of the E_{2g} and A_{1g} modes are similar, this structural change is likely due to a realignment of the grains and an increase in the proportion of in-plane texture on the counter bodies compared to the main body.
The probability densities for the tribological system with MoS_2:Cu lubrication are illustrated in Figure 5.4 (b). In particular, the Raman shift of the A_{1g} mode exhibits a discrepancy between the main and counter body. Given that the A_{1g} Raman mode is based

on out-of-plane vibration, the disparate Raman shifts observed for these modes may be attributed to the aforementioned cladding effect of Cu and its lubrication properties as a soft metal (compare with Section 2.6.6). Regarding the intensity ratio, a comparable variation is evident in the main and counter bodies, with a ratio most frequently observed between 1.5 and 1.6. Therefore, the MoS_2:Cu grains on the main body have undergone a comparable reorientation to that observed in the grains on the counter body. The broad distributions of the Raman shifts emphasize that the structural changes induced by tribology are subject to local variations.

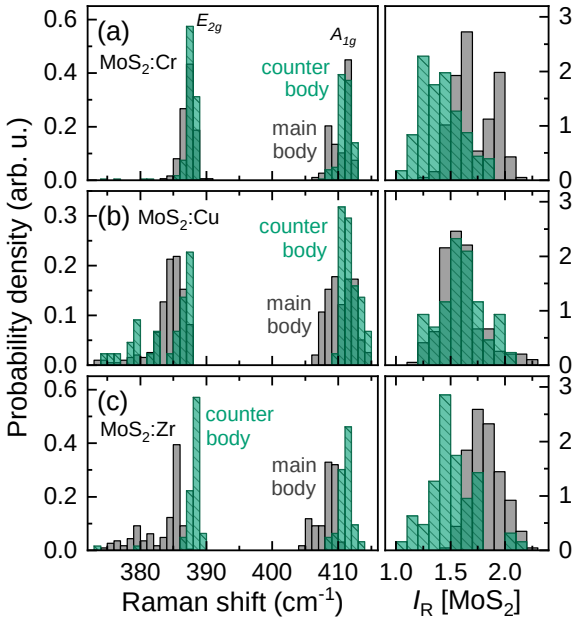


Figure 5.4: The probability densities of the measured Raman shifts of the E_{2g} and A_{1g} modes, as well as their intensity ratio I_R, are presented for the different tribosystems lubricated with either (a) MoS_2:Cr, (b) MoS_2:Cu, or (c) MoS_2:Zr. The probability densities were determined from Raman mappings (at least 150 measuring points each) of the main and counter body surfaces. The results of both bodies are considered separately to facilitate comparison and analysis of the structural differences. The MoS_2:V film is not included in this analysis, as Fe oxides are almost exclusively detectable on the main and counter body. Adapted from [367].

Upon MoS_2 film modification with Zr, a significant discrepancy is observed in the Raman shifts of the E_{2g} mode, as illustrated in Figure 5.4 (c). Since the E_{2g} mode is an in-plane vibrational phonon mode, different tensile stress could be responsible for this discrepancy. As outlined in Section 2.5.1, a sufficiently substantial tensile strain can negate the degeneracy of the E_{2g} mode, thus enabling the distinction between the E^-_{2g} and E^+_{2g} modes. Furthermore, this splitting impacts the peak position, giving rise to the observed shifts. Nevertheless, this behavior is not observable in the transfer material, which may be attributed to the fact that the MoS_2:Zr film has worn out only on the main body in the middle of the tribological contact area, as shown in Figure 5.2 (g). The changes in the intensity ratio on the main body and counter body exhibit a comparable behavior to that observed in the system lubricated with MoS_2:Cr (see Figure 5.4 (a)) and can be explained with the same reasoning.

5.1.2 Strain Distribution in MoS_2 Transfer Material on Counter Bodies

In this Section, only the transfer material of the MoS_2:Cr layer is considered as an example for the MoS_2:X layers (except MoS_2:V). This choice is based on the similarity in the strain distribution within the transfer material across the differnt modification elements, unless the layer is completely removed and only Fe oxides are measurable. A microscopic image of a typical tribological contact area present at the steel counter body is shown in Figure 5.5 (a). The spatial mapping points, defined for the confocal Raman scattering, are indicated by the green squares having an equal distance to each other of 15 µm along both directions. The Raman shifts of the LA, A_{1g} and E_{2g} phonon modes detected at the counter body within the tribological contact area are shown in Figure 5.5 (b)–(d).

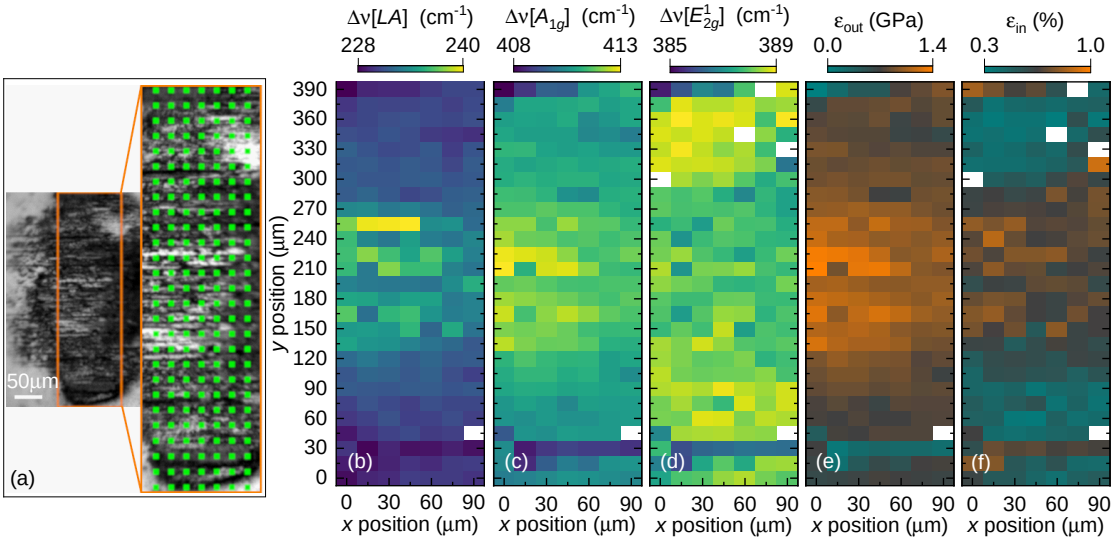


Figure 5.5: In the microscopic image of the tribological contact area on the steel counter body tested against MoS_2:Cr (after 5000 rotations), the mapping area is delineated by an orange frame. The locations at which Raman spectra are recorded during the mapping process are indicated by green squares. The individual MoS_2 signals in a Raman spectra are adjusted through equalization calculations, as illustrated in Figure 5.1 (b). The resulting spatial distribution of the Raman shift of the $LA(M)$ mode is depicted in (b), the $A_{1g}(\Gamma)$ mode in (c), and the $E^1_{2g}(\Gamma)$ mode in (d). As detailed in the main text, the Raman shift of the $A_{1g}(\Gamma)$ (c) and $E^1_{2g}(\Gamma)$ modes (d) can be employed to ascertain the spatial distribution of out-of-plane strains (e) and the distribution of in-plane strains (f). Adapted from [367].

When comparing the spatial position (Figure 5.5 (a)) and the Raman shift of the E_{2g} mode (Figure 5.5 (d)), a slight shift of the Raman peak position to lower frequencies is observed when the measuring point is closer to the center of the contact area. For the A_{1g} and LA mode, an opposite trend in the Raman shift is observed as shown in Figure 5.5 (b) and (c), where the A_{1g} phonon mode is blueshifted by spatially moving into the main/center of the tribologically stressed area. The Raman shift $\Delta\nu$ of a phonon mode is contingent upon the length of the chemical bond, the effective mass, and the coupling strength of the atoms involved in the phonon mode, as elucidated by the Equation 2.17. This shows that pulling the atoms apart lengthens the chemical bonds compared to the relaxed atom positions, resulting in a decrease in the phonon mode frequency, while the coupling strength remains

constant. Conversely, if the atoms in the atomic structure of the transfer material are moved closer together (shortening the chemical bond lengths) due to applied compressive stress the Raman shift grows. Due to the origin of these two modes, the type of induced strain can be further specified, as explained in Section 2.5.1. The blueshift of the out-of-plane (A_{1g}) mode indicates compressive strain ε_{out} along the *c*-axis. In contrast, the redshift of the in-plane E_{2g} mode indicates tensile strain ε_{in} in the *xy*-plane of the transfer material. The magnitude of the compressive or tensile strain can be estimated by comparing it with literature data. It should be noted, however, that in the existing literature, the influence on the Raman shift of the two modes is considered either by compressive or tensile strain, rather than by their superposition. Thus, when pressure is applied along the *c*-axis of the MoS_2 structure, a blueshift/stiffening of the A_{1g} mode with increasing pressure is observed, as well as a significant Raman shift of the E_{2g} mode [218, 589]. In contrast, tensile strain exerts mainly influence on the E_{2g} mode [221, 223] [2]. It is therefore reasonable to initially calculate the compressive strain from the measured Raman shift of the A_{1g} mode by comparison with the existing literature. The observed blueshift of the A_{1g} mode (up to $5.2\,cm^{-1}$) corresponds to approximately (1.4 ± 0.4) GPa compression strain according to the shift rates reported in the literature [218, 589]. The spatial compressive strain distribution is illustrated in Figure 5.5 (e), which shows that the central tribological area of the counter body is subjected to irreversible compressive deformation of the MoS_2 out-of-plane vibrations caused by the greatest pressures in the center of the contact area (see Section 2.6.2). This spatial distribution of the compressive strain is employed to calculate the Raman shift of the E_{2g} mode that would be anticipated if the transfer material were subjected exclusively to compressive deformation. Consequently, at a pressure of $\varepsilon_{out} = (1.4 \pm 0.4)$ GPa, the Raman shift of the E_{2g} mode should be approximately $2.3\,cm^{-1}$. However, a negative displacement of about $-3\,cm^{-1}$ is obseved here. From this, the tensile stress can be calculated. In the literature, different rates for the Raman shift are given as mentioned in Section 2.5.1. For the here preformed calculations, the average of the literature values of $(4.0 \pm 0.8)\,cm^{-1}$ per $\varepsilon_{in} = 1\,\%$ is used. Using this relation the mapping in Figure 5.5 (f) displays weak tensile strain (about 0.3 %) at the edges of the tribological contact, whereas at the center of the probed area the tensile strain rises to 1 %. Furthermore, as explained in Section 2.5.1, the tensile strain breaks the symmetry of the atomic structure in the transfer material, which cancels the degeneracy of the E_{2g} mode and leads to a band splitting into two singlet sub-bands E_{2g}^- and E_{2g}^+ [222, 224, 225]. The aforementioned splitting into two sub-bands is also observed in the center of the contact region, where $\varepsilon_{in} \approx 1\,\%$, in the form of a shoulder at the low-energy flank of the E_{2g} Raman line, which forms the E_{2g}^- subband. This splitting supports the in-plane tensile strain findings.
In addition, the increased separation of the E_{2g} and A_{1g} bands by spatially moving into the center of the tribologically stressed area is always accompanied by a decrease in the intensity ratio $R_I = I[A_{1g}]/I[E_{2g}]$, as shown in Figure 5.6 (c). This leads to the reasonable assumption that the R_I is also influenced by the spatially varying strains. Li et al. also considered the intensity ratio in their pressure experiments on MoS_2 [226]. The values of the intensity ratio are comparable to the ones measured here and also always ≥ 1, which can be explained by the stronger coupling of the A_{1g} mode to the excited d_{z^2} states [218].

[2] For a more detailed explanation of these Raman shifts of the A_{1g} and E_{2g} mode due to compressive or tensile strain, please refer to Section 2.5.1.

But an increase in the intensity ratio was observed with increasing pressure. Here, however, a decrease is observed, which could be because there are strains along the *c*-axis as well as within the *xy*-plane. In addition, Li et al. hardly recorded any data points in their experiments that are within our previously estimated pressure range, and the few data points tend to show a constant trend for pressures below 1.3 GPa. Among other things, Kukucska et al. theoretically investigated the influence of tensile strain on the intensity ratio R_I [227]. As in the measurements here, they observed a decrease in the ratio when the tensile strain increased. Furthermore, the relative change of the intensity ratio also agrees with ours.

5.1.3 Spatial Distribution of Tribochemical Reaction Products

The Raman spectra recorded in the transfer material at the counter body worn against main bodies with MoS_2:X (X = Cu, Cr, Zr) films revealed the presence of Raman signals attributable to MoS_2, as discussed in detail in the previous Sections 5.1.1 and 5.1.2. Furthermore, these Raman spectra frequently exhibit Raman signals that can be attributed to Mo and S oxides, as illustrated in Figure 5.6 (a) and (b). In particular, in the spectral range from about 700 cm^{-1} to about 1000 cm^{-1} Raman signals or broad Raman bands are recorded, which can be assigned to Mo_4O_{11}, a sub-oxide (Magnéli phase) of the stoichiometric MoO_3 [463, 590, 591, 592]. In addition to these Mo_4O_{11} signals, the O–S–O symmetric bending and S–O stretching modes are frequently measurable at 645 cm^{-1} and 926 cm^{-1} [593], respectively, as illustrated in Figure 5.6 (b). Equalization calculations are carried out to analyze the spatial distribution of the Mo and S oxides at the tribological contact area of the counter body. Thereby, a broad Gaussian function was selected to fit the Mo_4O_{11} signals, while a narrower Gaussian function was employed to fit the S–O mode. The spatial distribution of these Mo and S oxides, based on the calculated intensities, is shown in Figures 5.6 (d) and (e). These Figures present the distribution of the oxides in the transfer material of the steel ball run against the MoS_2:Cr film, as shown in Figure 5.5 (a). The spatial distributions indicate a weakening in Mo and S oxide signal intensity from the edge to the center.
The formation of Mo_4O_{11} is likely a thermally induced process, as heating of a MoS_2 crystal or a MoS_2 lubrication film in an oxygen-rich atmosphere results in the formation of various molybdenum oxides [594, 595]. Above certain temperatures in air (330 °C to 400 °C [594, 596, 597, 598, 599]), oxidation of the layer occurs more frequently. Regarding the formation of Mo_4O_{11}, it is astonishing that only Mo_4O_{11} can be identified and not other oxides such as simple ones like MoO_2 or MoO_3, or complex ones like Mo_8O_{23} or Mo_9O_{26}. For an explanation, a thermodynamic consideration seems to be helpful. The formation of Mo_4O_{11} has a Gibbs energy of formation of $\Delta_f G^0 = -2523.1$kJ/mol and is thus significantly lower than Gibbs formation energies of MoO_2 ($\Delta_f G^0 = -532.1$kJ/mol) or MoO_3 ($\Delta_f G^0 = -667.5$kJ/mol) [600]. Thus, from a thermodynamic point of view, the formation of Mo_4O_{11} is more likely than MoO_2 or MoO_3. Following this reasoning, Mo_4O_{11} should nevertheless not be formed, since Mo_8O_{23} ($\Delta_f G^0 = -5221.9$kJ/mol) and Mo_9O_{26} ($\Delta_f G^0 = -5866.5$kJ/mol) [600] have an even lower Gibbs energy. However, these large oxide structures are not detected. This phenomenon may be attributed to the kinetic inhibition and tribomechanical instability of even higher oxygen states (like Mo_8O_{23} or Mo_9O_{26}), due to their large spatial dimensions. Alternatively, the temperature in the tribological contact

may be insufficient to form this comparatively large oxide structure or a low concentration of oxygen in the contact area may lead to the development of a substoichiometric phase of Mo_4O_{11}, Mo_8O_{23}, or Mo_9O_{26}, as reflected in the Mo–O phase diagram [601, 602]. It is anticipated that the formation of Mo_4O_{11}, as a Magnéli-phase of MoO_3, will contribute to the maintenance of lubrication, as it also exhibits a layered structure similar to that of MoS_2 or graphite. Moreover, Mo oxides display chemical stability at elevated temperatures, making them a promising candidate for high-temperature solid lubricants [603, 604, 605]. A commercially available mixture of MoS_2 and MoO_3 is already employed in high-temperature applications [463].

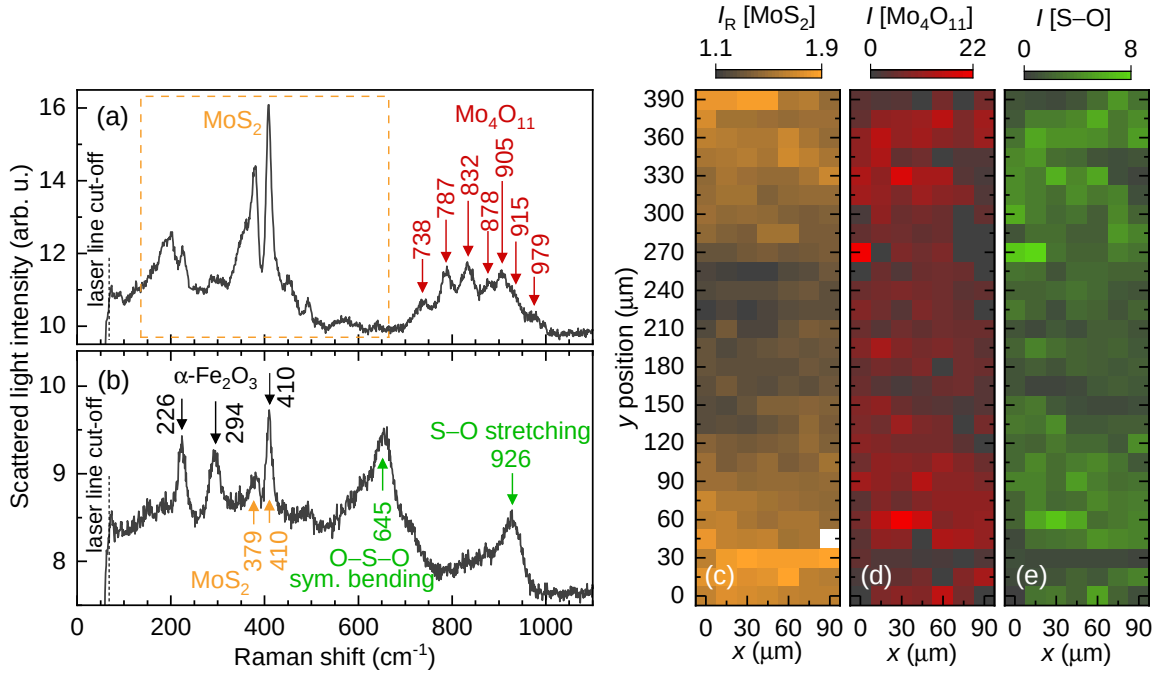


Figure 5.6: Raman spectra shown in (a) and (b) were recorded from the steel counter body worn against MoS_2:Cu and MoS_2:Zr, respectively, highlighting Raman signals related to Mo_4O_{11}, S oxides, MoS_2, and Fe_2O_3. Comparable results were observed for other counter bodies examined with MoS_2:Cr. Raman scattering mappings are presented in (c), (d), and (e), illustrating (c) the intensity ratio $I_R = I(A_{1g})/I(E^1_{2g})$, (d) the integral intensity of the Raman band associated with Mo_4O_{11}, and (e) the intensity of the S–O stretching mode. Adapted from [367].

However, these oxides are mainly found at the edge of the main contact surface. One reason could be that the oxides formed in the main contact area are displaced from it by the tribological process and accumulate at the edge. Another possible explanation would be that the oxygen required for the reaction can reach the edge area more easily since the contact pressure here is significantly lower due to the spherical shape of the ball counter body (see Section 2.6.2). To estimate the local temperatures required to initiate the tribo-oxidation processes, it is necessary to determine the crystallite size of the MoS_2 film, the spatial dimensions of the MoS_2 wear particles, and the temperature. However, this is not the case here, so the local temperature is not estimated. It should also be

noted that, according to current knowledge, Gibbs energy data are only available for gas phases, so no explicit formation mechanism of the S oxide phonon modes can be specified. In addition, a Mo–S–O network has presumably formed due to the tribological contact, which is constantly reorganized and reformed during the ball-on-disc test (mechanical mixing). The S oxide stretching and bending modes of such a Mo–S–O network have yet to be investigated.

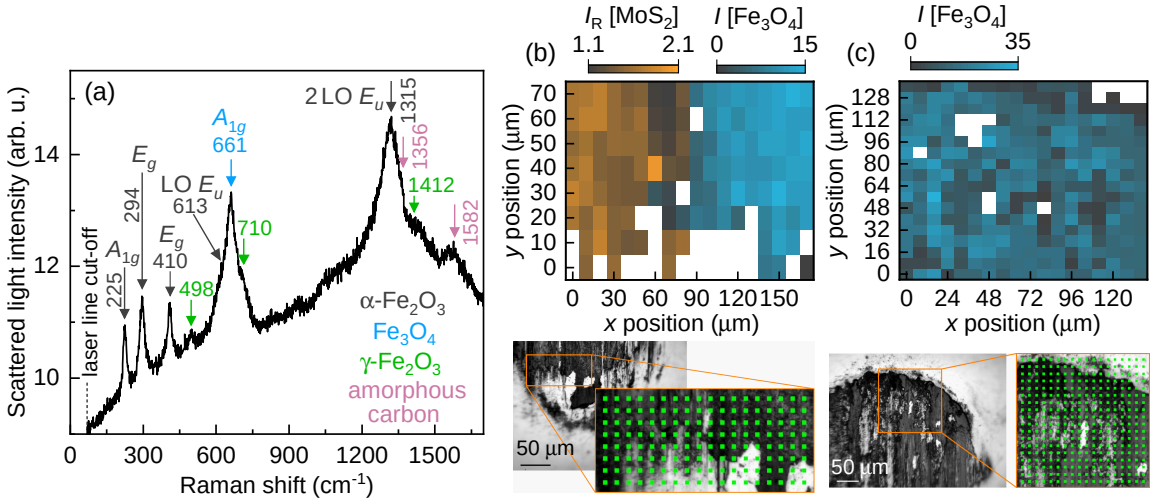


Figure 5.7: The Raman spectra in (a) allow the identification of the Fe oxides α-Fe_2O_3, γ-Fe_2O_3, and Fe_3O_4 based on their Raman signals, particularly in the middle of the tribological contact area on the surface of the counter body, which was worn against a MoS_2:V film. Panels (b) and (c) present microscopic images and Raman scattering mappings of the counter bodies worn against MoS_2:Zr and MoS_2:V, respectively. The intensity of the prominent magnetite Raman peak at approximately 661 cm^{-1}, indicated in (a), is employed as an indicator for oxidized Fe compounds. Adapted from [367].

The Raman spectra, obtained from the counter bodies worn against the MoS_2:X (X=V, Zr) films, revealed the presence of additional Raman signals, as illustrated in Figure 5.7 (a). These signals unambiguously demonstrate the existence of Fe oxides in the contact region of the counter body. In addition to the peak at about 661 cm^{-1}, the peaks at 225, 294, 410, and 1315 cm^{-1} are particularly striking. The latter four peaks seems to originate from hematite (α-Fe_2O_3) and belong to the A_{1g}, E_g, E_g, and $2E_u$ vibrations, respectively [459, 460, 461, 606, 607]. The longitudinal-optical (LO) E_u mode of α-Fe_2O_3 at about 613 cm^{-1} is compared to the previously mentioned modes not so intense. So this mode can not solely explain the observed intense and broad peak at 661 cm^{-1}, there must be another underlying Raman signal. Magnetite Fe_3O_4, another Fe oxide, has a characteristic and intense Raman band at around 667 cm^{-1} [459]. Therefore Fe_3O_4 is identified as the main contributor to this intense and broad peak observed here at 661 cm^{-1}. The additional Raman modes characteristic of magnetite could not be resolved due to their weak and broad nature, so they cannot be distinguished from other Raman signals, ultimately leading to their loss within the noise of the spectral data. For example, the broadening of the peak at 294 cm^{-1} to the higher wavenumber side may be attributed to the presence of an underlying magnetite mode at 308 cm^{-1} [460] and/or a hematite mode at 302 cm^{-1} [461]. Furthermore, weak

signals steaming from maghemite (γ-Fe_2O_3) are detected at 498, 710, and 1412 cm^{-1} [459, 460, 461, 608]. To sum this up, within the contact area of the counter body a mixed phase of Fe oxides can sometimes be identified, mainly consisting of hematite and magnetite.
To analyze the spatial distribution of these Fe oxides, the 661 cm^{-1} magnetite band is fitted by a Gaussian function, and its intensity $I[Fe_3O_4]$ is taken as a measure for the Fe oxides amount. These fitting results are depicted in comparison to the estimated MoS_2 intensity ratio $I[A_{1g}]/[E^1_{2g}]$ in Figure 5.7 (b) and (c). These Raman mappings are taken from the tribological contact areas at the steel balls, which were run against a MoS_x:Zr film, Figure 5.7 (b), or a MoS_x:V film, Figure 5.7 (c). The corresponding spatial Raman mappings are presented as microscope images at the bottom of the panels, with the measurement positions indicated by green squares. As illustrated in Figure 5.7 (b), the intensity ratio exhibits a notable decrease towards the center of the contact area, reaching a point where Fe oxides are measured. Conversely, the intensity of the magnetite 661 cm^{-1} peak demonstrates an increase towards the center of the contact area. The transition from MoS_2 at the edges to Fe_3O_4 in the center of the contact surface is characterized by a transition area of 30 µm width. In this area, the Raman signal signatures of MoS_2 and Fe_3O_4, as well as a combination of both, have been identified, depending on the measurement position. In contrast, no MoS_2 transfer material is detected in the contact surface of the steel ball that has been run against the MoS_2:V film. Instead, the surface of the worn counter body exhibits Raman scattering signals that are solely attributable to Fe oxides. It is noteworthy that no Fe oxides could be identified on the unloaded bare steel ball. Similarly, no Fe oxides are discernible by Raman spectroscopy in regions external to the contact area after tribological loading. Therefore, it can be concluded that the tribological contact induces oxidation and that there are also no thermal diffusion and strain fields over tens of micrometers that would promote the oxidation of steel (AISI 52100).
The formation of Fe oxides within the contact area on the counter bodies can be attributed to direct steel-steel contact, as previously discussed in Section 5.1.1. This direct contact is associated with high thermal and mechanical energies, which provide the energy necessary for the oxidation of the steel surface. In the case of the tribological system lubricated with MoS_2:V, the adsorption and incorporation of water molecules are primarily responsible for the observed tribological behavior, as discussed in Section 2.6.6. Furthermore, the local temperature and stress appear to exert a significant influence on the steel-steel contact, as evidenced by the spatial distribution of MoS_2 and Fe_3O_4 on the MoS_2:Zr counterpart (see Figure 5.7 (i) and (j)) in conjunction with the low wear coefficient (see Figure 5.2 (b)). Following Hertz's contact theory (see Section 2.6.2), the pressure is at its highest in the center of the contact surface. Consequently, the tribological material is subjected to the maximal stress in this area, which increases the probability of loosening. This is confirmed by the micrometer-resolved observation of Fe oxides in the center of the contact, while MoS_2 transfer material is agglomerated at the edges.
The formation of the various Fe oxides is governed by several phase transformations, which are frequently driven by thermal energy. The thermal transformation from magnetite and maghemite to hematite requires a temperature exceeding a specific threshold. The literature reports a wide range of transformation temperatures (370 °C to 600 °C), suggesting that the mechanism of thermal transformation may depend on the crystal size [609]. Furthermore, the oxygen partial and applied pressure have been identified as influencing factors in the transformation process [610, 611]. The number of unknown parameters (local tem-

peratures, contact pressure at the asperities, oxygen partial pressure within the tribological loaded area) is too great for a detailed analysis of the phase transformation. However, the observed mixed phase may indicate that the local temperature was below 370 °C, which could have resulted in a portion of the magnetite transforming to hematite. Additionally, the spatially varying parameters (local temperatures, contact pressure at the asperities, oxygen partial pressure within the tribological loaded area) within the tribological area, which induce local structural strain and lead to spontaneous nucleation, may also explain the mixed phase [609]. Moreover, the Raman spectra reveal the absence of Raman signals characteristic of zirconium oxides. This may be attributed to the potential broadening and overlapping of the Raman lines of ZrO_2 by those of MoS_2 and Fe oxides. Moreover, no evidence of oxidation of the other modification elements was observed. The low concentration of the modification element in the MoS_2:X layer (20 at. %) may be a factor in the lack of observed oxidation. Alternatively, the amount formed is potentially below the detection limit of the Raman spectrometer employed.

5.1.4 Tribological Induction of Few-Layer Graphene: Structural Characterization and Spatial Distribution

Apart from the formation of S and Mo oxides driven by tribological processes, another self-lubrication effect is associated with the development of amorphous carbon (a-C) and, particularly, few-layer graphene on the surfaces of the steel counter bodies. In the Raman spectra shown in Figure 5.7 (a) within the spectral range of 1000 cm^{-1} to 1800 cm^{-1} two broad signals at about 1356 cm^{-1} and 1582 cm^{-1} can be detected or a broad background is present under the hematite peak at 1315 cm^{-1} accompanied by a broad peak at about 1582 cm^{-1}. These signatures are identified as the D- and G-peak of sp^2 hybridized a-C with a low fraction of sp^3 hybridized carbon bondings. The presence of a-C may be attributed to adventitious contamination with hydrocarbons present in the ambient atmosphere on the MoS_2:X coating or the steel substrate [612, 613, 614], which has resulted in the formation of an a-C structure during tribological contact. Additionally, the release of carbon atoms from the steel substrate could also elucidate or contribute to the formation of the a-C structure, as the tribological contact results in wear of the MoS_2:X lubricating film maybe along with the release of carbon atoms from the bare steel surface. Nonetheless, further research is required to determine the precise mechanism behind a-C formation.
Moreover, at some sample positions of the counter bodies of the Cr-modified MoS_2 films, sharp D- (1356 cm^{-1}) and G-peaks (1587 cm^{-1}) are observed, as well as the D'- (1628 cm^{-1}) and 2D-peak (2600 cm^{-1}-2800 cm^{-1}). Figure 5.8 (a) shows exemplary two spectra recorded in a spatial Raman mapping on a MoS_2:Cr counter body. The positions where these spectra are taken are marked with circles in the microscopic image in Figure 5.8 (b). Thereby, the color correspond with the color in (a) and (c). Analysing the intensity by Voigt function fittings, the spectrum depicted in blue shows a 2.2-fold intensity of the G-peak, compared to the G-peak intensity of the red spectrum. Whereas the intensity of the D-peak has only slightly increased by a factor of 1.3. These sharp and intense peaks indicate the surprising formation of defective nanocrystalline graphite.
Furthermore, a splitting of the 2D band is observed. Figure 5.8 (c) shows two spectra taken directly next to each other (3 µm distance; marked positions in Figure 5.8 (b)), which show a 2D band splitting of $\Delta_{2D} = 36\,cm^{-1}$ and $\Delta_{2D} = 39\,cm^{-1}$, respectively. Thereby the $2D_1$-

and $2D_2$-peaks are evaluated from Voigt function fittings; see dashed lines in Figure 5.8 (c). In addition the larger splitting seems to be associated with an increased intensity of in particular the G-peak.

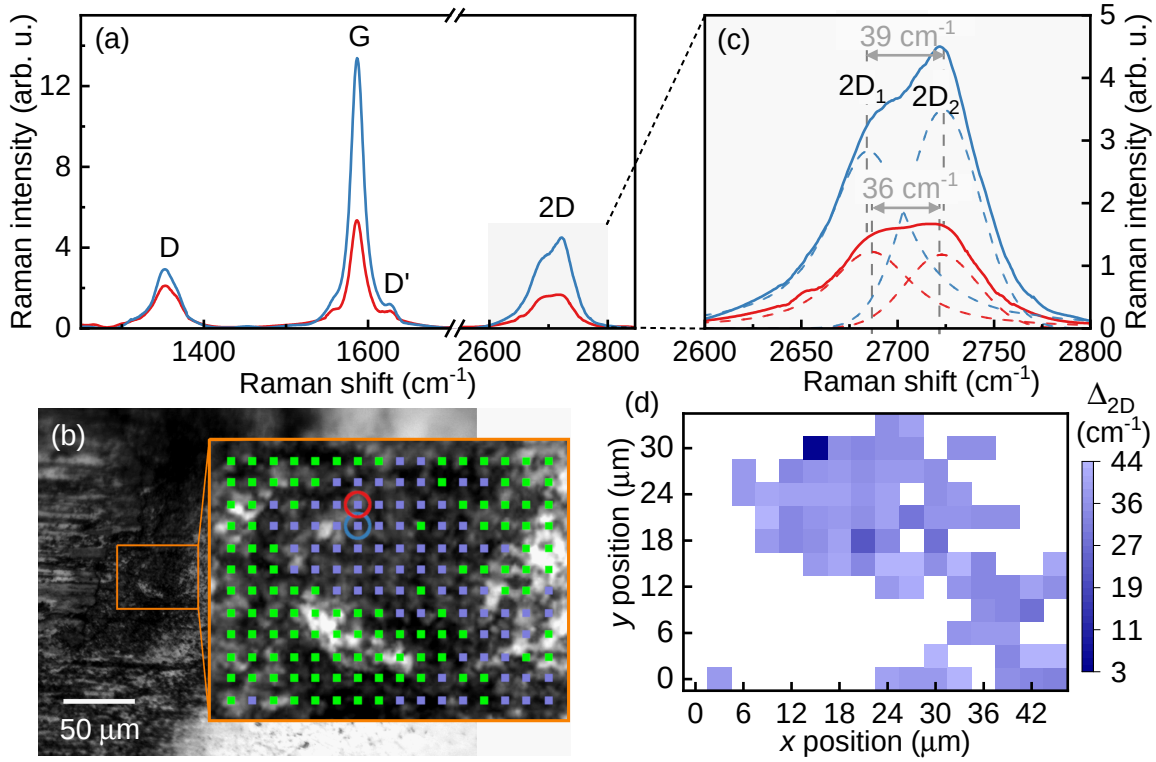


Figure 5.8: Raman spectra were collected from the tribological contact area on the counter body (ball) after conducting a ball-on-disc tribometer test that employed MoS_2:Cr as a lubricant, allowing for the identification of few-layer graphene. Panel (b) shows the scanned Raman mapping area, performed with a step size of 3 µm and a microscope at 20× magnification. The colored squares denote measurement locations, with blue squares indicating positions where few-layer graphene was detected. The measurement positions of the spectra shown in Figure (a) are marked with corresponding colored circles. The spectra reveal a 2D band splitting (c), and its spatial distribution within the mapping (b) is depicted in panel (d). Reproduced from [367].

The existing literature identifies three potential mechanisms for such 2D band splitting. One possible mechanism involves the application of a voltage to graphene. This possibility can be immediately excluded in the present context. Another mechanism is strain, which influences the size and shape of the Brillouin zone and thus enables the 2D band splitting [615]. An alternative explanation is the formation of a few graphene layers, which allows for various resonance processes of the phonons involved in the 2D band, resulting in a slight splitting of the 2D band, with the G-peak remaining unsplit [616]. However, the introduction of strain (or voltage) should also result in a notable splitting of the G-peak, which is not observed. Therefore, it can be assumed that multiple graphene layers have formed within the ball-on-disc tribological contact on the steel ball surface. Further insights into the formation of these graphene layers are gained by a spatially resolved Raman mapping, as illustrated in the microscopic image in Figure 5.8 (b). This mapping was performed on a counter body, which

has been run against a Cr-modified MoS_2 film. In all Raman spectra, the $2D_1$ and $2D_2$-peaks were fitted with two Voigt functions. The fit results allow for a more detailed analysis of the spatial distribution of Δ_{2D}, as illustrated in Figure 5.8 (d). The observable splitting ranges from $\Delta_{2D} = 2.7\,\mathrm{cm}^{-1}$ to $\Delta_{2D} = 43.8\,\mathrm{cm}^{-1}$, comparable to the findings reported in Ref. [616]. Nevertheless, in Ref. [616], the lowest splitting observed for two-layer graphene is $(19.0\pm1.5)\,\mathrm{cm}^{-1}$. Therefore, the value of $2.7\,\mathrm{cm}^{-1}$, calculated only once here, is presumed to be attributed to the fit model and can be interpreted as indicative of a one-layer graphene. The mean value for the 2D splitting is $\Delta_{2D} = (35.9\pm5.3)\,\mathrm{cm}^{-1}$. This observed value range is situated between the values for six-layer graphene $(28\pm2)\,\mathrm{cm}^{-1}$ and the splitting in HOPG $(44\pm2)\,\mathrm{cm}^{-1}$ [616]. Based on this and a comparison of the spectra shape with that presented in Ref. [617], it can be inferred that the formation of between six and 23 graphene layers is likely. Furthermore, the significant increase in the intensity of the G-peak can be attributed to more graphene layers [617]. As previously hypothesized, the requisite carbon for the tribologically induced formation of an initially amorphous carbon network is presumed to originate either from the steel of the main and/or counter body or from contamination with hydrocarbons. During the tribological contact, a highly ordered carbon structure is formed on the MoS_2:Cr counter body in the form of few-layer graphene flakes. The formation of this highly ordered structure on the MoS_2:Cr counterpart is presumed to be enabled by the low coefficient of friction and low wear. Therefore, the formation of an increasingly ordered structure is not disrupted by excessive thermomechanical energy input, resulting in the self-formation of multilayer graphene. In contrast, the tribosystem lubricated with the MoS_2:V film exhibits significantly elevated friction and wear, which impedes the formation of a carbon network. Instead, the predominant outcome is the formation of Fe oxides, which are detectable under these harsh tribological conditions. It would be beneficial for future studies to investigate further the thermal and mechanical energies required for graphene formation, as well as the presumed advantageous tribological influence of these few-layer graphene flakes. Furthermore, the local formation of these few-layer graphene flakes may be facilitated by the segregation of carbon in these areas. As outlined in Section 2.6.5, this segregation can occur during the production of the steel ball, resulting in the accumulation of carbon atoms, which may subsequently form an ordered carbon structure within the tribological contact.

5.1.5 Conclusion

During tribological contact between a main body coated with MoS_2:X and an uncoated counter body (case-hardened steel (AISI 52100)), material transfer to the latter was observed. The transfer material and the wear track on the main body were then subjected to spatial analysis using confocal Raman scattering spectroscopy. The measured Raman frequency shifts of the E_{2g} and A_{1g} modes indicate a spatial-dependent stress distribution, as illustrated in Figure 5.9. This demonstrates that both compressive and tensile strains during the tribological test are most significant at the center of the contact surface and that residual strains remain in the transfer material even after the tribological test. Therefore, a maximum relative compressive strain of $\varepsilon_{\mathrm{out}} = (1,4 \pm 0,4)\,\mathrm{GPa}$ is measured, along with a relative tensile strain variation between $\varepsilon_{\mathrm{in}} = 0.3\,\%$ and $1\,\%$. Moreover, the lower intensity ratio of these two modes observed in the center of the contact region, particularly in the transfer material of the MoS_2:(Zr, Cr) lubricated systems, indicates a reorientation of

MoS_2 grains from an out-of-plane to an in-plane orientation. The Raman shifts of the A_{1g} mode are particularly noteworthy when examining the Cu-modified MoS_2:Cu layer, as this mode is more disturbed on the main body than on the counter body. This disturbance of the out-of-plane vibration may be attributed to the cladding effect observed in Cu and its weak shear strength, both of which are more pronounced in the PVD-synthesised coating compared to the corresponding transfer material.

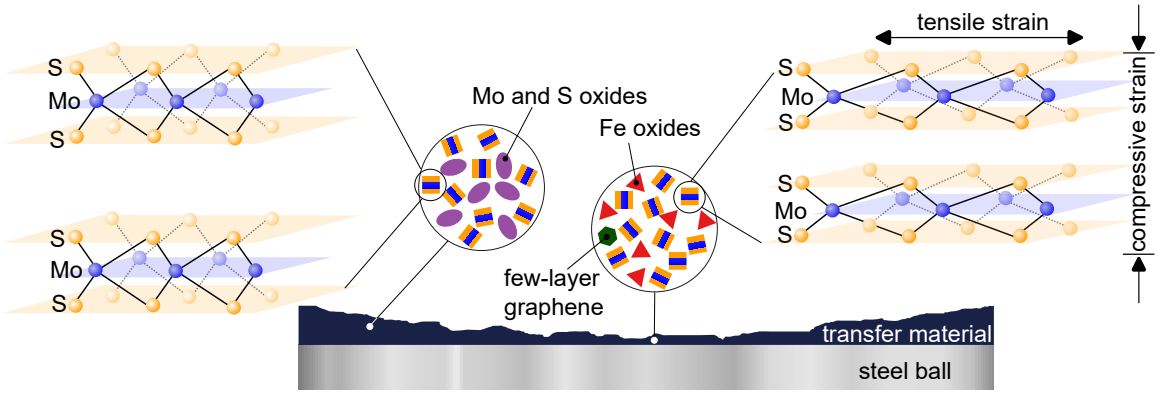


Figure 5.9: The schematic shows the distribution of structural changes and chemical compounds formed due to tribological contact in the MoS_2:X transfer material on the steel (AISI 52100) counter body. It highlights the strain distribution within the MoS_2 structure, as well as the locations of Mo, S, and Fe oxides and few-layer graphene produced during tribological testing. Reproduced from [367].

Furthermore, the formation of tribochemically induced compounds, including Mo-, S-, and Fe-oxides, was observed. The formation of these compounds is dependent on the modifying element. It is noteworthy that the oxidation of the modifying element itself was not detected. The formation of Mo and S oxides was almost independent of the modifying element, with the greatest concentration occurring at the edges of the tribological track (see Figure 5.9). However, these oxides were not identified on the main body with the MoS_2:Cu film. In contrast, Fe oxides (Fe_3O_4, α-, and γ-Fe_2O_3) were identified, particularly in the MoS_2:V system and to a lesser extent in the MoS_2:Zr system, within the tribological traces on the main and counter bodies. The presence of Fe oxides indicates the absence of the MoS_2:X layer and transfer material in the contact area, characterized by a steel-steel contact with high wear and friction. The deterioration of the lubricating properties can be attributed to the modification with V, which has a high affinity for water and results in the formation of brittle wear particles. In contrast, the tribological properties of the other modified MoS_2:X coatings are enhanced by the modification in comparison to the unmodified MoS_2 coating. These improved properties are likely attributable to a densification of the microstructure and the formation of a (002) basal-plane orientation. Notably, MoS_2:Cu exhibited the best tribological performance, which can be attributed to Cu-enriched clusters on the surface, the self-lubricating effect of Cu, and an increased cohesion between crystallites.
Moreover, the formation of a few graphene layers within the tribological track in the MoS_2:Cr (and W) tribosystems is observed by measuring sharp D-, G-, and 2D-peaks. Based on the 2D band splitting, the number of graphene layers can be estimated to vary between six and 23 layers.

Raman spectroscopy can elucidate the structural and chemical characteristics of element-modified MoS_2:X layers, facilitating the microscopic investigation of tribological behavior associated with material transfer and failure prediction. This approach can help optimize MoS_2-based lubricants for various industrial applications.

5.2 Determining the Thickness of Coatings on Geometrically Curved Surfaces Via Ablation-Raman Coating Thickness Analysis

In a variety of technical applications, components are frequently coated with protective layers for the dual purpose of protecting against wear and corrosion, while also reducing friction [73, 74, 75, 76]. The utilization of coatings has been demonstrated to enhance the functionality, durability, and overall efficiency of machine parts, with the thickness of the coating layer being a critical factor [77, 78, 79, 80]. In addition to their role in tribology, coating thickness plays a pivotal role in numerous other fields. To illustrate, in the context of lacquer or paint applications, the thickness of the coating exerts a direct influence on properties such as opacity, gloss, and long-term durability [94, 95, 96]. Similarly, in the field of microelectronics, the thickness of semiconductor films is of great consequence, as it has a significant impact on the electrical characteristics and performance of electronic components [618, 619]. Nevertheless, in the context of medical applications, for example, in the production of coated implants or coatings for medical devices, the layer thickness is also of significance to ensure the biocompatibility and functionality of the materials [87, 88, 89, 90, 91]. Moreover, the coating thickness is of great importance in optics, where optical coatings are utilized to enhance light transmission or reflection properties in devices such as filters and lenses [92, 93]. These examples illustrate the necessity of measuring coating thickness in a multitude of applications, where it is essential to guarantee not only performance and reliability but also safety and cost-effectiveness across various industries. The implementation of accurate measurement techniques is of paramount importance to achieve the desired properties and to guarantee that products meet the necessary specifications and regulatory requirements.

The thickness of thin coatings deposited on a steel substrate for tribological applications is typically determined by a cross-sectional analysis of the fracture surface. The process begins by preparing the cross-sectional area, which is then analyzed using a scanning electron microscope (SEM), offering high-resolution images of the structure. Furthermore, energy-dispersive X-ray spectroscopy (EDX) can be utilized to examine the chemical composition of the layers [72, 82, 83]. However, this technique damages the sample, and preparing cross-sections of curved geometries may present challenges that impede analysis. For thin layers, a high-resolution scanning electron microscope (SEM) or transmission electron microscopy (TEM) is essential to achieve accurate measurements. Another frequently employed method in tribological research for the determination of coating thickness is the calotte grinding method (CALO). This method entails the creation of a small, circular indentation, or calotte, in the coating, followed by subsequent analysis using an optical microscope [85, 86]. Nevertheless, its effectiveness hinges on the presence of a distinct optical contrast between the coating and substrate. It is most suited to flat surfaces or surfaces exhibiting only slight curvature. Consequently, the method is not applicable to components with

curved geometries. In contrast, non-destructive X-ray fluorescence analysis (XRF) provides an alternative method for measuring coating thickness and assessing material composition. This method is dependent on the intensity of the emitted fluorescence to determine coating thickness, thereby necessitating detailed knowledge of the various material characteristics, including absorption coefficients [620, 621]. It is of the utmost importance to conduct thorough calibration, particularly in cases where multi-material coating systems are involved. Additionally, strict adherence to safety protocols is imperative due to the potential risks associated with X-ray radiation. This frequently restricts the dimensions of the sample that can be analyzed, as they must be contained within protective enclosures. An alternative approach utilizes terahertz radiation, which permits non-destructive measurement of coating thickness across a variety of materials, including paints, plastics, and ceramics [622, 623]. This technology can create a three-dimensional profile of the depth of the coating layers. However, this method is not applicable to metallic samples, as these materials reflect terahertz radiation. Lastly mentioned here, ellipsometry represents another non-destructive measurement technique for measuring the coating thickness [624, 625]. For ellipsometry to be an effective technique, it is essential to characterize the optical constants of the materials involved. Furthermore, using a substrate that is not too strongly curved is necessary to obtain reliable data. Additionally, the simulation of a suitable layer model, particularly with metallic substrates, can prove to be challenging due to the inherent difficulties in accurately representing the optical properties of these materials.

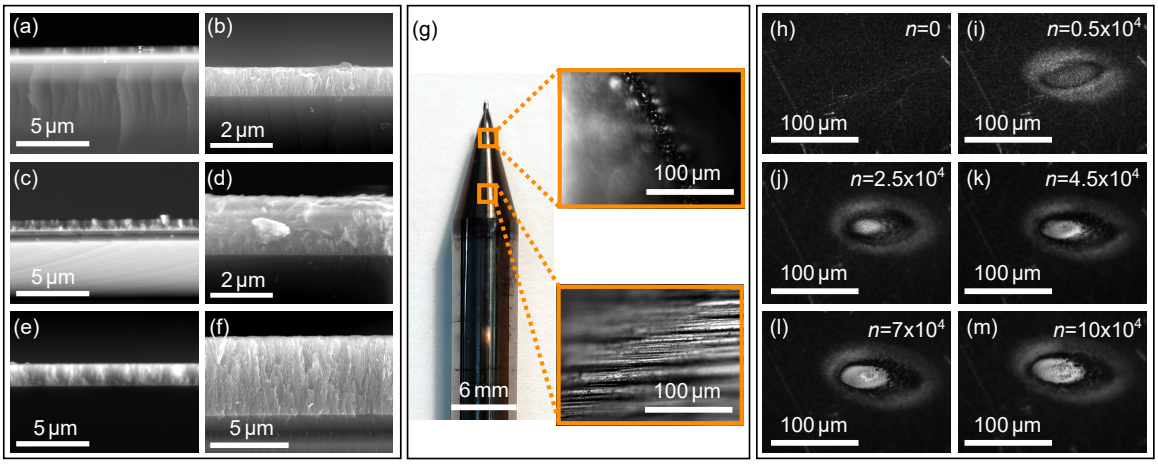


Figure 5.10: SEM images were used to measure the thicknesses of MoS_2 coatings on a Si wafer, revealing values of (a) (0.512 ± 0.025) µm, (b) (0.925 ± 0.025) µm, (c) (1.104 ± 0.035) µm, (d) (1.735 ± 0.050) µm, (e) (1.792 ± 0.050) µm, and (f) (4.987 ± 0.023) µm. These layers are utilized for calibrating the ARCTA experiment, which allows for measuring coating thicknesses on curved surfaces, such as a micro-milling cutter shown in (g). Areas chosen for ARCTA measurements do not affect the tool's functionality (marked by orange squares). The MoS_2 coating is gradually ablated with the high-energy laser as the number of pulses increases, as demonstrated in microscope images (h) to (m) for a 5 µm thick MoS_2 coating on a Si wafer.

To sum up, a variety of techniques are currently available for measuring coating thickness, each with its respective strengths and limitations. However, the majority of these techniques encounter difficulties when attempting to ascertain the layer thickness of tribological coat-

ings on metallic materials with curved geometries, such as those observed in drills or milling cutters. The method presented here, ablation-Raman coating thickness analysis (ARCTA), offers a promising alternative, as it is considered minimal-invasiv due to the measurements being taken adjacent to the tribological active surface, thereby avoiding any impairment of the coating's functionality. The ARCTA is based on a two-beam laser excitation, as described in more detail in Section 3.2.2. Here, MoS_2 PVD coatings are considered, and the synthesis process of these coatings is described in Section 3.2.1. By calibrating the laser ablation in the number of pulses and thickness in conjunction with an alternative method for determining the layer thickness (here SEM cross-section analysis), the thicknesses of surface layers with curved geometries or inaccessible areas for conventional methods can be analyzed. The coating thicknesses determined during the SEM examination of the cross-sectional area of the deposited MoS_2 coatings on the Si wafers are presented in the SEM images in Figure 5.10 (a) to (f). A total of three such SEM measurements are taken from the cross-sectional area of each coating to determine an average thickness. To calibrate the relationship between the number of laser pulses required until the surface coating has been deposited and the coating thickness, it is first necessary to consider flat Si wafers coated with MoS_2. Once the ARCTA setup has been calibrated for these MoS_2 coatings, the MoS_2 coating thickness can be determined on components with more curved geometry, such as micro-milling cutters, as illustrated in Figure 5.10 (g). The coating thickness can be measured at positions indicated by orange squares in Figure 5.10 (g), which have been coated but are not relevant to the functionality of the micro-milling cutter, which is located at the very top.

5.2.1 Laser Ablation Series of MoS_2 Layers on Si Wafers for Calibration of the ARCTA Method and Verification on Curved Surfaces

During a laser ablation series, the high power of the pulsed high-energy laser gradually creates/burns a hole/crater in the MoS_2 layer, as illustrated in the microscope images for a MoS_2 coating of 5 µm thickness in Figure 5.10 (h) to (m). Additionally, the microscope images demonstrate that an optical brightening can be observed after the sample is exposed to the high-energy laser for 0.1 s for the first time (see Figure 5.10 (i)). This indicates a structural change, as the optical properties of the sample have altered in this area. Further exposure of the sample to the high-energy laser results in the formation of an increasingly larger bright area in the center of the irradiated area (see Figure 5.10 (j) and (k)). This then gives rise to the formation of another even brighter area, which appears concentrically starting from the center (see Figure 5.10 (l)). Following a defined number of pulses, an optical change is also visible in this area, as illustrated in Figure 5.10 (m). Using the probe laser, a Raman spectrum can be recorded after each exposure of the sample to the pulsed high-energy laser, enabling a comparison between the optical appearance and the measured signals.

However, before illumination of the sample coated with MoS_2 by the pulsed high-energy laser, a Raman spectrum of the initial coating is recorded with the probe laser, as illustrated in Figure 5.11 (a) for a (1.104 ± 0.035) µm thick MoS_2 coating. The Raman spectra of the deposited MoS_2 layer exhibit Raman modes at 178, 220, 245, 293, 376, 403, 450, 544, 564, and 591 cm^{-1}. Given that the Raman modes at 245, 293, and 544 cm^{-1} are not measurable in bulk MoS_2 but are measurable in nanoparticles [205, 209], it can be assumed

that the layer has a nanocrystalline structure in its initial state. The weak Raman mode of MoS_2 at approximately 640 cm^{-1} is not observed. One potential explanation is that the structure of the deposited MoS_2 film may contribute to the broadening of this weak mode, making it indistinguishable from the background. An alternative explanation could be the performance of experiments utilizing non-resonant Raman scattering, which is known to exhibit a reduced number of Raman bands [44]. A Raman spectrum is recorded at the same spatial position on the sample after it has been illuminated by the pulsed high-energy laser for 0.1 s. This process is repeated until the Raman signals of the substrate are discernible to measure the coating thickness. However, a change in the Raman signals is already observed after the initial irradiation of the sample with the high-energy laser. In addition to the markedly weaker Raman signals of MoS_2, Raman signals are also measured at 126, 203, 228, 347, 363, 459, 467, 495, 571, 586, and 744 cm^{-1}. These signals can be assigned to MoO_2 [488, 626, 627]. Consequently, the energy input of the pulsed laser causes not only the ablation of a portion of the MoS_2 layer but also the (partial) oxidation of the remaining layer. As the number of laser pulses, n, increases, the signals of MoS_2 diminish, and only MoO_2 signals are observed (Figure 5.11 (a)).

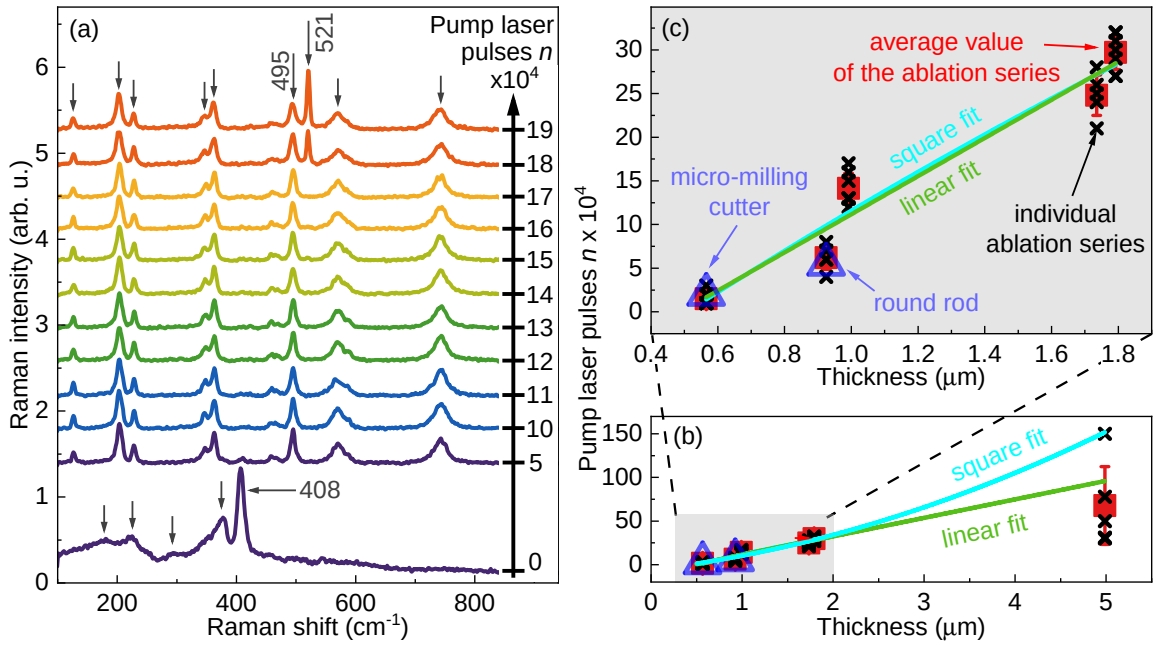


Figure 5.11: (a) Measured Raman spectrum after irradiating the (1.104 ± 0.035) µm thick MoS_2 coating with a number of high-energy laser pulses n (repetition frequency $f = 100$ kHz, peak power $P_{Peak} \approx 115$ W). After $n = 18 \times 10^4$ pulses, the Si-Signal at 521 cm^{-1} from the substrate is measured. At least five such laser ablation series are conducted for each coating thickness under consideration. The number of laser pulses required to measure the substrate signals is plotted against the layer thickness, as illustrated in (b) and (c). The resulting curve can be employed to ascertain the thicknesses of MoS_2 layers, even in the context of intricate geometries such as micro-mills (see Figure 5.10 (g)) or round rods (here with a diameter of 1 cm), indicated by the blue triangles.

Nevertheless, the laser-induced transformation of MoO_2 to MoO_3, as observed in Ref. [488], is not observed here, as Raman signals characteristic of MoO_3, including the intense Raman

signal at approximately $820\,\mathrm{cm}^{-1}$, are not detectable [626, 627, 628]. This is somewhat unexpected, given that, from a thermodynamic perspective, the formation of MoO_3 with a Gibbs energy of formation of $\Delta_f G^0 = -667.5$ kJ/mol is considerably lower than the Gibbs energy of formation of MoO_2 with $\Delta_f G^0 = -532.1$ kJ/mol [600]. This phenomenon may be attributed to the insufficient local temperatures [488] or the inadequate oxygen (O_2) content, which may not have been sufficient for phase transformation [602]. Additionally, the ejected coating atoms may have displaced air molecules, including O_2, reducing the O_2 available for the oxidation reaction.

After irradiating the sample with a certain number of high-energy laser pulses, in addition to the formation of MoO_2, a further Raman signal is observed at approximately $521\,\mathrm{cm}^{-1}$. As illustrated in Figure 5.11 (a), this signal is obtained following the irradiation of the sample with $n = 18 \times 10^4$ laser pulses and can be identified as a Raman signal of the Si wafer [629, 630], which serves as the substrate. Consequently, after $n = 18 \times 10^4$ laser pulses, the initial $(1.104 \pm 0.035)\,\mu\mathrm{m}$ thick MoS_2 coating within the probe laser spot is ablated. Such ARCTA measurements are repeated on MoS_2 layers of varying thicknesses, with a minimum of five measurements performed for each layer thickness. The number of pulses required to measure the substrate signal is plotted against the layer thickness. This yields the curve depicted in Figure 5.11 (b) and (c).

As illustrated in the Figure 5.11 (b) and (c), a precise number of pulses is not always necessary to ablate a MoS_2 layer of a given thickness. In contrast, coatings with a layer thickness under 2 µm show only slight variations in the values. When examining the MoS_2 coating with a thickness of $(4.987 \pm 0.023)\,\mu\mathrm{m}$, a significant increase in the scattering of n is observed, ranging from $n = 30 \times 10^4$ to $n = 150 \times 10^4$ laser pulses. The substantial fluctuations in these values complicate the determination of the layer thickness, presenting a potential limitation for the ARCTA experiments. The slight changes in required high-energy laser pulses can be linked to minimal coating thickness variations; however, these differences are so small that they do not fully explain the significant scattering, particularly for the $(4.987 \pm 0.023)\,\mu\mathrm{m}$ coating. Therefore, the observed fluctuations in n must be attributed to other factors. On the one hand, the spot size of the pulsed high-energy laser significantly impacts the power density, meaning even small changes can alter n. Nonetheless, efforts were made in the experiments to keep the spot size the same. On the other hand, during the 0.1 s exposure to the pulsed high-energy laser, some coating atoms do get ejected, but some of them are redeposited in the affected area. This redeposition, which is uncontrollable, is likely the most significant contributor to the observed scattering of the values.

When the number of high-energy laser pulses required for the ablation of the MoS_2 coating n is plotted against the coating thickness, as shown in Figure 5.11 (b) and (c), a monotonically increasing curve is obtained. This suggests that a linear or quadratic relationship exists between the number of laser pulses and the MoS_2 coating thickness within the considered range. The functions resulting from the fits are shown in Figure 5.11 (b) and (c), using only data points from MoS_2 coatings with a thickness of less than 2 µm. The thicker MoS_2 coating, measuring $(4.987 \pm 0.023)\,\mu\mathrm{m}$, was excluded from the fit due to significantly higher scatter of n. The quadratic function demonstrates a slightly superior correlation with the measured values ($R^2 = 0.9449$) compared to the linear function ($R^2 = 0.9443$). Nevertheless, a comparison of the subsequent curves calculated based on the data points with thicknesses $< 2\,\mu\mathrm{m}$ with the measured values for the approximately 5 µm thick sample reveals that the linear function more accurately represents the calculated mean value. Given

the relatively small difference in the R^2, a linear relationship is assumed.
Additionally, the blue open triangles in Figure 5.11 (b) and (c) illustrate the mean values derived from measurements on curved surfaces, including micro-mills (see Figure 5.10 (g)) and round rods. These values agree with those determined on flat Si wafer samples, thereby confirming the applicability of the ARCTA method presented here for measuring layer thicknesses on curved metallic samples.

5.2.2 Other Coating Systems and the ARCTA Method

Given the considerable scattering of the necessary high-energy laser pulses n to ablate the approximately 5 µm thick MoS_2 layer, a detailed investigation is conducted to ascertain the influence of the repetition frequency and the associated power of the pulsed high-energy laser. Therefore, a high-energy laser with a repetition frequency of 50 kHz is employed, which approximately doubles the power of a single laser pulse to $P_{\mathrm{Peak}} = 230\,\mathrm{W}$. The necessary number of high-energy laser pulses n to ablate a MoS_2 coating of a given thickness is illustrated in Figure 5.12 (a). A comparison of Figure 5.11 (b) (with a repetition frequency of $f = 100\,\mathrm{kHz}$) and Figure 5.12 (a) (with a repetition frequency of $f = 50\,\mathrm{kHz}$) shows a decrease in the average number of pulses from $n = (6.2 \pm 1.3) \times 10^4$ to $n = (1.08 \pm 0.19) \times 10^4$, when a $(0.925 \pm 0.025)\,\mu\mathrm{m}$ thick MoS_2 coating is analyzed. The difference is even more pronounced with a $(1.735 \pm 0.050)\,\mu\mathrm{m}$ [$(4.987 \pm 0.023)\,\mu\mathrm{m}$] thick MoS_2 coating. It was found that with $f = 50\,\mathrm{kHz}$ $n = (1.60 \pm 0.20) \times 10^4$ [$n = (9.4 \pm 2.1) \times 10^4$] high-energy laser pulses were required, whereas $f = 100\,\mathrm{kHz}$ necessitated an average of $n = (24.8 \pm 2.3) \times 10^4$ [$n = (67.8 \pm 44.6) \times 10^4$] high-energy laser pulses. Consequently, a reduction in the repetition frequency or an increase in the power density necessitates a greater quantity of material removal. Nevertheless, this increased material removal results in a diminution of precision and resolution with the ARCTA method, as the discrepancies in coating thickness are not truly discernible at thicknesses of less than 2 µm. However, this increased material removal also signifies that a reduced number of pulses is necessary for thicker layers. Additionally, as a random amount of redepositioned material occurs with each pulse, the resulting scattering of n is comparatively diminished. Consequently, the ARCTA method can also be used to measure thicker coatings, although this requires a higher laser pulse power and results in a reduction in resolution.
Moreover, an alternative substrate may be selected, such as steel. The number of pulses required to ablate the layer is then verified through the measurement of Fe oxide signals or, alternatively, through the absence of Raman signals, given that metals are typically not Raman active. For this reason, Figure 5.12 (b) illustrates an example of a laser ablation series with a repetition frequency of the high-energy laser of $f = 50\,\mathrm{kHz}$ for an about 5 µm thick coating of MoS_2 on a steel substrate (16MnCr5; AISI 5115). As mentioned above, Raman signals of MoS_2 and, after the first few high-energy laser pulses, Raman signals of MoS_2 and MoO_2 are observed. With increasing n the Raman signatures of MoS_2 decrease. Additionally, in this laser ablation series, after $n = 2.5 \times 10^4$ high-energy laser pulses, another Raman signal is identified at approximately $924\,\mathrm{cm}^{-1}$, which is likely derived from the S–O stretching mode [593]. The measurement of this Raman mode suggests that a Mo–O–S network formation. By increasing the number of high-energy laser pulses n to about $n = 8 \times 10^4$, the Mo signals are almost eliminated and only S–O stretching mode Raman signals are detected. The absence of Mo signals indicates that the original

MoS_2 layer, about 5 µm thick, has been completely removed after $n = 8 \times 10^4$ high-energy laser pulses. In comparison, Figure 5.12 (a) shows that the number of pulses required is consistent with the determined value for MoS_2 coatings on Si wafers, within the stated limits of variation. Therefore, the established relationship between the thickness of MoS_2 films and the number of high-energy laser pulses required for deposition can be generalized to MoS_2 films on other substrate materials. Moreover, the presence of the S–O stretching mode in the absence of Mo oxide signals suggests that during the preparation of the MoS_2 layer on the steel substrate, the S atoms are bound to the substrate surface, potentially with a stronger binding affinity than that of Mo. This may result in a higher deposition probability of Mo atoms than S atoms. Nevertheless, this hypothesis necessitates further investigation through alternative methodologies, given that the high-energy laser induces structural alterations and the observable repositioning effect influences the measurements. Upon further increase in the number of high-energy laser pulses, additional Raman signals that can be attributed to Fe oxides are discerned after $n = 15 \times 10^4$, as illustrated in Figure 5.12 (b). The Raman signals at 225, 294, 410, and 1320 cm^{-1} can be attributed to the A_{1g}, E_g, E_g, and $2E_u$ vibrations of hematite (α-Fe_2O_3) [459, 460, 461]. However, the intense Raman signal at approximately 661 cm^{-1} allows the identification of another Fe oxide, namely magnetite (Fe_3O_4) [459, 460, 461]. The broadening of this Fe_3O_4 A_{1g} Raman mode towards higher wavenumbers may indicate the presence of another Fe oxide, namely maghemite (γ-Fe_2O_3), which exhibits an intense A_{1g} Raman mode at approximately 700 cm^{-1} [459, 460, 461, 608]. This implies that following the application of $n = 15 \times 10^4$ high-energy laser pulses, the S–O layer was also removed, resulting in the oxidation of the steel substrate due to the high thermal energy input.

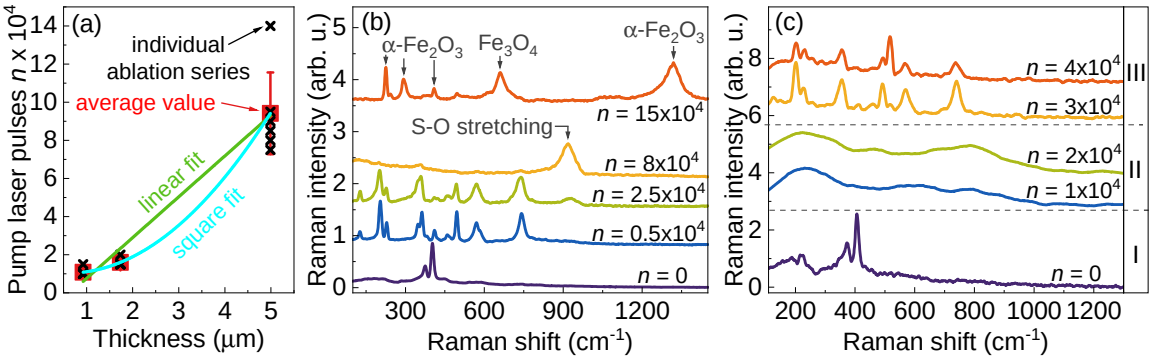


Figure 5.12: The required number of high-energy laser pulses to ablate a MoS_2 coating of a certain thickness, using a repetition frequency of $f = 50$ kHz (power per pulse of about $P_{Peak} \approx 230$ W), is shown in (a). (b) Measured Raman spectrum after irradiating the (4.987 ± 0.023) µm thick MoS_2 coating on a steel substrate with an increasing number of high-energy laser pulses n. Here after $n = 15 \times 10^4$ Fe oxides from the substrate are measured. (c) Raman signals measured in another laser ablation series with a (0.512 ± 0.025) µm thick MoS_2 coating on a TiAlN coating deposited on a Si coated micro-milling cutter. A repetition frequency of $f = 100$ kHz was used to demonstrate the ARCTA method using multilayer systems.

Furthermore, this ARCTA method presented here is not limited to thickness measurements of MoS_2 coatings. Furthermore, this coating thickness analysis method is also applicable to a range of materials. For instance, it has been demonstrated that carbon [631], TiAlN [632,

633], and CrN [634, 635, 636] coatings can be ablated through pulsed high-energy laser light. Still, an investigation of alternative coatings is feasible, provided that the structure or at least its oxides exhibit Raman activity. However, before applying this method to other materials, a calibration process is necessary. As demonstrated for the MoS_2 coating, the calibration establishes a correlation between the number of high-energy laser pulses (n) and the layer thickness.

The analysis of different coatings allows the study of multilayer systems using the ARCTA method, wherein each layer is successively ablated. This approach allows for the determination and evaluation of the thickness of individual layers within a multilayer system. Nevertheless, prior calibration of the ARCTA method for the particular layer materials is necessary. To illustrate this, a laser ablation series for a multilayer system is presented in Figure 5.12 (c). The laser ablation series was performed with a repetition frequency of $f = 100\,\text{kHz}$ on a multilayer system comprising a Si layer, a TiAlN layer, and an approximately 0.5 µm thick MoS_2 layer. These layers were deposited on a micro-milling cutter. As illustrated in Figure 5.12 (c), the Raman spectrum of the initial state ($n = 0$) exhibits the characteristic signatures of MoS_2. Upon first exposure of the coated micro-milling cutter to the high-energy laser for 0.1 s ($n = 1 \times 10^4$), the subsequent Raman spectrum measured with the probe laser exhibits a significantly different shape. This Raman spectrum reveals the presence of TiAlN, as indicated by the broad signals observed at 250, 465, and $780\,\text{cm}^{-1}$ [637, 638, 639]. In contrast, no signals were observed that could be attributed to Mo or S. This indicates that the MoS_2 layer is ablated. The value of $n = 1 \times 10^4$ determined here using the ARCTA method is in agreement with the value of $n = (1.5 \pm 0.6) \times 10^4$ determined on the MoS_2 coatings on the Si wafers for approximately 0.5 µm thick MoS_2 layers (see Figure 5.11 (c)).

When n is raised further, at $n = 3 \times 10^4$ the TiAlN signals disappear and the resulting Raman spectra exhibit the MoO_2 signals, as well as Si signal detected at approximately $520\,\text{cm}^{-1}$ (compare with Section 5.2.1). The intensity of the Si signal becomes even more pronounced with additional laser pulses. Consequently, after $n = 3 \times 10^4$ high-energy laser pulses, the TiAlN layer is also ablated, and the Si signal of the lowest layer is identified. This indicates that $n = 2 \times 10^4$ high-energy laser pulses were necessary to ablate the TiAlN layer. A similar ARCTA experiment could be conducted on the TiAlN layer, as was done on the MoS_2 coating, to estimate the layer thickness of the TiAlN layer based on the number of pulses. Moreover, following the application of $n = 3 \times 10^4$ high-energy laser pulses, the MoO_2 signals are also observed, which were previously discussed in Section 5.2.1 for pure MoS_2 coatings. The presence of MoO_2 can be attributed to the fact that, due to the energy input of the high-energy laser, there is also an accumulation of damage in the entire irradiated area, rather than solely in the center (see spatial investigations of the irradiated area in the next Section 5.2.3). Consequently, the material is also deposited in the vicinity of the probe laser position, which then accumulates randomly in the center. The presence of MoO_2 can therefore be attributed to the redeposition effect. This illustrative series of laser ablation experiments demonstrates that the configuration of the layers, comprising a top layer of MoS_2 (layer I), a middle layer of TiAlN (layer II), and a bottom layer of Si (layer III), as indicated in Figure 5.11 (c), can be verified and quantified using the Raman signals detected on the micro-milling cutter.

5.2.3 Spatial Investigation of the Irradiated Area on the MoS_2 Coating

It is crucial to ensure that the sample laser is positioned at the center of the area irradiated by the high-energy laser when employing this method. This is particularly evident from a Raman mapping of the irradiated area. Figure 5.13 (a) depicts the Raman mapping in a microscope image, with the edge indicated by green squares and the measurement positions, at which a Si signal can be detected, marked with pink squares. The measured Raman spectra are subjected to further analysis by equalization calculations, thereby facilitating observations about the structural alterations in the MoS_2 layer.

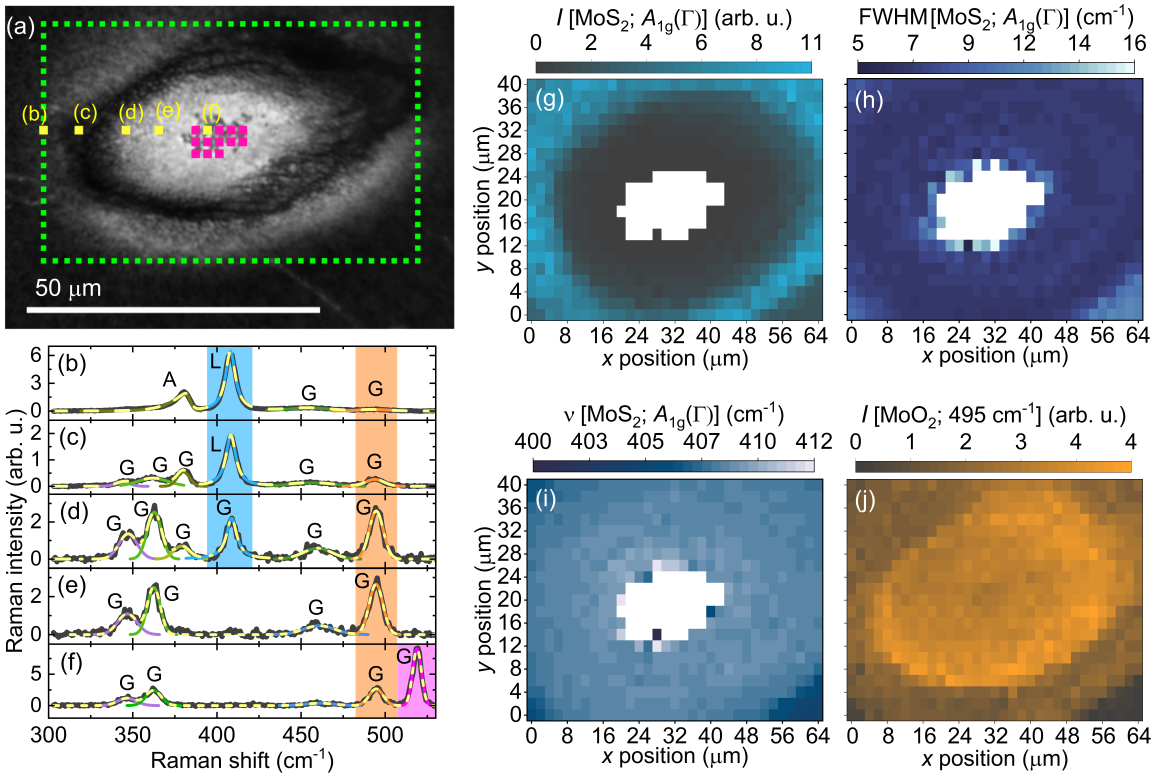


Figure 5.13: The optical microscope image in (a) shows a Raman mapping of a 1.735 µm thick MoS_2 coating on a Si wafer after being irradiated with $n = 25 \times 10^4$ high-energy laser pulses at a frequency of 100 kHz. Green squares outline the mapping edge, while pink squares indicate areas where signals from the Si substrate were detected. Yellow squares mark locations corresponding to spectra shown in (b) to (f), which are analyzed using various fitting functions such as Gaussian (G), Lorentz (L), and Asym2Sig (A). Panels (g), (h), and (i) present parameters regarding the intensity for the $A_{1g}(\Gamma)$ Raman mode of MoS_2. Additionally, the spatial distribution of the MoO_2 Raman mode intensity at approximately 495 cm^{-1} is illustrated in (j). These parameters illustrate a notable dependence on the spatial positions.

Upon examination of the Raman spectra from the periphery to the center of the irradiated area, five distinct types of spectra emerge, as illustrated in Figure 5.13 (b)–(f). The spatial positions at which the individual spectra were measured are indicated in the Raman mapping presented in Figure 5.13 (a). It is noteworthy that only the signals from MoS_2 are discernible in the outer region, where the measurement position (b) is located. Upon

moving into the center, the Raman signals change, resulting in the coexistence of MoS_2 and MoO_2 being observed. This observed coexistence may be attributed to the fact that the MoS_2 layer has only undergone superficial oxidation at this point, with the underlying coating volume remaining intact. This would be feasible in any case, as the penetration depth of the 532 nm probe laser light at normal incidence for MoO_2 is approximately 3.3 µm and for MoS_2 is 36.5 nm, compare with Section 3.1.1. It should be noted, however, that the calculated penetration depths are based on the extinction coefficient of crystalline materials and that the penetration depth of the laser light may deviate for nanocrystalline and/or amorphous materials, as investigated here.
Furthermore, the intensity of the $A_{1g}(\Gamma)$ Raman mode of the MoS_2 structure at about $408\,cm^{-1}$ and its full width at half maximum (FWHM) are also considered concerning the spatial position of the recorded Raman spectrum. As observable in Figure 5.13 (g) and (h), the intensity increases and the mode narrows when moving from the initial MoS_2 coating to the irradiated area (lower right-hand corner in the Raman mappings). The more intense and narrower Raman signals indicate a more crystalline structure. This suggests that the energy input of the high-energy laser results in superficial oxidation and healing of the underlying crystalline MoS_2 structure. Upon further investigation of the center of the irradiated area, it can be observed that the MoO_2 signals exhibited a notable increase in intensity compared to the MoS_2 signals. This phenomenon is observable in the spectra presented in Figure 5.13 (c) and (d), as well as in the spatial distribution of the intensities of the MoS_2 and MoO_2 signals in Figure 5.13 (g) and (j), respectively. Furthermore, the fit function for the A_{1g} mode of MoS_2 has been modified from a Lorentz function ($R^2 = 0.9586$) to a Gaussian function ($R^2 = 0.9597$), as this provides a superior reflection of the data (see Figure 5.13 (d)). Furthermore, this A_{1g} mode exhibits a slight broadening at approximately this distance from the center (see Figure 3(h)), accompanied by a further increase in the Raman shift $\nu[MoS_2;\ A_{1g}]$ (see Figure 5.13 (i)). The observed broadening, change in peak shape (Lorentz $\rightarrow$ Gaussian), and blueshift can be attributed to increasing disorder and local strain within the MoS_2 structure, as discussed in Section 5.1. Moreover, the intensity of the MoS_2 signals diminishes, as evidenced in Figure 5.13 (g), while the intensity of the MoO_2 Raman signals concurrently increases, as illustrated in Figure 5.13 (j). When these two observations are considered together, it can be concluded that the MoO_2 layer, which forms from and on top of the MoS_2 layer, has increased in volume compared to the MoS_2 layer. This phenomenon can be attributed to the Gaussian beam profile of the high-energy laser, which demonstrates an increase in power towards the center. Thus, the energy input is higher towards the center, thereby providing sufficient energy for oxidation.
The MoS_2 Raman signals, recorded at a greater depth, demonstrate a notable blueshift and broadening. The blueshift and broadening increase in magnitude until they ultimately disappear, and only the MoO_2 signals are detected (see Figure 5.13 (e), (h), and (i)). This phenomenon can be attributed to the fact that the residual MoS_2 structure becomes increasingly amorphous towards the center due to the elevated energy input, and is disrupted by strain until it is fully oxidized. Nevertheless, no substrate signals have been identified thus far, which is likely attributable to the fact that the penetration depth of the laser light is considerably less than previously estimated. The Raman measurements performed even further toward the center yield spectra comparable to the spectrum depicted in Figure 5.13 (f), where the Si Raman signal is detected at $521\,cm^{-1}$. Concurrently, the intensity

of the MoO_2 signals diminishes, as evidenced in Figure 5.13 (j). Consequently, the MoO_2 layer is now of such a thickness that the Raman signal of the substrate can be observed through it. As previously outlined, this criterion is chosen to confirm that the layer has undergone ablation.
The entirety of the measured Raman signals, from the exterior to the interior, mirror the progression of the Raman spectra observed in the ARCTA experiments. As the outermost area of the area mapped was not irradiated by the high-energy laser, the initial state of the MoS_2 layer was measured there. This is demonstrated by comparing the spectra in Figure 5.11 (a) at $n = 0$ with the spectrum in Figure 5.13 (b). Subsequently, the Raman signals are measured in the outer area of the irradiated surface after the ARCTA experiments (see Figure 5.13 (c) and (d)), which were initially measured in the center of the irradiated surface at the beginning of the ARCTA experiments (see Figure 5.11 (a) at $n = 5$). The Gaussian beam profile can account for this phenomenon, as the power density of a single laser pulse is lowest in this region, thus inducing minimal changes. However, following the ARCTA experiments, an accumulation of damage is observed in this region, resulting in the measured Raman spectra being comparable to those obtained from the center at the beginning. The same argumentation can be employed to elucidate the parallels between the Raman spectra detected in regions closer to or in the center of the irradiated area (see Figure 5.13 (e) and (f)) and those of the laser ablation series (see Figure 5.11 (a)). This observation demonstrates that the positioning of the probe laser at the center of the high-energy laser spot is of paramount importance for accurate coating thickness measurement.

5.2.4 Conclusion

The novel method, ARCTA, which combines Raman scattering with laser ablation, offers a promising alternative for measuring coating thickness. The ARCTA method employs two-beam laser excitation, enabling the measurement of the coating thickness without compromising its functionality, even on curved surfaces such as micro-milling cutters. The calibration of the laser pulses in terms of the coating thickness is discussed, which creates a method for measuring coatings such as MoS_2, other coatings, or multi-layer systems. However, redeposition effects impair the accuracy. Nevertheless, the results demonstrate the versatility of the ARCTA method and highlight the importance of strict calibration, opening avenues for further coating analyses with this ARCTA method in various industries.

Chapter 6

Outlook

This Chapter shifts the focus from the findings and discussions presented in Chapters 4 and 5 to the remaining open questions. The identified knowledge gaps are outlined alongside proposed directions for future research. For clarity, the recommendations are organized according to the core topics addressed in this thesis.

Hip Implant Taper Junctions:

Chapter 4 focused on investigating the adsorption and denaturation processes of the BCS, as well as the formation of tribomaterial resulting from fretting contact on the pin surfaces. However, the Ti6Al4V cylinder, composed of a different material, presents additional avenues of interest for similar investigations. Variations in hydrophilicity, for instance, may result in distinct interactions with the BCS [1]. Furthermore, tribochemical reaction products unique to the Ti6Al4V surface may emerge. For example, Raman spectroscopy was performed on the surface of the Ti6Al4V cylinder following fretting tests conducted for $n = 5 \times 10^4$ cycles against FeCr18Mn14Mo3CN0.9 or CoCr29Mo6C0.03 pins. The resulting spectra are similar to the spectrum shown in Figure 6.1 (a). The Raman spectrum reveals signals that are absent on any pin surface. Signals at 114, 143, 237, 444, 609, 691, and 801 cm^{-1} presumably originate from amorphous titanium dioxide (TiO_2), which likely forms as a result of the fretting contact [642, 643, 644, 645]. The formation of TiO_2 has potential benefits, such as enhancing wear resistance and reducing friction [645]. Consequently, some studies focus on the superficial oxidation of Ti6Al4V alloys and use it as a technique [643, 646, 647]. Additionally, the oxide formation may serve as a protective barrier, preventing the release of ions from the Ti6Al4V surface [648]. Thus, this TiO_2 formation also influences biocompatibility and corrosion resistance [649, 650, 651]. However, there is also a possibility that

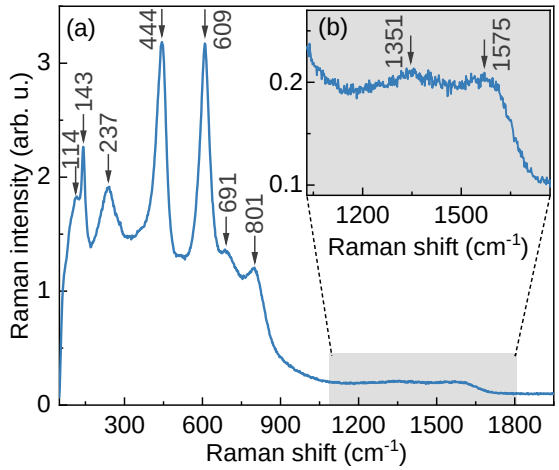


Figure 6.1: Raman spectrum recorded in the fretting track on a Ti6Al4V cylinder after $n = 5 \times 10^4$ fretting cycles in contact with a high-nitrogen steel pin.

[1] According to the literature [640, 641], the contact angle for Ti6Al4V varies between 46.22° and 82.23°, depending on the surface treatment. Such a range indicates that Ti6Al4V is generally considered a hydrophilic material.

TiO_2 could enter the human body, for example, as wear particles. Therefore, it would be interesting to investigate the locations where TiO_2 has formed, its distribution, and the quantity of material entering the human body.
Furthermore, the Raman signals of amorphous carbon, previously discussed in Section 4.3.2, can be measured. The G peak is identified at $1351\,cm^{-1}$ and the D peak at $1575\,cm^{-1}$, as indicated in Figure 6.1 (b). Overall, it is evident that a more thorough analysis of the tribomaterial and the AWP on the cylinder surface could be beneficial. This analysis would help identify additional reaction products, investigate their formation, and assess the extent of material transfer and/or mechanical mixing that may have occurred.
Additional Raman mappings could also provide information into the distribution of chemical-mechanical reaction products on the pin surfaces. Such mappings would be especially beneficial for the high-nitrogen steel pins, as Raman analyses in the FT have been less extensively conducted on these pins compared to the Co-alloy surfaces. Furthermore, detailed investigations of the wear products in the serum could be performed to assess their composition and quantity.
It would also be reasonable to analyze retrieved hip joints to determine whether a CoS_x film is detectable, similar to the findings in the laboratory experiments here. Although comparisons between the wear characteristics and underlying mechanisms of fretting corrosion observed in retrieval studies [380, 381] and those from the test rig run in BCS solution show similarities [382, 384, 385], the contact conditions within the human body may yield different results. Such a discrepancy may arise because the BCS solution does not precisely replicate synovial fluid. Additionally, blood in the fluid during surgery and potential variations in pH value due to illness may further influence a CoS_x film formation.
Based on the results of this thesis, it is also conceivable to carry out fretting tests using materials that are pre-coated with CoS_2. The influence of this coating layer on tribological behavior should be investigated in laboratory experiments. It is also interesting to consider the influence of the CoS_2 layer on the proteins. Furthermore, the effects of CoS_x formation on the cells and, ultimately, its implications for the human body should also be thoroughly examined.

Lubrication with Modified MoS_x:X Thin Films:

In Chapter 5, the MoS_x:X lubricating films and the transfer film were analyzed following tribometer tests. To gain deeper insights, it would be valuable to carry out *in situ* measurements to investigate the structural changes as a function of the load duration. This approach could help identify the timing of oxide formation and determine whether material failure can be predicted from the Raman spectra. Furthermore, the investigations presented here could be extended to explore the effects of other modification element concentrations or other elements. For practical applications, further studies should examine additional contact scenarios, such as rolling contacts, and the overall effectiveness of the lubricant should be evaluated in application trials.

ARCTA:

The ARCTA method for measuring coating thickness, as presented in this thesis (Section 5.2), could be extended to measure a broader range of coating thicknesses. Furthermore, further calibrations will be required to accommodate different applications, enabling the measurement of other materials or the analysis of layered systems. Depending on the samples being analyzed, selecting alternative wavelengths for one or both lasers may prove advantageous.

Bibliography

[1] I. Hutchings, P. Shipway, Introduction, in *Tribology,* 2nd ed., Elsevier, Oxford, UK (2017) 1–5.

[2] P. L. Menezes, M. Nosonovsky, S. V. Kailas, M. R. Lovell, Friction and Wear, in *Tribology for Scientists and Engineers,* Springer, New York, NY, USA (2013) 43–91.

[3] H. Jost, *Lubrication (Tribology): Education and Research - a Report on the Present Position and Industry's Needs,* Her Majesty's Stationery Office, London, UK (1966).

[4] H. Czichos, Tribologische Systeme, in *Tribologie-Handbuch,* Springer Fachmedien, Wiesbaden, Germany (2020) 41–53.

[5] G. Straffelini, Tribological Systems, in *Friction and Wear,* Springer International Publishing, Cham, Switzerland (2015) 237–276.

[6] Chapter 4 Classification of Wear Processes, in *Microstructure and Wear of Materials* (Ed.: K.-H. Z. Gahr), vol. 10, Elsevier, Amsterdam, Netherlands (1987) 80–131.

[7] H. Czichos, Reibung, in *Tribologie-Handbuch,* Springer Fachmedien, Wiesbaden, Germany (2020) 121–154.

[8] V. L. Popov, Das Coulombsche Reibungsgesetz, in *Kontaktmechanik und Reibung,* Springer, Berlin/Heidelberg, Germany (2015) 155–176.

[9] M. Sikorski, The adhesion of metals and factors that influence it, *Wear* **7** (1964) 144–162.

[10] H. Czichos, Verschleiß, in *Tribologie-Handbuch,* Springer Fachmedien, Wiesbaden, Germany (2020) 155–208.

[11] V. L. Popov, Verschleiß, in *Kontaktmechanik und Reibung,* Springer, Berlin/Heidelberg, Germany (2015) 303–320.

[12] T. Quinn, Review of oxidational wear: Part I: The origins of oxidational wear, *Tribol. Int.* **16** (1983) 257–271.

[13] T. Quinn, Oxidational wear modelling: Part II. The general theory of oxidational wear, *Wear* **175** (1994) 199–208.

[14] T. Quinn, Oxidational wear modelling Part III. The effects of speed and elevated temperatures, *Wear* **216** (1998) 262–275.

[15] G. Straffelini, Friction, in *Friction and Wear,* Springer International Publishing, Cham, Switzerland (2015) 21–60.

[16] I. Hutchings, P. Shipway, Friction, in *Tribology,* 2nd ed., Elsevier, Oxford, UK (2017) 37–77.

[17] K. L. Johnson, Thermoelastic contact, in *Contact Mechanics,* Cambridge University Press, Cambridge, UK (1985) 374–396.

[18] M. J. Neale, T. A. Polak, M. Priest, Series Editors' Foreword, in *Wear - Materials, Mechanisms and Practice* (Ed.: G. W. Stachowiak), John Wiley & Sons Ltd, Chichester, UK (2005) XVII.

[19] B. Bhushan, *Nanotribology and Nanomechanics* (Ed.: B. Bhushan), Springer, Berlin, Germany (2008).

[20] C. H. Scholz, Earthquakes and friction laws, *Nature* **391** (1998) 37–42.

[21] H. Czichos, Technik und Tribologie, in *Tribologie-Handbuch,* Springer Fachmedien, Wiesbaden, Germany (2020) 31–39.

[22] A. Neville, M. A., Wear and Chemistry of Lubricants, in *Wear - Materials, Mechanisms and Practice* (Ed.: G. W. Stachowiak), John Wiley & Sons Ltd, Chichester, UK (2005) 71–94.

[23] K. Holmberg, A. Erdemir, Influence of tribology on global energy consumption, costs and emissions, *Friction* **5** (2017) 263–284.

[24] I. P. on Climate Change, *Global Warming of 1.5 °C: An IPCC Special Report on the impacts of global warming of 1.5 °C above pre-industrial levels and related global greenhouse gas emission pathways, in the context of strengthening the global response to the threat of climate change, sustainable development, and efforts to eradicate poverty,* Accessed: 2024-12-10, Intergovernmental Panel on Climate Change, 2018.

[25] J. A. Singh, S. Yu, L. Chen, J. D. Cleveland, Rates of Total Joint Replacement in the United States: Future Projections to 2020-2040 Using the National Inpatient Sample, *J. Rheumatol.* **46** (2019) 1134–1140.

[26] I. Shichman, M. Roof, N. Askew, L. Nherera, J. C. Rozell, T. M. Seyler, R. Schwarzkopf, Projections and epidemiology of primary hip and knee arthroplasty in Medicare patients to 2040-2060, *JB JS Open Access* **8** (2023).

[27] B. Lanting, D. D. Naudie, R. W. McCalden, Clinical Impact of Trunnion Wear After Total Hip Arthroplasty, *JBJS Rev.* **4** (2016).

[28] X. Feng, J. Gu, Y. Zhou, Primary total hip arthroplasty failure: aseptic loosening remains the most common cause of revision, *Am. J. Transl. Res.* **14** (2022) 7080–7089.

[29] Y. Berthier, Third-Body Reality - Consequences and Use of the Third-Body Concept to Solve Friction and Wear Problems, in *Wear - Materials, Mechanisms and Practice* (Ed.: G. W. Stachowiak), John Wiley & Sons Ltd, Chichester, UK (2005) 291–316.

[30] K.-H. Habig, A. Fischer, Tribotechnische Werkstoffe, in *Tribologie-Handbuch,* Springer Fachmedien, Wiesbaden, Germany (2020) 313–446.

[31] K.-H. Habig, T. Mang, Schmierstoffe, in *Tribologie-Handbuch,* Springer Fachmedien, Wiesbaden, Germany (2020) 447–470.

[32] M. Godet, The third-body approach: A mechanical view of wear, *Wear* **100** (1984) 437–452.

[33] P. Heilmann, J. Don, T. Sun, D. Rigney, W. Glaeser, Sliding wear and transfer, *Wear* **91** (1983) 171–190.

[34] A. Fischer, W. Dudzinski, B. Gleising, P. Stemmer, Analyzing Mild- and Ultra-Mild Sliding Wear of Metallic Materials by Transmission Electron Microscopy, in *Advanced Analytical Methods in Tribology* (Eds.: M. Dienwiebel, M.-I. De Barros Bouchet), Springer International Publishing, Cham, Switzerland (2018) 29–59.

[35] A. Fischer, S. Fullam, P. Telouk, M. A. Wimmer, The mechanism-based approach of understanding run-in and steady state: A gross-slip fretting experiment to fathom tribocorrosion of total hip taper junctions, *Biotribology* **25** (2021) 100165.

[36] N. Espallargas, A. Fischer, A. Igual Muñoz, S. Mischler, M. A. Wimmer, In-situ generated tribomaterial in metal/metal contacts: Current understanding and future implications for implants, *Biotribology* **10** (2017) 42–50.

[37] R. Holinski, J. Gänsheimer, A study of the lubricating mechanism of molybdenum disulfide, *Wear* **19** (1972) 329–342.

[38] P. D. Fleischauer, Effects of Crystallite Orientation on Environmental Stability and Lubrication Properties of Sputtered MoS_2Thin Films, *A S L E Transactions* **27** (1984) 82–88.

[39] T. Dieing, O. Hollricher, J. Toporski, eds., *Confocal Raman Microscopy,* Springer, Berlin/Heidelberg, Germany (2011).

[40] E. L. Ivchenko, *Optical Spectroscopy of Semiconductor Nanostructures,* Alpha Science International, Oxford, UK (2005).

[41] M. Cardona, A. Pinczuk, E. Burstein, R. M. Martin, L. M. Falicov, M. H. Klein M. V. Brodsky, *Light Scattering in Solids II* (Eds.: M. Cardona, G. Güntherodt), Springer, Berlin/Heidelberg, Germany (1982).

[42] H. Moldenhauer, M. Bayer, J. Debus, A. Nikolov, A. Brümmer, Raman scattering study of micrometer-sized spots of magnetite and hematite formed at 18CrNiMo7-6 screw rotor surfaces due to liquid-free, unsynchronized operation, *IOP Conf. Ser. Mater. Sci. Eng.* **425** (2018) 012016.

[43] J. Debus, J. J. Schindler, P. Waldkirch, S. Goeke, A. Brümmer, D. Biermann, M. Bayer, Indication of worn WC/C surface locations of a dry-running twin-screw rotor by the oxygen incorporation in tungsten-related Raman modes, *Appl. Phys. Lett.* **109** (2016) 171601.

[44] H. Li, Q. Zhang, C. C. R. Yap, B. K. Tay, T. H. T. Edwin, A. Olivier, D. Baillargeat, From Bulk to Monolayer MoS_2: Evolution of Raman Scattering, *Adv. Funct. Mater.* **22** (2012) 1385–1390.

[45] G. Socrates, *Infrared and Raman Characteristic Group Frequencies,* Wiley, Chichester, UK (2001).

[46] K. Czamara, K. Majzner, M. Z. Pacia, K. Kochan, A. Kaczor, M. Baranska, Raman spectroscopy of lipids: a review, *J. Raman Spectrosc.* **46** (2014) 4–20.

[47] M. Dieterle, G. Weinberg, G. Mestl, Raman spectroscopy of molybdenum oxides Part I. Structural characterization of oxygen defects in MoO_{3-x} by DR UV/VIS, Raman spectroscopy and X-ray diffraction, *Phys. Chem. Chem. Phys.* **4** (2002) 812–821.

[48] Y. Liao, R. Pourzal, M. A. Wimmer, J. J. Jacobs, A. Fischer, L. D. Marks, Graphitic Tribological Layers in Metal-on-Metal Hip Replacements, *Science* **334** (2011) 1687–1690.

[49] Y. Liao, E. Hoffman, M. Wimmer, A. Fischer, J. Jacobs, L. Marks, CoCrMo metal-on-metal hip replacements, *Phys. Chem. Chem. Phys.* **15** (2013) 746–756.

[50] S. Balachandran, Z. Zachariah, A. Fischer, D. Mayweg, M. A. Wimmer, D. Raabe, M. Herbig, Atomic Scale Origin of Metal Ion Release from Hip Implant Taper Junctions, *Adv. Sci.* **7** (2020) 1903008.

[51] M. T. Mathew, P. S. Pai, R. Pourzal, A. Fischer, M. A. Wimmer, Significance of Tribocorrosion in Biomedical Applications: Overview and Current Status, *Adv. Tribol.* **2009** (2009) 1–12.

[52] Y. Berthier, L. Vincent, M. Godet, Velocity accommodation in fretting, *Wear* **125** (1988) 25–38.

[53] C. Greiner, J. Gagel, P. Gumbsch, Solids Under Extreme Shear: Friction-Mediated Subsurface Structural Transformations, *Adv. Mater.* **31** (2019).

[54] C. Haug, F. Ruebeling, A. Kashiwar, P. Gumbsch, C. Kübel, C. Greiner, Early deformation mechanisms in the shear affected region underneath a copper sliding contact, *Nat. Commun.* **11** (2020).

[55] I. Milošev, R. Trebše, S. Kovač, A. Cör, V. Pišot, Survivorship and Retrieval Analysis of Sikomet Metal-on-Metal Total Hip Replacements at a Mean of Seven Years, *J. Bone Joint Surg.* **88** (2006) 1173–1182.

[56] J. J. Jacobs, N. J. Hallab, Loosening and Osteolysis Associated with Metal-on-Metal Bearings: A Local Effect of Metal Hypersensitivity? *J. Bone Joint Surg.* **88** (2006) 1171–1172.

[57] P. F. Lachiewicz, Metal-on-Metal Hip Resurfacing: A Skeptic's View, *Clin. Orthop. Relat. Res.* **465** (2007) 86–91.

[58] C. Donnet, A. Erdemir, Solid Lubricant Coatings: Recent Developments and Future Trends, *Tribol. Lett.* **17** (2004) 389–397.

[59] G. Straffelini, Lubrication and Lubricants, in *Friction and Wear,* Springer International Publishing, Cham, Switzerland (2015) 61–84.

[60] C. Muratore, A. Voevodin, Chameleon Coatings: Adaptive Surfaces to Reduce Friction and Wear in Extreme Environments, *Annu. Rev. Mater. Res.* **39** (2009) 297–324.

[61] T. W. Scharf, S. V. Prasad, Solid lubricants: a review, *Journal of Materials Science* **48** (2012) 511–531.

[62] T. Gradt, T. Schneider, Tribological Performance of MoS_2 Coatings in Various Environments, *Lubricants* **4** (2016) 32.

[63] Z. Chen, X. He, C. Xiao, S. H. Kim, Effect of Humidity on Friction and Wear - A Critical Review, *Lubricants* **6** (2018) 74.

[64] X. Zhang, W. Lauwerens, J. He, J.-P. Celis, Structure and growth of basal and random oriented MoS_x coatings deposited by magnetron sputtering, *J. Vac. Sci. Technol. A* **21** (2003) 416–421.

[65] A. A. Tedstone, D. J. Lewis, P. O'Brien, Synthesis, Properties, and Applications of Transition Metal-Doped Layered Transition Metal Dichalcogenides, *Chem. Mater.* **28** (2016) 1965–1974.

[66] J.-F. Yang, B. Parakash, J. Hardell, Q.-F. Fang, Tribological properties of transition metal di-chalcogenide based lubricant coatings, *Front. Mater. Sci.* **6** (2012) 116–127.

[67] M. H. Cho, The role of transfer film and back transfer behavior on the tribological performance of polyoxymethylene in sliding, *J. Mech. Sci. Technol.* **23** (2009) 2291–2298.

[68] I. L. Singer, Role of third bodies in friction and wear of protective coatings, *J. Vac. Sci. Technol.* **A21 (5)** (2003) 232–241.

[69] A. Neville, M. A., Tribology of Engineered Surfaces, in *Wear - Materials, Mechanisms and Practice* (Ed.: G. W. Stachowiak), John Wiley & Sons Ltd, Chichester, UK (2005) 123–166.

[70] W. Tillmann, A. Wittig, D. Stangier, C.-A. Thomann, H. Moldenhauer, J. Debus, D. Aurich, A. Brümmer, Investigation of the Tribofilm Formation of HiPIMS Sputtered MoS_x Thin Films in Different Environments by Raman Scattering, *Lubricants* **7** (2019) 100.

[71] W. Tillmann, A. Wittig, H. Moldenhauer, C.-A. Thomann, J. Debus, D. Aurich, A. Bruemmer, Nitrogen doping of MoS_x thin films sputtered by reactive High Power Impulse Magnetron Sputtering, *J. Phys. D Appl. Phys.* (2020) 138267.

[72] W. Tillmann, A. Wittig, D. Stangier, H. Moldenhauer, C.-A. Thomann, J. Debus, D. Aurich, A. Bruemmer, Influence of the bias-voltage, the argon pressure and the heating power on the structure and the tribological properties of HiPIMS sputtered MoS_x films, *Surf. Coat. Technol.* **385** (2020) 125358.

[73] A. A. Voevodin, J. S. Zabinski, C. Muratore, Recent advances in hard, tough, and low friction nanocomposite coatings, *Tsinghua Sci. Technol.* **10** (2005) 665–679.

[74] J.-P. Hirvonen, J. Koskinen, J. R. Jervis, M. Nastasi, Present progress in the development of low friction coatings, *Surf. Coat. Technol.* **80** (1996) 139–150.

[75] M. Khadem, O. V. Penkov, H.-K. Yang, D.-E. Kim, Tribology of multilayer coatings for wear reduction: A review, *Friction* **5** (2017) 248–262.

[76] M. F. Montemor, Functional and smart coatings for corrosion protection: A review of recent advances, *Surf. Coat. Technol.* **258** (2014) 17–37.

[77] J. H. W. Siu, L. K. Y. Li, An investigation of the effect of surface roughness and coating thickness on the friction and wear behaviour of a commercial MoS_2–metal coating on AISI 400C steel, *Wear* **237** (2000) 283–287.

[78] K. Holmberg, A. Matthews, H. Ronkainen, Coatings tribology - contact mechanisms and surface design, *Tribol. Int.* **31** (1998) 107–120.

[79] C. Lorenzo-Martin, O. Ajayi, A. Erdemir, G. R. Fenske, R. Wei, Effect of microstructure and thickness on the friction and wear behavior of CrN coatings, *Wear* **302** (2013) 963–971.

[80] Y. Wang, E. J. Terrell, Influence of coating thickness and substrate elasticity on the tribological performance of PEEK coatings, *Wear* **303** (2013) 255–261.

[81] S. Hogmark, S. Jacobson, M. Larsson, Design and evaluation of tribological coatings, *Wear* **246** (2000) 20–33.

[83] W. Tillmann, N. F. Lopes Dias, D. Stangier, C. Schaak, S. Höges, Heat treatment of binder jet printed 17-4 PH stainless steel for subsequent deposition of tribo-functional diamond-like carbon coatings, *Mater. Des.* **213** (2022) 110304.

[84] S. Hogmark, S. Jacobson, P. Hedenqvist, M. Olsson, Tribosurface properties, in *Surface Characterization* (Eds.: D. Brune, R. Hellborg, H. J. Whitlow, O. Hunderi), Wiley-VCH Verlag, Weinheim, Germany (2008) 624–644.

[85] V. Varghese, A. K., M. Ramesh, D. Chakradhar, Investigation on the performance of AlCrN and AlTiN coated cemented carbide inserts during end milling of maraging steel under dry, wet and cryogenic environments, *J. Manuf. Process.* **43** (2019) 136–144.

[86] W. Wu, W. Chen, S. Yang, Y. Lin, S. Zhang, T.-Y. Cho, G. Lee, S.-C. Kwon, Design of AlCrSiN multilayers and nanocomposite coating for HSS cutting tools, *Appl. Surf. Sci.* **351** (2015) 803–810.

[87] H. A. Ching, D. Choudhury, M. J. Nine, N. A. Abu Osman, Effects of surface coating on reducing friction and wear of orthopaedic implants, *Sci. Technol. Adv. Mater.* **15** (2014) 014402.

[88] D. C. Leslie, A. Waterhouse, J. B. Berthet, T. M. Valentin, A. L. Watters, A. Jain, P. Kim, B. D. Hatton, A. Nedder, K. Donovan, E. H. Super, C. Howell, C. P. Johnson, T. L. Vu, D. E. Bolgen, S. Rifai, A. R. Hansen, M. Aizenberg, M. Super, J. Aizenberg, D. E. Ingber, A bioinspired omniphobic surface coating on medical devices prevents thrombosis and biofouling, *Nat. Biotechnol.* **32** (2014) 1134–1140.

[89] M. N. Helmus, D. F. Gibbons, D. Cebon, Biocompatibility: meeting a key functional requirement of next-generation medical devices, *Toxicol. Pathol.* **36** (2008) 70–80.

[90] M. Bosetti, A. Massè, E. Tobin, M. Cannas, Silver coated materials for external fixation devices: in vitro biocompatibility and genotoxicity, *Biomaterials* **23** (2002) 887–892.

[91] R. Junker, A. Dimakis, M. Thoneick, J. A. Jansen, Effects of implant surface coatings and composition on bone integration: a systematic review, *Clin. Oral Implants Res.* **20** (2009) 185–206.

[92] H. A. Macleod, *Thin-film optical filters,* CRC Press, Boca Raton, FL, USA (2017).

[93] F. Samson, Ophthalmic lens coatings, *Surf. Coat. Technol.* **81** (1996) 79–86.

[94] G. Mirschel, O. Savchuk, T. Scherzer, B. Genest, The effect of different gloss levels on in-line monitoring of the thickness of printed layers by NIR spectroscopy, *Anal. Bioanal. Chem.* **404** (2012) 573–583.

[95] R. S. Berns, E. R. de la Rie, The effect of the refractive index of a varnish on the appearance of oil paintings, *Stud. Conserv.* **48** (2003) 251–262.

[96] J. Mallégol, L. Gonon, J. Lemaire, J.-L. Gardette, Long-term behaviour of oil-based varnishes and paints 4. Influence of film thickness on the photooxidation, *Polym. Degrad. Stab.* **72** (2001) 191–197.

[97] J. A. Koningstein, *Introduction to the Theory of the Raman Effect,* D. Reidel Publishing Company, Dordrecht, Netherlands (1972).

[98] J. Tang, A. C. Albrecht, Developments in the Theories of Vibrational Raman Intensities, in *Raman Spectroscopy* (Ed.: H. A. Szymanski), vol. 2, Plenum Press, New York, NY, USA (1970) 33–68.

[99] A. C. Albrecht, On the Theory of Raman Intensities, *J. Chem. Phys.* **34** (1961) 1476–1484.

[100] J. Behringer, J. Brandmüller, Der Resonanz-Raman-Effekt Unter besonderer Berücksichtigung neuerer russischer Arbeiten, *Z. Elektrochem., Berich. Bunsen Gesell.* **60** (1956) 643–679.

[101] J. Behringer, Zur Theorie des Resonanz-Raman-Effektes, *Z. Elektrochem., Berich. Bunsen Gesell.* **62** (1958) 906–914.

[102] W. H. Weber, R. Merlin, eds., *Raman Scattering in Materials Science,* Springer, Berlin/Heidelberg, Germany (2000).

[103] F. A. Cotton, *Chemical applications of group theory,* John Wiley & Sons, Nashville, TN, USA (1990).

[104] D. C. Harris, M. D. Bertolucci, *Symmetry and Spectroscopy,* Oxford University Press, New York, NY, USA (1989).

[105] M. S. Dresselhaus, G. Dresselhaus, A. Jorio, *Group Theory,* Springer, Berlin/Heidelberg, Germany (2008).

[106] J. M. Hollas, *Symmetrie von Molekülen* (Ed.: R. Steudel), De Gruyter, Berlin, Germany (1975).

[107] M. Hargittai, I. Hargittai, *Symmetry through the eyes of a chemist,* Springer, New York, NY, USA (2006).

[108] H. Eyring, T. L. J. Walter, G. E. Kimball, *Quantum Chemistry,* John Wiley & Sons, New York, NY, USA (1944).

[109] J. Huheey, E. A. Keiter, R. L. Keiter, *Anorganische Chemie,* De Gruyter, Berlin, Germany (2014).

[110] M. Tinkham, *Group theory and quantum mechanics,* Dover Publications, Mineola, NY, USA (2003).

[111] A. Nussbaum, *Applied Group Theory for chemists, physicists and engineers,* Prentice-hall, Englewood, NJ, USA (1971).

[112] H. Czichos, K.-H. Habig, *Tribologie-Handbuch,* Springer Fachmedien, Wiesbaden, Germany (2020).

[113] V. L. Popov, *Kontaktmechanik und Reibung,* Springer, Berlin/Heidelberg, Germany (2015).

[114] I. Hutchings, P. Shipway, *Tribology,* Elsevier, Oxford, UK (2017).

[115] G. Straffelini, *Friction and Wear,* Springer International Publishing, Cham, Switzerland (2015).

[116] P. L. Menezes, S. P. Ingole, M. Nosonovsky, S. V. Kailas, M. R. Lovell, eds., *Tribology for scientists and engineers,* Springer, New York, NY, USA (2013).

[117] G. W. Stachowiak, ed., *Wear-materials, mechanisms and practice,* Wiley, Chichester, UK (2005).

[118] C. V. Raman, K. S. Krishnan, A New Type of Secondary Radiation, *Nature* **121** (1928) 501–502.

[119] L. D. Landau, E. M. Lifshitz, The Fermi and Bose Distributions, in *Statistical Physics,* 2nd ed., Pergamon Press, Oxford, UK (1970).

[120] C. Klingshirn, Optical properties of phonons, in *Advanced Texts in Physics,* 2nd ed., Springer, Berlin/Heidelberg, Germany (2005) 273–286.

[121] J. E. Huheey, E. A. Keiter, R. L. Keiter, 3. Symmetrie und Gruppentheorie, in *Anorganische Chemie,* De Gruyter, Berlin, Germany (2014) 57–108.

[122] M. S. Dresselhaus, G. Desselhaus, A. Jorio, Molecular Vibrations, Infrared, and Raman Activity, in *Group Theory,* Springer, Berlin/Heidelberg, Germany (2008) 147–178.

[123] X. X. Yang, J. W. Li, Z. F. Zhou, Y. Wang, L. W. Yang, W. T. Zheng, C. Q. Sun, Raman spectroscopic determination of the length, strength, compressibility, Debye temperature, elasticity, and force constant of the C-C bond in graphene, *Nanoscale* **4** (2012) 502–510.

[124] D. C. Harris, M. D. Bertolucci, A chemist's view of group theory, in *Symmetry and Spectroscopy,* Oxford University Press, New York, NY, USA (1989) 5–61.

[125] M. Hargittai, I. Hargittai, Helpful Mathematical Tools, in *Symmetry through the eyes of a chemist,* 3rd ed., Springer, New York, NY, USA (2006) 169–216.

[126] F. A. Cotton, in *Chemical applications of group theory,* 3rd ed., John Wiley & Sons, Nashville, TN, USA (1990).

[127] G. L. Breneman, Crystallographic symmetry point group notation flow chart, *J. Chem. Educ.* **64** (1987) 216.

[128] W. Borchardt-Ott, H. Sowa, Die Punktgruppen, in *Kristallographie,* Springer, Berlin/Heidelberg, Germany (2018) 127–196.

[129] W. Borchardt-Ott, H. Sowa, *Kristallographie,* Springer, Berlin/Heidelberg, Germany (2018).

[130] G. Burns, A. M. Glazer, Academic Press, Inc., San Diego, CA, USA (1990).

[131] T. Hahn, ed., Springer, Dordrecht, Netherlands (2006).

[132] R. S. Mulliken, Electronic Structures of Polyatomic Molecules and Valence. IV. Electronic States, Quantum Theory of the Double Bond, *Phys. Rev.* **43** (1933) 279–302.

[133] NobelPrize.org, *Robert S. Mulliken: Facts,* Nobel Prize Outreach AB 2024, URL: https://www.nobelprize.org/prizes/chemistry/1966/mulliken/facts/ (visited on 07/31/2024).

[134] F. A. Cotton, in *Chemical applications of group theory,* 3rd ed., John Wiley & Sons, Nashville, TN, USA (1990).

[135] R. J. Ouellette, J. D. Rawn, Amino Acids, Peptides, and Proteins, in *Organic Chemistry,* Elsevier, San Diego, CA, USA (2014) 953–991.

[136] M. B. Smith, Amino Acids, in *Biochemistry,* CRC Press, Boca Raton, FL, USA (2020) 253–260.

[137] M. Zorko, Amino Acids, in *Introdution to Peptides and Proteins,* CRC Press Taylor & Francis Group, Boca Raton, FL, USA (2010) 5–20.

[138] D. Voet, J. G. Voet, The Amino Acids of Proteins, in *Biochemistry,* 4th ed., John Wiley & Sons, Chichester, UK (2010) 67–81.

[139] M. D. Pluth, R. G. Bergman, K. N. Raymond, Acceleration of amide bond rotation by encapsulation in the hydrophobic interior of a water-soluble supramolecular assembly, *J. Org. Chem.* **73** (2008) 7132–7136.

[140] M. Zorko, Structural Organization of Proteins, in *Introdution to Peptides and Proteins,* CRC Press Taylor & Francis Group, Boca Raton, FL, USA (2010) 35–57.

[141] J. S. Richardson, The anatomy and taxonomy of protein structure, in *Advances in Protein Chemistry,* vol. 34, Elsevier, (1981) 167–339.

[142] M. B. Smith, Peptides and Proteins, in *Biochemistry,* CRC Press, Boca Raton, FL, USA (2020) 261–286.

[143] H. Felgueiras, J. Antunes, M. Martins, M. Barbosa, Fundamentals of protein and cell interactions in biomaterials, in *Peptides and Proteins as Biomaterials for Tissue Regeneration and Repair* (Eds.: M. A. Barbosa, M. Cristina, L. Martins), Elsevier, Duxford, UK (2018) 1–27.

[144] J. S. Richardson, Schematic drawings of protein structures, in *Methods in Enzymology,* Academic Press. Inc ., New York, NY, USA (1985) 359–380.

[145] M. B. Smith, The importance of water in biochemical systems, in *Biochemistry,* CRC Press, Boca Raton, FL, USA (2020) 55–82.

[146] M. Zorko, Posttranslational Modifications, in *Introdution to Peptides and Proteins,* CRC Press Taylor & Francis Group, Boca Raton, FL, USA (2010) 81–97.

[147] D. Voet, J. G. Voet, Protein Folding, Dynamics, and Structural Evolution, in *Biochemistry,* 4th ed., John Wiley & Sons, Chichester, UK (2010) 278–322.

[148] H. Sugeta, A. Go, T. Miyazawa, S-S and C-S stretching vibrations and molecular conformations of dialkyl disulfides and cystine, *Chem. Lett.* (1972) 83–86.

[149] H. Sugeta, A. Go, T. Miyazawa, Vibrational Spectra and Molecular Conformations of Dialkyl Disulfides, *Bull. Chem. Soc. Jpn.* **46** (1973) 3407–3411.

[150] D. A. Armstrong, Q. Kaas, K. J. Rosengren, Prediction of disulfide dihedral angles using chemical shifts, *Chem. Sci.* **9** (2018) 6548–6556.

[151] P. M. Harrison, M. J. E. Sternberg, The disulphide beta-cross: from cystine geometry and clustering to classification of small disulphide-rich protein folds, *J. Mol. Biol.* **264** (1996) 603–623.

[152] B. Schmidt, L. Ho, P. J. Hogg, Allosteric disulfide bonds, *Biochemistry* **45** (2006) 7429–7433.

[153] R. A. J. Latour, Biomaterials: Protein-Surface Interactions, in *Encyclopedia of Biomaterials and Biomedical Engineering* (Eds.: G. E. Wnek, G. L. Bowlin), 2nd ed., CRC Press, Boca Raton, FL, USA (2008).

[154] E. A. Vogler, Protein adsorption in three dimensions, *Biomaterials* **33** (2012) 1201–1237.

[155] L. Bacakova, E. Filova, M. Parizek, T. Ruml, V. Svorcik, Modulation of cell adhesion, proliferation and differentiation on materials designed for body implants, *Biotechnol. Adv.* **29** (2011) 739–767.

[156] W.-H. Lee, C.-Y. Loo, R. Rohanizadeh, A review of chemical surface modification of bioceramics: Effects on protein adsorption and cellular response, *Colloid. Surface. B* **122** (2014) 823–834.

[157] L. Tang, P. Thevenot, W. Hu, Surface Chemistry Influences Implant Biocompatibility, *Curr. Top. Med. Chem.* **8** (2008) 270–280.

[158] J. D. Andrade, V. Hlady, A. P. Wei, Adsorption of complex proteins at interfaces, *Pure Appl. Chem.* **64** (1992) 1777–1781.

[159] M. J. Yaszemski, B. D. Ratner, Introduction to Biology and Medicine-Key Concepts in the Use of Biomaterials in Surgery and Medical Devices, in *Biomaterials Science* (Eds.: W. R. Wagner, S. E. Sakiyama-Elbert, G. Zhang, M. J. Yaszemski), 4th ed., Elsevier, London, UK (2020) 643–644.

[160] T. A. Horbett, R. A. Latour, Adsorbed Proteins on Biomaterials, in *Biomaterials Science* (Eds.: W. R. Wagner, S. E. Sakiyama-Elbert, G. Zhang, M. J. Yaszemski), 4th ed., Elsevier, London, UK (2020) 645–660.

[161] A. Neville, Y. Yan, Biotribocorrosion: surface interactions in total joint replacement (TJR), in *Tribocorrosion of Passive Metals and Coatings* (Eds.: D. Landolt, S. Mischler), Woodhead Publishing, Oxford, UK (2011) 337–367.

[162] W. Norde, The behavior of proteins at interfaces, with special attention to the role of the structure stability of the protein molecule, *Clin. Mater.* **11** (1992) 85–91.

[163] J. P. Glusker, Structural Aspects of Metal Liganding to Functional Groups in Proteins, in *Advances in Protein Chemistry* (Eds.: C. B. Anfinsen, J. T. Edsall, F. M. Richards, D. S. Eisenberg), Academic Press, New York, NY, USA (1991) 1–76.

[164] J. A. Loo, R. R. O. Loo, H. R. Udseth, C. G. Edmonds, R. D. Smith, Solvent-induced conformational changes of polypeptides probed by electrospray-ionization mass spectrometry, *Rapid Commun. Mass Sp.* **5** (1991) 101–105.

[165] J. Antosiewicz, J. McCammon, M. K. Gilson, Prediction of Ph-dependent Properties of Proteins, *J. Mol. Biol.* **238** (1994) 415–436.

[166] M. Dockal, D. C. Carter, F. Rüker, Conformational Transitions of the Three Recombinant Domains of Human Serum Albumin Depending on pH, *J. Biol. Chem.* **275** (2000) 3042–3050.

[167] N. A. Cummings, G. L. Nordby, Measurement of synovial fluid pH in normal and arthritic knees, *Arthritis Rheum.* **9** (1966) 47–56.

[168] E. H. Jebens, M. E. Monk-Jones, On the viscosity and pH of synovial fluid and the pH of blood, *J. Bone Joint Surg. BR* **41-B** (1959) 388–400.

[169] I. Milošev, V. Levašič, J. Vidmar, S. Kovač, R. Trebše, pH and metal concentration of synovial fluid of osteoarthritic joints and joints with metal replacements, *J. Biomed. Mater. Res. B* **105** (2016) 2507–2515.

[170] C. Theil, T. Ackmann, G. Gosheger, J. Puetzler, B. Moellenbeck, J. Schwarze, M. Schulze, S. Klingebiel, Synovial fluid pH is as specific as synovial leukocyte count but less sensitive for the diagnosis of chronic prosthetic joint infection, *J. Orthop. Trauma* **23** (2022).

[171] J. D. Andrade, V. Hlady, A.-P. Wei, C.-H. Ho, A. S. Lea, S. I. Jeon, Y. S. Lin, E. Stroup, Proteins at Interfaces: Principles, Multivariate Aspects, Protein Resistant Surfaces, and Direct Imaging and Manipulation of Adsorbed Proteins, in *Biologically Modified Polymeric Biomaterial Surfaces,* Springer, Dordrecht, Netherlands (1992) 67–84.

[172] T. Peters Jr., Serum Albumin, in *Advances in Protein Chemistry,* vol. 37, Elsevier, Cooperatown, NY, USA (1985) 161–245.

[173] M. S. Lord, M. Foss, F. Besenbacher, Influence of nanoscale surface topography on protein adsorption and cellular response, *Nano Today* **5** (2010) 66–78.

[174] K. M. Woo, V. J. Chen, P. X. Ma, Nano-fibrous scaffolding architecture selectively enhances protein adsorption contributing to cell attachment, *J. Biomed. Mater. Res. A* **67A** (2003) 531–537.

[175] A. G. Harvey, E. W. Hill, A. Bayat, Designing implant surface topography for improved biocompatibility, *Expert Rev. Med. Devic.* **10** (2013) 257–267.

[176] K. Guth, C. Campion, T. Buckland, K. A. Hing, Surface Physiochemistry Affects Protein Adsorption to Stoichiometric and Silicate-Substituted Microporous Hydroxyapatites, *Adv. Eng. Mater.* **12** (2010).

[177] P. Roach, D. Farrar, C. C. Perry, Surface Tailoring for Controlled Protein Adsorption: Effect of Topography at the Nanometer Scale and Chemistry, *J. Am. Chem. Soc.* **128** (2006) 3939–3945.

[178] D. F. Williams, I. N. Askill, R. Smith, Protein adsorption and desorption phenomena on clean metal surfaces, *J. Biomed. Mater. Res.* **19** (1985) 313–320.

[179] L. Thadikkaran, M. A. Siegenthaler, D. Crettaz, P.-A. Queloz, P. Schneider, J.-D. Tissot, Recent advances in blood-related proteomics, *Proteomics* **5** (2005) 3019–3034.

[180] S. Schenk, G. J. Schoenhals, G. de Souza, M. Mann, A high confidence, manually validated human blood plasma protein reference set, *BMC Med. Genomics* **1** (2008).

[181] S. Miyamoto, K. Shimono, Molecular Modeling to Estimate the Diffusion Coefficients of Drugs and Other Small Molecules, *Molecules* **25** (2020) 5340.

[182] S. L. Hirsh, D. R. McKenzie, N. J. Nosworthy, J. A. Denman, O. U. Sezerman, M. M. Bilek, The Vroman effect: Competitive protein exchange with dynamic multilayer protein aggregates, *Colloid. Surface. B* **103** (2013) 395–404.

[183] S.-Y. Jung, S.-M. Lim, F. Albertorio, G. Kim, M. C. Gurau, R. D. Yang, M. A. Holden, P. S. Cremer, The Vroman Effect: A Molecular Level Description of Fibrinogen Displacement, *J. Am. Chem. Soc.* **125** (2003) 12782–12786.

[184] L. Vroman, A. L. Adams, Findings with the recording ellipsometer suggesting rapid exchange of specific plasma proteins at liquid/solid interfaces, *Surf. Sci.* **16** (1969) 438–446.

[185] A. Baszkin, Surface phenomena in biocomponent-polymer systems: A case study of mucin adsorption on polymers with different hydrophilicities, *Clin. Mater.* **11** (1992) 119–123.

[186] V. Hlady, J. Buijs, Protein adsorption on solid surfaces, *Curr. Opin. Biotech.* **7** (1996) 72–77.

[187] C. M. Alves, R. L. Reis, J. A. Hunt, The dynamics, kinetics and reversibility of protein adsorption onto the surface of biodegradable materials, *Soft Matter* **6** (2010) 4135.

[188] W. Norde, Adsorption of proteins from solution at the solid-liquid interface, *Adv. Colloid Interfac.* **25** (1986) 267–340.

[189] NobelPrize.org, *Irving Langmuir: Facts,* Nobel Prize Outreach AB 2024, URL: `https://www.nobelprize.org/prizes/chemistry/1932/langmuir/facts/` (visited on 06/19/2024).

[190] I. Langmuir, The adsorption of gases on plane surfaces of glass, mica and platinum. *J. Am. Chem. Soc.* **40** (1918) 1361–1403.

[191] R. A. Latour, The langmuir isotherm: A commonly applied but misleading approach for the analysis of protein adsorption behavior, *J. Biomed. Mater. Res. A* **103** (2014) 949–958.

[192] C. F. Wertz, M. M. Santore, Effect of Surface Hydrophobicity on Adsorption and Relaxation Kinetics of Albumin and Fibrinogen: Single-Species and Competitive Behavior, *Langmuir* **17** (2001) 3006–3016.

[193] A. Magnani, F. M. Piras, Hemocompatible Materials, in *Encyclopedia of Biomaterials and Biomedical Engineering* (Eds.: G. E. Wnek, G. L. Bowlin), 2nd ed., CRC Press, Boca Raton, FL, USA (2008).

[194] J. Yang, K. Merritt, Detection of antibodies against corrosion products in patients after Co-Cr total joint replacements, *J. Biomed. Mater. Res.* **28** (1994) 1249–1258.

[195] F. H. Arnold, Metal-Affinity Separations: A New Dimension in Protein Processing, *Nat. Biotechnol.* **9** (1991) 151–156.

[196] E. Ueda, P. Gout, L. Morganti, Current and prospective applications of metal ion-protein binding, *J. Chromatogr. A* **988** (2003) 1–23.

[197] J. Porath, J. Carlsson, I. Olsson, G. Belfrage, Metal chelate affinity chromatography, a new approach to protein fractionation, *Nature* **258** (1975) 598–599.

[198] M. Schmacht, E. Lorenz, M. Senz, Microbial production of glutathione, *World J. Microb. Biot.* **33** (2017).

[199] W. Bal, M. Sokołowska, E. Kurowska, P. Faller, Binding of transition metal ions to albumin: Sites, affinities and rates, *BBA-Gen. Subjects* **1830** (2013) 5444–5455.

[200] N. Wakabayashi, H. G. Smith, R. M. Nicklow, Lattice dynamics of hexagonal MoS_2 studied by neutron scattering, *Phys. Rev. B* **12** (1975) 659–663.

[201] A. Lansdown, Chapter 4. Properties of molybdenum disulphide, in *Molybdenum Disulphide Lubrication* (Ed.: D. Dowson), 1st ed., vol. 35, Elsevier, (1999) 31–45.

[202] A. V. Kolobov, J. Tominaga, Raman Scattering of 2D TMDCs, in *Two-Dimensional Transition-Metal Dichalcogenides,* Springer International Publishing, Cham, Switzerland (2016) 227–294.

[203] X. Luo, Y. Zhao, J. Zhang, Q. Xiong, S. Y. Quek, Anomalous frequency trends in MoS_2 films attributed to surface effects, *Phys. Rev. B* **88** (2013).

[204] G. F. Koster, J. O. Dimmock, R. G. Wheeler, H. Statz, *Properties of the thirty two point groups,* M.I.T. Press, Cambridge, MA, USA (1963).

[205] G. L. Frey, R. Tenne, M. J. Matthews, M. S. Dresselhaus, G. Dresselhaus, Raman and resonance Raman investigation of MoS_2 nanoparticles, *Phys. Rev. B* **60** (1999) 2883–2892.

[206] T. J. Wieting, J. L. Verble, Infrared and Raman Studies of Long-Wavelength Optical Phonons in Hexagonal MoS_2, *Phys. Rev. B* **3** (1971) 4286–4292.

[207] S. Cortijo-Campos, P. Kung, C. Prieto, A. de Andrés, Forbidden and Second-Order Phonons in Raman Spectra of Single and Few-Layer MoS_2 Close to C Exciton Resonance, *J. Phys. Chem. C* **125** (2021) 23904–23910.

[208] C. Lee, H. Yan, L. E. Brus, T. F. Heinz, J. Hone, S. Ryu, Anomalous Lattice Vibrations of Single- and Few-Layer MoS_2, *ACS Nano* **4** (2010) 2695–2700.

[209] B. Chakraborty, H. S. S. R. Matte, A. K. Sood, C. N. R. Rao, Layer-dependent resonant Raman scattering of a few layer MoS_2, *J. Raman Spectrosc.* **44** (2012) 92–96.

[210] A. Molina-Sánchez, L. Wirtz, Phonons in single-layer and few-layer MoS_2, *Phys. Rev. B* **84** (2011).

[211] K. K. Kam, B. A. Parkinson, Detailed photocurrent spectroscopy of the semiconducting group VIB transition metal dichalcogenides, *J. Phys. Chem.* **86** (1982) 463–467.

[212] K. F. Mak, C. Lee, J. Hone, J. Shan, T. F. Heinz, Atomically Thin MoS_2: A New Direct-Gap Semiconductor, *Phys. Rev. Lett.* **105** (2010).

[213] D. Xiao, G.-B. Liu, W. Feng, X. Xu, W. Yao, Coupled Spin and Valley Physics in Monolayers of MoS_2 and Other Group-VI Dichalcogenides, *Phys. Rev. Lett.* **108** (2012).

[214] H. Zeng, J. Dai, W. Yao, D. Xiao, X. Cui, Valley polarization in MoS_2 monolayers by optical pumping, *Nat. Nanotechnol.* **7** (2012) 490–493.

[215] F. Rose, M. O. Goerbig, F. Piéchon, Spin- and valley-dependent magneto-optical properties of MoS_2, *Phys. Rev. B* **88** (2013).

[216] A. Webb, J. Feldman, E. Skelton, L. Towle, C. Liu, I. Spain, High pressure investigations of MoS_2, *J. Phys. Chem. Solids* **37** (1976) 329–335.

[217] A. G. Bagnall, W. Y. Liang, E. A. Marseglia, B. Welber, Raman studies of MoS_2 at high pressure, *Physica* **99** (1980) 343–346.

[218] S. V. Bhatt, M. P. Deshpande, V. Sathe, R. Rao, S. H. Chaki, Raman spectroscopic investigations on transition-metal dichalcogenides MX_2 (M = Mo, W; X = S, Se) at high pressures and low temperature, *J. Raman Spectrosc.* **45** (2014) 971–979.

[219] S. Sugai, T. Ueda, High-pressure Raman spectroscopy in the layered materials 2H-MoS_2, 2H-$MoSe_2$, and 2H-$MoTe_2$, *Phys. Rev. B* **26** (1982) 6554–6558.

[220] N. Bandaru, R. S. Kumar, D. Sneed, O. Tschauner, J. Baker, D. Antonio, S.-N. Luo, T. Hartmann, Y. Zhao, R. Venkat, Effect of Pressure and Temperature on Structural Stability of MoS_2, *J. Phys. Chem. C* **118** (2014) 3230–3235.

[221] C. Rice, R. J. Young, R. Zan, U. Bangert, D. Wolverson, T. Georgiou, R. Jalil, K. S. Novoselov, Raman-scattering measurements and first-principles calculations of strain-induced phonon shifts in monolayer MoS_2, *Phys. Rev. B* **87** (2013).

[222] H. J. Conley, B. Wang, J. I. Ziegler, R. F. Haglund, S. T. Pantelides, K. I. Bolotin, Bandgap Engineering of Strained Monolayer and Bilayer MoS_2, *Nano Lett.* **13** (2013) 3626–3630.

[223] Z. Li, Y. Lv, L. Ren, J. Li, L. Kong, Y. Zeng, Q. Tao, R. Wu, H. Ma, B. Zhao, D. Wang, W. Dang, K. Chen, L. Liao, X. Duan, X. Duan, Y. Liu, Efficient strain modulation of 2D materials via polymer encapsulation, *Nat. Commun.* **11** (2020).

[224] D. Doratotaj, J. R. Simpson, J.-A. Yan, Probing the uniaxial strains in MoS_2 using polarized Raman spectroscopy: A first-principles study, *Phys. Rev. B* **93** (2016).

[225] Y. Wang, C. Cong, C. Qiu, T. Yu, Raman spectroscopy study of lattice vibration and crystallographic orientation of monolayer MoS_2 under uniaxial strain, *Small* **9** (2013) 2857–2861.

[226] X. Li, J. Li, K. Wang, X. Wang, S. Wang, X. Chu, M. Xu, X. Fang, Z. Wei, Y. Zhai, B. Zou, Pressure and temperature-dependent Raman spectra of MoS_2 film, *Appl. Phys. Lett.* **109** (2016).

[227] G. Kukucska, J. Koltai, Theoretical Investigation of Strain and Doping on the Raman Spectra of Monolayer MoS_2, *Phys. Status Solidi B* **254** (2017).

[228] S. Sahoo, A. P. S. Gaur, M. Ahmadi, M. J.-F. Guinel, R. S. Katiyar, Temperature-Dependent Raman Studies and Thermal Conductivity of Few-Layer MoS_2, *J. Phys. Chem. C* **117** (2013) 9042–9047.

[229] M. Thripuranthaka, R. V. Kashid, C. Sekhar Rout, D. J. Late, Temperature dependent Raman spectroscopy of chemically derived few layer MoS_2 and WS_2 nanosheets, *Appl. Phys. Lett.* **104** (2014).

[230] W. Gordy, A Relation between Bond Force Constants, Bond Orders, Bond Lengths, and the Electronegativities of the Bonded Atoms, *J. Chem. Phys.* **14** (1946) 305–320.

[231] P. Vandenabeele, Theoretical Aspects, in *Practical Raman Spectroscopy - An Introduction,* John Wiley & Sons, Ltd, Chichester, UK (2013) 1–38.

[232] M. C. Chen, R. C. Lord, Laser-excited Raman spectroscopy of biomolecules. VIII. Conformational study of bovine serum albumin, *J. Am. Chem. Soc.* **98** (1976) 990–992.

[233] K. A. Majorek, P. J. Porebski, A. Dayal, M. D. Zimmerman, K. Jablonska, A. J. Stewart, M. Chruszcz, W. Minor, Structural and immunologic characterization of bovine, horse, and rabbit serum albumins, *Mol. Immunol.* **52** (2012) 174–182.

[234] G. Fanali, A. di Masi, V. Trezza, M. Marino, M. Fasano, P. Ascenzi, Human serum albumin: From bench to bedside, *Molecular Aspects of Medicine* **33** (2012) 209–290.

[235] F. A. de Wolf, G. M. Brett, Ligand-binding proteins: their potential for application in systems for controlled delivery and uptake of ligands, *Pharmacol. Rev.* **52** (2000) 207–236.

[236] D. C. Carter, J. X. Ho, Structure of Serum Albumin, in *Lipoproteins, Apolipoproteins, and Lipases* (Eds.: C. Anfinsen, J. T. Edsall, F. M. Richards, D. S. Eisenberg), vol. 45, Academic Press, San Diego, CA, USA (1994) 153–203.

[237] J. F. Foster, Some aspects of the structure and conformational properties of serum albumin, in *Albumin: Structure, Function and Uses* (Eds.: V. M. ROSENOER, M. ORATZ, M. A. ROTHSCHILD), Pergamon, Oxford, UK (1977) 53–84.

[238] K. Murayama, M. Tomida, Heat-Induced Secondary Structure and Conformation Change of Bovine Serum Albumin Investigated by Fourier Transform Infrared Spectroscopy, *Biochemistry* **43** (2004) 11526–11532.

[239] S. Tayyab, N. Sharma, M. Mushahid Khan, Use of Domain Specific Ligands to Study Urea-Induced Unfolding of Bovine Serum Albumin, *Biochem. Biophys. Res. Commun.* **277** (2000) 83–88.

[240] B. Ahmad, M. Z. Ahmed, S. K. Haq, R. H. Khan, Guanidine hydrochloride denaturation of human serum albumin originates by local unfolding of some stable loops in domain III, *Biochim. Biophys. Acta* **1750** (2005) 93–102.

[241] K. Nakamura, S. Era, Y. Ozaki, M. Sogami, T. Hayashi, M. Murakami, Conformational changes in seventeen cystine disulfide bridges of bovine serum albumin proved by Raman spectroscopy, *FEBS Lett.* **417** (1997) 375–378.

[242] S. G. K. Belén Hernández Fernando Pflüger, M. Ghomi, Characteristic Raman lines of phenylalanine analyzed by a multiconformational approach, *J. Raman Spectrosc.* **44** (2013) 827–833.

[243] B. Hernández, L. Tinacci, Y.-M. Coïc, A. Chenal, R. Cohen, S. Sanchez-Cortes, M. Ghomi, Tryptophan Tight Binding to Gold Nanoparticles Induces Drastic Changes in Indole Ring Raman Markers, *J. Phys. Chem. C* **122** (2018) 13034–13046.

[244] B. Hernández, Y.-M. Coïc, F. Pflüger, S. G. Kruglik, M. Ghomi, All characteristic Raman markers of tyrosine and tyrosinate originate from phenol ring fundamental vibrations, *J. Raman Spectrosc.* **47** (2016) 210–220.

[245] S. Schlücker, C. Liang, K. R. Strehle, J. J. DiGiovanna, K. H. Kraemer, I. W. Levin, Conformational differences in protein disulfide linkages between normal hair and hair from subjects with trichothiodystrophy: A quantitative analysis by Raman microspectroscopy, *Biopolymers* **82** (2006) 615–622.

[246] B. Hernández, F. Pflüger, A. Adenier, S. G. Kruglik, M. Ghomi, Vibrational Analysis of Amino Acids and Short Peptides in Hydrated Media. VIII. Amino Acids with Aromatic Side Chains: L-Phenylalanine, L-Tyrosine, and L-Tryptophan, *J. Phys. Chem. B* **114** (2010) 15319–15330.

[247] C.-H. Wang, C.-C. Huang, L.-L. Lin, W. Chen, The effect of disulfide bonds on protein folding, unfolding, and misfolding investigated by FT-Raman spectroscopy, *J. Raman Spectrosc.* **47** (2016) 940–947.

[248] A. Schirmeisen, L. Jansen, H. Hölscher, H. Fuchs, Temperature dependence of point contact friction on silicon, *Appl. Phys. Lett.* **88** (2006).

[249] N. Saka, A. Eleiche, N. Suh, Wear of metals at high sliding speeds, *Wear* **44** (1977) 109–125.

[250] S. E. Quiñones-Cisneros, C. K. Zéberg-Mikkelsen, E. H. Stenby, The friction theory (f-theory) for viscosity modeling, *Fluid Phase Equilibr.* **169** (2000) 249–276.

[251] E. Popova, V. L. Popov, The legacy of Coulomb and generalized laws of friction, *Proc. Appl. Math. Mech.* **20** (2021).

[252] N. Kumar, G. Gautam, R. K. Gautam, A. Mohan, S. Mohan, Wear, friction and profilometer studies of insitu AA5052/ZrB2 composites, *Tribol. Int.* **97** (2016) 313–326.

[253] M. Scherge, K. Pöhlmann, A. Gervé, Wear measurement using radionuclide-technique (RNT), *Wear* **254** (2003) 801–817.

[254] J. Zhang, A. Alpas, Transition between mild and severe wear in aluminium alloys, *Acta Mater.* **45** (1997) 513–528.

[255] M. Chen, T. Perry, A. Alpas, Ultra-mild wear in eutectic Al-Si alloys, *Wear* **263** (2007) 552–561.

[256] American Society for Metals, *ASM handbook Friction, Lubrication and Wear Technology* (Ed.: P. J. Blau), vol. 18, ASM International, (1992).

[257] Y. Wang, T. Lei, J. Liu, Tribo-metallographic behavior of high carbon steels in dry sliding, *Wear* **231** (1999) 1–11.

[258] G. Straffelini, Wear Processes, in *Friction and Wear,* Springer International Publishing, Cham, Switzerland (2015) 115–158.

[259] D. Landolt, S. Mischler, M. Stemp, Electrochemical methods in tribocorrosion: a critical appraisal, *Electrochim. Acta* **46** (2001) 3913–3929.

[260] M. Wimmer, J. Loos, R. Nassutt, M. Heitkemper, A. Fischer, The acting wear mechanisms on metal-on-metal hip joint bearings: in vitro results, *Wear* **250** (2001) 129–139.

[261] F. Klocke, *Fertigungsverfahren 4: Umformen,* Springer, Berlin/Heidelberg, Germany (2017).

[262] H. Czichos, E. Santner, Tribologische Beanspruchung, in *Tribologie-Handbuch,* Springer Fachmedien, Wiesbaden, Germany (2020) 57–120.

[263] E. M. L. L. D. Landau, Grundgleichungen, in *Lehrbuch der Theoretischen Physik Band VII: Elastizitätstheorie* (Ed.: H.-G. Schöpfer), Akademie-Verlag, Berlin, Germany (1989) 1–47.

[264] H. Hertz, Ueber die Berührung fester elastischer Körper. *J. Reine Angew. Math.* **1882** (1882) 156–171.

[265] V. L. Popov, Rigorose Behandlung des Kontaktproblems - Hertzscher Kontakt, in *Kontaktmechanik und Reibung,* Springer, Berlin/Heidelberg, Germany (2015) 59–84.

[266] M. Bahshwan, C. W. Myant, T. Reddyhoff, M.-S. Pham, The role of microstructure on wear mechanisms and anisotropy of additively manufactured 316L stainless steel in dry sliding, *Mater. Des.* **196** (2020) 109076.

[267] I. M. Allam, M. Maslehuddin, H. Saricimen, A. I. Al-Mana, Influence of atmospheric corrosion on the mechanical properties of reinforcing steel, *Constr. Build. Mater.* **8** (1994) 35–41.

[268] M. Stratmann, The Atmospheric Corrosion of Iron - A Discussion of the Physico-Chemical Fundamentals of this Omnipresent Corrosion Process Invited Review, *Berich. Bunsen. Gesell.* **94** (1990) 626–639.

[269] C. Kleber, J. Weissenrieder, M. Schreiner, C. Leygraf, Comparison of the early stages of corrosion of copper and iron investigated by in situ TM-AFM, *Appl. Surf. Sci.* **193** (2002) 245–253.

[270] F. Klocke, *Fertigungsverfahren 1: Zerspanung mit geometrisch bestimmter Schneide,* Springer, Berlin/Heidelberg, Germany (2018).

[271] F. Klocke, *Fertigungsverfahren 2: Zerspanung mit geometrisch unbestimmter Schneide,* Springer, Berlin/Heidelberg, Germany (2018).

[272] F. Klocke, W. König, *Fertigungsverfahren 3: Abtragen, Generieren und Lasermaterialbearbeitung,* Springer, Berlin/Heidelberg, Germany (2007).

[273] F. Klocke, *Fertigungsverfahren 5: Gießen und Pulvermetallurgie,* Springer, Berlin/Heidelberg, Germany (2018).

[274] A. Atkinson, R. I. Taylor, A. E. Hughes, A quantitative demonstration of the grain boundary diffusion mechanism for the oxidation of metals, *Philos. Mag. A* **45** (1982) 823–833.

[275] H. Dugdale, D. E. Armstrong, E. Tarleton, S. G. Roberts, S. Lozano-Perez, How oxidized grain boundaries fail, *Acta Mater.* **61** (2013) 4707–4713.

[276] K. S. Chan, A Grain Boundary Fracture Model for Predicting Dynamic Embrittlement and Oxidation-Induced Cracking in Superalloys, *Metall. Mater. Trans. A* **46** (2015) 2491–2505.

[277] B. Bhushan, Nanotribology and Nanomechanics of MEMS/NEMS and BioMEMS/BioNEMS Materials and Devices, in *Nanotribology and Nanomechanics* (Ed.: B. Bhushan), 4th ed., Springer International Publishing, Cham, Switzerland (2017) 797–907.

[278] R. P. Feynman, There's plenty of room at the bottom: An invitation to enter a new field of physics, *Engineering and Science* **23** (1960) 22–36.

[279] NobelPrize.org, *Richard P. Feynman: Facts,* Nobel Prize Outreach AB 2024, URL: `https://www.nobelprize.org/prizes/physics/1965/feynman/facts/` (visited on 01/16/2024).

[280] G. Binnig, C. F. Quate, C. Gerber, Atomic Force Microscope, *Phys. Rev. Lett.* **56** (1986) 930–933.

[281] NobelPrize.org, *Gerd Binnig: Facts,* Nobel Prize Outreach AB 2024, URL: `https://www.nobelprize.org/prizes/physics/1986/binnig/facts/` (visited on 01/16/2024).

[282] N. Beckmann, P. A. Romero, D. Linsler, M. Dienwiebel, U. Stolz, M. Moseler, P. Gumbsch, Origins of Folding Instabilities on Polycrystalline Metal Surfaces, *Phys. Rev. Appl.* **2** (2014).

[283] A. Fischer, D. Stickel, C. Schoss, R. Bosman, M. Wimmer, On the Growth Rate of Tribomaterial in Bovine Serum Lubricated Sliding Contacts, *Lubricants* **4** (2016) 21.

[284] K.-H. Zum Gahr, Wear by hard particles, *Tribol. Int.* **31** (1998) 587–596.

[285] Q. J. Wang, Y.-W. Chung, eds., *Encyclopedia of Tribology,* Boston, MA, 2013.

[286] G. He, M. H. Müser, M. O. Robbins, Adsorbed Layers and the Origin of Static Friction, *Science* **284** (1999) 1650–1652.

[287] H. Ronkainen, J. Likonen, J. Koskinen, S. Varjus, Effect of tribofilm formation on the tribological performance of hydrogenated carbon coatings, *Surf. Coat. Technol.* **79** (1996) 87–94.

[288] P. U. Aldana, B. Vacher, T. Le Mogne, M. Belin, B. Thiebaut, F. Dassenoy, Action Mechanism of WS2 Nanoparticles with ZDDP Additive in Boundary Lubrication Regime, *Tribol. Lett.* **56** (2014) 249–258.

[289] P. Forsberg, P. Hollman, S. Jacobson, Wear mechanism study of exhaust valve system in modern heavy duty combustion engines, *Wear* **271** (2011) 2477–2484.

[290] Y. Yan, A. Neville, D. Dowson, Biotribocorrosion of CoCrMo orthopaedic implant materials - Assessing the formation and effect of the biofilm, *Tribol. Int.* **40** (2007) 1492–1499.

[291] P. L. Menezes, Kishore, S. V. Kailas, On the effect of surface texture on friction and transfer layer formation - A study using Al and steel pair, *Wear* **265** (2008) 1655–1669.

[292] J. Zhou, Z. Wu, Z. Zhang, W. Liu, Q. Xue, *Tribol. Lett.* **8** (2000) 213–218.

[293] P. L. Menezes, Kishore, S. V. Kailas, M. R. Lovell, Tribological response of soft materials sliding against hard surface textures at various numbers of cycles, *Lubr. Sci.* **25** (2012) 79–99.

[294] X. Zhu, W. Lauwerens, P. Cosemans, M. Van Stappen, J. Celis, L. Stals, J. He, Different tribological behavior of MoS_2 coatings under fretting and pin-on-disk conditions, *Surf. Coat. Tech.* **163-164** (2003) 422–428.

[295] A. Erdemir, C. Bindal, J. Pagan, P. Wilbur, Characterization of transfer layers on steel surfaces sliding against diamond-like hydrocarbon films in dry nitrogen, *Surf. Coat. Tech.* **76-77** (1995) 559–563.

[296] S. Bahadur, The development of transfer layers and their role in polymer tribology, *Wear* **245** (2000) 92–99.

[297] Z. Liu, C. Patzig, S. Selle, T. Höche, P. Gumbsch, C. Greiner, Stages in the tribologically-induced oxidation of high-purity copper, *Scr. Mater.* **153** (2018) 114–117.

[298] J. S. Lehmann, R. Schwaiger, M. Rinke, C. Greiner, How Tribo-Oxidation Alters the Tribological Properties of Copper and Its Oxides, *Adv. Mater. Interfaces* **8** (2020) 2001673.

[299] B. R. Lawn, O. Borrero-Lopez, H. Huang, Y. Zhang, Micromechanics of machining and wear in hard and brittle materials, *J. Am. Ceram. Soc.* **104** (2020) 5–22.

[300] S. Liu, H. Yu, Y. Wang, X. Zhang, J. Li, S. Chen, C. Liu, Cracking, Microstructure and Tribological Properties of Laser Formed and Remelted K417G Ni-Based Superalloy, *Coatings* **9** (2019) 71.

[301] Y. Ohya, Z.-e. Nakagawa, K. Hamano, Grain-Boundary Microcracking Due to Thermal Expansion Anisotropy in Aluminum Titanate Ceramics, *J. Am. Ceram. Soc.* **70** (1987) C-184-C–186.

[302] Z. C. Cordero, B. E. Knight, C. A. Schuh, Six decades of the Hall-Petch effect - a survey of grain-size strengthening studies on pure metals, *Int. Mater. Rev.* **61** (2016) 495–512.

[303] T. G. Langdon, Grain boundary sliding revisited: Developments in sliding over four decades, *J. Mater. Sci.* **41** (2006) 597–609.

[304] R. Raj, M. F. Ashby, On grain boundary sliding and diffusional creep, *Metall. Trans.* **2** (1971) 1113–1127.

[305] F. Martin, C. García, Y. Blanco, Influence of residual porosity on the dry and lubricated sliding wear of a powder metallurgy austenitic stainless steel, *Wear* **328-329** (2015) 1–7.

[306] P. Lu, R. J. K. Wood, Tribological performance of surface texturing in mechanical applications-a review, *Surf. Topogr.* **8** (2020) 043001.

[307] A. Voevodin, J. Zabinski, Nanocomposite and nanostructured tribological materials for space applications, *Compos. Sci. Technol.* (2005).

[308] P. Lejcek, *Grain Boundary Segregation in Metals,* Springer, Berlin/Heidelberg, Germany (2010).

[309] D. McLean, *Grain boundaries in metals,* Clarendon Press, Oxford, UK (1957).

[310] A. P. Sutton, R. W. Balluffi, *Interfaces in crystalline materials,* Oxford University Press, Oxford, UK (1996).

[311] G. Colas, A. Saulot, N. Bouscharain, C. Godeau, Y. Michel, Y. Berthier, How far does contamination help dry lubrication efficiency? *Tribol. Int.* **65** (2013) 177–189.

[312] T. Spalvins, Lubrication with sputtered MoS_2 films: Principles, operation, and limitations, *J. Mater. Eng. Perform.* **1** (1992) 347–351.

[313] S. M. Tan, A. Ambrosi, Z. Sofer, Š. Huber, D. Sedmidubský, M. Pumera, Pristine Basal- and Edge-Plane-Oriented Molybdenite MoS_2 Exhibiting Highly Anisotropic Properties, *Chemistry* **21** (2015) 7170–7178.

[314] G. Levita, P. Restuccia, M. Righi, Graphene and MoS_2 interacting with water: A comparison by ab initio calculations, *Carbon* **107** (2016) 878–884.

[315] P. D. Fleischauer, Fundamental aspects of the electronic structure, materials properties and lubrication performance of sputtered MoS_2 films, *Thin Solid Films* **154** (1987) 309–322.

[316] C. Muratore, A. Voevodin, Control of molybdenum disulfide basal plane orientation during coating growth in pulsed magnetron sputtering discharges, *Thin Solid Films* **517** (2009) 5605–5610.

[317] J. F. Curry, M. A. Wilson, H. S. Luftman, N. C. Strandwitz, N. Argibay, M. Chandross, M. A. Sidebottom, B. A. Krick, Impact of Microstructure on MoS_2 Oxidation and Friction, *ACS Appl. Mater. Interfaces* **9** (2017) 28019–28026.

[318] B. Vierneusel, T. Schneider, S. Tremmel, S. Wartzack, T. Gradt, Humidity resistant MoS_2 coatings deposited by unbalanced magnetron sputtering, *Surf. Coat. Tech.* **235** (2013) 97–107.

[319] D. O. Dumcenco, H. Kobayashi, Z. Liu, Y.-S. Huang, K. Suenaga, Visualization and quantification of transition metal atomic mixing in $Mo_{1-x}W_xS_2$ single layers, *Nat. Commun.* **4** (2013).

[320] T. Liu, C. Fang, B. Yu, Y. You, H. Niu, R. Zhou, J. Zhang, J. Xu, Vanadium-doping in interlayer-expanded MoS_2 nanosheets for the efficient electrocatalytic hydrogen evolution reaction, *Inorg. Chem. Front.* **7** (2020) 2497–2505.

[321] J. S. Zabinski, M. S. Donley, S. D. Walck, T. R. Schneider, N. T. Mcdevitt, The Effects of Dopants on the Chemistry and Tribology of Sputter-Deposited MoS_2 Films, *Tribol. T.* **38** (1995) 894–904.

[322] M. Simmonds, A. Savan, E. Pflüger, H. van Swygenhoven, Mechanical and tribological performance of MoS_2 co-sputtered composites, *Surf. Coat. Tech.* **126** (2000) 15–24.

[323] H. Li, G. Zhang, L. Wang, Low humidity-sensitivity of MoS_2/Pb nanocomposite coatings, *Wear* **350-351** (2016) 1–9.

[324] C. Kuru, Controlled Vanadium Doping of MoS_2 Thin Films Through Co-sputtering and Thermal Sulfurization, *Cumhuriyet Science Journal* **41** (2020) 305–310.

[325] J. R. Lince, M. R. Hilton, A. S. Bommannavar, Metal incorporation in sputter-deposited MoS_2 films studied by extended x-ray absorption fine structure, *J. Mater. Res.* **10** (1995) 2091–2105.

[326] D. G. Teer, J. Hampshire, V. Fox, V. Bellido-Gonzalez, The tribological properties of MoS_2/metal composite coatings deposited by closed field magnetron sputtering, *Surf. Coat. Tech.* **94-95** (1997) 572–577.

[327] G. Jayaram, L. D. Marks, M. R. Hilton, Nanostructure of Au-20% Pd layers in MoS_2 multilayer solid lubricant films, *Surf. Coat. Tech.* **76-77** (1995) 393–399.

[328] M. R. Hilton, R. Bauer, S. V. Didziulis, M. T. Dugger, J. M. Keem, J. Scholhamer, Structural and tribological studies of MoS_2 solid lubricant films having tailored metal-multilayer nanostructures, *Surf. Coat. Tech.* **53** (1992) 13–23.

[329] X. Qin, Microstructure, mechanical and tribological behaviors of MoS_2-Ti composite coatings deposited by a hybrid HIPIMS method, *Surf. Coat. Tech.* **228** (2013) 275–281.

[330] Z. Hui, Z. Jun, W. Qing-ping, W. Zhi-hua, S. Rui-peng, The effect of Ti content on the structural and mechanical properties of MoS_2 Ti composite coatings deposited by unbalanced magnetron sputtering system, *Phys. Procedia* **18** (2011) 234–239.

[331] N. Renevier, J. Hamphire, V. Fox, J. Witts, T. Allen, D. Teer, Advantages of using self-lubricating, hard, wear-resistant MoS_2-based coatings, *Surf. Coat. Tech.* **142-144** (2001) 67–77.

[332] E. Arslan, F. Bülbül, A. Alsaran, A. Celik, I. Efeoglu, The effect of deposition parameters and Ti content on structural and wear properties of MoS_2-Ti coatings, *Wear* **259** (2005) 814–819.

[333] X.-z. Ding, X. Zeng, X. He, Z. Chen, Tribological properties of Cr- and Ti-doped MoS_2 composite coatings under different humidity atmosphere, *Surf. Coat. Tech.* **205** (2010) 224–231.

[334] M. Ye, G. Zhang, Y. Ba, T. Wang, X. Wang, Z. Liu, Microstructure and tribological properties of MoS_2+Zr composite coatings in high humidity environment, *Appl. Surf. Sci.* **367** (2016) 140–146.

[335] N. Renevier, V. Fox, D. Teer, J. Hampshire, Coating characteristics and tribological properties of sputter-deposited MoS_2/metal composite coatings deposited by closed field unbalanced magnetron sputter ion plating, *Surf. Coat. Tech.* **127** (2000) 24–37.

[336] T. Spalvins, Frictional and morphological properties of Au-MoS_2 films sputtered from a compact target MoS_x, *J. Phys. D Appl. Phys.* **118** (1984) 375–384.

[337] C.-T. Duong, J.-H. Lee, Y. Cho, J.-S. Nam, H.-N. Kim, S.-S. Lee, S. Park, Effect of protein concentrations of bovine serum albumin and γ-globulin on the frictional response of a cobalt-chromium femoral head, *J. Mater. Sci. Mater. Med.* **23** (2012) 1323–1330.

[338] J. Charnley, The Lubrication of Animal Joints in Relation to Surgical Reconstruction by Arthroplasty, *Ann. Rheum. Dis.* **19** (1960) 10–19.

[339] D. Dowson, Z.-M. Jin, Metal-on-metal hip joint tribology, *Proc. Inst. Mech. Eng. H* **220** (2006) 107–118.

[340] I. Reimann, J. Stougaahd, A. Northeved, S. J. Johnsen, Demonstration of Boundary Lubrication by Synovial Fluid, *Acta Orthop. Scand.* **46** (1975) 1–10.

[341] H. Stevenson, M. Jaggard, P. Akhbari, U. Vaghela, C. Gupte, P. Cann, The role of denatured synovial fluid proteins in the lubrication of artificial joints, *Biotribology* **17** (2019) 49–63.

[342] M. Wimmer, C. Sprecher, R. Hauert, G. Täger, A. Fischer, Tribochemical reaction on metal-on-metal hip joint bearings, *Wear* **255** (2003) 1007–1014.

[343] M. Gispert, A. Serro, R. Colaço, B. Saramago, Friction and wear mechanisms in hip prosthesis: Comparison of joint materials behaviour in several lubricants, *Wear* **260** (2006) 149–158.

[344] M. Wimmer, M. Laurent, M. Mathew, C. Nagelli, Y. Liao, L. Marks, J. Jacobs, A. Fischer, The effect of contact load on CoCrMo wear and the formation and retention of tribofilms, *Wear* **332-333** (2015) 643–649.

[345] A.-M. Trunfio-Sfarghiu, Y. Berthier, M.-H. Meurisse, J.-P. Rieu, Multiscale analysis of the tribological role of the molecular assemblies of synovial fluid. Case of a healthy joint and implants, *Tribol. Int.* **40** (2007) 1500–1515.

[346] T. Pratap, K. Patra, Mechanical micro-texturing of Ti-6Al-4V surfaces for improved wettability and bio-tribological performances, *Surf. Coat. Technol.* **349** (2018) 71–81.

[347] M. Łępicka, A. Ciszewski, K. Golak, M. Grądzka-Dahlke, A Comparative Study of Friction and Wear Processes of Model Metallic Biomaterials Including Registration of Friction-Induced Temperature Response of a Tribological Pair, *Materials* **12** (2019) 4163.

[348] D. Sun, J. A. Wharton, R. J. K. Wood, Effects of proteins and pH on tribocorrosion performance of cast CoCrMo - a combined electrochemical and tribological study, *Tribol. - Mater. Surf. Interfaces* **2** (2008) 150–160.

[349] J. Eichler, H.-J. Eichler, Ausbreitung von Lichtwellen, in *Laser: Bauformen, Strahlführung, Anwendungen,* Springer, Berlin/Heidelberg, Germany (2010) 231–263.

[351] M. Fox, Introduction, in *Optical properties of solids,* 2nd ed., Oxford University Press, London, UK (2010).

[352] P. Johnson, R. Christy, Optical constants of transition metals: Ti, V, Cr, Mn, Fe, Co, Ni, and Pd, *Phys. Rev. B* **9** (1974) 5056–5070.

[353] W. S. M. Werner, K. Glantschnig, C. Ambrosch-Draxl, Optical Constants and Inelastic Electron-Scattering Data for 17 Elemental Metals, *J. Phys. Chem. Ref. Data* **38** (2009) 1013–1092.

[354] M. R. Querry, *Optical Constants,* `https://apps.dtic.mil/sti/citations/ADA158623`, 1985, (accessed: 30.06.2024).

[355] T. R. Leite, L. Zschiedrich, O. Kizilkaya, K. M. McPeak, Resonant Plasmonic–Biomolecular Chiral Interactions in the Far-Ultraviolet: Enantiomeric Discrimination of sub-10 nm Amino Acid Films, *Nano Lett.* **22** (2022) 7343–7350.

[356] D. J. Rowe, D. Smith, J. S. Wilkinson, Complex refractive index spectra of whole blood and aqueous solutions of anticoagulants, analgesics and buffers in the mid-infrared, *Sci. Rep.* **7** (2017).

[357] F. Cheng, P.-H. Su, J. Choi, S. Gwo, X. Li, C.-K. Shih, Epitaxial Growth of Atomically Smooth Aluminum on Silicon and Its Intrinsic Optical Properties, *ACS Nano* **10** (2016) 9852–9860.

[358] E. T. Arakawa, M. W. Williams, T. Inagaki, Optical properties of arc-evaporated carbon films between 0.6 and 3.8 eV, *J. Appl. Phys.* **48** (1977) 3176–3177.

[359] K. Sato, Reflectivity Spectra and Optical Constants of Pyrites (FeS_2, CoS_2 and NiS_2) between 0.2 and 4.4 eV, *J. Phys. Soc. Jpn.* **53** (1984) 1617–1620.

[360] J. Cook, M. van der Meer, The optical properties of sputtered Co3O4 films, *Thin Solid Films* **144** (1986) 165–176.

[361] A. B. Djurišić, E. H. Li, Optical properties of graphite, *J. Appl. Phys.* **85** (1999) 7404–7410.

[362] A. R. Beal, H. P. Hughes, Kramers-Kronig analysis of the reflectivity spectra of 2H-MoS_2, 2H-$MoSe_2$ and 2H-$MoTe_2$, *J. Phys. C Solid State* **12** (1979) 881–890.

[363] O. de Melo, Y. González, A. Climent-Font, P. Galán, A. Ruediger, M. Sánchez, C. Calvo-Mola, G. Santana, V. Torres-Costa, Optical and electrical properties of MoO_2 and MoO_3 thin films prepared from the chemically driven isothermal close space vapor transport technique, *J. Phys. Condens. Matter* **31** (2019) 295703.

[364] L. Lajaunie, F. Boucher, R. Dessapt, P. Moreau, Strong anisotropic influence of local-field effects on the dielectric response of α-MoO_3, *Phys. Rev. B* **88** (2013).

[365] K. Sarakinos, J. Alami, S. Konstantinidis, High power pulsed magnetron sputtering: A review on scientific and engineering state of the art, *Surf. Coat. Technol.* **204** (2010) 1661–1684.

[366] G. Greczynski, I. Petrov, J. E. Greene, L. Hultman, Paradigm shift in thin-film growth by magnetron sputtering: From gas-ion to metal-ion irradiation of the growing film, *J. Vac. Sci. Technol. A* **37** (2019).

[368] M. Dieterle, G. Mestl, Raman spectroscopy of molybdenum oxides Part II. Resonance Raman spectroscopic characterization of the molybdenum oxides Mo_4O_{11} and MoO_2, *Phys. Chem. Chem. Phys.* **4** (2002) 822–826.

[369] S. Koch, R. Büscher, I. Tikhovski, H. Brauer, A. Runiewicz, W. Dudzinski, A. Fischer, Mechanical, chemical and tribological properties of the nickel-free high-nitrogen steel X13CrMnMoN18-14-3 (1.4452), *Materialwiss. Werkst.* **33** (2002) 705–715.

[370] S. Radice, M. Q. Neto, A. Fischer, M. A. Wimmer, Nickel-free high-nitrogen austenitic steel outperforms CoCrMo alloy regarding tribocorrosion in simulated inflammatory synovial fluids, *J. Orthop. Res.* **40** (2022) 1397–1408.

[372] M. Mölders, A. Fischer, M. Wiemann, Biocompatibility of a nickel-free austenitic steel assayed by osteoblastic MC3T3-E1 cells, *Materialwiss. Werkst.* **33** (2002) 775–778.

[373] M. Fini, N. N. Aldini, P. Torricelli, G. Giavaresi, V. Borsari, H. Lenger, J. Bernauer, R. Giardino, R. Chiesa, A. Cigada, A new austenitic stainless steel with negligible nickel content: An in vitro and in vivo comparative investigation, *Biomaterials* **24** (2003) 4929–4939.

[374] P. Torricelli, M. Fini, V. Borsari, H. Lenger, J. Bernauer, M. Tschon, V. Bonazzi, R. Giardino, Biomaterials in orthopedic surgery: Effects of a nickel-reduced stainless steel on in vitro proliferation and activation of human osteoblasts, *Int. J. Artif. Organs* **26** (2003) 952–957.

[375] M. Fini, G. Giavaresi, R. Giardino, H. Lenger, J. Bernauer, L. Rimondini, P. Torricelli, V. Borsari, L. Chiusoli, R. Chiesa, A. Cigada, A new austenitic stainless steel with a negligible amount of nickel: An in vitro study in view of its clinical application in osteoporotic bone, *J. Biomed. Mater. Res. B.* **71** (2004) 30–37.

[376] Y. Yu, T. Ding, Y. Xue, J. Sun, Osteoinduction and long-term osseointegration promoted by combined effects of nitrogen and manganese elements in high nitrogen nickel-free stainless steel, *J. Mater. Chem. B* **4** (2016) 801–812.

[377] M. Becerikli, H. Jaurich, C. Wallner, J. Wagner, M. Dadras, B. Jettkant, F. Pöhl, M. Seifert, O. Jung, B. Mitevski, A. Karkar, L. Marcus, A. Fischer, M. Kauther, B. Behr, P2000 - A high-nitrogen austenitic steel for application in bone surgery, *PLoS One* **14** (2019) e0214384.

[378] M. D. Kauther, K. Gödde, M. Burggraf, G. Hilken, A. Wissmann, C. Krüger, S. Lask, O. Jung, B. Mitevski, A. Fischer, M. Dudda, B. Behr, M. Herten, In-vivo comparison of the Ni-free steel X13CrMnMoN18-14-3 and titanium alloy implants in rabbit femora - A promising steel for orthopedic surgery, *J. Biomed. Mater. Res. B.* **109** (2021) 797–807.

[379] S. W. Alfons Fischer, M. Wimmer, The tribological difference between biomedical steels and CoCrMo-alloys, *J. Mech. Behav. Biomed. Mater.* **4** (2012) 50–62.

[380] D. Hall, R. Pourzal, M. Mathew, H. Lundberg, J. Jacobs, R. Urban, Degradation Modes of CoCrMo and Ti6Al4VAlloys in Modular Head-Neck Junctions of Retrieved Hip Prostheses, *Transactions of ORS* (2016) 0400.

[381] D. J. Hall, R. Pourzal, H. J. Lundberg, M. T. Mathew, J. J. Jacobs, R. M. Urban, Mechanical, chemical and biological damage modes within head-neck tapers of CoCrMo and Ti6Al4V contemporary hip replacements, *J. Biomed. Mater. Res. B.* **106** (2018) 1672–1685.

[382] A. Fischer, D. Janssen, M. Wimmer, The Influence of Molybdenum on the Fretting Corrosion Behavior of CoCr/TiAlV Couples, *Biotribology* **11** (2017) 8–19.

[383] M. A. Wimmer, S. Radice, D. Janssen, A. Fischer, Fretting-corrosion of CoCr-alloys against TiAl6V4: The importance of molybdenum in oxidative biological environments, *Wear* **477** (2021) 203813.

[385] A. Fischer, P. Telouk, M. A. Wimmer, The gross slip fretting corrosion mechanisms of biomedical ceramic-metal couples, *Biotribology* **35-36** (2023) 100252.

[386] M. Johnson, Fetal Bovine Serum, *Mater. Methods* **2** (2012).

[387] R. I. Freshney, Defined Media and Supplements, in *Culture of Animal Cells,* 6th ed., Wiley, Hoboken, NJ, USA (2010) 99–114.

[388] H. Maradit Kremers, D. R. Larson, C. S. Crowson, W. K. Kremers, R. E. Washington, C. A. Steiner, W. A. Jiranek, D. J. Berry, Prevalence of Total Hip and Knee Replacement in the United States, *J. Bone Joint Surg. Am.* **97** (2015) 1386–1397.

[389] A. Wengler, U. Nimptsch, T. Mansky, Hip and Knee Replacement in Germany and the USA, *Dtsch. Arztebl. Int.* (2014).

[390] E. W. Karlson, L. A. Mandl, G. N. Aweh, O. Sangha, M. H. Liang, F. Grodstein, Total hip replacement due to osteoarthritis: the importance of age, obesity, and other modifiable risk factors, *Am. J. Med.* **114** (2003) 93–98.

[391] C. D. Fryar, M. D. Carroll, C. L. Ogden, *Prevalence of overweight, obesity, and extreme obesity among adults aged 20 and over: United States, 1960-1962 through 2011-2014.* 2016, URL: `https://www.cdc.gov/nchs/data/hestat/obesity_adult_13_14/obesity_adult_13_14.htm`.

[392] E. Winter, Entwicklung und aktueller Stand der Hüftendoprothetik, in *Medizintechnik* (Eds.: E. Wintermantel, S.-W. Ha), 5th ed., Springer, Berlin/Heidelberg, Germany (2009).

[393] Y.-H. Kim, J.-W. Park, J.-S. Kim, There Is No Significant Difference in Fretting and Corrosion at the Trunnion of Metal and Ceramic Heads, *Orthopedics* **42** (2019).

[394] J. B. Mistry, M. Chughtai, R. K. Elmallah, A. Diedrich, S. Le, M. Thomas, M. A. Mont, Trunnionosis in total hip arthroplasty: a review, *J. Orthop. Traumatol.* **17** (2016) 1–6.

[395] D. J. Berry, M. P. Abdel, J. J. Callaghan, What Are the Current Clinical Issues in Wear and Tribocorrosion? *Clin. Orthop. Relat. R.* **472** (2014) 3659–3664.

[396] J. L. Gilbert, C. A. Buckley, J. J. Jacobs, In vivo corrosion of modular hip prosthesis components in mixed and similar metal combinations. The effect of crevice, stress, motion, and alloy coupling, *J. Biomed. Mater. Res.* **27** (1993) 1533–1544.

[397] J. R. Goldberg, J. L. Gilbert, J. J. Jacobs, T. W. Bauer, W. Paprosky, S. Leurgans, A multicenter retrieval study of the taper interfaces of modular hip prostheses, *Clin. Orthop. Relat. Res.* **401** (2002) 149–161.

[398] J. J. Jacobs, R. M. Urban, J. L. Gilbert, A. K. Skipor, J. Black, M. Jasty, J. O. Galante, Local and distant products from modularity, *Clin. Orthop. Relat. R.* **319** (1995) 94–105.

[399] C. Lohmann, R. Hameister, G. Singh, Allergies in orthopaedic and trauma surgery, *Orthop. Traumatol. Surg. Res.* **103** (2017) S75–S81.

[400] K. A. Pacheco, Allergy to Surgical Implants, *Clin. Rev. Allergy Immunol.* **56** (2019) 72–85.

[401] R. M. Urban, J. J. Jacobs, J. L. Gilbert, J. O. Galante, Migration of corrosion products from modular hip prostheses. Particle microanalysis and histopathological findings, *J. Bone Joint Surg.* **9** (1994) 1345–1359.

[402] W. Rostoker, J. O. Galante, P. Lereim, Evaluation of couple/crevice corrosion by prosthetic alloys under in vivo conditions, *J. Biomed. Mater. Res.* **12** (1978) 823–829.

[403] W. Rostoker, C. W. Pretzel, J. O. Galante, Couple corrosion among alloys for skeletal prostheses, *J. Biomed. Mater. Res.* **8** (1974) 407–419.

[404] M. Geetha, A. Singh, R. Asokamani, A. Gogia, Ti based biomaterials, the ultimate choice for orthopaedic implants - A review, *Prog. Mater. Sci.* **54** (2009) 397–425.

[405] A. Bandyopadhyay, F. Espana, V. K. Balla, S. Bose, Y. Ohgami, N. M. Davies, Influence of porosity on mechanical properties and in vivo response of Ti6Al4V implants, *Acta Biomater.* **6** (2010) 1640–1648.

[406] F. A. España, V. K. Balla, S. Bose, A. Bandyopadhyay, Design and fabrication of CoCrMo alloy based novel structures for load bearing implants using laser engineered net shaping, *Mater. Sci. Eng. C Mater. Biol. Appl.* **30** (2010) 50–57.

[407] E. F. Morgan, G. U. Unnikrisnan, A. I. Hussein, Bone Mechanical Properties in Healthy and Diseased States, *Annu. Rev. Biomed. Eng.* **20** (2018) 119–143.

[408] R. Burchard, J. A. Graw, C. Soost, J. Schmitt, Stress shielding effect after total hip arthroplasty varies between combinations of stem design and stiffness-a comparing biomechanical finite element analysis, *Int. Orthop.* **47** (2023) 1981–1987.

[409] D. Savio, A. Bagno, When the Total Hip Replacement Fails: A Review on the Stress-Shielding Effect, *Processes* **10** (2022) 612.

[410] M. Ridzwan, S. Shuib, A. Hassan, A. Shokri, M. Mohamad Ib, Problem of Stress Shielding and Improvement to the Hip Implant Designs: A Review, *J. Med. Sci.* **7** (2007) 460–467.

[411] H. C. Bäcker, C. H. Wu, A. Kienzle, C. Perka, C. Gwinner, Mechanical failure of total hip arthroplasties and associated risk factors, *Arch. Orthop. Trauma Surg.* **143** (2022) 1061–1069.

[412] P. M. Pellicci, E. A. Salvati, H. J. Robinson, Mechanical failures in total hip replacement requiring reoperation, *J. Bone Joint Surg.* **61** (1979) 28–36.

[413] B. Aksakal, Ö. S. Yildirim, H. Gul, Metallurgical failure analysis of various implant materials used in orthopedic applications, *J. Fail. Anal. Prev.* **4** (2004) 17–23.

[414] G. Wick, A. Backovic, E. Rabensteiner, N. Plank, C. Schwentner, R. Sgonc, The immunology of fibrosis: innate and adaptive responses, *Trends Immunol.* **31** (2010) 110–119.

[415] Y. Abu-Amer, I. Darwech, J. C. Clohisy, Aseptic loosening of total joint replacements: mechanisms underlying osteolysis and potential therapies, *Arthritis Res. Ther.* **9** (2007) S6.

[416] A. F. Mavrogenis, R. Dimitriou, J. Parvizi, G. C. Babis, Biology of implant osseointegration, *J. Musculoskelet Neuronal Interact.* **9** (2009) 61–71.

[417] C. S. M. Hoenders, M. C. Harmsen, M. J. A. van Luyn, The local inflammatory environment and microorganisms in "aseptic" loosening of hip prostheses, *J. Biomed. Mater. Res. B Appl. Biomater.* **86B** (2007) 291–301.

[418] G. Tan, J. Xu, W. M. Chirume, J. Zhang, H. Zhang, X. Hu, Antibacterial and anti-inflammatory coating materials for orthopedic implants: A review, *Coatings* **11** (2021) 1401.

[419] J. Schierholz, J. Beuth, Implant infections: a haven for opportunistic bacteria, *J. Hosp. Infect.* **49** (2001) 87–93.

[420] D. C. Coraça-Huber, L. Kreidl, S. Steixner, M. Hinz, D. Dammerer, M. Fille, Identification and morphological characterization of biofilms formed by strains causing infection in orthopedic implants, *Pathogens* **9** (2020) 649.

[421] K. A. Pacheco, Allergy to Surgical Implants, *Clin. Rev. Allergy Immunol.* **56** (2018) 72–85.

[422] P. Thomas, L. R. Braathen, M. Dörig, J. Auböck, F. Nestle, T. Werfel, H. G. Willert, Increased metal allergy in patients with failed metal-on-metal hip arthroplasty and peri-implant T-lymphocytic inflammation, *Allergy* **64** (2009) 1157–1165.

[423] P. Sadoghi, M. Liebensteiner, M. Agreiter, A. Leithner, N. Böhler, G. Labek, Revision Surgery After Total Joint Arthroplasty: A Complication-Based Analysis Using Worldwide Arthroplasty Registers, *The Journal of Arthroplasty* **28** (2013) 1329–1332.

[424] J. C. Clohisy, G. Calvert, F. Tull, D. McDonald, W. J. Maloney, Reasons for Revision Hip Surgery: A Retrospective Review, *Clinical Orthopaedics and Related Research* **429** (2004) 188–192.

[425] M. Sundfeldt, L. V Carlsson, C. B Johansson, P. Thomsen, C. Gretzer, Aseptic loosening, not only a question of wear: A review of different theories, *Acta Orthopaedica* **77** (2006) 177–197.

[426] T. McTighe, *Cementless Modular Stems,* 2002, URL: `http://www.jisrf.org/pdfs/cementless-modular-stems.pdf` (visited on 10/19/2021).

[427] H. Krishnan, S. P. Krishnan, G. Blunn, J. A. Skinner, A. J. Hart, Modular neck femoral stems, *Bone Joint J.* **95-B** (2013) 1011–1021.

[428] S. Y. Jauch, G. Huber, K. Sellenschloh, H. Haschke, M. Baxmann, T. M. Grupp, M. M. Morlock, Micromotions at the taper interface between stem and neck adapter of a bimodular hip prosthesis during activities of daily living, *J. Orthop. Res.* **31** (2013) 1165–1171.

[429] S. A. Brown, C. A. C. Flemming, J. S. Kawalec, H. E. Placko, C. Vassaux, K. Merritt, J. H. Payer, M. J. Kraay, Fretting corrosion accelerates crevice corrosion of modular hip tapers, *J. Appl. Biomater.* **6** (1995) 19–26.

[430] A. Panagiotidou, T. Cobb, J. Meswania, J. Skinner, A. Hart, F. Haddad, G. Blunn, Effect of impact assembly on the interface deformation and fretting corrosion of modular hip tapers: An in vitro study, *J. Orthop. Res.* **36** (2017) 405–416.

[431] C. Compère, M.-N. Bellon-Fontaine, P. Bertrand, D. Costa, P. Marcus, C. Poleunis, C.-M. Pradier, B. Rondot, M. G. Walls, Kinetics of conditioning layer formation on stainless steel immersed in seawater, *Biofouling* **17** (2001) 129–145.

[432] S. Sarkar, S. Kundu, Protein (BSA) adsorption on hydrophilic and hydrophobic surfaces, *Mater. Today Proc.* (2023).

[433] N. J. Hallab, K. Mikecz, C. Vermes, A. Skipor, J. J. Jacobs, Differential lymphocyte reactivity to serum-derived metal-protein complexes produced from cobalt-based and titanium-based implant alloy degradation, *J. Biomed. Mater. Res.* **56** (2001) 427–436.

[434] P. F. Doorn, P. A. Campbell, J. Worrall, P. D. Benya, H. A. McKellop, H. C. Amstutz, Metal wear particle characterization from metal on metal total hip replacements: Transmission electron microscopy study of periprosthetic tissues and isolated particles, *J. Biomed. Mater. Res.* **42** (1998) 103–111.

[435] I. Catelas, P. A. Campbell, J. D. Bobyn, J. B. Medley, O. L. Huk, Wear particles from metal-on-metal total hip replacements: Effects of implant design and implantation time, *Proc. Inst. Mech. Eng. H* **220** (2006) 195–208.

[436] C. Brown, S. Williams, J. L. Tipper, J. Fisher, E. Ingham, Characterisation of wear particles produced by metal on metal and ceramic on metal hip prostheses under standard and microseparation simulation, *J. Mater. Sci.: Mater. Med.* **18** (2006) 819–827.

[437] C. Colombie, Y. Berthier, A. Floquet, L. Vincent, M. Godet, Fretting: Load carrying capacity of wear debris, *J. Tribol.* **106** (1984) 194–201.

[438] N. Fillot, I. Iordanoff, Y. Berthier, Wear modeling and the third body concept, *Wear* **262** (2007) 949–957.

[439] K. Subramanian, J.-H. Wu, D. A. Rigney, The role of vorticity in the formation of tribomaterial during sliding, *MRS Online Proceedings Library* **821** (2004) 330–335.

[440] D. A. Rigney, S. Karthikeyan, The evolution of tribomaterial during sliding: A brief introduction, *Tribol. Lett.* **39** (2010) 3–7.

[441] K. Wolff, Z. Liu, D. Braun, J. Schneider, C. Greiner, Chronology of the microstructure evolution for pearlitic steel under unidirectional tribological loading, *Tribol. Int.* **102** (2016) 540–545.

[442] D. Rigney, J. Hammerberg, Mechanical mixing and the development of nanocrystalline material during the sliding of metals. In *Advanced materials in the 21st century: The 1999 Julia R. Weertman Symposium* (Eds.: Y. Chung, D. Dunand, . Liaw, G. Olson), The Minerals, Metals & Materials Society, Warrendale, PA, USA, () 465–474.

[443] T. Quinn, Review of oxidational wear Part II: Recent developments and future trends in oxidational wear research, *Tribol. Int.* **16** (1983) 305–315.

[444] M. Godet, The third-body approach: A mechanical view of wear, *Wear* **100** (1984) 437–452.

[445] B. K. Muralidhara, V. Prakash, Molten globule state of human serum albumin in urea, *Curr. Sci. India* **72** (1997) 831–834.

[446] K. Takeda, A. Wada, K. Yamamoto, Y. Moriyama, K. Aoki, Conformational change of bovine serum albumin by heat treatment, *J. Protein Chem.* **8** (1989) 653–659.

[447] R. Wetzel, M. Becker, J. Behlke, H. Billwitz, S. Böhm, B. Ebert, H. Hamann, J. Krumbiegel, G. Lassmann, Temperature Behaviour of Human Serum Albumin, *Eur. J. Biochem.* **104** (1980) 469–478.

[448] N. Tanaka, H. Nishizawa, S. Kunugi, Structure of pressure-induced denatured state of human serum albumin: a comparison with the intermediate in urea-induced denaturation, *BBA-Protein Struct. M.* **1338** (1997) 13–20.

[449] R. Pourzal, E. Martin, S. Vajpayee, Y. Liao, M. Wimmer, K. Shull, Investigation of the role of tribofilms in self-mating CoCrMo systems utilizing a quartz crystal microtribometer, *Tribol. Int.* **72** (2014) 161–171.

[450] H. Matusiewicz, Potential release of in vivo trace metals from metallic medical implants in the human body: from ions to nanoparticles–a systematic analytical review, *Acta Biomater.* **10** (2014) 2379–2403.

[451] M. Godoy-Gallardo, U. Eckhard, L. M. Delgado, Y. J. D. de Roo Puente, M. Hoyos-Nogués, F. J. Gil, R. A. Perez, Antibacterial approaches in tissue engineering using metal ions and nanoparticles: From mechanisms to applications, *Bioact. Mater.* **6** (2021) 4470–4490.

[452] A. Hartmann, F. Hannemann, J. Lützner, A. Seidler, H. Drexler, K.-P. Günther, J. Schmitt, Metal ion concentrations in body fluids after implantation of hip replacements with metal-on-metal bearing–systematic review of clinical and epidemiological studies, *PLoS One* **8** (2013) e70359.

[453] A. K. Madl, M. Liong, M. Kovochich, B. L. Finley, D. J. Paustenbach, G. Oberdörster, Toxicology of wear particles of cobalt-chromium alloy metal-on-metal hip implants Part I: Physicochemical properties in patient and simulator studies, *Nanomedicine* **11** (2015) 1201–1215.

[454] B. Scharf, C. C. Clement, V. Zolla, G. Perino, B. Yan, S. G. Elci, E. Purdue, S. Goldring, F. Macaluso, N. Cobelli, R. W. Vachet, L. Santambrogio, Molecular analysis of chromium and cobalt-related toxicity, *Sci. Rep.* **4** (2014) 5729.

[455] A. J. Hart, P. D. Quinn, B. Sampson, A. Sandison, K. D. Atkinson, J. A. Skinner, J. J. Powell, J. F. W. Mosselmans, The chemical form of metallic debris in tissues surrounding metal-on-metal hips with unexplained failure, *Acta Biomater.* **6** (2010) 4439–4446.

[456] D. Wu, M. Gucwa, M. P. Czub, D. R. Cooper, I. G. Shabalin, R. Fritzen, S. Arya, U. Schwarz-Linek, C. A. Blindauer, W. Minor, A. J. Stewart, Structural and biochemical characterisation of Co^{2+}-binding sites on serum albumins and their interplay with fatty acids, *Chem. Sci.* **14** (2023) 6244–6258.

[457] M. Sokołowska, M. Wszelaka-Rylik, J. Poznański, W. Bal, Spectroscopic and thermodynamic determination of three distinct binding sites for Co(II) ions in human serum albumin, *J. Inorg. Biochem.* **103** (2009) 1005–1013.

[458] E. Mothes, P. Faller, Evidence that the principal CoII-binding site in human serum albumin is not at the N-terminus: implication on the albumin cobalt binding test for detecting myocardial ischemia, *Biochemistry* **46** (2007) 2267–2274.

[459] D. S. Dunn, M. B. Bogart, C. S. Brossia, G. A. Cragnolino, Corrosion of iron under alternating wet and dry conditions, *Corrosion* **56** (2000) 470–481.

[460] I. Chamritski, G. Burns, Infrared- and Raman-active phonons of magnetite, maghemite, and hematite: a computer simulation and spectroscopic study, *J. Phys. Chem. B* **109** (2005) 4965–4968.

[461] A. M. Jubb, H. C. Allen, Vibrational spectroscopic characterization of hematite, maghemite, and magnetite thin films produced by vapor deposition, *ACS Appl. Mater. Interfaces* **2** (2010) 2804–2812.

[462] Y. Li, W. Qiu, F. Qin, H. Fang, V. G. Hadjiev, D. Litvinov, J. Bao, Identification of Cobalt Oxides with Raman Scattering and Fourier Transform Infrared Spectroscopy, *J. Phys. Chem. C* **120** (2016) 4511–4516.

[463] I. A. de Castro, R. S. Datta, J. Z. Ou, A. Castellanos-Gomez, S. Sriram, T. Daeneke, K. Kalantar-Zadeh, Molybdenum oxides - from fundamentals to functionality, *Adv. Mater.* **29** (2017) 1701619.

[465] C. Pettenkofer, I. Pockrand, A. Otto, Surface enhanced Raman spectra of oxygen adsorbed on silver, *Surf. Sci.* **135** (1983) 52–64.

[466] B. Champagnon, G. Panczer, B. Chazallon, L. Arnaud, P. Duval, V. Lipenkov, Nitrogen and oxygen guest molecules in clathrate hydrates: different sites revealed by Raman spectroscopy, *J. Raman Spectrosc.* **28** (1997) 711–715.

[467] H. Takeuchi, Raman structural markers of tryptophan and histidine side chains in proteins, *Biopolymers* **72** (2003) 305–317.

[468] A. G. Walton, W. B. Rippon, J. L. Koenig, Raman spectroscopy of proline oligomers and poly-L-proline, *J. Am. Chem. Soc.* **92** (1970) 7455–7459.

[469] V. J. C. Lin, J. L. Koenig, Raman Studies of Bovine Serum Albumin, *Biopolymers* **15** (1976) 203–218.

[470] D. R. Parachalil, B. Brankin, J. McIntyre, H. J. Byrne, Raman spectroscopic analysis of high molecular weight proteins in solution – considerations for sample analysis and data pre-processing, *Analyst* **143** (2018) 5987–5998.

[471] H. Horiue, M. Sasaki, Y. Yoshikawa, M. Toyofuku, S. Shigeto, Raman spectroscopic signatures of carotenoids and polyenes enable label-free visualization of microbial distributions within pink biofilms, *Sci. Rep.* **10** (2020).

[472] F. Madzharova, Z. Heiner, J. Kneipp, Surface Enhanced Hyper-Raman Scattering of the Amino Acids Tryptophan, Histidine, Phenylalanine, and Tyrosine, *J. Phys. Chem. C* **121** (2017) 1235–1242.

[473] N. Kuhar, S. Umapathy, Probing the Stepwise Unfolding of Bovine Serum Albumin Using 2D Correlation Raman Spectroscopic Analysis, *Anal. Chem.* **92** (2020) 13509–13517.

[474] W.-T. Cheng, M.-T. Liu, H.-N. Liu, S.-Y. Lin, Micro-Raman spectroscopy used to identify and grade human skin pilomatrixoma, *Microsc. Res. Techniq.* **68** (2005) 75–79.

[475] J. Marx, G. Hudry-Clergeon, F. Capet-Antonini, L. Bernard, Laser Raman spectroscopy study of bovine fibrinogen and fibrin, *Biochim. Biophys. Acta* **578** (1979) 107–115.

[476] Y.-S. Li, K. Wang, P. He, B. X. Huang, P. Kovacs, Surface-enhanced Raman spectroelectrochemical studies of corrosion films on implant Co-Cr-Mo alloy in biosimulating solutions, *J. Raman Spectrosc.* **30** (1999) 97–103.

[477] T. Hoar, D. Mears, Corrosion-resistant alloys in chloride solutions: materials for surgical implants, *P. R. Soc. Lond. Ser. A* **294** (1966) 486–510.

[478] A. Ouerd, C. Alemany-Dumont, B. Normand, S. Szunerits, Reactivity of CoCrMo alloy in physiological medium: Electrochemical characterization of the metal/protein interface, *Electrochim. Acta* **53** (2008) 4461–4469.

[479] M. Talha, C. Behera, O. Sinha, A review on nickel-free nitrogen containing austenitic stainless steels for biomedical applications, *Mater. Sci. Eng. C* **33** (2013) 3563–3575.

[480] J. E. Maslar, W. S. Hurst, T. A. Vanderah, I. Levin, The Raman spectra of Cr_3O_8 and Cr_2O_5, *J. Raman Spectrosc.* **32** (2001) 201–206.

[481] O. Monnereau, L. Tortet, C. Grigorescu, D. Savastru, C. Iordanescu, F. Guinneton, R. Notonier, A. Tonetto, T. Zhang, I. Mihailescu, D. Stanoi, H. Trodahl, *J. Optoelectron. Adv. M.* **12** (2010) 1752–1758.

[482] R. L. Frost, Raman microscopy of selected chromate minerals, *J. Raman Spectrosc.* **35** (2004) 153–158.

[483] J. D. Ramsey, L. Xia, M. W. Kendig, R. L. McCreery, Raman spectroscopic analysis of the speciation of dilute chromate solutions, *Corrosion Science* **43** (2001) 1557–1572.

[484] Y. W. Long, W. W. Zhang, L. X. Yang, Y. Yu, R. C. Yu, S. Ding, Y. L. Liu, C. Q. Jin, Pressure-induced structural phase transition in $CaCrO_4$: Evidence from Raman scattering studies, *Appl. Phys. Lett.* **87** (2005) 181901.

[485] L. Hu, S. Zheng, S. Cheng, Z. Chen, B. Huang, Q. Liu, S. Xiao, J. Yang, Q. Chen, $CrPO_4$/C composite as a novel anode material for lithium-ion batteries, *J. Power Sources* **441** (2019) 227180.

[486] K. Kanamori, K. Kawai, Raman spectral study on the solution structure of the chromium(III)-EDTA complex, *Inorg. Chem.* **25** (1986) 3711–3713.

[487] L. Seguin, M. Figlarz, R. Cavagnat, J.-C. Lassègues, Infrared and Raman spectra of MoO_3 molybdenum trioxides and $MoO_3 \cdot xH_2O$ molybdenum trioxide hydrates, *Spectrochim. Acta A* **51** (1995) 1323–1344.

[488] M. Camacho-López, L. Escobar-Alarcón, M. Picquart, R. Arroyo, G. Córdoba, E. Haro-Poniatowski, Micro-Raman study of the m-MoO_2 to α-MoO_3 transformation induced by cw-laser irradiation, *Opt. Mater.* **33** (2011) 480–484.

[489] J. Mougin, T. L. Bihan, G. Lucazeau, High-pressure study of Cr_2O_3 obtained by high-temperature oxidation by X-ray diffraction and Raman spectroscopy, *J. Phys. Chem. Solids* **62** (2001) 553–563.

[490] H. Takeuchi, I. Harada, Normal coordinate analysis of the indole ring, *Spectrochim. Acta A* **42** (1986) 1069–1078.

[491] H. Schulz, M. Baranska, Identification and quantification of valuable plant substances by IR and Raman spectroscopy, *Vib. Spectrosc.* **43** (2007) 13–25.

[492] Y.-S. Liao, H. McKellop, Z. Lu, P. Campbell, P. Benya, The effect of frictional heating and forced cooling on the serum lubricant and wear of UHMW polyethylene cups against cobalt–chromium and zirconia balls, *Biomaterials* **24** (2003) 3047–3059.

[493] V. K. Maskiewicz, P. A. Williams, S. J. Prates, J. G. Bowsher, I. C. Clarke, Characterization of protein degradation in serum-based lubricants during simulation wear testing of metal-on-metal hip prostheses, *J. Biomed. Mater. Res. B.* **94B** (2010) 429–440.

[494] Y. Yan, H. Yang, Y. Su, L. Qiao, Albumin adsorption on CoCrMo alloy surfaces, *Sci. Rep.* **5** (2015).

[495] Y. Liu, Q. Zhu, C. Wang, J. Li, Tribological behavior of CoCrMo artificial knee joint with symmetrically biomimetic textured surfaces on PEEK, *Opt. Laser Technol.* **157** (2023) 108774.

[496] K. Nakashima, Y. Sawae, T. Murakami, Study on Wear Reduction Mechanisms of Artificial Cartilage by Synergistic Protein Boundary Film Formation, *JSME Int. J. Ser. C* **48** (2005) 555–561.

[497] Y. S. Tremsina, V. I. Sevastianov, S. Petrash, W. Dando, M. D. Foster, Competitive adsorption of human serum albumin and gamma-globulin from a binary protein mixture onto hexadecyltrichlorosilane coated glass, *J. Biomater. Sci. Polym. Ed.* **9** (1998) 151–161.

[498] L. E. Jamieson, A. Li, K. Faulds, D. Graham, Ratiometric analysis using Raman spectroscopy as a powerful predictor of structural properties of fatty acids, *R. Soc. Open Sci.* **5** (2018) 181483.

[499] T. Cui, W. Fan, Z. Dai, Q. Guo, G. Yu, F. Wang, Variation of the coal chemical structure and determination of the char molecular size at the early stage of rapid pyrolysis, *Appl. Energy* **179** (2016) 650–659.

[500] J. A. Orrego-Ruiz, R. Cabanzo, E. Mejía-Ospino, Study of Colombian coals using photoacoustic Fourier transform infrared spectroscopy, *Int. J. Coal Geol.* **85** (2011) 307–310.

[501] T. Ma, P. Wan, Y. Cui, G. Zhang, J. Li, J. Liu, Y. Ren, K. Yang, L. Lu, Cytocompatibility of High Nitrogen Nickel-Free Stainless Steel for Orthopedic Implants, *J. Mater. Sci. Technol.* **28** (2012) 647–653.

[502] R. D. K. Misra, C. Nune, T. C. Pesacreta, M. C. Somani, L. P. Karjalainen, Interplay between grain structure and protein adsorption on functional response of osteoblasts: Ultrafine-grained versus coarse-grained substrates, *J. Biomed. Mater. Res. A.* **101A** (2012) 1–12.

[503] A. Allred, Electronegativity values from thermochemical data, *J. Inorg. Nucl. Chem.* **17** (1961) 215–221.

[504] R. C. de Guzman, S. Y. Rabbany, PEG-Immobilized Keratin for Protein Drug Sequestration and pH-Mediated Delivery, *J. Drug Deliv.* **2016** (2016) 1–9.

[505] K. Athmakuri, M. Rohovie, C. Padala, R. Cole, R. S. Kane, Influence of Chain Length on the Diffusion and Electrophoresis of DNA Adsorbed on Heterogeneous Supported Lipid Bilayers, *Langmuir* **26** (2010) 13393–13398.

[506] R. Tilton, A. Gast, C. Robertson, Surface diffusion of interacting proteins. Effect of concentration on the lateral mobility of adsorbed bovine serum albumin, *Biophys. J.* **58** (1990) 1321–1326.

[507] A. C. Ferrari, J. Robertson, Interpretation of Raman spectra of disordered and amorphous carbon, *Phys. Rev. B* **61** (2000) 14095–14107.

[508] W. Tillmann, N. F. L. Dias, D. Stangier, M. Bayer, H. Moldenhauer, J. Debus, M. Schmitz, U. Berges, C. Westphal, Interaction effects of cathode power, bias voltage, and mid-frequency on the structural and mechanical properties of sputtered amorphous carbon films, *Appl. Surf. Sci.* **487** (2019) 857–867.

[509] A. Grill, Diamond-like carbon coatings as biocompatible materials—an overview, *Diam. Relat. Mater.* **12** (2003) 166–170.

[510] C. Love, R. Cook, T. Harvey, P. Dearnley, R. Wood, Diamond like carbon coatings for potential application in biological implants–a review, *Tribol. Int.* **63** (2013) 141–150.

[511] P. Stemmer, R. Pourzal, Y. Liao, L. Marks, M. Morlock, J. J. Jacobs, M. A. Wimmer, A. Fischer, Microstructure of Retrievals Made from Standard Cast HC-CoCrMo Alloys, in *Metal-On-Metal Total Hip Replacement Devices,* ASTM International, West Conshohocken, PA, USA (2013) 251–267.

[512] J. Giacchi, O. Fornaro, H. Palacio, Microstructural evolution during solution treatment of Co-Cr-Mo-C biocompatible alloys, *Mater. Charact.* **68** (2012) 49–57.

[513] R. Rosenthal, B. R. Cardoso, I. S. Bott, R. P. R. Paranhos, E. A. Carvalho, Phase characterization in as-cast F-75 Co-Cr-Mo-C alloy, *J. Mater. Sci.* **45** (2010) 4021–4028.

[514] J. A. Stammeier, B. Purgstaller, D. Hippler, V. Mavromatis, M. Dietzel, In-situ Raman spectroscopy of amorphous calcium phosphate to crystalline hydroxyapatite transformation, *MethodsX* **5** (2018) 1241–1250.

[515] J. E. Pemberton, L. Latifzadeh, J. P. Fletcher, S. H. Risbud, Raman spectroscopy of calcium phosphate glasses with varying calcium oxide modifier concentrations, *Chem. Mater.* **3** (1991) 195–200.

[516] T. Schmid, P. Dariz, Shedding light onto the spectra of lime: Raman and luminescence bands of CaO, $Ca(OH)_2$ and $CaCO_3$, *J. Raman Spectrosc.* **46** (2014) 141–146.

[517] X. Zhang, X.-F. Qiao, W. Shi, J.-B. Wu, D.-S. Jiang, P.-H. Tan, Phonon and Raman scattering of two-dimensional transition metal dichalcogenides from monolayer, multilayer to bulk material, *Chem. Soc. Rev.* **44** (2015) 2757–2785.

[518] S. Mignuzzi, A. J. Pollard, N. Bonini, B. Brennan, I. S. Gilmore, M. A. Pimenta, D. Richards, D. Roy, Effect of disorder on Raman scattering of single-layer MoS_2, *Phys. Rev. B* **91** (2015).

[519] H. Vogt, T. Chattopadhyay, H. Stolz, Complete first-order Raman spectra of the pyrite structure compounds FeS_2, MnS_2 and SiP_2, *J. Phys. Chem. Solids* **44** (1983) 869–873.

[520] T. P. Mernagh, A. G. Trudu, A laser Raman microprobe study of some geologically important sulphide minerals, *Chem. Geol.* **103** (1993) 113–127.

[521] A. K. Kleppe, A. P. Jephcoat, High-pressure Raman spectroscopic studies of FeS_2 pyrite, *Mineral. Mag.* **68** (2004) 433–441.

[522] M. Cheever, R. Versteegen, A. Master, A method for differentiating fetal bovine serum from newborn calf serum, *BioProcess. J.* **16** (2017).

[523] M. R. Habib, S. Wang, W. Wang, H. Xiao, S. M. Obaidulla, A. Gayen, Y. Khan, H. Chen, M. Xu, Electronic properties of polymorphic two-dimensional layered chromium disulphide, *Nanoscale* **11** (2019) 20123–20132.

[524] H. Xiao, W. Zhuang, L. Loh, T. Liang, A. Gayen, P. Ye, M. Bosman, G. Eda, X. Wang, M. Xu, Van der Waals Epitaxial Growth of 2D Layered Room-Temperature Ferromagnetic CrS_2, *Adv. Mater. Interfaces* **9** (2022) 2201353.

[525] W. Yang, A. L. Coughlin, L. Webster, G. Ye, K. Lopez, H. A. Fertig, R. He, J.-A. Yan, S. Zhang, Highly tunable Raman scattering and transport in layered magnetic Cr_2S_3 nanoplates grown by sulfurization, *2D Mater.* **6** (2019) 035029.

[526] S. Zhou, R. Wang, J. Han, D. Wang, H. Li, L. Gan, T. Zhai, Ultrathin Non-van der Waals Magnetic Rhombohedral Cr_2S_3: Space-Confined Chemical Vapor Deposition Synthesis and Raman Scattering Investigation, *Adv. Funct. Mater.* **29** (2018) 1805880.

[527] S. G. Lyapin, A. N. Utyuzh, A. E. Petrova, A. P. Novikov, T. A. Lograsso, S. M. Stishov, Raman studies of nearly half-metallic ferromagnetic CoS_2, *J. Phys. Condens. Matter* **26** (2014) 396001.

[528] L. Zhu, D. Susac, M. Teo, K. Wong, P. Wong, R. Parsons, D. Bizzotto, K. Mitchell, S. Campbell, Investigation of CoS_2-based thin films as model catalysts for the oxygen reduction reaction, *J. Catal.* **258** (2008) 235–242.

[529] E. Anastassakis, C. H. Perry, Light scattering and ir measurements in XS_2 pryite-type compounds, *J. Chem. Phys.* **64** (1976) 3604–3609.

[530] N. Kornienko, J. Resasco, N. Becknell, C.-M. Jiang, Y.-S. Liu, K. Nie, X. Sun, J. Guo, S. R. Leone, P. Yang, Operando Spectroscopic Analysis of an Amorphous Cobalt Sulfide Hydrogen Evolution Electrocatalyst, *J. Am. Chem. Soc.* **137** (2015) 7448–7455.

[531] J. Schwan, S. Ulrich, V. Batori, H. Ehrhardt, S. R. P. Silva, Raman spectroscopy on amorphous carbon films, *J. Appl. Phys.* **80** (1996) 440–447.

[532] R. J. Angel, M. Murri, B. Mihailova, M. Alvaro, Stress, strain and Raman shifts, *Z. Kristallogr. Cryst. Mater.* **234** (2018) 129–140.

[533] É. Blanco, P. Afanasiev, G. Berhault, D. Uzio, S. Loridant, Resonance Raman spectroscopy as a probe of the crystallite size of MoS_2 nanoparticles, *C. R. Chim.* **19** (2016) 1310–1314.

[534] J. Zuo, C. Xu, Y. Liu, Y. Qian, Crystallite size effects on the Raman spectra of Mn_3O_4, *Nanostructured Mater.* **10** (1998) 1331–1335.

[535] V. Swamy, Size-dependent modifications of the first-order Raman spectra of nanostructured rutile TiO_2, *Phys. Rev. B Condens. Matter Mater. Phys.* **77** (2008).

[536] M. N. Islam, A. Pradhan, S. Kumar, Effects of crystallite size distribution on the Raman-scattering profiles of silicon nanostructures, *J. Appl. Phys.* **98** (2005).

[537] P. Makreski, G. Petruševski, S. Ugarković, G. Jovanovski, Laser-induced transformation of stibnite (Sb_2S_3) and other structurally related salts, *Vib. Spectrosc.* **68** (2013) 177–182.

[538] A. Jagminas, G. Niaura, R. Žalnėravičius, R. Trusovas, G. Račiukaitis, V. Jasulaitiene, Laser Light Induced Transformation of Molybdenum Disulphide-Based Nanoplatelet Arrays, *Sci. Rep.* **6** (2016).

[539] H. Li, G. Lu, Y. Wang, Z. Yin, C. Cong, Q. He, L. Wang, F. Ding, T. Yu, H. Zhang, Mechanical Exfoliation and Characterization of Single- and Few-Layer Nanosheets of WSe_2, TaS_2, and $TaSe_2$, *Small* **9** (2012) 1974–1981.

[540] O. N. Shebanova, P. Lazor, Raman study of magnetite (Fe_3O_4): laser-induced thermal effects and oxidation, *J. Raman Spectrosc.* **34** (2003) 845–852.

[541] D. L. A. de Faria, S. V. Silva, M. T. de Oliveira, Raman microspectroscopy of some iron oxides and oxyhydroxides, *J. Raman Spectrosc.* **28** (1997) 873–878.

[542] S. D. Harvey, T. J. Peters, B. W. Wright, Safety Considerations for Sample Analysis Using a Near-Infrared (785 nm) Raman Laser Source, *Appl. Spectrosc.* **57** (2003) 580–587.

[543] V. G. Hadjiev, M. N. Iliev, I. V. Vergilov, The Raman spectra of Co_3O_4, *J. Phys. C Solid State* **21** (1988) L199–L201.

[544] M. Rashad, M. Rüsing, G. Berth, K. Lischka, A. Pawlis, CuO and Co_3O_4 Nanoparticles: Synthesis, Characterizations, and Raman Spectroscopy, *J. Nanomater.* **2013** (2013) 1–6.

[545] B. Rivas-Murias, V. Salgueiriño, Thermodynamic CoO-Co_3O_4 crossover using Raman spectroscopy in magnetic octahedron-shaped nanocrystals, *J. Raman Spectrosc.* **48** (2017) 837–841.

[546] A. V. Ravindra, B. C. Behera, P. Padhan, Laser Induced Structural Phase Transformation of Cobalt Oxides Nanostructures, *J. Nanosci. Nanotechnol.* **14** (2014) 5591–5595.

[547] M. S. Faber, K. Park, M. Cabán-Acevedo, P. K. Santra, S. Jin, Earth-Abundant Cobalt Pyrite (CoS_2) Thin Film on Glass as a Robust, High-Performance Counter Electrode for Quantum Dot-Sensitized Solar Cells, *J. Phys. Chem. Lett.* **4** (2013) 1843–1849.

[548] E. A. Vogler, Structure and reactivity of water at biomaterial surfaces, *Adv. Colloid Interface Sci.* **74** (1998) 69–117.

[549] T. T. Paterlini, L. F. B. Nogueira, C. B. Tovani, M. A. E. Cruz, R. Derradi, A. P. Ramos, The role played by modified bioinspired surfaces in interfacial properties of biomaterials, *Biophys. Rev.* **9** (2017) 683–698.

[550] S. Radice, J. Yao, J. Babauta, M. Laurent, M. Wimmer, The effect of hyaluronic acid on the corrosion of an orthopedic CoCrMo-alloy in simulated inflammatory conditions, *Materialia* **6** (2019) 100348.

[551] S. Radice, A. Impergre, A. Fischer, M. A. Wimmer, Corrosion resistance of the nickel-free high-nitrogen steel FeCrMnMoN0.9 under simulated inflammatory conditions, *J. Biomed. Mater. Res. B.* **109** (2020) 902–910.

[552] R. Shah, M. Woydt, N. Huq, A. Rosenkranz, Tribology meets sustainability, *Ind. Lubr. Tribol.* **73** (2021) 430–435.

[553] K. Holmberg, P. Andersson, A. Erdemir, Global energy consumption due to friction in passenger cars, *Tribol. Int.* **47** (2012) 221–234.

[554] K. Holmberg, P. Andersson, N.-O. Nylund, K. Mäkelä, A. Erdemir, Global energy consumption due to friction in trucks and buses, *Tribol. Int.* **78** (2014) 94–114.

[555] K. Holmberg, P. Kivikytö-Reponen, P. Härkisaari, K. Valtonen, A. Erdemir, Global energy consumption due to friction and wear in the mining industry, *Tribol. Int.* **115** (2017) 116–139.

[556] K. Holmberg, R. Siilasto, T. Laitinen, P. Andersson, A. Jäsberg, Global energy consumption due to friction in paper machines, *Tribol. Int.* **62** (2013) 58–77.

[557] T. Mang, K. Bobzin, T. Bartels, *Industrial Tribology: Tribosystems, Friction, Wear and Surface Engineering, Lubrication,* Wiley, Weinheim, Germany (2010).

[558] T. Mang, W. Dresel, eds., *Lubricants and Lubrication,* Wiley, Weinheim, Germany (2017).

[559] E. W. Roberts, Thin solid lubricant films in space, *Tribol. Int.* **23** (1990) 95–104.

[560] E. W. Roberts, Space tribology: its role in spacecraft mechanisms, *J. Phys. D Appl. Phys.* **45** (2012) 503001.

[561] A. Savan, E. Pflüger, P. Voumard, A. Schröer, M. Simmonds, Modern solid lubrication: Recent developments and applications of MoS_2, *Lubr. Sci.* **12** (2000) 185–203.

[562] C. Kajdas, A. Karpińska, A. Kulczycki, Industrial Lubricants, in *Chemistry and Technology of Lubricants,* Springer Netherlands, Dordrecht, Netherlands (2009) 239–292.

[563] J. Daniel, J. Duliškovič, O. Skála, K. Liška, V. Buršíková, T. Fořt, Š. Houdková, Influence of thickness and surface roughness on impact wear and impact lifetime of HVOF-sprayed coatings, *Surf. Coat. Technol.* **488** (2024) 131058.

[564] L. Fang, D.-M. Liu, Y. Guo, Z.-M. Liao, J.-B. Luo, S.-Z. Wen, Thickness dependent friction on few-layer MoS_2, WS_2, and WSe_2, *Nanotechnology* **28** (2017) 245703.

[565] E. W. Roberts, B. J. Williams, J. A. Ogilvy, The effect of substrate surface roughness on the friction and wear of sputtered MoS_2 films, *J. Phys. D Appl. Phys.* **25** (1992) A65–A70.

[566] J. Takadoum, H. H. Bennani, Influence of substrate roughness and coating thickness on adhesion, friction and wear of TiN films, *Surf. Coat. Technol.* **96** (1997) 272–282.

[567] A. Dorner, C. Schürer, G. Reisel, G. Irmer, O. Seidel, E. Müller, Diamond-like carbon-coated Ti6Al4V: influence of the coating thickness on the structure and the abrasive wear resistance, *Wear* **249** (2001) 489–497.

[568] M. R. Vazirisereshk, A. Martini, D. A. Strubbe, M. Z. Baykara, Solid Lubrication with MoS_2: A Review, *Lubricants* **7** (2019) 57.

[570] H. Çiçek, Ö. Gözübüyük, İ. Efeoğlu, Effect of thermal oxidation on structural and tribological properties of MoS_2 films, *Lubr. Sci.* **35** (2022) 144–154.

[571] K. P. Furlan, J. D. B. de Mello, A. N. Klein, Self-lubricating composites containing MoS_2: A review, *Tribol. Int.* **120** (2018) 280–298.

[572] P. J. Blau, Elevated-temperature tribology of metallic materials, *Tribol. Int.* **43** (2010) 1203–1208.

[573] K. Holmberg, H. Ronkainen, A. Matthews, Tribology of thin coatings, *Ceramics International* **26** (2000) 787–795.

[574] Z. Wu, H. Bao, Y. Xing, L. Liu, Tribological characteristics and advanced processing methods of textured surfaces: a review, *Int. J. Adv. Manuf. Technol.* **114** (2021) 1241–1277.

[575] M. Minn, S. K. Sinha, Molecular Orientation, Crystallinity, and Topographical Changes in Sliding and their Frictional Effects for UHMWPE Film, *Tribol. Lett.* **34** (2009) 133–140.

[576] V. Vandalon, A. Sharma, A. Perrotta, B. Schrode, M. A. Verheijen, A. A. Bol, Polarized Raman spectroscopy to elucidate the texture of synthesized MoS_2, *Nanoscale* **11** (2019) 22860–22870.

[577] V. Buck, Lattice parameters of sputtered MoS_2 films, *J. Phys. D Appl. Phys.* **198** (1991) 157–167.

[578] P. D. Fleischauer, J. R. Lince, A comparison of oxidation and oxygen substitution in MoS_2 solid film lubricants, *Tribol. Int.* **32** (1999) 627–636.

[579] Z. Chen, X. He, C. Xiao, S. H. Kim, Effect of humidity on friction and wear-A critical review, *Lubricants* **6** (2018) 74.

[580] C. Muratore, Control of molybdenum disulfide basal plane orientation during coating growth in pulsed magnetron sputtering discharges, *Thin Solid Films* **517** (2009).

[581] P. D. Fleischauer, R. Bauer, Chemical and Structural Effects on the Lubrication Properties of Sputtered MoS_2 Films, *Tribol. T.* **31** (1988) 239–250.

[582] C. Rameshan, M. Ng, A. Shavorskiy, J. Newberg, H. Bluhm, Water adsorption on polycrystalline vanadium from ultra-high vacuum to ambient relative humidity, *Surf. Sci.* **641** (2015) 141–147.

[583] D. Goodacre, M. Blum, C. Buechner, H. Hoek, S. M. Gericke, V. Jovic, J. B. Franklin, S. Kittiwatanakul, T. Söhnel, H. Bluhm, K. E. Smith, Water adsorption on vanadium oxide thin films in ambient relative humidity, *J. Chem. Phys.* **152** (2020) 044715.

[584] S. Descartes, Y. Berthier, Rheology and flows of solid third bodies: background and application to an $MoS_{1.6}$ coating, *Wear* **252** (2002) 546–556.

[585] W. Dai, A. Wang, Q. Wang, Microstructure and mechanical property of diamond-like carbon films with ductile copper incorporation, *Surf. Coat. Tech.* **272** (2015) 33–38.

[586] C. Donnet, A. Erdemir, Solid Lubricant Coatings: Recent Developments and Future Trends, *Tribol. Lett.* **17** (2004) 389–397.

[587] V. An, E. Anisimov, V. Druzyanova, N. Burtsev, I. Shulepov, M. Khaskelberg, Study of tribological behavior of Cu-MoS_2 and Ag-MoS_2 nanocomposite lubricants, *SpringerPlus* **5** (2016) 72.

[588] V. An, Y. Irtegov, Tribological Properties of Nanolamellar MoS_2 Doped with Copper Nanoparticles, *Journal of Nanomaterials* **2014** (2014) 1–7.

[589] A. Bagnall, W. Liang, E. Marseglia, B. Welber, Raman studies of MoS_2 at high pressure, *Physica B+C* **99** (1980) 343–346.

[590] M. Dieterle, G. Weinberg, G. Mestl, Raman spectroscopy of molybdenum oxides, *Phys. Chem. Chem. Phys.* **4** (2002) 822–826.

[591] K. A. Olson, G. L. Schrader, Laser deposition of molybdenum oxide thin films from organometallic precursors, *Mater. Res. Soc. Symp. Proc.* **187** (1990).

[592] A. Magnéli, The Crystal Structure of Mo_4O_{11} (gamma-Molybdenum Oxide). *Acta Chem. Scand.* **2** (1948) 861–871.

[593] L. Mandrile, I. Cagnasso, L. Berta, A. M. Giovannozzi, M. Petrozziello, F. Pellegrino, A. Asproudi, F. Durbiano, A. M. Rossi, Direct quantification of sulfur dioxide in wine by Surface Enhanced Raman Spectroscopy, *Food Chem.* **326** (2020) 127009.

[594] M. N. Gardos, The synergistic effects of graphite on the friction and wear of MoS_2 Films in air, *Tribol. Trans.* **31** (1988) 214–227.

[595] T. N. Walter, F. Kwok, H. Simchi, H. M. Aldosari, S. E. Mohney, Oxidation and oxidative vapor-phase etching of few-layer MoS_2, *J. Vac. Sci. Technol. B Nanotechnol. Microelectron.* **35** (2017) 021203.

[596] H. E. Sliney, Solid lubricant materials for high temperatures-a review, *Tribol. Int.* **15** (1982) 303–315.

[597] R. Ebrahimi Kahrizsangi, M. H. Abbasi, A. Saidi, Model-Fitting Approach to Kinetic Analysis of Non-Isothermal Oxidation of Molybdenite, *Iran. J. Chem. Chem. Eng.* **26** (2007).

[598] M. Yamamoto, T. L. Einstein, M. S. Fuhrer, W. G. Cullen, Anisotropic etching of atomically thin MoS_2, *J. Phys. Chem. C Nanomater. Interfaces* **117** (2013) 25643–25649.

[599] J. Wu, H. Li, Z. Yin, H. Li, J. Liu, X. Cao, Q. Zhang, H. Zhang, Layer thinning and etching of mechanically exfoliated MoS_2 nanosheets by thermal annealing in air, *Small* **9** (2013) 3314–3319.

[600] L. Glasser, Systematic thermodynamics of magnéli-phase and other transition metal oxides, *Inorg. Chem.* **48** (2009) 10289–10294.

[601] F. Predel, Phase diagram of Mo–O (molybdenum-oxygen) system, in *Phase Equilibria, Crystallographic and Thermodynamic Data of Binary Alloys,* Springer, Berlin/Heidelberg, Germany (2016) 81.

[602] W. G. Moffatt, *Handbook of binary phase diagrams,* vol. 4, Genium Publishing Corporation, (1984), 7/84.

[603] W. Gulbiński, T. Suszko, Thin films of MoO_3-Ag_2O binary oxides - the high temperature lubricants, *Wear* **261** (2006) 867–873.

[604] S. Balendhran, S. Walia, H. Nili, J. Z. Ou, S. Zhuiykov, R. B. Kaner, S. Sriram, M. Bhaskaran, K. Kalantar-zadeh, Two-dimensional molybdenum trioxide and dichalcogenides, *Adv. Funct. Mater.* **23** (2013) 3952–3970.

[605] M. Cura, X. Liu, U. Kanerva, S. Varjus, A. Kivioja, O. Söderberg, S.-P. Hannula, Friction behavior of alumina/molybdenum composites and formation of MoO_{3-x} phase at 400°C, *Tribol. Int.* **87** (2015) 23–31.

[606] S.-H. Shim, T. S. Duffy, Raman spectroscopy of Fe_2O_3 to 62 GPa, *Am. Mineral.* **87** (2002) 318–326.

[607] I. V. Chernyshova, M. F. Hochella Jr, A. S. Madden, Size-dependent structural transformations of hematite nanoparticles. 1. Phase transition, *Phys. Chem. Chem. Phys.* **9** (2007) 1736–1750.

[608] M. A. G. Soler, G. B. Alcantara, F. Q. Soares, W. R. Viali, P. P. C. Sartoratto, J. R. L. Fernandez, S. W. da Silva, V. K. Garg, A. C. Oliveira, P. C. Morais, Study of molecular surface coating on the stability of maghemite nanoparticles, *Surf. Sci.* **601** (2007) 3921–3925.

[609] R. M. Cornell, U. Schwertmann, Transformations, in *The Iron Oxides: Structure, Properties, Reactions, Occurences and Uses,* 2nd ed., Wiley-VCH Verlag GmbH & Co. KGaA, Weinheim, Germany (2004) 365–407.

[610] L. Petrás, A. Preisinger, K. Mereiter, Phase transition of iron oxide at high temperature, *Mater. Sci. For.* **278-281** (1998) 396–401.

[611] S. M. Clark, S. G. Prilliman, C. K. Erdonmez, A. P. Alivisatos, Size dependence of the pressure-induced γ to α structural phase transition in iron oxide nanocrystals, *Nanotechnology* **16** (2005) 2813–2818.

[612] S. Park, S. Siahrostami, J. Park, A. H. B. Mostaghimi, T. R. Kim, L. Vallez, T. M. Gill, W. Park, K. E. Goodson, R. Sinclair, X. Zheng, Effect of adventitious carbon on pit formation of monolayer MoS_2, *Adv. Mater.* **32** (2020) e2003020.

[613] A. Kozbial, X. Gong, H. Liu, L. Li, Understanding the Intrinsic Water Wettability of Molybdenum Disulfide (MoS_2), *Langmuir* **31** (2015) 8429–8435.

[614] J. Landoulsi, M. J. Genet, S. Fleith, Y. Touré, I. Liascukiene, C. Méthivier, P. G. Rouxhet, Organic adlayer on inorganic materials: XPS analysis selectivity to cope with adventitious contamination, *Appl. Surf. Sci.* **383** (2016) 71–83.

[615] O. Frank, M. Mohr, J. Maultzsch, C. Thomsen, I. Riaz, R. Jalil, K. S. Novoselov, G. Tsoukleri, J. Parthenios, K. Papagelis, L. Kavan, C. Galiotis, Raman 2D-band splitting in graphene: theory and experiment, *ACS Nano* **5** (2011) 2231–2239.

[616] D. Graf, F. Molitor, K. Ensslin, C. Stampfer, A. Jungen, C. Hierold, L. Wirtz, Spatially resolved Raman spectroscopy of single- and few-layer graphene, *Nano Lett.* **7** (2007) 238–242.

[617] D. Yoon, H. Moon, H. Cheong, J. Choi, J. Choi, B. Park, Variations in the Raman spectrum as a function of the number of Graphene layers, *J. Korean Phys. Soc.* **55** (2009) 1299–1303.

[618] Y. Wang, X. W. Sun, G. K. L. Goh, H. V. Demir, H. Y. Yu, Influence of channel layer thickness on the electrical performances of inkjet-printed in-Ga-Zn oxide thin-film transistors, *IEEE Trans. Electron Devices* **58** (2011) 480–485.

[619] P. Barquinha, A. Pimentel, A. Marques, L. Pereira, R. Martins, E. Fortunato, Influence of the semiconductor thickness on the electrical properties of transparent TFTs based on indium zinc oxide, *J. Non Cryst. Solids* **352** (2006) 1749–1752.

[620] J. Vrielink, R. Tiggelaar, J. Gardeniers, L. Lefferts, Applicability of X-ray fluorescence spectroscopy as method to determine thickness and composition of stacks of metal thin films: A comparison with imaging and profilometry, *Thin Solid Films* **520** (2012) 1740–1744.

[621] M. Mantler, M. Schreiner, X-ray fluorescence spectrometry in art and archaeology, *X-Ray Spectrom.* **29** (2000) 3–17.

[622] J. Jonuscheit, Terahertz Waves for Thickness Analyses: Non-destructive component analysis using terahertz time domain spectroscopy, *Optik & Photonik* **11** (2016) 30–33.

[623] M. Naftaly, N. Vieweg, A. Deninger, Industrial Applications of Terahertz Sensing: State of Play, *Sensors* **19** (2019) 4203.

[624] H. G. Tompkins, *A User's Guide to Ellipsometry,* Elsevier, San Diego, CA, USA (1993).

[625] F. L. McCrackin, E. Passaglia, R. R. Stromberg, H. L. Steinberg, Measurement of the thickness and refractive index of very thin films and the optical properties of surfaces by ellipsometry, *J. Res. Natl. Bur. Stand. A Phys. Chem.* **67A** (1963) 363.

[626] P. A. Spevack, N. S. McIntyre, Thermal reduction of molybdenum trioxide, *J. Phys. Chem.* **96** (1992) 9029–9035.

[627] L. Kumari, Y.-R. Ma, C.-C. Tsai, Y.-W. Lin, S. Y. Wu, K.-W. Cheng, Y. Liou, X-ray diffraction and Raman scattering studies on large-area array and nanobranched structure of 1D MoO_2 nanorods, *Nanotechnology* **18** (2007) 115717.

[628] M. Py, K. Maschke, Intra- and interlayer contributions to the lattice vibrations in MoO_3, *Physica B & C* **105** (1981) 370–374.

[629] J. H. Parker, D. W. Feldman, M. Ashkin, Raman scattering by silicon and germanium, *Phys. Rev.* **155** (1967) 712–714.

[630] T. R. Hart, R. L. Aggarwal, B. Lax, Temperature dependence of Raman scattering in silicon, *Phys. Rev.* **1** (1970) 638–642.

[632] B. Gaković, M. Zamfirescu, P. Panjan, C. Luculescu, C. Albu, S. Petrović, Laser ablation and LIPSS formation at static and dynamic multi-pulse regime on protective Al_2O_3/TiAlN coating, *Opt. Quantum Electron.* **56** (2024).

[633] S. Jeon, C. J. Van Tyne, H. Lee, Degradation of TiAlN coatings by the accelerated life test using pulsed laser ablation, *Ceram. Int.* **40** (2014) 8677–8685.

[634] K. Bobzin, T. Brögelmann, A. Gillner, N. C. Kruppe, C. He, M. Naderi, Laser-structured high performance PVD coatings, *Surf. Coat. Technol.* **352** (2018) 302–312.

[635] M. Kot, W. A. Rakowski, Ł. Major, R. Major, J. Morgiel, Effect of bilayer period on properties of Cr/CrN multilayer coatings produced by laser ablation, *Surf. Coat. Technol.* **202** (2008) 3501–3506.

[636] K. Inumaru, T. Ohara, K. Tanaka, S. Yamanaka, Layer-by-layer deposition of epitaxial TiN-CrN multilayers on MgO(001) by pulsed laser ablation, *Appl. Surf. Sci.* **235** (2004) 460–464.

[637] S. Das, S. Guha, R. Ghadai, D. Kumar, B. P. Swain, Structural and mechanical properties of CVD deposited titanium aluminium nitride (TiAlN) thin films, *Appl. Phys. A Mater. Sci. Process.* **123** (2017).

[638] C. P. Constable, J. Yarwood, W.-D. Münz, Raman microscopic studies of PVD hard coatings, *Surf. Coat. Technol.* **116-119** (1999) 155–159.

[639] H. C. Barshilia, K. S. Rajam, Raman spectroscopy studies on the thermal stability of TiN, CrN, TiAlN coatings and nanolayered TiN/CrN, TiAlN/CrN multilayer coatings, *J. Mater. Res.* **19** (2004) 3196–3205.

[640] G. Strnad, N. Chirila, C. Petrovan, O. Russu, Contact Angle Measurement on Medical Implant Titanium Based Biomaterials, *Procedia Technol.* **22** (2016) 946–953.

[641] Y. Yan, E. Chibowski, A. Szczes, Surface properties of Ti-6Al-4V alloy part I: Surface roughness and apparent surface free energy, *Mater. Sci. Eng. C* **70** (2017) 207–215.

[642] M. D. Wadge, M. J. Carrington, H. Constantin, K. Orange, J. Greaves, M. T. Islam, K. M. Zakir Hossain, T. P. Cooper, Z. R. Kudrynskyi, R. M. Felfel, I. Ahmed, D. M. Grant, Characterization of potential nanoporous sodium titanate film formation on Ti6Al4V and TiO_2 microspherical substrates via wet-chemical alkaline conversion, *Mater. Charact.* **185** (2022) 111760.

[643] S. Wang, Z. Liao, Y. Liu, W. Liu, Influence of thermal oxidation duration on the microstructure and fretting wear behavior of Ti6Al4V alloy, *Mater. Chem. Phys.* **159** (2015) 139–151.

[644] J. Arnoux, G. Sutter, G. List, P. Bourson, H. Chaynes, Raman characterization of Ti-6Al-4V oxides and thermal history after kinetic friction, *Phase Transitions* **87** (2014) 559–570.

[645] K. Singh, S. G. S. Raman, R. Gnanamoorthy, Effect of Thermal Oxidation Duration on Fretting Wear Behavior of Ti6Al4V in Ringer's Solution, *Trans. Indian Inst. Met.* **75** (2022) 1629–1639.

[646] L. Benea, E. Mardare-Danaila, J.-P. Celis, Increasing the tribological performances of Ti-6Al-4V alloy by forming a thin nanoporous TiO_2 layer and hydroxyapatite electrodeposition under lubricated conditions, *Tribol. Int.* **78** (2014) 168–175.

[647] S. Durdu, M. Sancak, E. Yalcin, M. Usta, E. Akagunduz, A. Altinkok, Surface characterization of TiO_2 nanotube arrays produced on Ti6Al4V alloy by anodic oxidation, *Surf. Coat. Technol.* **428** (2021) 127903.

[648] X. Liu, P. Chu, C. Ding, Surface modification of titanium, titanium alloys, and related materials for biomedical applications, *Mater. Sci. Eng. R Rep.* **47** (2004) 49–121.

[649] A. Aladjem, Anodic oxidation of titanium and its alloys, *J. Mater. Sci.* **8** (1973) 688–704.

[650] J. Pan, D. Thierry, C. Leygraf, Electrochemical impedance spectroscopy study of the passive oxide film on titanium for implant application, *Electrochim. Acta* **41** (1996) 1143–1153.

[651] J. González, J. Mirza-Rosca, Study of the corrosion behavior of titanium and some of its alloys for biomedical and dental implant applications, *J. Electroanal. Chem.* **471** (1999) 109–115.

List of author's publications

[82] W. Tillmann, N. F. L. Dias, D. Stangier, A. Nienhaus, C. A. Thomann, A. **Wittrock,** H. Moldenhauer, J. Debus, Effect of the bias voltage on the structural and tribo-mechanical properties of Ag-containing amorphous carbon films, *Diam. Relat. Mater.* **105** (2020) 107803.

[350] A. Wittrock, S. Heermant, C. Beckmann, M. A. Wimmer, A. Fischer, M. Aßmann, J. Debus, Protein-metal interactions due to fretting corrosion at the taper junction of hip implants: An in vitro investigation using Raman spectroscopy, *Acta Biomater.* **189** (2024) 621–632.

[367] A. Wittrock, A. Wittig, C. A. Thomann, D. Stangier, N. F. Lopes Dias, W. Tillmann, J. Debus, Spectroscopic Study of Strain, Oxidation, and Formation of Few-Layer Graphene at Steel Surfaces Tribologically Tested against MoS_2 Films, *ACS Appl. Mater. Interfaces* **16** (2024) 54818–54828.

[371] A. Fischer, P. Telouk, C. Beckmann, S. Heermant, A. **Wittrock,** J. Debus, M. A. Wimmer, Performance of Austenitic High-Nitrogen Steels under Gross Slip Fretting Corrosion in Bovine Serum, *J. Funct. Biomater.* **15** (2024) 110.

[384] A. Fischer, C. Beckmann, S. Heermant, A. **Wittrock,** P. Telouk, J. Debus, M. A. Wimmer, Topography rules the ultra-mild wear regime under boundary lubricated gross-slip fretting corrosion, *Wear* **522** (2023) 204716.

[464] A. **Wittrock,** C. Beckmann, M. A. Wimmer, A. Fischer, S. M. Das, C. H. Liebscher, J. Debus, Formation of quasi-2D CoS_x tribomaterial at hip implant taper junction, *Acta Biomater.* (submitted).

[569] A. **Wittrock,** N. F. Lopes Dias, W. Tillmann, J. Debus, Determining the thickness of curved coatings by Raman scattering combined with laser ablation, *Appl. Phys. Lett.* (In preparation for submission).

[631] C. A. Thomann, A. **Wittrock,** A. Wittig, N. F. Lopes Dias, D. Stangier, W. Tillmann, J. Debus, Tuning of solid-to-solid structural transitions in amorphous carbon films by optical pumping and chemical modification, *APL Mater.* **11** (2023) 031106.

Acknowledgements

Finally, it is time to express my deepest gratitude to everyone who has supported me during the course of this thesis.
First and foremost, I thank my supervisor, Dr. Jörg Debus, for the possibility to conduct my PhD in his group and explore the fascinating interdisciplinary field of tribology. His expertise, continuous support, and constructive feedback have greatly contributed to the success of this work. I would also like to express my gratitude to Prof. Dr. Carsten Westphal, who introduced me to the world of physics during my first lectures and has graciously agreed to serve as the second reviewer for my thesis.
I am grateful to all project partners for their assistance, advice, and encouragement during my academic journey. I have greatly enjoyed the interdisciplinary collaboration with the mechanical engineers, which I found both exciting and very fruitful. The diverse perspectives we bring to our work have been incredibly enriching and instructive, not only from a scientific standpoint but also personally. I would especially like to thank Prof. Dr. Alfons Fischer for his many insightful explanations and engaging conversations. I learned a great deal from him, particularly about tribological processes and material sciences. My sincere thanks also go to Prof. Dr. Christian Liebscher and Prof. Dr. Markus A. Wimmer for their excellent cooperation in the experiments and writing process. Additionally, I would like to thank my colleagues Dr. Alexandra Wittig, Dr. Dominic Stangier, Bennett Sprafke, Daniel Aurich, and especially Dr. Nelson Filipe Lopes Dias for the enjoyable close collaboration and our numerous meetings - whether over burgers, coffee, cocoa, or cake - where we not only had scientifically stimulating and inspiring discussions but also shared many enjoyable moments.
I would also like to express my sincere thanks to my Bachelor's and Master's students for contributing to my personal growth. I am especially grateful for the supportive and positive atmosphere they helped create in the lab, making even the longest measurement sessions enjoyable (even during COVID-19). Their contributions have significantly enriched my research experience. I would like to extend a special thank you to Saskia Heermant and Christian Beckmann, who not only became valued PhD students but also close friends.
I would like to extend my thanks to my colleagues for their warm welcome and constant support throughout my thesis journey. The list of individuals is too long to mention here, but each of you, in your own way, has contributed significantly to my growth - whether through shared knowledge, constructive feedback, or simply offering a friendly environment that made daily work enjoyable. I truly appreciate the collaborative spirit and camaraderie that made even the most challenging moments during my PhD student time more manageable.
Additionally, I would like to express my gratitude to our secretary Michaela Wäscher for her constant administrative support. My thanks also go to our technician, Lars Wieschollek, whose expertise and assistance were essential in ensuring that all technical aspects of the lab were taken care of and liquide nitrogen is provided.

I would like to express my immense gratitude to everyone who helped me with proofreading my thesis: Dr. Carl Arne Thomann, Dr. Nelson Filipe Lopes Dias, Katharina Bartsch, and especially Daria Wittrock. Your meticulous attention to detail and thoughtful suggestions greatly improved the clarity and quality of this work. I am deeply thankful for the time and effort you dedicated to reviewing my thesis. Additionally, I would like to thank all of my friends for making my studies so enjoyable. Your support, encouragement, and the many moments of joy and laughter throughout these years made the challenges of academia more manageable and rewarding. Each of you, in your own way, contributed to creating a balanced and fulfilling experience during my studies.
I would especially like to express my heartfelt gratitude to my parents, Dorothee and Andreas Wittrock, for their continuous and unwavering support throughout my entire life. Their love, encouragement, and belief in me, even during the most challenging times, have been a constant source of strength. I am deeply thankful for the sacrifices they made and for always being there, offering guidance, warmth, and the kind of support that made everything possible. I am equally grateful for the wonderful, unconditional friendship I share with my sister, Daria. Your constant presence, understanding, and ability to make even the most challenging moments brighter have been a true gift. I couldn't imagine a better sister, and I feel incredibly fortunate to share such a strong and meaningful bond with you. A special thank you goes to my girlfriend, Katharina, whose love, care, and emotional support have been invaluable. Through the ups and downs, she has stood by my side, providing not only understanding and motivation but also joy and balance in my life. I am truly lucky to have such a loving and supportive family and partner by my side.